Cranfield University

School of Engineering

Ph.D. Thesis

J.B.M Pierce

Prediction of Smoke Properties and Obscuration in Compartment Fires

Supervisor: Professor J.B.Moss

December 2002

This thesis is submitted for the degree of Doctor of Philosophy

Abstract

This study describes the simulation and experimental investigation of a heptane pool fire, burning within a small compartment, in which interaction between a number of key physical processes is amplified. In particular, the configuration emphasises the coupling of buoyancy induced ventilation, smoke production and radiation heat transfer to the liquid fuel surface, from the luminous flame zone, from the smoke filled ceiling layer and from the confining walls. This study contrasts with those customarily performed for the purpose of model validation in compartment fires, which employ gas burners and so simplify much of the interaction.

Initial experiments were carried out using a 0.23m diameter circular pan burning fixed amounts of heptane. Subsequently, a constant supply was used with a smaller circular pan of 0.17m in diameter, in order to introduce experimental longevity under safe, controllable conditions whilst establishing a quasi steady-state system. Issues of non-stationarity in relation to heat-feedback to the fuel surface - an important pool fire mechanism - are discussed.

In addition to probe measurements of velocity and thermocouple temperature, the smoke yield was determined using a light extinction technique employing a 670*nm* wavelength diode laser and photo-diode detector, housed within a novel fully-traversible water-cooled probe. Data from these experiments illustrate the importance of accounting for room ventilation in terms of overall production of smoke and sound a cautionary note to the labelling of soot by a convenient marker such as temperature.

Numerical simulation of the compartment fire is performed using the field model SOFIE,

incorporating a simple evaporation model, which relates the mass-loss-rate of fuel to the net heat flux to the fuel surface and heat of gasification. This relationship assumes that heat losses to the pan, re-radiation by the fuel surface and other enthalpy loss terms, are small. Simulations of compartment fire scenarios using this model to calculate the rate of heat release are reported. Further comparisons are made between the industry standard 'Eddy-Breakup' combustion model and the 'Laminar Flamelet' model. In general both the eddy-breakup model and laminar flamelet model tend to underpredict the yields of CO, whilst the eddy-breakup model over-predicts temperature and thus soot. The laminar flamelet approach shows more promise and shows particularly good agreement with the experimental measurements reported here under well ventilated conditions.

SOFIE, the predictive tool employed in this research, has proved invaluable in discerning the reason for apparent ambiguities in the experimental measurements of soot concentration. The results suggest that an alternative simplified zone model approach would overpredict visibility in smoke in terms of concentration, but underpredict in terms of layer depth, due to its inability to capture the important shape of the hot upper layer, which varies significantly from the homogenous, laterally uniform distribution which is assumed. The incorporation of a simple evaporation model which relies on accurate prediction of heat transfer in ultimately determining the heat release rate has been shown to be in very good agreement with the experiments. Despite the irregularity in predicted distribution of mass loss rate across the fuel surface - caused mainly due to the 'ray effect' of the radiation model - the main trend of lower heat transfer at the centre of the burner is demonstrated, in agreement with the experiments performed. This phenomenon is captured despite the lack of description of fuel vapour radiation blockage above the fuel surface, suggesting that this process may be disregarded. The heat flux distribution which is found here is in contrast to research conducted by other workers for similar sized pans in an open environment, which show a higher measured heat transfer at the centre of the burner.

It has been shown that significant improvements could be made in experimental design

of compartment fire experiments if CFD prediction is considered for the determination of suitable measurement locations in regions with lower local spatial variations.

"For every problem,
there is a solution that is
simple, neat and wrong".

(H.L Mencken)

Acknowledgements

Many people have contributed in their own important way to this work. Without them none of this would have been achieved. My gratitude must lay firstly with my supervisor Professor Barrie Moss for his patience and support throughout all the "trying times" brought about by my sometimes inexplicable and tangential approach. Thank you. All of the technicians that I worked with in the test area, especially Dick Kennewell. The rest of the combustion group at Cranfield for their support and encouragement - particularly Victoria Sanderson for her SOFIE knowledge base and the late Cecil Stewart for his experimental assistance, improvisation and Bach duets. To all staff at the FRS division of BRE, in particular Steve Welch who has supported me in all aspects throughout.

Lastly for my family, particularly my Mother and Grandmother and my husband Nic', for all the sacrifices we had to make and who married me nonetheless!

Funding of this research was provided by EPSRC and is gratefully acknowledged.

Tempus fugit...

Nomenclature

A	Arrhenius pre-exponential coefficient
$\bar{C}_p$	Mean mixture specific heat
C,Cr	Model coefficients
D	Distance
d_p	Soot Particle Diameter
E	Arrhenius activation energy
e	Rate of strain
F(x)	Velocity similarity function
f_v	Soot volume fraction
Fr	Froude number
G(x)	Velocity similarity function
G	Gibbs free energy
g_i	Species i specific free energy
G	Buoyancy turbulence generation term
g	Acceleration due to gravity
H	Specific enthalpy
h_i	Species i specific enthalpy
I	Radiation intensity
k	Thermal conductivity
k	Turbulent kinetic energy
k_i	Arrhenius reaction rate
l	Length
ℓ	Characteristic lengthscale

$\dot{m}_i$	Species i mass diffusion flux
N_i	Number of moles of species i
N_o	Avogadros number
Nu	Nusselt number
n	Number of soot particles
P	Production term
P	Pressure
Pr	Prandtl number
p	Partial pressure
$P(\phi)$	Probability density function
$\dot{q}$	Heat flux
R,Ra	Species mass fraction reaction rate term
Re	Reynolds number
R_t	Turbulence Reynolds number
S	Source term
S	Specific entropy
s	Stoichiometric mass ratio
t	Time
T	Temperature
u_i	i direction velocity component
V_i	Species i diffusion velocity
W_i	Species i molecular weight
X_i	Species i mole fraction
Y_i	Species i mass fraction

Greek

α	Soot model nucleation term (number density)
β	Soot model coagulation term
γ	Soot model surface growth term
Γ	Soot model collisional frequency
Γ_ϕ	Effective scalar viscosity
δ	Soot model nucleation term (soot mass)
ε	Turbulence eddy dissipation rate
ζ	Conserved diffusion flame property
κ_v	Radiation absorption coefficient
μ	Viscosity
ξ	Mixture fraction
$\widetilde{\xi''^2}$	Mixture fraction variance
ρ	Density
σ_t	Prandtl-Schmidt number
σ	Stefan-Boltzman constant
τ	Shear stress
τ	Thermocouple time constant
τ_{chem}	Chemical timescale
ϕ	Equivalence ratio
ϕ	Scalar variable
ω	Soot model oxidation term
$\dot{\omega}_i$	Species chemical production rate
$\mathcal{D}$	Coefficient of mass diffusion

Subscripts

bg	Background signal
c	Corrected value
f,fuel	Fuel
ref	Reference signal or value
sig	Measured signal
g	Gas
k	Kolmogorov scale
mix	Mixture mean value
o	Integral scale
ox	Oxidizer
r,net	Net radiation
s	Solid
s	Soot
t	Turbulence
w	Wall
	0
Oxidizer stream	1
Fuel stream	

Superscripts

$\bar{}$	Reynolds (time) averaged
$\bar{\imath}$	Reynolds (time) averaged ; fluctuating component
$\tilde{}$	Favre (density weighted) averaged
$\tilde{\imath}$	Favre (density weighted) averaged; fluctuating component

Contents

List of Figures

List of Tables

Chapter 1

Introduction

1.1 Background

1.1.1 Introduction

"...Oh the miserable and calamitous spectacle! such as haply the world had not seen since the foundation of it, nor be outdone till the universal conflagration thereof. All the sky was of a fiery aspect, like the top of a burning oven, and the light seen above 40 miles round for many nights. God grant mine eyes may never behold the like, who now saw above 10,000 houses all in one flame; the noise and cracking and thunder of people, the fall of towers, houses and churches, was like an hideos storm, and the air all about so hot and inflamed that at last one was not able to approach it, so that they were forced to stand still and let the flames burn on, which they did for near two miles in length and one in breadth. The clouds also of smoke were dismal and reached in computation near 50 miles in length. Thus I left it this afternoon burning, a resemblance of Sodom, or the last day. It forcibly called to my mind that passage - *non emim hic habemux stabilem civitatus*: the ruins resembling the pictures of Troy. London was, but is no more! Thus I returned...".

Despite the lack of a fundamental appreciation of the special and complex relationships

created by the physical and chemical interaction between a fire and its environment[1], to say nothing of his dubious powers of distance estimation, John Evelyn, along with Samuel Pepys, provides us with our best glimpse into the social world of 17th century London and the 'Great Fire' of September 2 , 1666. This tragedy destroyed around four-fifths of the city, including roughly 13,200 houses, nearly 90 parish churches and 50 livery company halls - in all an area more than 430 acres. Astonishingly, only 16 lives were lost.

Figure 1.1: Great Fire of London 1666

The 'Great Fire of London' provided much impetus with respect to traditional building techniques in their application to fire safety. The case studies summarised below serve as a reminder that even today, over 300 years later, there is still much to be learned...

1.1.2 UK Fire Statistics

In 1993 it was estimated [2] that the gross cost of building fires from insurance claims amounted to some £424 million for commercial property and £224 million for domestic property. This figure however is not truly representative for domestic property as it was found by the British Crime Survey (BCS) [3] that one third of households were not insured against domestic fire loss. In the same survey details of the place of origin of fires and their spread to other parts of the building are also published. It was discovered that two thirds of all building fires in England and Wales originated in the kitchen, with the next most common room being the lounge/dining room. Table 1.1 illustrates the

[1] Indeed it was during this period that the hypothesis of phlogiston was propounded and was to remain unchallenged for a further 100 years.

BCS findings for years 1994-1996. Of additional importance is the fact that fires which originated in the kitchen rarely spread to other rooms in the building and only one tenth of fires originating elsewhere did so. Over half (58%) of household fires reported were caused by cooking accidents, of which the largest percentage (26%) involved fat or oil catching fire.

Table 1.1: Origin of fire in domestic dwellings[2,3]

	1994 BCS %	1996 BCS %
Kitchen	66	65
Lounge/dining room	18	14
Bedroom	6	7
Bedsit	-	1
Other place in the house	4	3
Garage	1	2
Shed/greenhouse	2	1
Garden	2	4
Other outside the house	3	4
Total	100	100

The experiments conducted in this research and the associated modelling follow the main trend of these statistics in examining the phenomenon of fire by looking at the most common scenario in its application to single rooms, that is with no spread to other parts of the building. The data from these can nevertheless be extrapolated in terms of quantification of the products of combustion exiting the system, with potential for travelling remote from the fire source. Although their ability to do so is recognised, an analysis is beyond the scope of this thesis. Parameters relevant to human tenability in building fires are directly compared throughout with the extensive research of Jin [4, 5] *q.v.*

[2]Columns do not necessarily total 100% because of rounding.
[3]Source 1994 and 1996 BCS (weighted data). Covers England and Wales.

Smoke produced in building fires hinders the escape of occupants by obscuring signs and egress routes and by impairing respiration and mobility. It thus represents the major life-threat in very many fire scenarios, and, along with CO inhalation, accounts for around 60% of all fire deaths. In response, numerical simulation of smoke movement in building fires, using field modelling techniques, has become an established component of the design process for complex building layouts and fire safety provision. Many important quantitative aspects of such simulations - for example, the rate of fire growth or the concentration of buoyantly transported smoke and toxic gases - are, however, simply prescribed or inferred from empirical correlation, rather than computed in the course of the simulation. However, it is desirable in the context of room fires, to be able to relate parameters such as the mass loss rate (MLR) of fuel and the ventilation provision to the amount of smoke produced. More comprehensive models of the fire source are therefore needed if accurate predictions of life-threat are to form part of these assessments.

1.1.3 Recent Case Studies

The following case studies exemplify where the presence of smoke on escape routes led to deaths of individuals. They also serve to illustrate the fast growth in fire development and the slowness of people to recognise the need to escape.

King's Cross Underground Fire

The tragedy on 18th November, 1987, at the King's Cross underground station, resulted in the loss of 31 lives including 1 fire-fighter.

The station comprises a complex system of tunnels, passageways and escalators on five levels, serving the Picadilly, Victoria, Metropolitan, Northern and British Rail lines. The fire occurred at 7.30pm when the station was busy. A Public Enquiry was held with the main aim of discovering the fire origin, what led to a flashover and why the fire resulted

in such a large loss of life. The most probable cause of fire was ascertained from a matrix of forensic evidence, experimental scale models, computer simulations and eye witnesses.

The enquiry concluded that the culprit was a discarded lit match which fell between the edge of the escalator tread and the skirting board onto the running board beneath - igniting accumulated grease and dust. Once the fire was detected by passengers, one pressed the emergency stop button which stopped the escalator. The principal mechanism of fire growth up the escalator was explained by scientists at Harwell and the Health and Safety Executive (HSE) by the 'trench effect'. This is described as follows. Once the flames extended across the full width of the escalator they would only be able to entrain air from above or below. An upward inclined slope (in this case 30°) would cause the flames to lean towards the slope so that they lay down along and within the trench. Once the flame plume 'laid down' in the trench, fire spread accelerated dramatically. Also, the perceived hazard would be less and the fire would look relatively innocuous. Fifteen minutes after detection, the fire conditions dramatically changed as flashover occurred. The flames preheated the wood and extended rapidly, channelling up the escalator trench. As the fire grew it involved fascia boards, advertisements, ceiling and ceiling paint in the escalator shaft. A jet of flame emerged from the top of the escalator, igniting materials in the ticket hall. The fatalities were due to smoke inhalation and/or flames. The enquiry's recommendations included the need to improve the fire precautions, communication and housekeeping, to develop emergency and emergency training procedures, to replace old escalators and to make the management of safety less diffuse.

Gothenburg

On October 28th, 1998, a fire occurred in a nightclub in Gothenburg, Sweden. It was estimated that there were around 400 people in attendance, whereas the dance hall was only licensed to hold a maximum of 150 people.

The following significant factors were considered as to have contributed to the loss of

life and property.

- Overcrowding
- Lack of a fire alarm system
- Ignition of combustible storage in a stairwell

There were no automatic fire sprinkler or fire alarm systems in the building, although there were lighted exit signs at each end of the hall. Shortly before midnight, the disc jockey opened a door leading to a stairwell. Smoke from the stairwell came into the hall. It is unknown whether the door was closed again after the fire was detected. The stairway was impassable and was not used during the evacuation. Realising how crowded the hall was, the disc jockey after ringing the fire brigade, broke out a window and jumped from the building. As fire officers approached the building a large number of injured parties lay below windows after jumping from the second storey. As a result, fire-fighters were unable to place ground ladders up to the windows of the building. However, a fire-fighter was able to enter the dance hall through one of the windows and stated that the interior was "dark, smoky and hot, but that there was not any heavy fire involvement at this time".

A total of 63 people died in the fire, mostly from smoke inhalation and a further one hundred and eighty people were injured.

1.1.4 Introduction to Compartment Fire Experiments

The standard room fire experiments which have been used for field model development and evaluation, such as those reported by Steckler et al [6] for example, generally employ gas burners and weakly sooting fuels like methane. Whilst the computation of heat exchange is important to the fluid dynamic behaviour of fire plumes and ceiling layers, the sensitivity to detailed soot concentration levels is generally small and, in particular,

the fuel flow rate is entirely decoupled from the radiation field. Larger scale experiments involving liquid fuels often embrace both weakly and heavily sooting specimens, like methylated spirits and kerosine, but detailed measurements, most notably of spatially distributed properties such as smoke concentration, tend to be limited.

The experiments in this study are therefore intended as a compromise between complexity in relation to the fuel source and its interaction with the confining walls of the compartment, realism as a simulation of practical relevance and accessibility to the detailed measurement necessary for field model validation.

A feature inherent in the production of smoke and other stable gaseous species such as CO from which is derived much concern in the realms of fire safety, lies in their ability to be transported over great distances remote from the fire source. Whereas in the majority of cases, as already mentioned, fires in buildings are contained in a single room [3], the majority of fire deaths occur remotely from the fire source. In addition, due to the relatively cool nature of soot at such distances, the indoor environment becomes a necessary feature to be considered - particularly in the case of heated, ventilated and air conditioned (HVAC) buildings where the smoke may become stratified - an issue of obvious importance regarding visibility in smoke. Other methods of active fire protection, such as the interaction of smoke with sprinkler spray, could exacerbate this effect by encouraging smoke logging [7]. Other factors, for instance building evacuation and fire rescue situations, can potentially have important influences on ventilation conditions as doors are opened and shut, or windows broken [8]. Of additional importance is adequate smoke detector response, which has been shown to be particularly sensitive to the rate of soot particle coagulation [9] *inter alia*. This is further discussed in the literature survey. The present work in essence seeks to contribute to the continuing effort to build more accurate models of this particular fire hazard, specifically directed towards compartment fires.

Combustion is an exothermic reaction which is dependent upon the nature of the fuel, the oxidant and the ignition energy. The fuel must be in a gaseous form and, for liquid

fuels, the conversion to vapour form occurs due to evaporation. Evaporation can occur within a wide range of temperatures depending upon the equilibrium vapour pressure of the liquid. In the case of solid fuels, the vaporisation process is known as pyrolysis and involves the thermal decomposition of the solid into a gaseous form. The gaseous fuel must be in the presence of sufficient oxygen in order to produce a combustible mixture of fuel and oxidant.

One of the physically characteristic features of a compartment fire is the development of a hot ceiling layer in which the combustion products accumulate. The formation of this layer is important in the early stages of fire growth and ultimately to the phenomenon of flashover. During the early stages of fire development, air is entrained into the rising plume, setting up rapid mixing of the combustion products which are usually well segregated in a well-stirred ceiling layer whose properties are roughly homogenous. As the layers are stably stratified, little mass crosses the interface.

The transition to a fully developed fire is called a 'flashover'. A theoretical treatment of the flashover phenomenon effectively involving the fundamentals of classic explosion theory has been demonstrated by Thomas et al [10]. Further development of this approach has also been made by Bishop et al [11] with the application of modern non-linear dynamics.

Visually, flashover has been reported as a discrete event in full-scale tests and by the fire service in actual fire incidents. Numerous variables can affect the transition of a compartment fire to flashover. Thermal influences where radiative and convective heat flux are assumed to be the driving forces are clearly important. Ventilation conditions, compartment volume and the chemistry of the hot gas layer can also influence the occurrence of flashover. The rapid transition to flashover adds to the uncertainty of attempts to quantify its onset with laboratory measurements.

The occurrence of flashover within a room is of considerable interest since it is perhaps the ultimate signal of untenable conditions within the room of fire origin and a sign of greatly increased risk to other rooms within the building. Many experimental studies

of full-scale fires have been performed that quantify the onset of flashover in terms of measurable physical properties.

Research has shown, that the following values for the upper gas layer temperature and heat flux at the floor appear to be predictive of the onset of full-room involvement: upper gas layer temperature >600°C or heat flux to the floor >20kW/m^2.

Analytical models for predicting fire growth have been evolving since the 1960's. During this time, the comprehensiveness of the models has grown. These models have progressed to the point of providing predictions of fire behaviour with an accuracy suitable for engineering applications. The advent of CFD modelling has introduced a further dimension in which the boundaries of understanding the largely intractable eccentricity of compartment fires draw ever closer. These models, classically known as 'field models', in reference to their solution of field equations, make fewer assumptions about the nature of the fire, or make them at a more microscopic level, and represent the physics and chemistry of the problems more fully than zone models. Recent advances with computer technology, in particular its capacity, have meant increasing accessibility of these 'field models'.

For ease of classification, the following are those typically depicted as being the various stages of fire growth in a compartment fire.

1. *Ignition.* The ignition of flammable mixture, i.e a mixture of fuel and oxidant which is above the lower flammability limit, requires sufficient energy to initiate the combustion reaction which is dependent upon the mixture. This energy can be in the form of a spark, or a surface or local air volume sufficiently high in temperature.

2. *Growth.* Following ignition, fire grows at a rate dependent upon *inter alia,* the type of fuel, access to oxygen and the configuration of the compartment. Heat transfer to contiguous and nearby combustible surfaces can raise these to temperatures at which they will begin to burn. The gaseous phase may be viewed as a

primary energy transmitter between the burning and virgin fuel. During this stage, hot gases produced by the fire rise due to buoyancy entraining the surrounding air and a fire plume is formed. Impingement of a fire plume on the ceiling of the compartment gives rise to formation of a hot smoke layer in the upper part of the room.

3. *Flashover*. Flashover is a rapid transition from the growth period to a fully developed fire, causing the remaining fuel to outgas, resulting in the total surface of the combustible material being involved in the fire. Flashover represents a thermal instability caused primarily by strong radiation from the smoke layer to combustible materials within the enclosure.

4. *Fully developed fire*. At this stage, the rate of heat release reaches its maximum and the development of the fire is often limited by the availability of the oxygen. The average temperatures in the compartment are very high, in the range of 700-1200°C.

5. *Decay*. During this stage, the energy release rate diminishes as the fuel is consumed or the supply of oxidant is exhausted.

For ease of illustration, figure 1.2 depicts these stages graphically. The broken line represents depletion of fuel before flashover has occurred, or alternatively, indicates that the available oxygen has been consumed in a closed room environment.

Elevated levels of soot and CO are produced under fuel rich conditions such as those found in a post flashover room when the fire is no longer controlled by the amount of fuel available, but by the amount of air entering the room. At this point, conditions in the room containing the fire source are untenable, but the danger has now been re-located by convecting these combustion products to other areas within the building. Depending upon the circumstances of ventilation provision, they are capable of travelling distances far removed from the origin [12]. This in turn exacerbates the level of soot and CO which is produced by promoting vitiation, in which air which has been contaminated

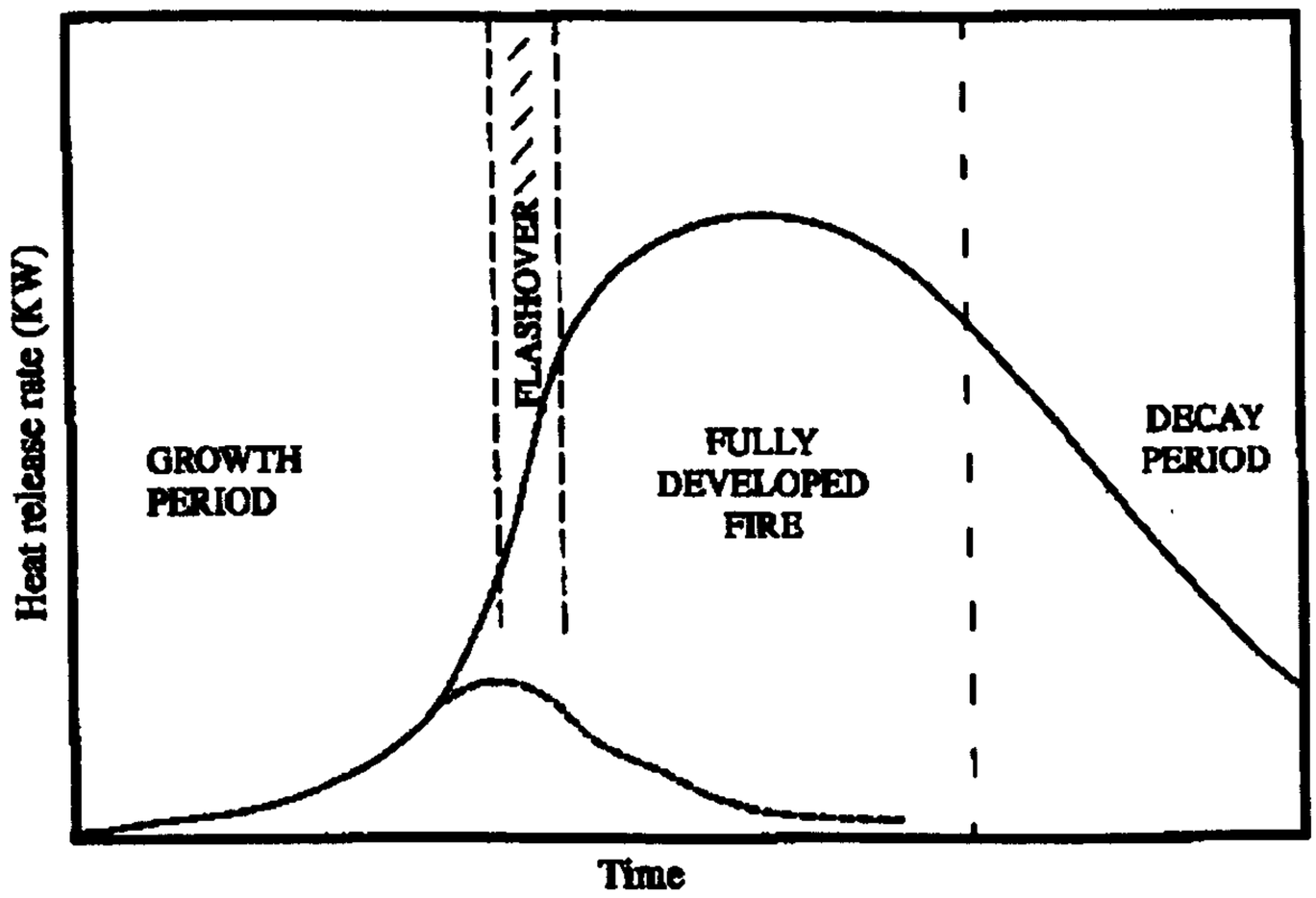

Figure 1.2: Stages of fire growth in a well ventilated compartment fire

is entrained into the fire plume causing a local reduction in ambient oxygen levels, and in so doing reduces the actual combustion temperature. This synergy then leads to the generation of more products of incomplete combustion.

In the interest of safety, the experimental parameters of the research in this study are restricted to consideration of well-ventilated fires only. In these the effect of only partial vitiation is apparent. However, the interest in, and indeed the main objective of, the research lies in the requirement for a simple reproducible experiment on which to base and validate predictive models which can then be suitably extended to best serve actual real-life scenarios, in which building design and layout may be complex.

Additionally, full-scale fire experiments are costly to perform, with many unknown parameters which are difficult to probe in sufficient detail to minimize the risk of ambiguity. The half-scale room is a suitable compromise between scale and the improvement of accessibility to these unknowns. Advances in computer processing power has encouraged the twin-track approach of experiment versus numerical simulation. Accordingly, numerical methods devoted to the area of combustion have been popularised. In the context of compartment fires this is in the area of heat transfer, buoyancy, soot formation, gas radiation and absorption, and low Reynolds number turbulence.

Following this introduction, Chapter 2 will review the existing literature and expand in detail on the necessary theory, background and methodology employed in the present work. Chapter 3 will describe the experiments carried out on compartment fires in various scenarios and present the results. Here the objective is to adequately map the distribution of soot and discover the effects of parameter variations in each compartment fire investigated. Chapter 4 makes a comparison of the enclosure fire experiments with an open pool fire configuration burning a number of fuels utilising identical burners. These open pool fires allow the investigation of several conditions which were difficult to demonstrate and reproduce physically within the confines of a compartment. Chapter 5 will introduce the physical models employed in the finite volume CFD code SOFIE (Simulation of Fires in Enclosures), which is under continual development at Cranfield University. Chapter 6 continues by presenting the results of the compartment fire simulations, which are carried out under several different scenarios for each of which exists an equivalent experiment. The objective of this chapter is to investigate the underlying physics of the various stages in soot production, from soot inception to its oxidation, by verification of the models already implemented in SOFIE against measurements made in the compartment. In addition, recommendations are also made regarding the use of a simple evaporation model relating the mass loss rate of fuel to the net heat flux to the fuel surface and heat of vapourisation. A comparison is then made between the results of these simulations and those comprising the more common approach of pre-prescribing the heat release, but based upon real mass loss measurements as made in the compartment and an ideal heat of combustion. Chapter 7 will bring together the various components and compare the results finishing with a summary of the conclusions and recommendations for future work.

Chapter 2

Literature Review and Methodology

2.1 Introduction

This chapter contains a review of the published literature in the global context of compartment fires, but more specifically geared towards the production of soot.

During the mid-seventies, extensive research was carried out by Jin [5] into human tenability in building fires. The main focus of the research was the development of a model whereby the level of soot concentration could be directly related to visibility therein. Although the model correlations are of a simplistic nature, the research is still commonly cited and forms the basis of the validation of much more complex models. Prediction of smoke production and its properties in latter years has gained much ground, prompted in part by the number of deaths attributed to the inhalation of toxic gases and smoke [13].

There are great number of very good recent examples where adequate representation of smoke in a building fire could have saved many lives. One example which has already been mentioned is the fire at Kings Cross underground station, London which resulted in the loss of 31 lives. The majority of fatalities were attributed to a 'fireball' (flashover) which engulfed the main ticket hall and the accumulation of dense smoke in areas above

the escalators which were the only means of escape [14]. Research conducted on small scale models at the Building Research Establishment, Watford concluded that the fire which started beneath wooden escalators built in the 1950's was enhanced by the trench effect in which the flames were directed at an angle of 30°.

Improvements to fire safety in underground stations were immediately effected. Wooden escalators in all London underground stations were removed and significant active and passive fire safety improvements were implemented.

2.2 Compartment Fire Experiments

A number of important issues still surround 'typical' enclosure fire experiments - particularly in the validation of zone models which rely on the simplified assumption that the compartment may be segregated into two well separated homogenous layers. In well cited studies such as those of Satoh et al [15], Steckler et al [6], Markatos et al [16] and Simcox et al [17], the effect of environmental factors such as the thermal stratification of the ambient medium surrounding the opening or the thermal stratification generated within the enclosure did not receive much attention. However, a considerable amount of work has been done on external flows such as plumes and boundary layers in the presence of a stable, thermal ambient stratification.

A fire within an enclosure interacts with its surroundings through the opening. The ambient medium may be thermally stratified by some earlier fire activity or by a fire in a different location. It is well known that, in such natural convection flows, the mean velocity levels are typically smaller and the disturbance levels much larger than those observed in forced flows. This disturbance or turbulence level is of interest, because it enhances mixing and thus promotes transport of both momentum and energy. As a result, a well-mixed region of essentially uniform temperature is generated in the compartment fire. The stratification level is also of particular importance because its influence is felt in two ways. At first, in an enclosure fire, it affects the location of

the interface between the hot combustion products and the cold inflow at the bottom (hot-cold interface) by inhibiting the rise of fire or thermal plume above the heat source. The knowledge of the location of this hot-cold interface is, therefore, very crucial to the detection and control of a fire. Secondly, when the thermal stratification is stable, it results in a decay of the turbulence and, hence, leads to a relaminarisation of the flow. This may alter the transport processes and distort the simplistic concept of two homogenous gas layers.

2.2.1 Ventilation-controlled Burning

The rate of burning and consequent heat release rate may be ventilation-controlled or fuel-controlled.

In rooms with small or medium sized windows, post-flashover fires are ventilation controlled, so the rate of combustion depends on the size and shape of ventilation openings. It is usually assumed that all window glass (other than wired glass or fire resistant glass) will break and fall out at the time of flashover as a result of the rapid rise in temperature. If the glass does not fall out, the fire will still be ventilation controlled, but because of the smaller openings it will burn for a longer time at a lower rate of heat release.

In a ventilation-controlled fire, the rate of combustion is limited by the volume of cool air that can enter and the volume of hot gases that can leave the room. There is insufficient air flow for all the combustible gases to burn inside the room, so the flames extend out of the windows and additional combustion takes place where the hot unburned gaseous fuel mixes with the outside air. For a room with a single opening, Kawagoe [18] used many experiments to show that the mass loss rate of burning wood fuel in the form of cribs $\dot{m}$ can be approximated by:

$$\dot{m} = 0.092 A_v \sqrt{H_v} (kg/s) \tag{2.1}$$

where A_v is the area of the ventilation opening (m^2), and H_v the height of the ventilation

opening (m).

The dependence of burning rate on $A_v\sqrt{H_v}$ has been observed in many studies. This is often expressed in terms of an opening factor F_v given by:

$$F_v = A_v\sqrt{H_v}/A_1(m^{0.5}) \tag{2.2}$$

where A_1 is the total area of the bounding surfaces of the room (m^2) excluding the area of the vent.

Equation 2.1 is widely used, but not always found to be accurate. Even if the burning rate is known precisely, the calculation of heat release rate is not accurate because an unknown proportion of the pyrolysis products burn as flames outside the ventilation opening rather than inside the compartment. Other sources of uncertainty arise because some proportion of the fuel may not be available for combustion and the fire may change to fuel controlled after a period of time.

Additional areas of concern are listed as follows:-

1. The burning rate can only be predicted by this expression over a limited range [19];

2. The expression implies that the burning rate is only influenced by the ventilation rate, when the radiative contribution to the burning rate in a compartment is known to be significant since the radiative influence is a function of T^4 [19].

3. The expression is based on wood cribs as the source of fuel. It could be envisaged that fuel in this form shield the fire from radiative effects, thereby reducing the burning rate from what would be experienced in a "real fire" scenario.

4. The assumption is made that the fire is ventilation-controlled; whilst this is relevant to the experiments reported in this thesis, the burning rate is independent of the ventilation factor in fuel-controlled fires.

Drysdale [19] shows how equation 2.1 can be derived by considering the flows of air and combustion products through an opening. In a ventilation-controlled fire there are complex interactions between the radiant heat flux to the fuel, the rate of pyrolysis (or evaporation) of the fuel, the rate of combustion of the gaseous products, the inflow of air to support the combustion and the outflow of combustion gases and unburned fuel gases through opening. The interactions depend on the geometry of the fuel, the type of fuel (solid or liquid), the shape of the room and the ventilation openings.

Some tests have shown departures from equation 2.1. Results from a large number of small-scale compartment fires with wood cribs reported by Thomas and Heseldon [20] and those of Law [21] proposed a slightly more refined equation for burning rate, finding that the burning rate is not directly proportional to $A_v\sqrt{H_v}$ but also depends on the floor shape of the compartment. Thomas and Bennetts also showed that the burning rate also depends heavily on the shape of the room and the width of the ventilation opening in proportion to the wall in which it is located [22]. If the width of the opening is less than the full width of the wall, the burning rate is seen to be much higher than predicted by equation 2.1 because of the increased turbulent flow at the edges of the opening. However, the burning rate in the compartment used in this research may be drawn from the correlation of Kawagoe due to its fortuitous relation to a vent area opening fraction and vent to enclosure size ratio almost identical to the ASTM room. Account must although be made of the differences in conditions under which wood cribs and other fuels burn. In reference [23] Babrauskas states that, unlike a pool fire which can burn in a room under highly fuel-rich conditions, a wood crib does not burn more than 30-40% fuel-rich.

Equation 2.1 applies to a single ventilation opening in one wall of the compartment. If there is more than one opening, the same equation is often used, with A_v being the total area of all the opening and H_v weighted by the area of the openings. If the openings are on several walls, the use of equation 2.1 implies an assumption that the air flow is similar in all openings and that there is no cross-flow through the room.

Although equation 2.1 is not universally applicable, it is a useful approximation to typical behaviour for an experiment and forms the basis of most empirically-based computational studies of post flashover fires.

2.2.2 Fuel-controlled Burning

The burning rate in an enclosure may also be governed by the surface area of the fuel, especially in situations where large, well ventilated rooms containing fuel items which have a limited area of combustible surfaces are to be found. In this case, the rate of burning will be similar to that which would occur for the fuel item burning in the open air, with enhancement from radiant feedback from the hot upper layer of gases and confining walls of the compartment. Depending on the fuel location, most fires become fuel-controlled in the decay period when the exposed surface area of the fuel decreases and the thicker items of the fuel continue to burn. In fuel-controlled burning, all of the heat is released inside of the room, with no flames projecting out of ventilation openings.

2.3 Production of Smoke

From the outset it is important to define categorically the usage of the term 'smoke', a term which is classically, but nonetheless loosely used to describe only that which affects our visibility in building fires - carbonaceous soot. In fact, smoke constituents are much more complex and are a literal soup of ingredients. Although these can be physically separated into solid, liquid and gaseous components, their interdependencies cannot be so readily ascribed and thus decomposition into separate entities is perhaps only accepted as a necessary simplification. If this simplification is accepted, then research into the production of soot and its properties is probably one of the most historical and tremendously researched topics in the combustion community. Yet, still with this supposed simplification, along with the abundance of research papers already published, we are still undecided as to the fundamental chemical and physical processes which are

actually involved. The Society of Fire Protection Engineers (SFPE) defines the term 'smoke' as being "the smoke aerosol or condensed phase component of the products of combustion", whereas the American Society for Testing and Materials (ASTM) extends this definition to include the evolved gases. For the purposes of this research, which concentrates on the human visibility aspect, the first definition is the most pertinent, but in addition it is important to address other 'smoke' components in the global context of compartment fires and to endeavour to account for the association of solid soot with the production of the liquid and gaseous phases found in incomplete combustion systems.

One problem in eliciting an explanation of the formation of soot from published literature is the tremendous number of experimental scenarios under different conditions of operation that are considered by researchers in their studies. Data are published on premixed and diffusion flames, laminar and turbulent flow, with further degrees of freedom born from differing pressures, temperatures and diluents to name but a few. Literally hundreds of different fuels are examined from the weakly sooting, such as methane, to heavy aromatic hydrocarbons. Shock-tube and flow reactors provide still more sources of data, each with its own experimental ideosyncrasities. Practical design systems, for instance diesel engines, are also used to subjectively provide published data pertaining to correlations between their operating parameters and the production of soot. In drawing inferences across the wide ranging experiments, allowances must be made for different time/temperature/concentration histories in each system and for steep gradients of concentration and temperature induced diffusive transport which can be greater than the mean convective process. The 'secrets' of soot formation may be already available, but it may require a perfect and persistent logician to extract them!

Over the years, the theories and models of combustion and soot formation have become increasingly sophisticated. This is not a reflection of scientist quality, but of advances in technology. Lasers have become increasingly popular and commonplace in the modern laboratory after once being found only at wealthy institutions or in the world of medicine. Measurement of particles and radicals had been difficult or impossible before

the use of lasers became routine. The second major advance is in computers. Large kinetic models may now be integrated numerically in relatively short periods of time. Whereas early theories were often founded upon qualitative data, we can now further complex ideas to a point of quantification.

2.3.1 Bench-scale Tests

The traditional means of determining properties of fire or products of combustion is to carry out small scale tests on materials, in isolation from the scenario of interest. This inadequacy is further exacerbated by the inability of the majority of these tests to investigate more than a single property or to be able to combine properties. Moreover, there is often no attempt to correlate results with those of full-scale fires.

Smoke obscuration measurement has been conventionally carried out in the NBS smoke chamber (ASTM 662). This instrument measures the obscuration inside a static 500L chamber, after a sample has been exposed vertically to a 25kW/m^2 radiant (source) heat flux. There are many inadequacies with this procedure. Criticism includes the limited irradiance range, the absence of continuous specimen mass loss measurements and the small, fixed amount of oxygen available for combustion. Of utmost concern in the context of compartment fires is the lack of correlation with full-scale fires. However, it is often considered the definitive measurement and is referenced often for regulatory or specification purposes. The International Standards Organisation (ISO) Technical Committee TC92 (Fire Tests for Building Materials) initiated an irradiance range of 10 to 50 kW/m^2 and a specimen assembly which allows either a horizontal of vertical orientation. This development is now being continued in ISO/TC61/SC4 (Fire Tests for Plastics). The modified procedure has already been shown to be valuable in evaluating the smoke emission characteristics of thermoplastics, which are often underestimated when testing only in a vertical orientation due to melting.

In addition, it is well known that the opacity and volume of smoke generated by materials is significantly affected by their burning mode, especially non-flaming combustion

compared to flaming combustion.

Where optical measurements are made during large-scale tests, the difficulty lies generally with the vast quantity of smoke which is produced. As a result, dynamic measurements are made which may vary considerably due to the amount of dilution and mixing of the smoke stream which takes place before the point of measurement.

Bench-scale methods, such as the cone calorimeter, have been used relatively successfully as a basis for room fire prediction, in which the measurement of soot concentration - now accepted as commonplace - is performed in addition to the measurement of heat release by oxygen calorimetry, for which it was originally designed (see for example [24] and [25]). Cautionary notes by [26] and [27] amongst others have although been sounded concerning the use of the cone calorimeter for this purpose.

2.3.2 Chronology of Soot Formation

In one of the first systematic studies of the parameters of soot formation, Street and Thomas discuss some of the mechanisms which had been proposed at that time. The condensation of PAH was suggested because C_2 is observed spectroscopically in flames. This theory was rejected by Street and Thomas on the grounds of insufficient concentration. Condensation of PAH was considered as a soot formation route because of the structure of the soot is graphite-like, similar to an infinite PAH, and also because aromatic fuels tend to promote soot. Wolfhard and Parker argued against this because they could not find evidence of intermediates spectroscopically. They instead proposed graphitization of droplets of polymers.

Porter [28] promoted the idea of direct polymerization of C_2H_2 to carbon. His experiments involving the photolysis of C_2H_4, showed the conversion of substrate to C_2H_2 and then to carbon with no hydrogen intermediates. The reaction $C_2H_2 \rightarrow 2C + H_2$ is thermally favoured by 54 kcal/mol. An argument on transition state theory shows the existence of a threshold temperature, above which polymerization of fuel to form

soot cannot occur. It is estimated that this threshold is at 1000°C. Porter recognised that oxidation is a process competitive to that of particulate formation and that oxidation can have an enhanced effect through initiation of chain reactions. The presence of oxygen, however, should not change the soot *formation* process.

Palmer and Cullis [29] wrote the first comprehensive review paper in 1965. In it they observed that there is a great deal of similarity across different combustion conditions.

> "With diffusion flames and premixed flames, investigations have been made both of the properties of the carbon formed and of the extent of carbon formation under various experimental conditions. In general, however, the properties of the carbons formed in flames are remarkably little affected by the type of flame, the nature of fuel being burnt and the other conditions which are produced. Any complete and comprehensive theory of carbon formation must of course be able to account for this striking observation."

Bonne, Homann and Wagner [30] used a molecular beam/mass spectrometer apparatus to investigate a rich, premixed, low-pressure acetylene flame. In this pioneering study, the authors were able to take direct measurements of stable species and free radicals. Bonne *et al* concluded that polyacetylenes are important in soot nucleation due to their proliferation at the soot nucleation zone.

The argument that the proliferation of PAHs is fundamental to soot formation has recently been criticised. The most important objections come from:

1. D'Alessio and co-workers [31] who discovered that primary soot particles do not absorb light in the visible wavelengths and concluded that soot particles are not giant aggregates of large condensed PAHs and

2. Tesner et al [32] who found that the pyrolysis of mixtures of Napthalene and acetylene produced about one-tenth of the number of particles produced in the

pyrolysis of pure Napthalene. Since the presence of acetylene is known to promote the growth of PAHs, as shown by both kinetic schemes and experiment, this decrease in the number density of particles clearly rejects the idea of a dominating roles for PAHs in soot nucleation.

In view of the disagreement between workers, Krestinin [33] examined in more detail the acetylene pathway of soot formation, first put forward by Berthelot [34]. Proponents of this hypothesis emphasize that the thermodynamic stability of acetylene (and the whole family of polyynes), grows at higher temperatures, whereas the stability of all other hydrocarbons decreases.

The length of time occupied by research into the fundamental mechanism of soot formation only serves to substantiate the view of the level of complex issues which surround the process. A certain degree of persistency along with the recognition of the significant practical importance of soot in combustion systems, still excites contemporary research into developing "a solution", such as is proposed with the recent announcement of NIST's 'designer soot'.

2.3.3 Fuel Effects

Deliberation of the effects of fuel structure on the formation of soot may be considered one of the most demanding problems, judging by the controversy to be found in the literature. One of the main difficulties is the fact that different fuels have different flame temperatures. Several methods are available to quantify the tendency of a fuel to produce soot. One of the most common methods is to measure the height of a diffusion flame at which soot just starts to break through the top as the fuel flow rate is increased. ASTM has developed a simple method to test aviation turbine fuel (ASTM D 1322-85) which correlates the flame height at the point of smoke formation to sooting tendency of fuel. A marginally quantitative method is to measure the critical equivalence ratio[1]

[1] ϕ = (actual fuel/air ratio)/(stoichiometric fuel air ratio), $\phi > 1$ for a rich system

(ϕ_c) at which soot just starts to be emitted in a flame, usually determined by the visible yellow emission from the flame (black body radiation from the soot particles). This is not however a robust technique because the flame type and burner have major effects.

Kinetically, the critical equivalence ratio represents the point at which the rate of formation of soot pre-cursors is just balanced by the rate of their oxidation. It is important to keep in mind that (ϕ_c) is not necessarily related to the soot yield in a richer system. The critical sooting tendencies in pre-mixed flames are in the order:

$$\text{aromatics} > \text{alkanes} > \text{alkenes} > \text{alkynes}$$

In diffusion flames the order is somewhat different:

$$\text{aromatics} > \text{alkynes} > \text{alkenes} > \text{alkanes}$$

The switch in position of alkynes for the two flames types is suggested by Glassman [35] to be due to temperature. Higher temperature flames induce a greater rate of pyrolytic growth of soot pre-cursors and an enhanced concentration of OH which destroys these pre-cursors. The temperature sensitivity is greater for OH production, so hotter flames produce less soot. This effect is not seen in a diffusion flame because the fuel pyrolysis occurs in an oxidant free environment.

As a general consensus, it was considered that aromatic fuels produce more soot because growth can occur readily on intact ring structures. The work of Harris and Weiner [36] confounded this in an experiment in which toluene was added to an ethylene flame. Care was taken to maintain the same temperature and equivalence ratio between the doped and control flames. The result was perhaps surprising as no difference in the level of soot attained was apparent. This suggested that toluene was broken down to a point where it was no more effective than an non-aromatic in producing soot.

2.3.4 Temperature Effects

The general complexity of the temperature, species and flow field in a diffusion flame makes it difficult to identify and control the separate parameters which influence soot

formation.

Kent and Wagner [37] investigated a number of fuels in terms of their sooting characteristics. Fundamentally, they observed that smoke is emitted when burnout ceases if the soot temperature drops below about 1300K, regardless of other conditions.

2.3.5 Ventilation

Both optical and soot mass fraction measurements may be expected to be a function of the available oxygen concentration. Tewarson [38] conducted studies showing that oxygen concentration has a profound effect on the smoke and sooting tendency for fuel-rich combustion, as would occur in the later stages of a fire or after flashover. For fuel-lean combustion, which is typical of the early fire stages, it was shown that the effect of oxygen levels on smoke and soot production is small-to-negligible.

The effect of fire ventilation on combustion behaviour is generally expressed in terms of the ratio Y_{CO}/Y_{CO_2}. The increase in the ratio is indicative of the increase in the incompleteness of combustion accompanied by higher amounts of CO and other products resulting possibly in an increase in the toxicity of the environment.

2.3.6 Turbulent Versus Laminar Flame Sooting

An overall measure of sooting tendency is the gaseous fuel flow rate, or flame length of a round laminar jet flame which just produces smoke emission (the smoke point). Fuels with a high sooting propensity produce smoke at low flow rates and short flame lengths whereas low sooting fuels require higher flow rates to produce smoke.

Kent [37] concluded from tests conducted on a range of gaseous and pre-vapourized liquid fuels, that a characteristic soot volume fraction (as defined in appendix B) was found largely to be independent of residence time in the flame. In addition, the soot volume fraction was found to be related to its laminar flame counterpart and found to be predictable from the laminar flame smoke-point flow rate.

2.3.7 Smoke Control Methodology

Smoke control in buildings is the method by which means of escape (and emergency services access) are maintained tenable and protected. This is specified in the relevant Codes of practice and Standards in order to satisfy the requirements of the Building Regulations, the associated Approved Document (AD) and the Fire Precautions Act along with other legislative enactments in England and Wales. The present Building Regulations (reviewed in 1995) allow trade-offs between passive and active fire protection and a fire safety engineering approach to building design. As a result of the availability and possibility of alternative design advice *apropos* smoke control in buildings, much research has been conducted in this area over a number of years.

Although a great simplification, for the purposes of smoke control, buildings can be considered to be large undivided volumes in the case of covered shopping precincts, atria, industrial premises and warehouses and multi-compartmented buildings, in the case of offices, flats and maisonettes. The preferred method of smoke control is dependent upon the building type. Choices include: containment and ventilation for lobbies, pressurisation/depressurisation and smoke clearance for multi-compartmented buildings and smoke ventilation and/or depressurisation for large undivided volumes - mainly large atria.

The intention of a well designed smoke control system, is to keep smoke in the upper reaches of the building, leaving clear air near floor level to allow people to move freely.

However, evacuation of a building can result in variations of smoke movement [39]. For example fire exit doors would be continuously opened and closed and windows on the fire floor may be broken by the heat of the fire or intentionally broken by the fire fighters to vent smoke and heat. These actions, which create large openings in the barriers of the compartments, can create avenues for the movement of smoke and negate the operation of smoke-control systems that are based on controlling pressure differences.

2.3.8 Soot Measurement Devices

Many different measurement devices and techniques are available for the measurement of soot, including electron microscopy [40], laser induced incandescence [41], gravimetric analysis [42], as well as the more classical light extinction and scattering techniques which are reviewed by Black et al [43]. A number of commercially available instruments for smoke characterization are listed in the SFPE Handbook [44]. More sophisticated techniques include Thermocouple Particle Densometry (TPD) first introduced by Mcenally [45], and multi-wavelength radiative emission [46]. However, even with miniaturisation of probes and the introduction of iso-kinetic sampling, intrusive techniques still suffer from unknown variations in the flow field at, or downstream of the sampling point. For this reason, non-intrusive based systems are therefore attractive, so long as the barrier of optical access is overcome.

Since the early 1960s, the diode laser has evolved from being a tool of significance solely in the research laboratory environment, into a fundamental component of many household appliances - particularly with the advent of compact disc music digitalisation. Diode lasers themselves offer several major advantages over the more conventional solid and gas lasers systems. Advantages include their compactness and a high rate of efficiency (up to 90% internal power conversion), which allows output powers exceeding 250mW for single chip ridge waveguide type lasers up to a few hundred Watts for continuous wave (cw) power for stacked devices. In addition, mass production is easily achieved along with the flexibility in wavelength, which although is restricted by the material combination, can still provide for a variation of around 100nm.

The majority of laser diodes are fabricated from compound semi-conductors consisting of group III elements such as Ga, Al and In, and group V elements such as P and As due to the direct bandgap transition in the near infra-red to visible wavelength range (0.5-1.6μm) that these materials exhibit. It would go too far to describe the complete laser mechanism for semi-conductor lasers here in detail.

The adequate discernment of the levels of soot present is not solely reliant upon the

measurement method adopted, which may or may not be relatively accurate. The correct interpretation of the measurements is equally important.

Even with a smokeless fire, thermal gradients in the hot zone cause density gradients which refract the laser beam into a random high-frequency pattern known as 'beam-steering' with the potential result of spurious measurements.

2.3.9 Optical Properties of Soot

The optical properties of smoke depends on the particle size distribution, concentration and refractive index of the particles. The particle size distribution and number concentration are a function of the type of fire and ageing processes, but the refractive index of the particles is dependent on their composition which is determined by the type of chemical reactions taking place and the initial material. Mullins and Williams [47] proposed a refractive index of 1.89-0.44i for n-Heptane soot which has been used throughout this research for the calculation of soot volume fraction.

The presence of H_2O in the fire atmosphere will have a direct effect on the light absorbing and scattering characteristics of smoke and the relative humidity influences the growth of hygroscopic particles. In considering the equilibrium vapour pressure surrounding the particles, the surface growth mechanism may increase by a factor of around 2 when the relative humidity is raised from 30% to 90%. As the water vapour saturation pressure is approached, the growth factor increases. This has important implications for fire extinguishment.

2.3.10 Fractal Dimension of Soot Aggregates

The first scaling feature of aggregates that received wide attention in the literature, and the one that remains of great interest to those attempting to characterise the structure of soot 'flocs', is the mass (or number) scaling. The equation which embodies the whole concept of the fractal structure of aggregates is very simple:

$$M \propto R^{D_f} \tag{2.3}$$

where M is the mass of particles and R is a linear measure of size.

Since the bulk of the literature on this subject is concerned with the structure of aggregates from monodisperse spherical particles, the distinction between mass and number is rarely made. It is quite usual for authors to write an equation such as 2.3 in terms of number of particles, N, and refer to the quantity D_f as the mass fractal dimension. This point is rather semantic because the mass and number fractal dimensions are obviously the same thing when the particles are monodisperse.

Equation 2.3 is often written as:

$$N = k_g \left(\frac{R_g}{r_0} \right)^{D_f} \tag{2.4}$$

where Rg is the radius of gyration of the aggregate, r_0 is the radius of the primary particles and k_g is known as the power law prefactor. The subscript g is added to the power law prefactor to clearly associate it with linear aggregate size defined in terms of the radius of gyration, which is the r.m.s distance of the mass elements from their centre of mass.

One interesting feature of fractal aggregates is the dynamics of the processes by which they are formed. Not only are these aggregates fractal in terms of their physical structure, but the kinetics of aggregation also exhibit (with time) the scale invariance associated with fractals. The Smoluchowski equation [48] describes kinetics of irreversible aggregation in terms of the reaction probability between clusters as a function of their masses i and j. The time evolution of the concentration N_h of the aggregates of a particular size h is then given by:

$$\frac{dN_h}{dt} = \frac{1}{2} \sum_{ij, i+j=h} N_i N_j K_{ij} - N_h \sum_j K_{hj} N_j \tag{2.5}$$

2.4 Visibility Studies

To prevent unnecessary duplication of material, the reader is encouraged to consider the guidance in the form of ISO 5659, which has been adopted as a UK national standard. This recognises the clear relationship between optical density and visibility in smoke and highlights the research carried out in the late seventies by Jin [4] to whom this theory is credited.

Optically dense smoke affects way-finding ability and the speed of movement of building occupants. A smoke barrier may be subjectively perceived as being impenetrable, depending upon the concentration (optical density) of the smoke and its irritancy to the eyes and respiratory tract. In experiments where people were asked to walk through a smoke-logged corridor [5], Jin found that for non-irritant smoke, walking speed decreased with smoke density and that at an optical density of 0.5 OD m^{-1} (extinction coefficient 1.15) walking-speed decreased from approximately 1.2 m s^{-1} under 'no-smoke' conditions to 0.3 m s^{-1}. Under these conditions, people behaved as if they were in total darkness, feeling their way along the walls. When people were exposed to irritant smoke, which was produced by burning wood chippings, movement speed was reduced to that of darkness at a much lower optical density of 0.2 OD m^{-1} (extinction coefficient of 0.5) and the subjective experience was found to be much more distressing.

In addition to these effects upon movement speed, there is the problem of deciding whether or not people will move at all. In a number of studies of fires in buildings, a proportion of people (approximately 30%) were found to turn back rather than continue through smoke logged areas. The average density at which people turned back was at a 'visibility' distance of 3 metres (0.33 OD m^{-1}) and women were more likely to turn back than men. A difficulty with this kind of statistic is that, in many fires in buildings there is a choice between passing through smoke to an exit, or turning back to take refuge in a place of relative safety such as a closed room. In some situations, people have moved through very dense smoke when the fire was behind them, while in other cases people have failed to move at all.

One major advantage to the direct correlation of optical density to visibility [49], [5] is that it is a gross property - unlike, for instance, toxicity, where the chemical nature of the individual constituents is paramount.

Conventionally, the optical density of smoke may be determined by measuring the attenuation of light in accordance with Bouguers Law:

$$I = I_0 exp(-\kappa CL) \tag{2.6}$$

where I_0 and I are the unattenuated and attenuated light intensity respectively, κ is the extinction coefficient, C is the mass concentration of smoke particles and L is the path length of the optical beam passing through the smoke. The optical density can then be inferred in terms of either natural logarithms [50]:

$$D_e = -log_e\left(\frac{I}{I_0}\right) = \kappa CL \tag{2.7}$$

or common logarithms [49]:

$$D_{10} = -10log_{10}\frac{I}{I_o} = \frac{10}{2.303}.\kappa CL \tag{2.8}$$

The concentration of smoke therefore may be seen to be directly proportional to the optical density. The factor of 10 is introduced to be consistent with measurement of the attenuation of sound and electrical signals, in decibels or db.

Visibility may also be expressed in terms of the extinction coefficient again derived from equation 2.6. The following simple equation is that which commonly describes the extinction coefficient determined from experimental measurements

$$\kappa_{ext} = \frac{\ln\left(\frac{I_o}{I}\right)}{L} \tag{2.9}$$

In which I_o is the unattenuated signal and I is the attenuated signal over the optical

pathlength L.

Figure 2.1 taken from [51] describes how visibility varies with the extinction coefficient from the experiments of Jin. Immediately apparent is the disparity between visibility achieved in smoke of the same density produced from flaming (black smoke) and that of smouldering (white smoke) combustion.

Optical techniques are particularly attractive owing to their non-intrusive nature. The light extinction method is a popular and accurate way of measuring soot concentration due to its simplicity. An assumption is generally made that light is scattered elastically, which is the process whereby no energy exchange is carried out between the incident photons and the target particles. The scattered light therefore has the same frequency as that incident. Conventionally, the combined use of light extinction and scattering is used in deducing the soot particle size. Complete descriptions of light scattering from small particles are available in books written by Van de Hulst [52], Kerker [53] and Bohren and Huffman [54].

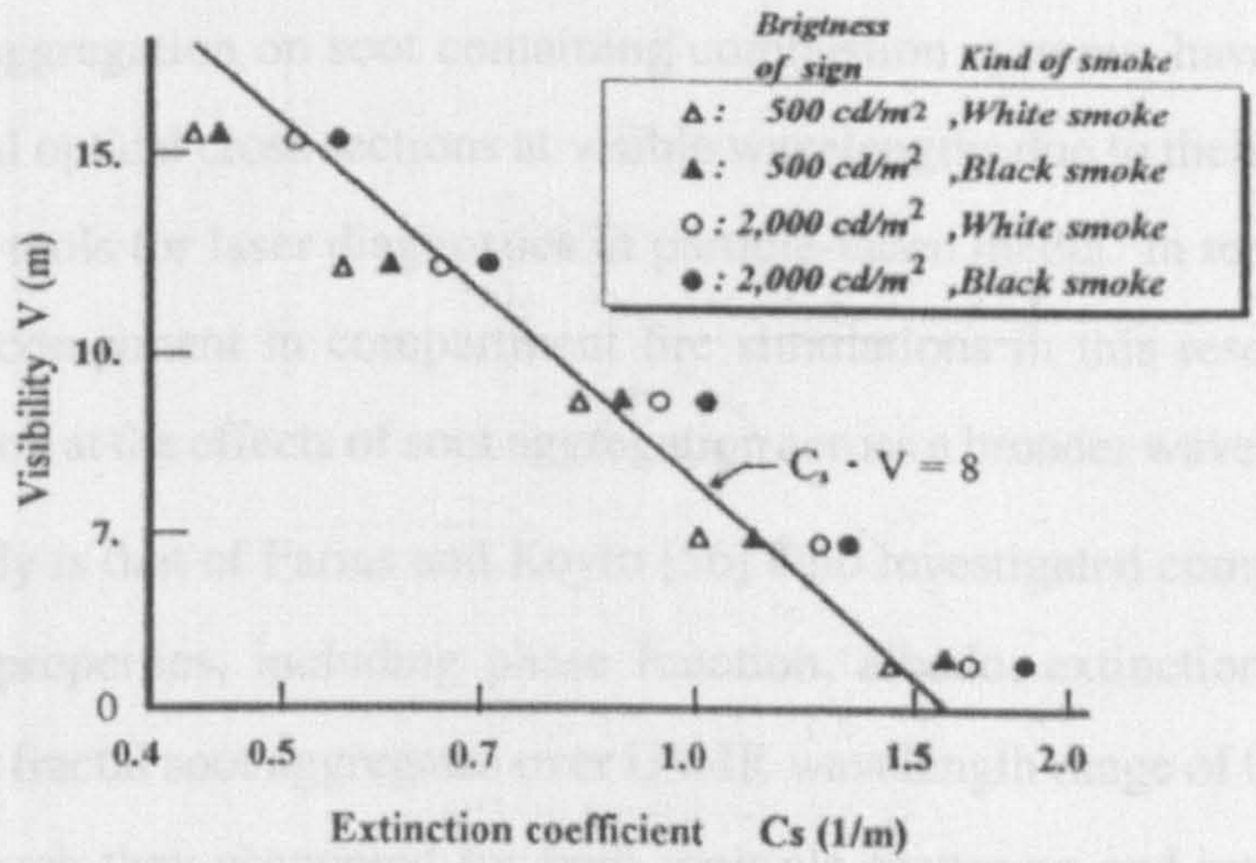

Figure 2.1: Relationship between visibility of light-emitting signs at the obscuration threshold and the extinction coefficient

The soot measurements referred to in this research are generally presented as a soot volume fraction to enable direct comparison with the various detailed experimental conditions and techniques that have been published in the area of soot formation. The

calculation of soot volume fraction may be found in appendix B. Where appropriate, in presenting the findings regarding visibility in smoke, the measurements will be translated directly from the extinction coefficient derived experimentally using equation 2.8 to a visibility distance in metres. However, it must be noted that visibility is also a function of contrast. Significant diffusion to the walls of the compartment occurs during the course of an experiment, resulting in decreasing contrast levels with experimental progress. Due to the difficulty in adequately defining this process and its neglect in published literature with which the experiments documented as part of this research are compared, it is not considered.

2.5 Effects of Soot Aggregation on Radiative Heat Transfer

Studies conducted relatively recently [55],[56] (and references cited within), concerning the effect of aggregation on soot containing combustion systems, have been restricted to fundamental optical cross sections at visible wavelengths due to their specific interest in developing tools for laser diagnostics in particle-laden media. In terms of validating the radiation component in compartment fire simulations in this research, it is more pertinent to look at the effects of soot aggregation across a broader wavelength spectrum.

One such study is that of Farias and Koylu [56] who investigated computationally several spectral properties, including phase function, albedo, extinction coefficient and emissivity for fractal soot aggregates over UV-IR wavelength range of $0.2\mu m$ to $6.2\mu m$. In their approach they accounted for both multiple scattering and interactions among small particles. All radiative properties computed were normalised by the predictions based on the same formulation for primary (unaggregated) particles using the spectral refractive indices of Chang and Charalampopulous [57].

Reference [56] reports that the total computed emissivities of isothermal clouds of soot aggregates relative to that of unaggregated primary particles shows no significant influ-

ence of temperature in the range 1500-2000K and that the ratio of aggregated to non-aggregated soot is always between the range 1.00-1.13. These results therefore signify a difference of generally less than 13%, which implies that radiative properties of soot aggregates may be treated by considering only the unaggregated primary particles. Significant simplifications in the treatment of radiation modelling under these assumptions, is then possible.

2.6 Spectral Emittance

In addition to securing important information concerning the contribution of heat transfer from soot radiation, measurements of emittance may also be used to estimate the level of soot concentration in combustion systems.

Radiative emittance of soot may be calculated approximately by Mie theory, if the soot concentration, flame thickness and temperature are known. The main alternatives are empirically based on the formulations of Hottel [58]. The discovery by Hottel, that the spectral absorption coefficient of soot is inversely proportional to the wavelength raised to a power allows simple relationships for the calculation of luminous flame temperatures from optical pyrometry data. This is achieved upon substitution into Wiens displacement formula, which is an approximation to Planck's black-body distribution.

Svet [59] investigates extensively, the spectral reflectance and transmittance of soot layers on transparent substrates at room temperature. From this set of experiments it was shown that the reflectance of soot is only 0.006 to 0.05. Conservation of energy demands that reflectance plus absorption must equal unity, which leads to the reasoning that due to negligible reflectance, the emittance of soot must increase with increasing deposition thickness. Work conducted at NASA by Liebert and Hibbard as early as 1970 (see [59] for reference) concludes irrefutably that this is the case for soot layers of 0.14-1μm thickness and in the temperature range 300-670 degrees Kelvin, confirming that the emittance of the soot layer did not vary with temperature but varied greatly

with thickness and wavelength. At all wavelengths at this temperature range, it was shown that emittance varies greatly with thickness. Thinner layers display strongly selective emittance at shorter wavelengths. Increasing the thickness of the layer produces a broadening of spectral emittance.

2.7 Toxicological Effects

The physiological effects of exposure to toxic smoke and heat in fires consists of varying degrees of incapacitation which may also lead to death or permanent injury [60]. These incapacitating effects include:

1. Impaired vision resulting from the optical opacity of smoke and from the painful effects of irritant smoke products and heat on the eyes.

2. Respiratory tract pain and breathing difficulties or even respiratory tract injury resulting from the inhalation of irritant smoke which may be very hot. In extreme cases, this can lead to collapse within a few minutes from asphyxia due to laryngeal spasm and/or bronchoconstriction. Lung inflammation may also occur, usually after a period of several hours, which can also lead to varying degrees of respiratory distress.

3. Narcosis from the inhalation of asphyxiant gases resulting in confusion and loss of consciousness.

4. Pain to exposed skin and the upper respiratory tract followed by burns, and hyperthermia, due to the effects of heat, thus preventing escape and leading to collapse.

All of the effects listed above can lead to permanent injury, and all except the first can be fatal if the degree of exposure is sufficient.

Up to a certain level of severity, these hazards cause a partial incapacitation by reducing the efficiency and speed of escape.

In the majority of fires CO, CO_2 and particulates are the dominant products present in smoke. CO is considered to be a contributing cause in the 60% of fire deaths based on data published by HMSO [13]. Carbon Monoxide binds with red blood cells to form carboxyhaemoglobin (COHb), which interferes with oxygen transport in the body. COHb concentrations of 50 to 60% are generally accepted as fatal. CO_2 on the other hand, is not toxic up to 5% but synergism with CO plays an important part due to its ability to stimulate breathing - at 3%, the volume of air breathed per minute is approximately doubled and at 5% is tripled [61].

Tables 2.1, 2.2 and 2.3 provide Health and Safety Executive [62] (HSE) Short Term Exposure Limit (STEL), Occupational Exposure Limit (OEL) and World Health Organisation [63] (WHO) mean limits for Carbon Monoxide and Carbon Dioxide. These limits are used to ascertain levels of tenability in the compartment fire experiments.

Standard	Concentration (ppm)
HSE OEL 8 hour	30
HSE OEL 15 minute STEL	200

Table 2.1: HSE Standards and Guideline Levels for Exposure to Carbon Monoxide

Standard	Concentration (ppm)
WHO 8 hour mean	9
WHO 1 hour mean	26
WHO 30 minute mean	52
WHO 15 minute mean	85

Table 2.2: WHO Standards and Guideline Levels for Exposure to Carbon Monoxide

Standard	Concentration (ppm)
HSE OEL 8 hour	5000
HSE OEL 15 minute STEL	15000

Table 2.3: HSE Standards and Guideline Levels for Exposure to Carbon Dioxide

All of these complexities obviously have a knock-on effect on soot formation modelling. Validation of these models forces reliance on adequate and detailed measurements of the

mechanisms involved. From a fundamental perspective, one could argue that a representative percentage of soot could be physically mapped onto the domain and transported passively, thus negating the computing requirement of accompanying reactions that may take place.

2.8 Heat Flux

The hazard posed by large, fully turbulent hydrocarbon fires may be defined by the history of the net heat flux from the fire to the system of interest, primarily associated with participating media radiative transport. Fires in this regime are characterised by high temperatures. (1000-1500K) as measured for example, by Gritzo and Moya [64] and relatively low velocities (5-15m s^{-1}). As a consequence of the soot yield in heptane pool fires, in which radiative emission and absorption by the soot particles dominate, it is necessary to be able to calculate the temperature and radiative properties of the soot independently, without reliance solely on a measured thermocouple temperature. In addition, due to the turbulent nature of these fires, it is necessary to include measurements that are capable of high temporal resolution.

Under the weighted sum of gray gases (WSGG) approximation [65], the gases responsible for radiation emission and absorption comprise only CO_2 and H_2O. This assumption ignores the presence of CO produced by incomplete combustion and any fuel vapours or pyrolysis gases. Further, although this type of homogenous gray model has achieved considerable success in spite of its simplifying assumptions, it is also recognised that the flame can be significantly non-uniform in temperature and species concentrations. This non-uniform radiative feedback to the fuel surface would then cause a non-uniform evaporation of the fuel with resulting complex motions set up in both the gas and liquid phases and consequently affect the flame shape.The importance of non-gray effects was presented by Buckius and Tien [66] who concluded that for sooty fuels, such as polystyrene, the radiant emission is dominated by the presence of soot and that gas

emissions are negligible. However, whilst this may be true for heavily sooting fuels, for mildly sooting fuels like heptane, neglecting gas emission may significantly underestimate the overall heat transfer to the surface.

It is established that during the combustion process, a thin, fuel-rich core region exists just above the fuel surface. In large-scale fires, where radiation is the dominant mechanism for energy feedback, the attenuation of the radiant flux by the core gases can significantly affect the mass vaporisation rate. Conversely, Orloff [67] found that the radiation blockage due to pyrolysis gases was not important for fires of size relevant to this study. It must be noted that Orloff reached this conclusion based on solid PMMA fires which has a much greater heat of gasification compared to that of heptane.

Shinotake et al [68] conducted experiments during which, heptane was burnt in circular pans of varying size in the range 0.3-1.0m diameter. The internal radiative heat flux to the fuel surface was measured using Gardon-type heat-flux meters and comparisons were made with external flux data. Simultaneous light extinction measurements through the flame were conducted using a HeNe laser as the light source. They found that as the pan size increased and during the initial transient stage of the fire evolution, the internal heat-flux showed an initial overshoot followed by a considerable fall which had greater importance in the larger fires. When compared to the external heat flux during steady-state combustion, the ratio of intensities decreased with increased pool size. Both were interpreted as indications of a "radiation blockage" effect.

2.9 Mass Loss Rate and Fire Spread

Flame spread over condensed fuels in an oxidizing environment is an important topic in fire research. The process of flame spread is dependant on energy, momentum, and species transfer in the region surrounding the flame reaction zone. The problem is further complicated by the chemical processes involved. By understanding the significance of each of these processes, relevant problems in fire safety such as ignition, flame spread

rate, and extinction can be solved.

The dominant mechanism of flame spread is the heat transfer from the flame's reaction zone to the unburnt fuel ahead of the flame. The possible modes of heat transfer are conduction through the solid, and convection, conduction and radiation through the gas. There are many parameters which determine the dominant mode of heat transfer and spread rate. Fuel type, fuel thickness, geometry, orientation with respect to the gravity vector, ambient conditions, flame scale, and strength of gravitational field are some parameters that have been studied.

The four fuel orientations that have been frequently studied are vertical downward, vertical upward, horizontal topside and horizontal underside. For vertical downward and horizontal topside fires, the direction of flame propagation is opposite to the direction of the buoyancy induced gas flow. The forward heat conduction and radiation are balanced by the opposed convective heat transfer, creating a flame that spreads at a constant rate. For vertical upward and horizontal underside fires all modes of heat transfer are in the same direction, creating a rapidly accelerating flame.

To better understand this complicated phenomenon of flame spread, it is best to try to fully understand its most simple cases. A vertical downward spreading flame over a thermally thick vertical slab of polymethylmethacrylate (PMMA) is a case that has been frequently studied (for example [69]). A thermally thick fuel is the limiting case where the flame characteristics become independent of the fuel thickness. PMMA is commonly used because it is a relatively clean burning fuel, behaves well - i.e does not char or melt and its physical and chemical properties are well known.

Another situation that is commonly studied, is the downward flame spread over a thermally thin sheet of ashless filter paper. A thermally thin fuel is the limiting case where the temperature is constant across the thickness of the solid fuel. For this situation the flame spread rate is dependant on the thickness of the fuel.

Experimental, analytical and numerical methods have been used to find the spread rates, temperature fields, and other flame properties for these two limiting cases. The domi-

nant mode of heat transfer can be deduced from this information. Since each of these methods of analysis introduces its own source of error, it is necessary to correlate the results as much as possible.

Several reviews articles have been published in the area of flame spread. Wichman [70] for example summarized analytical, experimental and numerical works on opposed flow flame spread.

Fernandez-Pello [71], [72] performed extensive studies on laminar flame spread over flat PMMA surfaces. In this work he presented results from thermocouple probing, photography, interferometry, radiometer measurements, gas sample chromatography, and particle-track photography. He concluded that the dominant mode of heat transfer was conduction through the solid. Other conclusions of the study included that the rate of flame spread velocity is dependent upon thickness of the sample. Where the sample thickness is greater than the thermal layer thickness, the rate of flame spread will be at its minimum.

In 1983 Fernandez-Pello and Hirano [73] summarized recent experiments on flame spread over combustible solids. Results from thickness studies on downward and horizontal flame spread over PMMA showed the transition to the thermally thick limit. These results were shown in plots of spread rate and forward heat transfer versus thickness. Experiments on external effects on spread rate were also presented. Effects of surface temperature, external radiant heat flux, opposed flow velocity, and oxygen mass fraction, on spread rate were analyzed. Finally it was shown that these results could be condensed and represented in non- dimensional form.

Downward flame spread experiments on thermally thick PMMA slabs were performed by Ito and Kashiwagi [74]. Temperature measurements were obtained by counting the interference fringes produced by a holographic image. It was concluded that 57% of the heat transfer to the unburnt fuel was through the gas phase. This result contradicts the previous result by Fernandez-Pello [71].

Fernandez-Pello, Ray and Glassman [75] performed experiments to determine the ef-

fect of opposed forced flow and ambient oxygen concentration on flame spread rate over thick and thin fuels. It was shown that for thick PMMA at high oxygen concentrations, flame spread rate increases as the opposed flow velocity is increased. However, for thin paper sheets at all oxygen concentrations, and thick PMMA at low oxygen concentrations, flame spread rate decreases as the opposed flow velocity increased. The results were also represented in a non- dimensional plot of flame spread rate versus Damkohler number, D_a defined by Quintiere [76] as:-

$$D_a = \frac{\upsilon_g \kappa}{\rho_g u_\infty^2} \tag{2.10}$$

where υ_g is the gas-phase kinematic viscosity, u_∞^2 is the velocity of the predominant flow, ρ_g is the gas phase density and κ is the rate of fuel consumption.

Parker [77] investigated downward flame spread over thin cellulose index cards. A surface temperature profile was obtained using an embedded thermocouple. An artificial flame spread burner was built to emulate a cellulose downward spreading flame. The experimentalists used natural gas to create a stationary flame with the same characteristics as a downward spreading flame. From this model it was concluded that the release of pyrolysis gases occurs underneath the flame rather than ahead of it. It was also concluded that the dominant mode of heat transfer to the unburnt fuel was conduction through the gas phase.

Hirano et al. [78] also measured temperature and velocity profiles over thin paper at various positions. Particle tracing methods and fine wire thermocouples were used to collect data. It was concluded that 80% of the heat transfer to the unburnt fuel was in the gas phase within 1 mm of the flame front.

Chapter 3

Compartment Fire Experiments

3.1 Introduction

The majority of room fire experiments, for example the commonly cited eponymous Steckler room [6], employ a simple gas burner as the heat source, in which the fuel flow-rate and thus heat release is pre-determined and therefore inter-dependencies on room conditions such as the level of ventilation are not available. In addition, weakly sooting fuels such as methane have been chosen, with the result of artificially simplifying the complex interactions introduced by the production of soot and the associated radiative loss, which may significantly affect the flow-fields which are customarily measured in room fire scenarios, such as in door openings, and upon which simple empirical models commonly used in fire hazard assessment are based.

Furthermore, room fire experiments in which alternative, more sooting fuels have been burnt, have either totally excluded the measurement of soot, or it has been merely represented by performing single-point light intensity measurements across the exhaust duct, at which point the products of combustion are assumed to be well mixed. In the experiments reported here, the design and use of a novel fully traversable water-cooled probe, which houses a 670 nm diode-laser and photo-diode detector, enabling light extinction measurements to be made inside the compartment, provides us with a spatial resolution

of soot concentration not previously achieved, a consideration of obvious importance when discerning the level of obscuration in a compartment fire scenario. Other important measurements carried out, which have been neglected in previous work, include heat-loss to the surroundings from the compartment - important when considering any boundary conditions imposed for numerical prediction - along with measurements made close to the burner source.

In excess of 100 experiments have been performed as part of this research. Therefore, due to the vast quantity of data which has been amassed, reference should also be made to a separate report [79] designed to accompany this dissertation, which contains full data-sets from each experiment.

Results from experimental measurements made in the compartment are compared with their numerical prediction in Chapter 6.

3.2 Experimental Design

3.2.1 Fuel Selection

The choice of liquid heptane as the fuel in these experiments, is seen as a suitable alternative to gaseous fuel, based on its relatively well defined chemistry for which several empirically optimised reaction mechanisms are available (for example [80] and [81]) and for its suitable sooting propensity. The use of a liquid fuel also enables a means of establishing the important interactions specific to compartment fires which govern the mass loss rate of fuel, such as radiation from the hot smoky layer and confining walls.

3.2.2 Room Geometry

The American Standards for Testing and Measurement (ASTM) have established a standard room size which is adopted by many experimentalists, for example [82]. Figure

3.1 shows a schematic of the basic experimental geometry. The fire compartment used in each of the experiments is an exact half-scale of the ASTM room, having specific dimensions of 1.2m in width and height and 1.8m in depth. Figure 3.2 is a photograph taken of the actual experimental room. The walls comprise insulating Supalux - a calcium silicate fibrous board of 12 mm thickness with a thermal conductivity rating of 0.17 W m^{-1} K^{-1}. A number of thermal and physical properties of Supalux are listed in table 3.1. Additional insulation is provided by an inner lining of Durablanket - a light-weight flexible blanket of 25 mm thickness, made from ceramic fibres of SiO_2 and Al_2O_3, which is secured to the inner surface of the walls by silica based adhesive.

Only one doorway exists in one of the shorter walls of the room. The ventilation rate can be varied by reducing the door-width from a maximum of 0.36 m, which is representative of a fully opened 'standard' door. The variability of door-width enables the study of ventilation/vitiation effects on the total amount of smoke produced. The possibility of changes in smoke particulate morphological and chemical characteristics under different conditions of ventilation is discussed in the literature review.

thermal conductivity $(W/m/K)$	0.17
density (kg/m^3)	880
specific heat capacity $(J/kg/K)$	1000
thermal interia $(W/m^2/K.s^{0.5}$	386.78
thermal diffusivity (m^2/s)	1.93E-07

Table 3.1: Thermal and Physical Properties of Supalux

3.2.3 Parameter Investigations and Burner Design

There were two main criteria considered when designing the burner. The first was to permit both transient and steady-state experiments. Initial scoping studies in which a simple natural gas burner as the source of heat release, showed that the thermal equilibrium of the compartment was such that an experimental duration in excess of eight minutes was needed in order to achieve steady-state. Given the difficulty in validating a

transient simulation of the compartment, the majority of experiments were conducted to steady-state conditions using a constant supply of fuel to a burner, whose diameter was of the size to minimise the risk of flashover in the compartment.

For each experiment, a single pool tray of either 0.17 m or 0.23 m diameter was situated at the centre of the compartment. The smallest and simpler of the two burners engaged two fuel inlet ports at equidistant radial positions and an additional port to which was attached an external fuel level indicator situated remote from the fire source. Both transient and steady-state experiments were achieved either by burning fixed amounts of heptane or utilising a constant supply of fuel fed directly from a 250 litre capacity pressure vessel operating at 8 p.s.i via a *Fischer Porter* $\frac{1}{4}$ inch tri-flat flow meter with a stainless steel float.

The second criteria attached to the pan design was based on the fact that very minimal (if any) near-field measurements are carried out in typical room fire experiments (for example, ASTM guide to room fire experiments [83]). Because of the uncertainty *apropos* CFD modelling caused by the neglect of such measurements, conditions at the burner source were investigated in more detail in these series of experiments than is typical. This led to a more sophisticated design for the larger pan (see figure 3.3) which houses a number of 'sight-bosses' located at its base. These 'sight-bosses' act as locators for Gardon Type total heat flux meters [84] and a right-angled sight-tube containing a 45° mirror which reflects radiative emission to the fuel surface to a grating emission spectrometer situated beneath the burner. Furthermore, the pan was attached to a separate fully rotatable rig base in order to vary the view factor of the instruments. In summary there were three phases to these experiments.

1. Initial classification of the stages in fire growth relevant to the burner size and level of room ventilation as a function of thermal inertia of the compartment.

2. Parameter investigation based on relevance to the already determined fire growth stages.

3. Main data gathering experiments using the determined parameters.

The burner was piloted in each experiment until ignition by a simple natural gas torch operated manually.

Figures 3.4 a,b,c and d clearly illustrate the means of ignition in addition to capturing the progress of flame spread as highlighted by the blue reaction zone, across the entire surface of the pool. The pictures were taken with a digital hand-held video camera at a frame speed circa 25 frames per second.

3.2.4 Experimental Conditions

Table 3.2 below indicates the number of different conditions which were imposed on the compartment in order to realise the robustness of the CFD model when applied to a number possible scenarios met in a typical compartment fire.

Burner Diameter (m)	Doorwidth (m)	Steady-state?
0.23	0.36	×
0.17	0.36	✓
0.17	0.25	✓
0.17	0.15	×

Table 3.2: Experimental Conditions

As mentioned previously, varying the burner size and doorwidth enabled both transient and steady-state conditions to be achieved. From initial experiments it was shown that the thermal inertia of the compartment is such that a quasi steady-state is achievable for the full doorwidth case after around 8 minutes from ignition using the smaller diameter pan. This time-scale closely reflects the findings from the initial set of experiments burning natural gas. This time to steady-state correspondingly increases with the reduction in ventilation in excess of 15 minutes with the 0.25 m door. Due to safety considerations, only a limited number of experiments were conducted for the smallest 0.15 m doorwidth. In addition, the duration of each experiment was deliberately shortened

such that a steady-state was never achieved. As an illustration of the high temperatures achieved in this configuration , figure 3.5 shows a photograph taken of radiant soot seen exiting the doorway of the compartment shortly after ignition.

3.3 Measurable Parameters

3.3.1 Heat Release Rate

The Heat Release Rate (HRR) was calculated based on actual fuel mass loss measurements as determined from rotameter readings, whilst ensuring the fuel level in in the pan remained constant. Mass air flow rates into and out of the compartment are also calculated base on the doorway temperature and velocity profile. Table 6.4 shows the heat release rates achieved for each set of experiments listed in table 3.2 along with predicted values and are presented for the 0.23m burner and 0.17m burner with all doorwidth configurations; the largest error is for the 0.23m diameter burner due to uncertainty introduced by measurements made in a transient experiment.

3.3.2 Gas Sampling

Many molecules will absorb infrared radiation and the wavelengths at which this occurs depends predominantly on the nature and disposition of atoms and functional groups within the molecule. Absorption of infrared radiation results in changes in the vibrational energy of molecules and this gives rise to an absorption spectrum which is characteristic of a compound. For a molecule to be infrared-active, there must be a change in its dipole moment during the course of the vibration. If one of the absorption bands for a particular compound is relatively removed in wavelength from bands of other compounds it is possible to use this particular band to quantify the compound in mixtures. Non-dispersive infrared analysers are designed to produce infrared radiation over a rel-

atively narrow band of wavelengths which are selected to provide maximum absorption of the wanted compound with minimum absorption of the unwanted compounds.

The basic components of the analyser are an infrared radiation source, a cell containing the test specimen and a detector at the opposite end of the cell from the source. By varying the path length, gas concentrations as low as a few parts per million are measured. These non-dispersive infrared analysers are commonly used for the quantification of oxides of carbon due to their high degree of selectivity towards these gases and their ability to give continuous measurements. A substance which exhibits paramagnetism is attracted into a magnetic field. Oxygen and Nitric Oxide are such compounds. All other common gases exhibit diamagnetism and as such are repelled by a magnetic field. In a paramagnetic substance, the individual atoms, ions or molecules possess a permanent magnetic dipole moment which lines up parallel to an external magnetic field giving a net contribution to the magnetic susceptibility. Paramagnetic analysers generally consist of a diamagnetic material suspended in a magnetic field to produce a turning moment. When a paramagnetic substance is placed between the magnetic field and the diamagnetic material, the influence of the field is reduced and the turning moment diminishes. This is measured as a rotation of the diamagnetic body and converted to a signal representative of the concentration of paramagnetic material present. Paramagnetic methods are commonly used for measuring oxygen due to its marked property of paramagnetism. Oxygen levels were measured in an on-line commercially produced paramagnetic monitor (Servomex Portable Oxygen Analyser, Model 572). The analyser has a measuring range of 0-100% with an accuracy of 0.3% oxygen. The oxygen concentration is detected by means of a dumb-bell suspended by a torsion fibre in a non-linear magnetic field. The dumb-bell consists of two hollow spheres filled with a diamagnetic gas, in this case Nitrogen, and the paramagnetic Oxygen in the surrounding test atmosphere causes it to deflect from its rest position. Around the dumb-bell is a coil of wire through which a current is passed to restore it to its original position. The restoring current is proportional to the concentration of Oxygen in the test atmosphere.

Carbon Dioxide was continuously monitored by a double beam Luft-type non-dispersive infrared gas analyser which is manufactured to a specification suitable for fire atmospheres by the Analytical Development Company. For CO_2, concentration ranges of 0-0.2%, 0-2% and 0-20% were possible. However, the concentration of CO_2 present in the compartment was such that it necessitated the use of the larger 0-20% range. The analyser consists of an infrared radiation source split into two identical beams, one of which passes through a sample tube, and the other through a reference tube filled with a non-infrared-absorbing gas (in this case Nitrogen). The detector, filled with a pure sample of the gas being analysed, is divided into two cells by a pressure-sensitive diaphragm such that the 'reference' and 'sample' radiation beams are incident on either side. When the gas to be measured enters the analyser, it passes through the sample tube and absorbs radiation in proportion to the concentration present, thus decreasing the level of energy reaching the sample side of the detector. The energy received by the detector is absorbed and the pure gas on each side of the diaphragm is heated, the sample side to a lesser degree than the reference side. The greater expansion of the gas in the reference side of the detector causes a movement of the diaphragm, which is proportional to the concentration of gas in the sample tube. The principle of operation of the Carbon Monoxide gas analyser (ADC7000) follows that for Carbon Dioxide. During operation, the signal is periodically compared with reference gas (usually at zero) and automatically adjusted to achieve calibration. The standard resolution of the instrument is 0.1% over the gas range 0-10%. Manufacturers advise that reading interference is noticeable in the presence of 20mb of water vapour and 100mb of Carbon Dioxide. The analysers were calibrated using a gas of known composition; in this case 0.40% CO, 0.42 CO_2 and the balance made up from N_2. A two point calibration was carried out using this calibration gas and N_2 to establish a zero reading. For the Oxygen analyser, ambient air was used for the second point of 20.9%. An output signal voltage, corresponding to the concentration of the individual species was continuously monitored with the data acquisition system. Because only a limited pressure differential exists between the sampling probe and the compartment interior, the combustion product was continuously sampled

at a rate of 1.0 L min^{-1} by means of a simple vacuum pump.

Due to the inherent sooting propensity of heptane and the possibility of erroneous concentration levels introduced by the presence of water vapour, a series of moisture and particulate traps comprising Calcium Chloride and glass wool were placed in series with the gas analysers. There are two main concerns regarding gas sampling in a soot-laden environment. The first is physical in terms of restricting the sample lines and the second is chemical arising from the risk of soot oxidation which artificially elevates the apparent level of CO.

The signal voltage output from the gas analysers represents the concentration of CO, CO_2 and O_2 and provides a continuous analogue signal output the data-logger.

Four cylindrical sample probes of simple design were inserted at around 300mm into the compartment at various heights half-way along one of the compartment side-walls. Care was taken to ensure the probe orifice was outside the flame boundary, thus better representing the main compartment environment. Reactions ideally should be quenched at the probe tip. The fall in pressure across the mouth of the probe will reduce the temperature and terminate most reactions. Additional cooling of the tip by pumping water around it would enhance this effect. However, given the levels of soot present in the compartment it was envisaged (in the light of previous experiments) that the benefit of this would be largely outweighed by the risk of soot deposition by thermophoresis [85].

The three separate gas analysers were aligned in series. The sample delay time had already been investigated during calibration using a standard gas sample bag and external pump which had a specified pumping rate of 1.0 L min^{-1}. The sample delay for the last analyser in series was around 50s and so the measurement period over which the concentration was monitored at each height was safely in excess of this at 2 minutes at each position.

An area of some difficulty was the sample handling after the probe. The arrangement of components was changed on several occasions. The sample tube length was found

to have a significant effect upon species concentration initially, particularly for CO due to its relatively low production in the compartment. The sample length was shortened until no significant difference in apparent concentration was noticeable and as an added precaution, the CO analyser was placed first in series with the sample probe. The gas sample was filtered, dried and passed through meters in the order CO, CO_2 and O_2.

The sample filters were out of necessity changed regularly, particularly in the case of IMS due to the high production of water vapour. After each filter change the analysers were re-calibrated for consistency with previous runs. Meter exhausts were discharged into a neighbouring corridor adjacent to the laboratory. Personal CO alarms were also used in the proximity of this experiment at all times.

Emission rates for CO_2 and CO and rates of consumption of O_2, are calculated for each experiment based on non-linear regression using Newton-Raphson iterative techniques. Typical examples for the full doorwidth configuration using the smaller 0.17m diameter burner may be seen in figures 3.6, 3.7 and 3.8.

3.3.3 Temperature Measurement

The majority of compartment fire experiments utilise thermocouple probing techniques to map the internal temperature distribution. In high temperature environments, Platinum/Rhodium thermocouples are commonly found. For the experiments in this study it is sufficient to use lower melting point type K Nickel/Chromium thermocouples.

The thermocouple wire was 200 microns in diameter and housed in a protective fibre-glass sheath. All thermocouples used in the experiments were manufactured in-house. A typical junction bead diameter of 500 microns was established by spark discharge in an inert environment to mitigate the risk of oxidation. Metal-sheathed thermocouple compensating cable, housing wires comprising of the same physical properties as those of the thermocouple, are attached to the free ends of the thermocouple for direct connection to the individual data-logger analogue input channels.

Three thermocouple stacks (see figure 3.9 for visual location of thermocouple stacks) were situated in the compartment interior at windward and leeward positions and to one side of the burner. These thermocouple stacks are comprised of a simple stainless steel tube of 1.5 m length and 10 mm diameter, in which a series of 5 mm holes were drilled at 150 mm intervals. Individual thermocouple wires were fed into the tube and forced through a single hole thus exposing the bead to the compartment interior.

Because of the formation of the hot smoky layer in the compartment ceiling, during the course of an experiment it is observed that a substantial amount of soot is deposited onto the thermocouple bead when located in this region - therefore altering both its emissivity and bead size. This phenomenon was mitigated as much as possible by the removal of any soot deposition from those thermocouples that were in accessible locations in between experiments, by systematic insertion of the bead into the oxidising region of the pilot flame. The effect of this has been investigated by NIST [86] in terms of effective bead size and emissivity and the effect on the apparent temperature of the thermocouple.

Corrections to the apparent thermocouple temperature may be calculated from an energy balance between radiative and convective heat transfer to and from the thermocouple, the maximum expected error at a mean peak temperature measured in the compartment is around 40K based on a nominal bead size of 500 microns. This represents a worst case scenario because local gas temperatures are not known and therefore the assumption is made that the bead is radiating to ambient conditions.

Because one of the main objectives to this research is to validate SOFIE against experimental measurements, it is important that corrected temperatures should be used when making a comparison.

Digital data acquisition was used to determine the mean temperatures of the thermocouple bead from the thermal emf at a sample rate of 40 Hz. However, the rate was ultimately instrumentally determined based on the number of channels in simultaneous operation. Analogue/digital conversion was through a 19 bit system (*S13535 Scorpio Datalogger*) supplied by Schlumberger Instruments. Zero drift of the thermocouple was

accounted for by cold junction compensating on the signal conditioning board, prior to analogue/digital conversion. Signal accuracy in the compartment temperature range is between 0.01 and 0.1°C with a total system accuracy of between 0.5 and 0.55°C after cold junction compensation. The data was post processed for the radiation correction.

The nominal bead size of the thermocouples is such that taking into account the nominal time constant is rather superficial in its importance. In addition, due to the thermocouple positions in the compartment being largely outside the flame region, where the thermocouple/flame physical interaction was impossible to discern, account of the effect of the thermocouple time constant would be extremely difficult. However, the time response of the flame has no bearing on the mean value and would only affect the mean variance of the thermocouple signal.

Figures 3.10 and 3.11 present experimental doorway temperature profiles for each doorwidth. The average peak temperatures at steady-state are used to compare with SOFIE in Chapter 6.

The thermocouples were attached to bi-directional velocity probes as described in section 3.3.5.

3.3.4 Soot Measurement

The fundamental objective of this work is the investigation of the spatial and temporal distribution of soot within the compartment. Due to the complex process of soot formation and its strong temperature dependence, the parameters thought to be important in its formation were physically mapped in the same temporal environment.

Optical techniques to characterize smoke particulates are especially attractive since they provide continuous measurements without disturbing the environment. Of the majority of compartment fire experiments reported in the literature, those that consider soot concentration usually make measurements across the exhaust duct under the assumption that the hot combustion products are well mixed. The advantage of this method

is that is utilises well established techniques to measure the extinction of light though the combustion products. Moreover, it is outside the region of elevated temperature and therefore no account need to be taken of its potential to physically influence the instrument operation. The main disadvantage, of course, is that mapping of the compartment is unavailable with results only pertinent to a mean production rate of smoke. Concentrations within the compartment can only then be inferred using other convenient markers such as temperature whilst prescribing the initial soot concentration from the determined mean under the assumption of its passive transportation.

In developing novel instrumentation to enable such measurement of internal soot loading using conventional light extinction techniques, several factors were considered important. These are:-

1. To maintain the temperature of the instrumentation below a given threshold to be determined.

2. To provide a suitable measurement pathlength as a compromise between adequate resolution against signal to noise ratio.

3. To ensure that no deposition occurs on the exposed surfaces of the instruments namely:-

   (a) laser lens

   (b) photo-diode

4. To ensure that interference from radiation from the flame and other external sources is minimised

5. To ensure that the 'beam steering' effect from local density variations is minimised or accounted for.

Suitable housing of the instrumentation resulted in the development of a novel 'soot probe' - the physical dimension of which was largely dictated by the confines of the

compartment and its disturbance on the local flow environment. Simulations using SOFIE were carried out in order to discern this level of disturbance which was found to be negligible.

The resultant size of the 'soot probe' necessitated the use of a small 0.9 mW diode laser emitting at a wavelength of 670 nm as the source of light, accompanied by a large surface area (100mm^2) Gallium Arsenide photo-diode. Figure 3.12 shows the final design of the probe used throughout each experiment. Water cooling of the soot probe was effected by a double spiral enabling water to flow throughout each cylindrical housing at a flow-rate of 2.5 L min^{-1}.

The pathlength necessary to provide a level of light extinction within a suitable range was provided from preliminary experiments, in which the instruments were mounted on a simple platform and submerged into a stratified layer in a small rectangular compartment. The layer was formed from the controlled release of artificial smoke into the compartment, pre-heated to provide the necessary level of buoyancy to maintain the layer.

Artificial smoke was used to discount influences of the high temperature environment and comprised a condensed mineral oil, refined with the majority of PAHs removed. The mineral oil is supplied by Concept Oil Ltd as standard and manufactured by Shell Ondina. The particles generated were of a known diameter (200 nm).

A pathlength of 150 mm was determined to be suitable from these experiments, which equated to around 40% absorption. Following on from the other conditions attached to the design of the probe, it was necessary to purge the probe in order to prevent soot deposition on the optical surfaces. During the preliminary experiments with artificial smoke, a purge rate of 0.2-0.3 ms^{-1}was considered suitable, determined from its effect on the apparent level of smoke concentration. The purge level was reduced steadily until there was no discernible difference in the level of extinction whilst still being high enough to ensure no smoke ever reached the important exposed surfaces of the instruments.

Due to safety considerations, all compartment fire experiments were carried out in a well lit laboratory. Potential radiation sources from the laboratory lights and more importantly the flame were mitigated by the inclusion of a narrow band-pass filter, centred at 670 nm and positioned directly in front of the photo-diode detector. Because flame-emitted radiation at the same wavelength as that emitted by the diode laser would still reach the detector, the contribution to the background intensity by the flame was measured with the signal photodiode whilst the laser was off. No effect of flame radiation on the photo-diode was observed with the 'soot probe' positioned at 500 mm inside the compartment.

The effect of beam steering on the soot measurements was also an important consideration. This 'beam steering' phenomenon is the result of turbulent and thermal gradients in the combustion medium which cause gradients in the local refractive index. Whilst ensuring the orifice in the probe was such that any slight deviation in the laser beam would still be captured by the photo-diode it was of equal importance to be confident in the uniformity of the detector surfaces - both of the photo-diode and band-pass filter. Any distortion or deformity of these surfaces would obviously result in an apparent variation in soot concentration.

Elevated temperatures would directly interfere with measurements of light extinction due to a typical emission wavelength change of 0.3 nm to 0.4 nm per degree centigrade, along with a decrease in power output for a fixed driving current. Clearly if a stable wavelength output is required, the temperature of the diode laser must be maintained at a constant level.

The local gas temperature in the compartment where the 'soot probe' was located at any one time was in excess of 300 °C for a period not less than 6 minutes. Cooling of the soot probe to a temperature below that of the threshold value is therefore critical. Two thermocouples were sited inside the probe alongside the diode laser and photo-diode. These thermocouples were carefully monitored during the course of the experiment, which on average indicated an environment of 18.0°C for the diode laser and 17.4°C for

the photo-diode.

An additional check for temperature effects on the operation of the soot probe was considered during the combustion of methanol in which no visible soot was emitted. The signal remained unattenuated despite the probe being exposed to temperatures in excess of 150 °C although it is recognised that the temperatures experienced by the soot probe in a methanol fire were much lower than those of heptane.

One significant advantage with this current probe design is its ability to be fully traversed during the course of the experiment. As well as providing a resolution not previously achieved within the context of compartment fires, this also means that errors introduced by experimental repetition in which conditions may have changed slightly can be discounted. Consequently, the number of experiments required for any sensitivity analysis is then immediately reduced. Given that over 100 experiments were performed, any factors which could reduce the experimental time-scale are of significant benefit.

A tri-axial traverse of the probe enabled both translational and rotational movements to be carried out during the experiments. Rotation of the probe was however limited to less that 30° from horizontal due to its effect on the inability of the water at bore pressure to adequately maintain the same level of water cooling at greater angles. This is due to the cooling water inlets being separately located at the outer ends of both the laser and photo-diode housing. Positional accuracy using this system traverse was 0.1 mm.

In order to investigate the transient formation of the hot smoke layer, single point measurements were made at a location equivalent to head-height in a full scale room. For the experiments which achieved steady-state, the soot probe was traversed to provide spatial distribution profiles of soot. Due to the time taken to reach steady-state for the 0.25m doorwidth configuration, single traverses only of the soot probe were possible during the course of a single experiment, whereas multiple traverses were possible for the 0.36m doorwidth.

Thermophoretic sampling of soot was undertaken in the plume exiting the doorway for investigation under a Scanning Electron Microscope. The results of the electron

microscopy work described here was not intended to be comprehensive, but only to provide cursory examination of the size of primary particles and indicate the level of polydispersivity. Figure 3.13 and 3.14 show a selection of soot images. Individual particles may be seen in the agglomerated structures.

Figures 3.15 to 3.16 present single-point soot volume fraction at the equivalent of head height in a standard room. Also plotted is the corresponding distance for general visibility in smoke according to equation 2.8. Due to RF interference on measurements made during the operation of the extract hood, results for the 0.15m doorwidth are shown over a period of only 3 minutes at the peak of the experiment when the extract was off.

Figure 3.17 presents multiple point measurements made in the 0.36m doorwidth configuration, where the probe was traversed into the compartment at various heights.

3.3.5 Mass Air Flow Measurement

One device that is suitable for the measure of low-velocity buoyancy-driven flows associated with gaseous products of combustion is a bi-directional probe, developed by McCaffrey and Heskestad [87]. The rationale behind this choice of instrument is that it is robust, easily calibrated and does not require careful alignment - important considerations under harsh environmental conditions such as those experienced in a typical room fire. Figure 3.18 shows the actual arrangement of the velocity probes, which are positioned vertically at several heights. For greater accuracy, the vertical location of these probes varied slightly according to the anticipated neutral layer height, but taking the 0.23 m burner as an example, these heights were typically around 9.7 cm, 18.7 cm, 32.5 cm, 42.5 cm, 50.0 cm, 61.5 cm, 71.5 cm, 82.0 cm and 94.0 cm assuming the floor to be set at 0.0 cm. All measurements were taken at the mid-line of the enclosure door.

Despite its suitability and inherent simplicity of use, the bi-directional probe does present difficulties. The paper by McCaffrey and Heskestad recommend that the probes should be installed horizontally with the transducers located at the same height as the probe, in

order to mitigate buoyancy effects in the lead tubes. This was not considered practical for these experiments.

The bi-directional probe is well described by McCaffrey and Heskestad and so will not be described in detail here. The probe and dimension used in the room fire experiments are shown schematically in figure 3.19.

The probe's steel tubes are used to carry the pressure signal from the head of the probe and also allow mounting on a vertical column. The inlets of each probe were connected via lengths of twinned silicone rubber tubing to an electronic micromanometer. The micromanometer gives an analogue voltage output which is calibrated against a null-reading tilting U-tube micromanometer. The output signal is then fed directly to the data-logger.

A ten point calibration for the micromanometer was carried out against the reference U-tube micromanometer, with a range of 0 to 30 mm wg. The calibration was performed in the ranges 0 to 10 mm wg, 0 to 1 mm wg and 0 to 0.1 mm wg assuming a linear relationship between the applied (absolute) pressure against the electronic micromanometer reading.

Calibration of the velocity probes was performed using a wind tunnel and suitable orifice plate to produce a flow velocity of similar range to that expected in the compartment doorway. The pressure difference across the wind tunnel orifice plate was measured using a calibrated electronic micromanometer. The air temperature was measured using a mercury in glass thermometer, at the beginning of each probe's calibration. This was repeated for all eight probes that were used in the experiments.

Figures 3.20 to 3.21 show doorway velocity profiles resulting from all doorwidth experiments using using the velocity probe arrangement described.

Repeatability of experiments is generally excellent. Figure 3.22 illustrates this with average peak doorway temperatures achieved in three successive experiments for identical burner and doorwidth configurations.

From an observational point of view, with decreasing door-width there appeared an increasing tendency for the flame to 'blow-off' the burner. In some instances, the flame was seen to detach itself completely. A good illustration of this may be seen in figure 3.23 for the 0.15m door width case. In addition, from freezing frames taken sequentially from digital recording, 'flame-pulsing' was observed to be associated with local vortex formation, similar to the influence of cross-flow on a turbulent jet. These vortex rings were seen to progress upwards from the base of the flame to its tip. These vortices can be clearly seen in figure 3.24.

3.3.6 Thermal Stratification and Interface Height

The height of the neutral layer is determined from the velocity profile in the doorway. Accurate measurement and prediction of the neutral plane is of paramount importance for the determination of visibility in smoke. Table 3.3 details the height of the neutral plane for each experimental configuration. The values in the table refer to steady-state averages. It can be clearly seen that the layer height and neutral plane lowers with a reduction in doorwidth. Oscillatory motion setup at the neutral plane interface is evident from the results of the nearest velocity probe (see the profile pertaining to a height of 46 cm in figure 3.20(a) for example).

Doorwidth (m)	Neutral Layer Height (m)
0.36	0.50
0.25	0.46
0.15	< 0.39

Table 3.3: Neutral layer height as determined from doorway velocity profile

The picture in figure 3.25 illustrates the influence of the compartment on the shape of the hot layer. The picture is taken from the centre of the compartment floor where previously the burner had presided. The zone-model assumption that the upper and lower layers are clearly defined with a consistent layer depth, does not appear to be so readily applicable at each corner of the compartment, due to the visibly concave nature

of the layer. This phenomenon is reproduced during the course of the compartment fire simulations in chapter 6.

3.3.7 Total Heat Flux

Two types of total heat flux gauges are commercially available. Figure 3.26 shows a schematic of the Gardon gauge type which is used in this research. Radial heat flow in a metallic foil, develops a temperature difference between the foil's centre - the hot junction, and the other peripheral junction at the outer water-cooled jacket. An assumption is made where, as a result of the calibration curves being remarkably linear, the electrical signal output is independent of body temperature and is simply proportional to the imposed heat flux. The calibration of the heat flux gauges were carried out under varying water-cooling temperatures and the results from this can be seen in figure 3.27. An in-line heater provided the elevated water temperature required to test the sensitivity of the cooling water to the apparent heat flux. The heater relies somewhat crudely on the correct water through-flow in order to control the temperature. It was found that very fine regulation using a needle valve, was required to govern the heater temperature by the regulated flow of water at the supply inlet. Further difficulty with regulating the correct water flow for the in-line heater was apparent in the open-pool fire experiments, where an elevated temperature was required in order to heat the gauges above that of the boiling point of water at standard pressure. In order to increase the pressure to achieve temperatures of around 130°C, the regulator valve was situated at the outlet end. Care was needed due to the enhanced time-lag between fine flow adjustment and supply to the heater.

The desired black-body furnace temperature used to calibrate the heat flux gauges, is manually set by the user. An automatic control switch then maintains the furnace at this temperature. The control on-off switch relies on the measured temperature being outside of a given range, therefore it is difficult to ensure that the black-body furnace is at steady-state throughout. The inability to control this precisely is apparent in figure

3.27, which highlights the error involved when assuming that the furnace is at a steady-state throughout the calibration. However, the absolute accuracy is still within 2°C and given the difficulties associated with the in-line heater that have already been mentioned, it was deemed that the effect of this would be negligible. In fact the raising of the furnace temperature would only serve to compensate for the increase in water cooling temperature which is also clearly demonstrated in the figure.

At the worst conditions to test the robustness of this assumption, where the cooling water was at an elevated temperature of around 130 °C, this represented a 5% reduction in output signal, when exposed to a radiant source. Sensitivity of measurements using Gardon gauges below 15 kW m^{-2}were conducted by Robertson and Ohlemiller [88] who in addition to cautioning against assuming signal linearity with different cooling water temperatures, also introduced the concept that convective components may counteract the radiative heat flux due to cooling by ambient air. This is of particular concern in the context of compartment fires, where under ventilation controlled conditions, a strong element of convective heat transfer exists. A further error is the exchange of heat with its surroundings by both radiation and buoyant convection, which occurs if its surface temperature differs from that of the surroundings.

Figures 3.28 to 3.29 show the level of total heat flux experienced by two heat flux transducers for each doorwidth. One gauge was positioned high in a compartment sidewall so that it would be immersed in the hot layer; the other was located on the floor of the compartment to one side of the burner.

Two total heat flux transducers were also placed in the locating bosses housed in the base of the 0.23 m pan. To ensure consistency with the smaller burner, heat flux gauges were also located in the floor - outside the flaming region and in one of the side walls of the compartment, in order that it may be full engulfed by the hot smoky layer.

Ideally, the position of the heat flux gauges in the burner, would be flush with the surface of the fuel to ensure identical view factors. However, this is impossible to achieve where significant boiling of the fuel occurs, unless the gauges are aspirated to prevent liquid

from splashing on to the important upper surface. Despite setting the gauges to around 5mm higher than the fuel level in the burner, significant concerns still arose from the layer of condensed fuel vapour that formed on the upper surfaces of the mounted gauges. This generally remained throughout the experiments and either finally evaporated close to flame extinction or more commonly ignited to produce small independent flames. Although the layer of heptane is considered transparent to radiation is was necessary to discount that the apparent heat flux was merely a function of the thermal properties of the liquid and the evaporative cooling that would occur.

Due to the constraints in access to the compartment, more detailed investigations of the behaviour of the heat flux gauges were restricted to separate sets of experiments in an open pool-fire configuration and are further explained in the next chapter.

3.3.8 Compartment Heat Loss

One common and major criticism of compartment fire experiments which are publically well documented, is their neglect of heat loss from the enclosure boundaries. The assumption is generally made that where the compartment walls comprise of super-insulated materials, the enclosure may be considered adiabatic and as thus does not represent a significant threat to accuracy in the global context. However, the formation of soot is seen to be dependent on a fairly narrow range of conditions (see figures 5.2 to 5.13), where temperature plays an important part. The importance of correct specification of wall boundary conditions for numerical modelling will be highlighted in chapter 5, particularly in the simulation of soot production.

In order to quantify the level of heat loss from the compartment, a series of 21 surface thermocouples were fixed to the external walls of the compartment using ceramic adhesive. The thermocouples were equally spaced along the width and length of the ceiling and at different heights along one of the compartment side walls (see figures 3.30 and 3.31 for their exact locations). In addition, because the compartment has a multi-layered insulation structure, three thermocouples were installed, the first in the interior of the

room, the second between the inner insulating material (durablanket) and the Supalux and the third on the exterior of the room. Because the thermal conductivity is known for each of the materials concerned, it is possible to directly compare the calculated heat loss with those found experimentally. Figure 3.32 shows a typical time-temperature profile for the temperature reached between the outer surfaces of the durablanket and compartment exterior.

Figure 3.33 depicts the time evolution of the compartment side wall external surface temperature. The sub-figure seen superimposed on the main chart shows the peak surface temperature averaged over the period 23.5 to 24.5 minutes. Although the wall appears to reach a quasi steady-state at just over 20 minutes, this is simply as a result of flame extinction occurring at around 18 minutes experimental duration.

The calculation of surface heat flux from transient temperature histories measured in a heat conducting solid poses some difficulties, due to having to account for the energy absorbed by the compartment walls. Figure 3.34 illustrates the penetration depth of supalux achieved with time calculated using the properties in table 3.1. The thickness of this layer is 12mm, the time taken for this penetration depth to be achieved is just under 600 seconds from the graph. Therefore, calculated heat loss from the compartment may be considerably simplified after this period of time in the compartment fire under the assumption of steady-state conditions and one-dimensional heat transfer.

Figure 3.35 depicts the total convective heat loss from the compartment assuming steady-state conditions have already been reached.

The magnitude of uncertainty in the thermo-physical properties of supalux were established by using THELMA, a finite element code designed specifically for solving two-dimensional thermal problems and developed at the Building Research Establishment.

THELMA requires an input of properties such as thermal conductivity, for each layer in the structure of the compartment walls. In addition, a temperature-time curve for the exposed inner surface of the durablanket is required for input to the model based on exper-

imental measurements. Figure 3.36 illustrates very good agreement between THELMA predictions of external surface temperature compared with those found experimentally, giving credibility to the use of manufacturers values for material properties in the calculation of heat loss (under the assumptions of steady-state already highlighted).

3.3.9 Burner Heat Loss

The burner itself is manufactured from 3mm steel. No insulation is provided apart from the rim where it is in direct contact with the compartment floor. As such, enthalpy losses are considered to be mono-dimensional. A thermocouple was attached to a central location on the base of the pan in order to discern if these thermal losses are significant.

As you can see from figure 3.37, if the experiment is conducted with an initial pan temperature equal to ambient, the maximum temperature attained is around 50°C which is around 50°C lower than the boiling point of heptane. Unsurprisingly after an initial plateau is reached, the temperature starts to steadily increase corresponding to a reduced fuel level in the burner. The temperature increases significantly towards the end of the experiment (see figure 3.38) as the fuel level in the pan drops, the flame shortens and sits below the rim of the pan close to the base of the burner. This'over-shoot' which is seen to occur at the end of each experiment, is common with other such experiments where an un-insulated pan is used. After the main flame has extinguished, there remains small flame structures due to fuel vapours being continually burnt at the fuel inlet ports until the level in these ports subside and the flame is quenched.

3.3.10 Emission Spectroscopy

Instantaneous spectrally resolved radiation intensity measurements were made at various locations perpendicular to the pool fire surface and external to the compartment pointing though the door, using a Rees Instrument scanning monochromator. This system comprises a number of scanning monochromators which are connected to a control

unit and interfaced to an IBM compatible computer. Control of the instruments is via the appropriate software. The monochromators consist of a motor-driven, constantly spinning diffraction grating which rotates inside the monochromators at a frequency of 12Hz and a detector unit which sends an analogue signal to the main control unit. The magnitude of this signal is proportional to the incident radiative energy. Spectra were generally acquired at 20 second intervals and readings were averaged over ten data points for the full wavelength range. However, single wavelengths were also investigated for a more detailed description of time dependency on the emission signal. Two detectors are available for this system, depending on the wavelength range of interest. The range 500-5000nm utilizes a cooled lead selenide detector. Although not utilized for these interim measurements, long pass filters should ideally be used in conjunction with the detector in order to prevent mirroring of the spectra at twice their original wavelength.

A right-angled sight-tube containing a mirror at 45°, was fitted to the end of the monochromator and mounted in position just above the fuel surface inside the burner. The design rationale for this sight-tube was to permit optical access looking vertically through the flame, to match the radiative flux as perceived by the fuel surface. In addition, droplets are simultaneously prevented from entering the system. The inner-wall of the sight-tube was blackened using a fuel-rich propane flame to minimise the risk of internal reflections. The height of the sight-tube was adjusted to match that of the heat-flux gauges.

The spectrometer was calibrated in the same way as the heat flux gauges, using a black-body furnace at a temperature of 850 $°C$.

Figure 3.39 shows transient emission spectra over the range 1500-5000 nm for the 0.23m burner burning in the 0.36m doorwidth compartment. Readings were averaged over 20s intervals. Integrated total heat flux for each 20s time step is 7.6kW m^{-2}, 25.0kW m^{-2}, 14.2kW m^{-2}, 21.1kW m^{-2}, 15.2kW m^{-2} and 13.8kW m^{-2} for 20s, 40s, 60s, 80s, 100s, and 120s respectively. At the beginning of the experiments significant variation between successive measurements can be seen. Obvious disparities could

be explained during the transient and steady-state stages, and the transition from free-burning to ventilation controlled conditions where the flame trajectory changes, thus altering the optical path-length. Further disagreement could be explained by a significant change in temperature. Although this line of enquiry was not pursued in this research, Choi [46] did utilise ionization gauges in conjunction with emission measurements. The current flow across the ionization probe was used as an indication of flame presence due to the flame generated ions. From these measurements it could be determined whether a reduction in emission was due to the flame being outside the optical path length or reduced temperature.

A 3mm sapphire window was placed at the end of the sight-tube which protruded through the centre of the base of the burner. This was to prevent any liquid from travelling down and accumulating on the mirror at the right-angled bend, producing potentially spurious readings.

Single crystal sapphire windows are ideal for demanding applications such as emission spectroscopy because of their extreme surface hardness, high thermal conductivity, high dielectric constant and resistance to common chemical acids and alkalis. Sapphire is the second hardest crystal next to diamond and, because of their structural strength, sapphire windows can be made much thinner than other common dielectric windows with improved transmittance. Chemically, sapphire is a single crystal aluminum oxide (Al_2O_3) and is ideal for the emission measurements carried out in the compartment fire due to its high transmittance in the range 150 to 5500nm.

Care was taken to ensure that the end of the sight-tube remained flush with the top of the sight-boss. However, uncertainty remained as to whether the apparent significant drop in emission intensity at around $3.4\mu m$ was due to absorption by the fuel-rich layer above the surface of the heptane, or whether it was simply due to a condensed vapour sink in the small 1mm recess where the sapphire window was seated. The sight-probe was uncooled, thus lessening the risk of liquid logging. However, occasionally it was found subsequent to an experiment, that a thin clear sticky residue would appear on the

centre of the window.

At the end of each experiment the sapphire window was carefully cleaned to remove this residue and a deposit of soot which usually occurred at the end of the experiment due to the lapping of flames which accompanied flame-length shortening just prior to extinction.

Due to the concerns as to the effect of a build up of a fuel-rich region of heptane, bench tests were carried out exposing the spectrometer to a radiant heat source and placing a small amount of liquid heptane onto the upper surface of the sapphire window. Figure 3.40 illustrates the effect of this thin layer of heptane on the apparent level of emission over the range 1500-5000 nm.

The first two sets of instantaneous spectra are taken without the layer of heptane to provide base-line data and to ensure consistency in time of the radiant source. The next spectra (3rd spectra) shows a dramatic fall in intensity over the full wavelength range, with a slight drop at around 2300 nm and a sharp drop at 3400-3500 nm. Each successive spectra then indicates a slight increase in intensity, more prominent over the entire range rather than at 3400-3500 nm, suggesting that this is due to evaporation of the heptane.

A second test was carried out with the spectrometer exposed to the same radiant source without the sapphire window in place. A small drop of liquid heptane was placed just inside the sight-tube which upon evaporation would demonstrate the effect of fuel vapour on the apparent radiant emission. The results in figure 3.41 again illustrate the first two sets of data without the heptane vapour, the latter sets are influenced by the vapour which demonstrate again the drop in intensity.

3.3.11 Steady-State Time-Scales

In addition to the thermal inertia of the compartment boundaries, the time taken to reach a steady-state is also seen in these experiments to be dependent upon the level of venti-

lation. Although pre-heating of the compartment and the burner does seem to influence the absolute time scale, in relative terms decreasing the doorwidth from 0.36m to 0.25m results in a two-fold increase in time taken to achieve steady-state before flashover occurs. As already explained due to safety considerations, the experimental duration for the 0.15m doorwidth case was much shorter than that needed to reach steady-state - if one was certain it could be achieved. Only a small number of experiments were conducted using the smallest doorwidth, due to the difficulty in replication with the CFD model. However, there is such a striking contrast in results that these experiments are still valuable in qualitatively demonstrating the effects of restricted ventilation provision.

One of the more interesting features of the measurements made was the apparent time difference between soot and other scalars in their approach to steady-state.

Figure 3.42 depicts one of the most striking examples of observed differences between scalar variable time-scales. The measurement is taken at the centre of the door, in the full doorwidth configuration. The figure shows the approach to steady-state from soot volume fraction and thermocouple temperature time histories measured at the same vertical height. The large difference between soot and temperature implies differential transportiveness.

Figure 3.43 illustrates independent results, again from an experiment in the full doorwidth configuration. Total heat flux measurements to the compartment floor and to the upper part of one of side-walls are plotted along with soot volume fraction as determined with the soot probe. For this set of parameters, it may be clearly seen that the progress level of soot closely follows that of the heat flux gauges. This result is anticipated due to the close coupling between radiation and soot particle concentration.

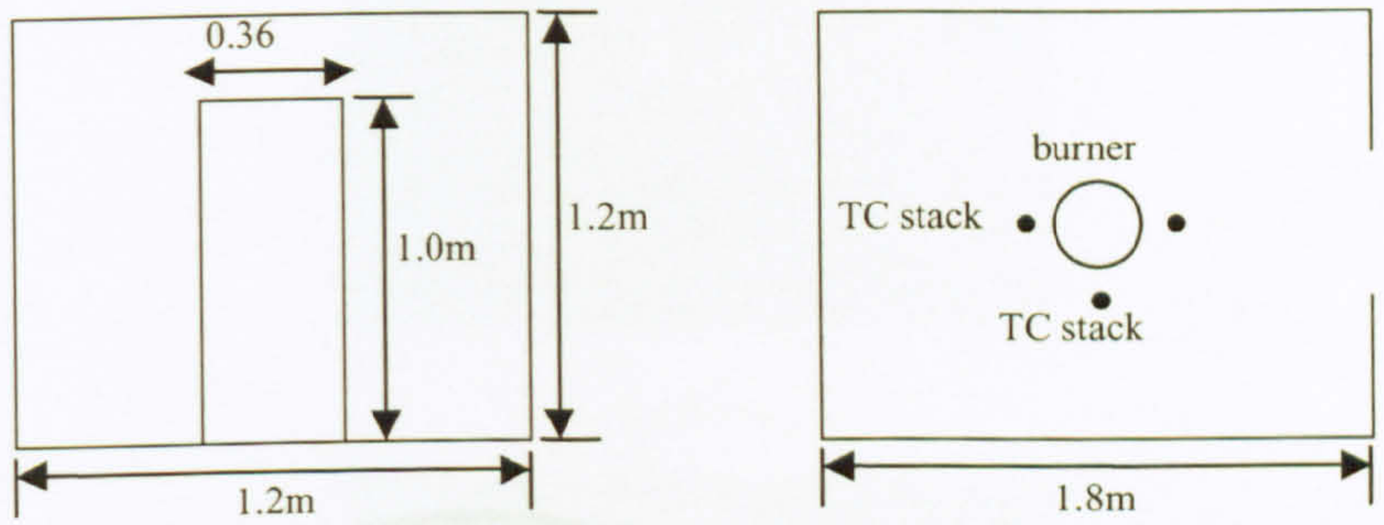

Figure 3.1: Half-scale ASTM experimental room schematic

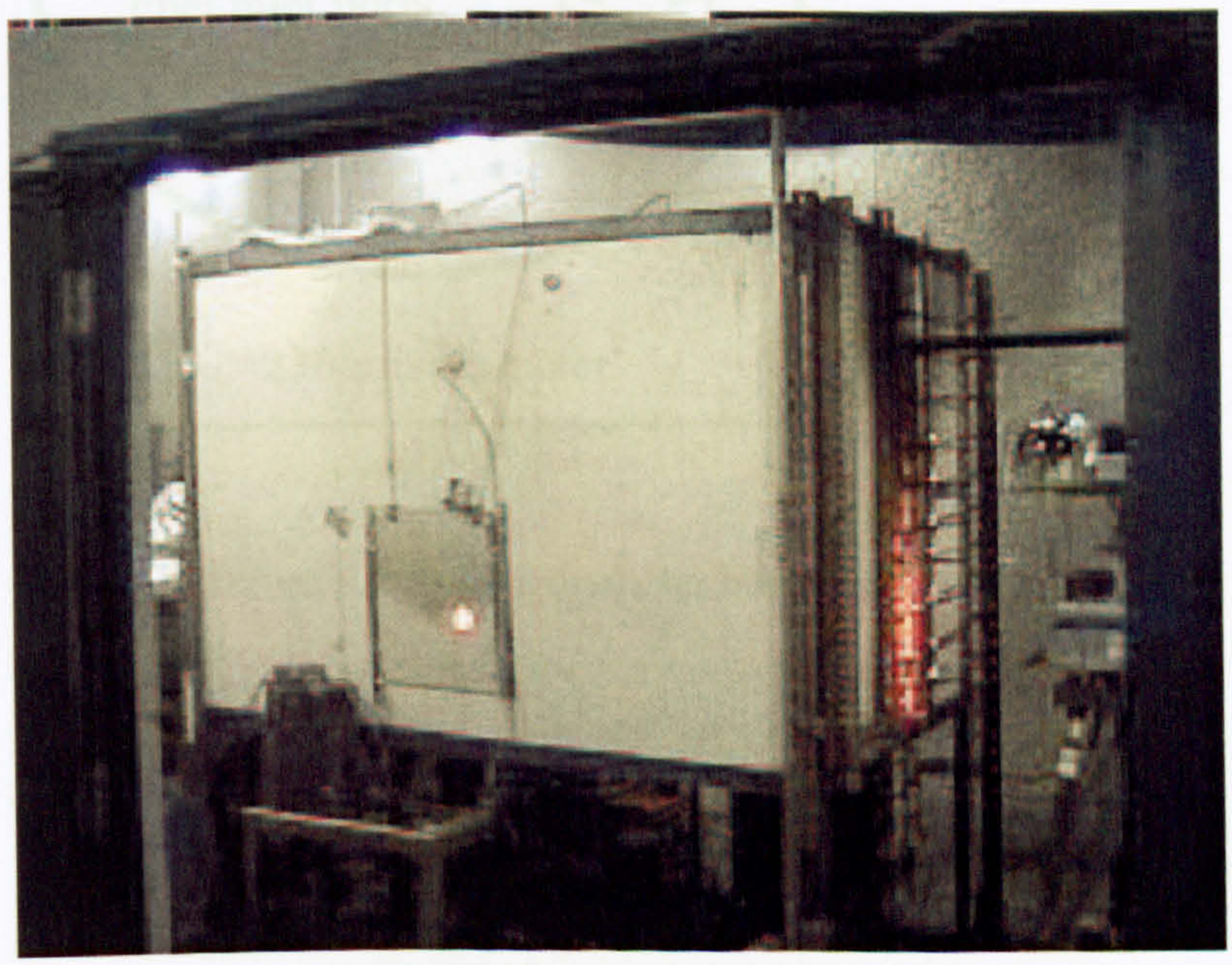

Figure 3.2: 1/2 scale ASTM experimental room picture

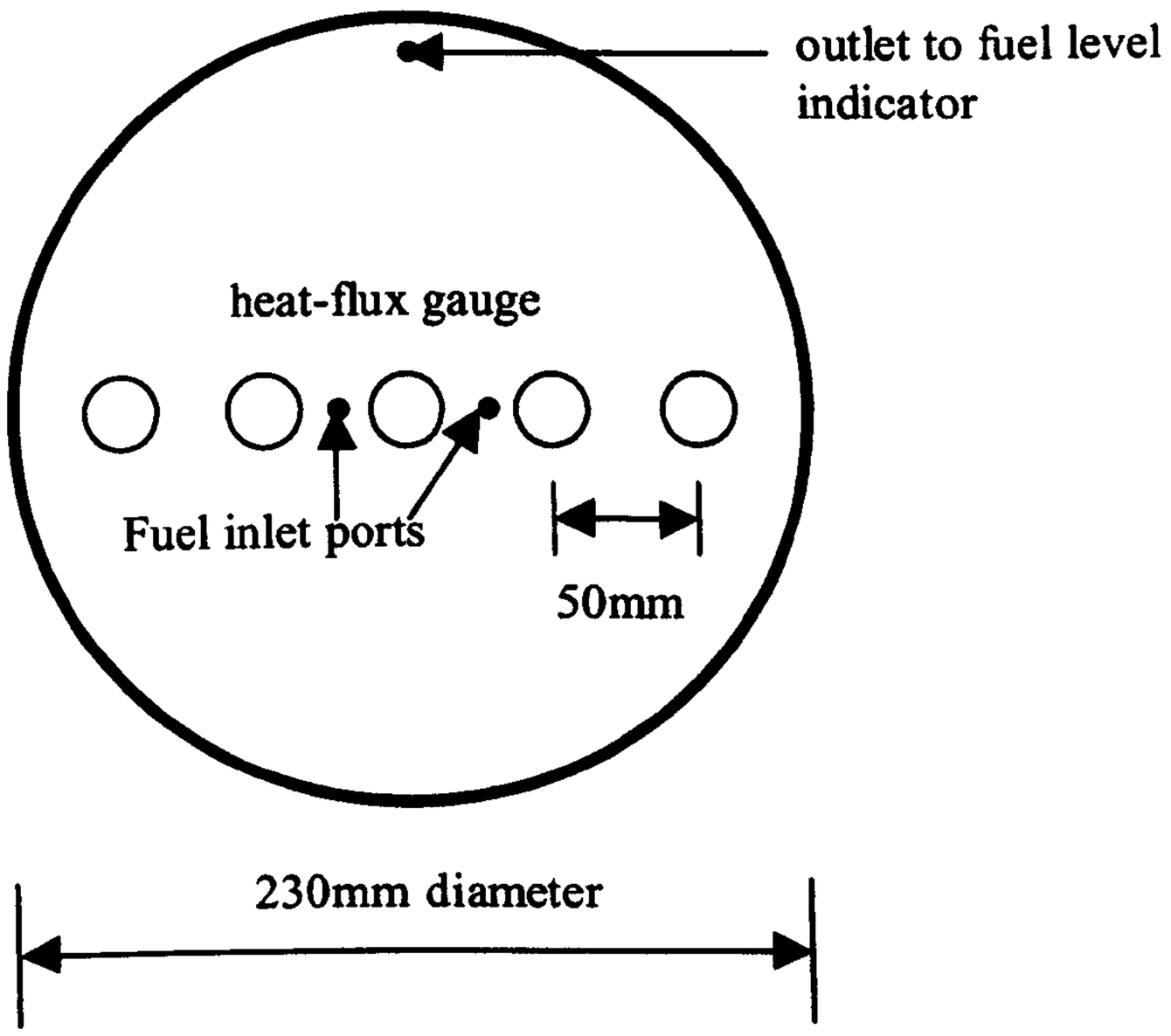

Figure 3.3: 0.23m diameter burner schematic

(a) 0.04s

(b) 0.08s

(c) 0.12s

(d) 0.16s

Figure 3.4: Successive still images captured by digital video recording illustrating flame front movement across the pool surface upon ignition

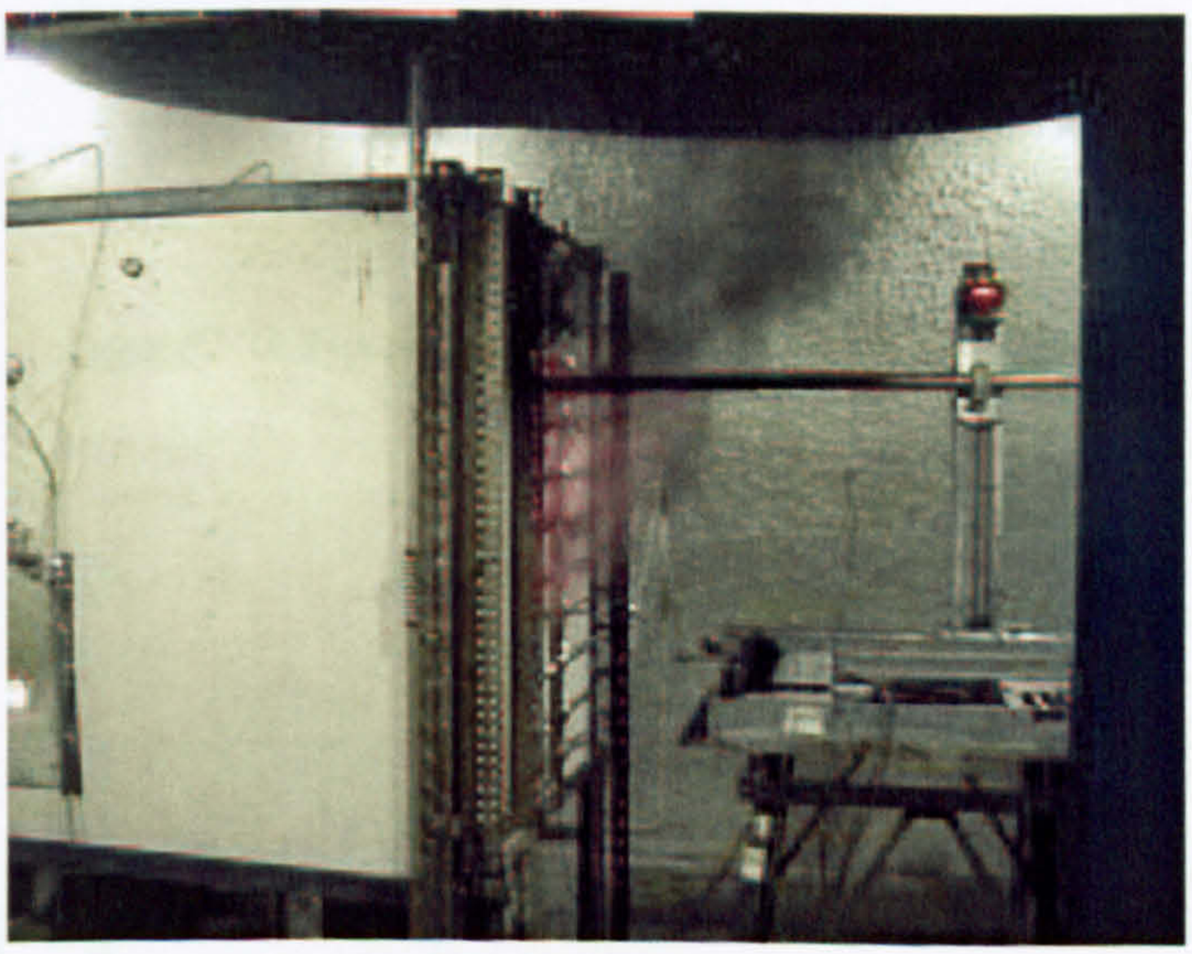

Figure 3.5: ASTM room showing radiant soot exiting 0.15m door

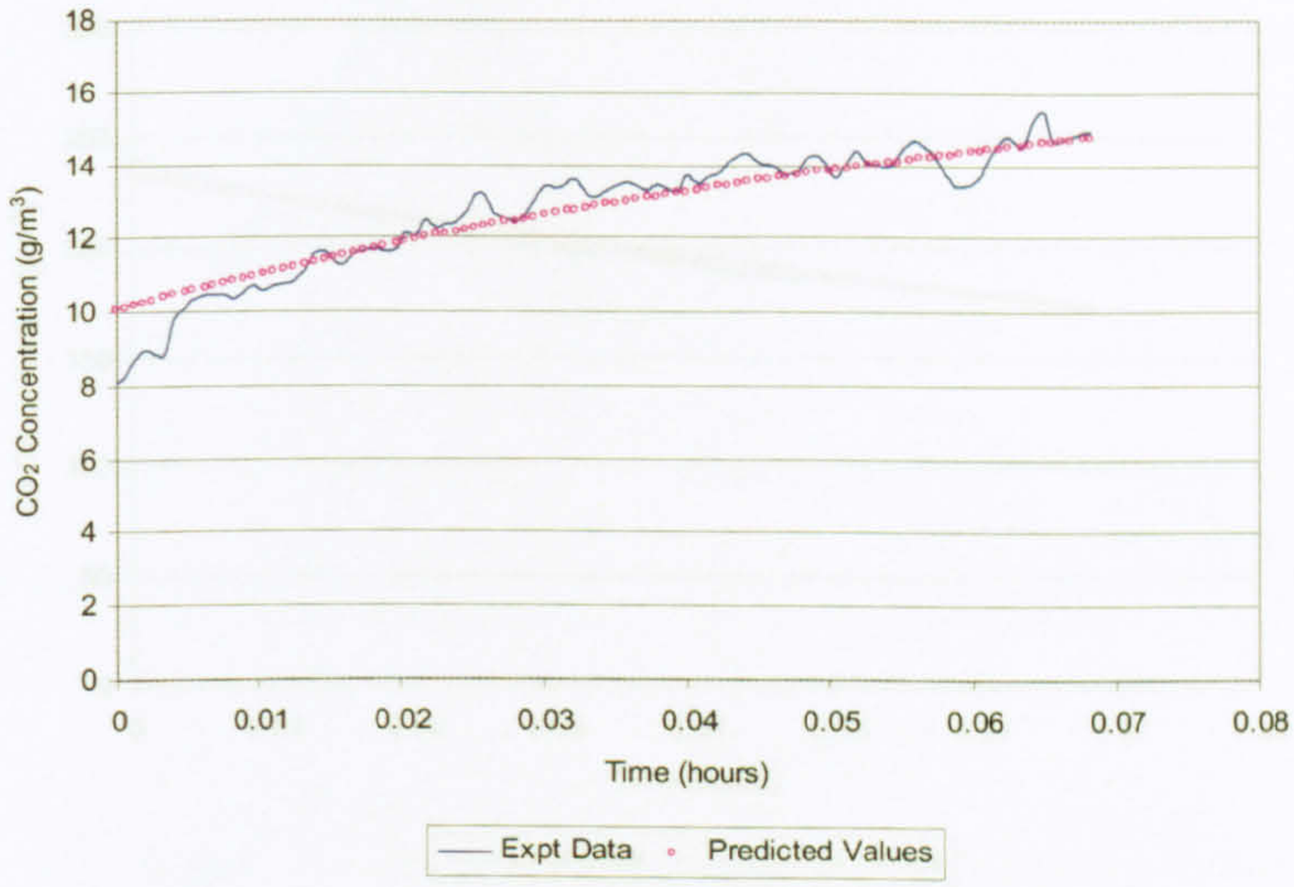

Figure 3.6: Non-linear Regression of CO_2 Emission

Figure 3.7: Non-linear Regression of CO Emission

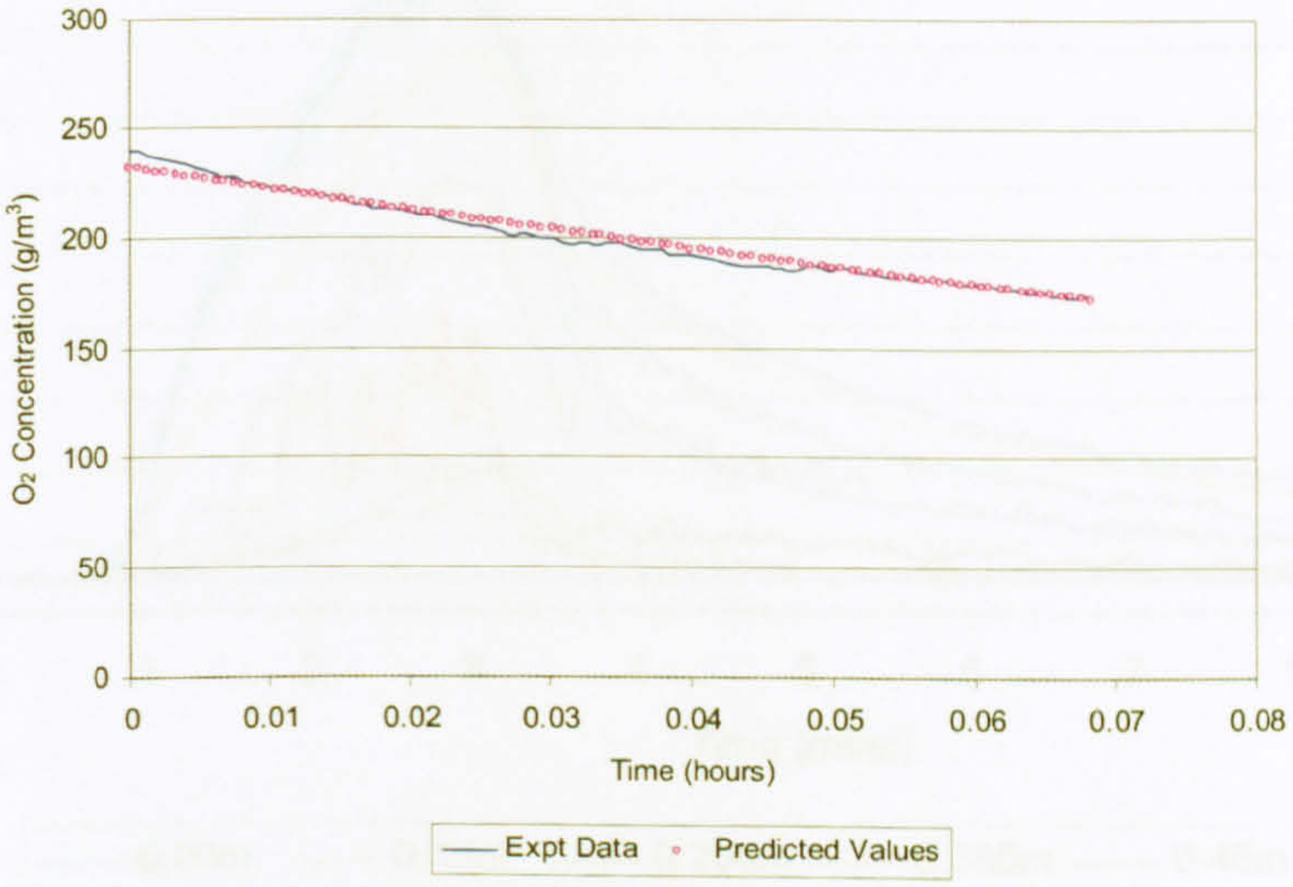

Figure 3.8: Non-linear Regression of O_2 Consumption

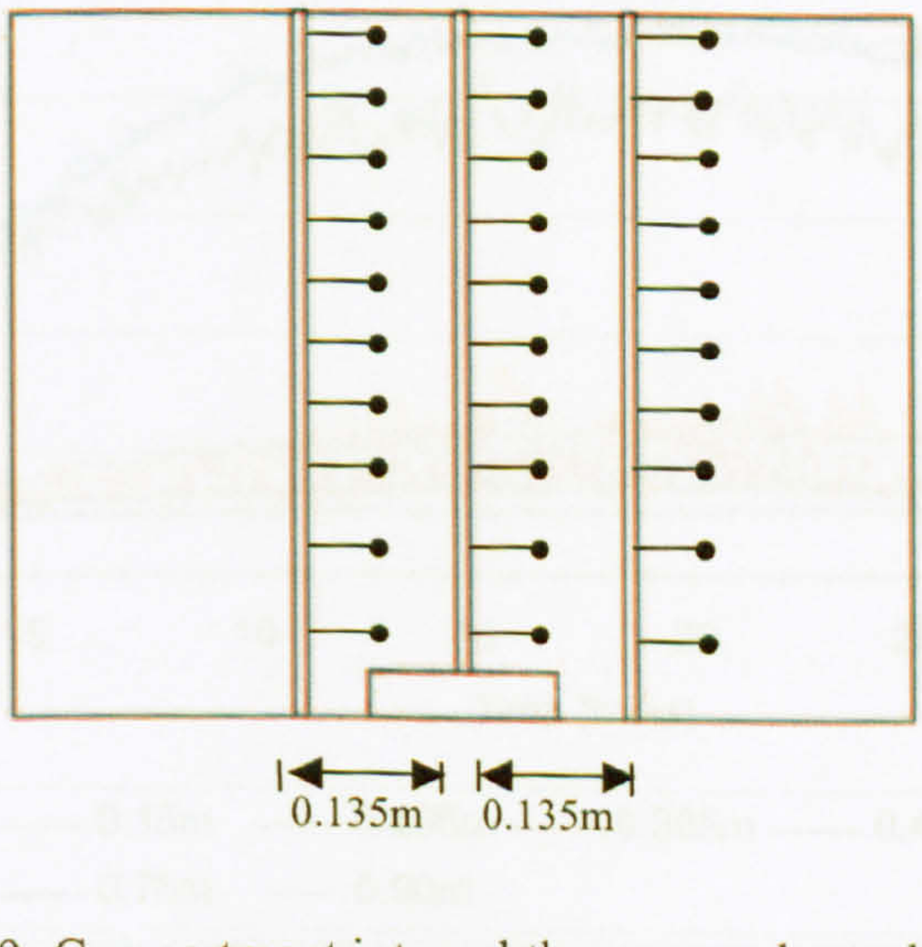

Figure 3.9: Compartment internal thermocouple stack locations

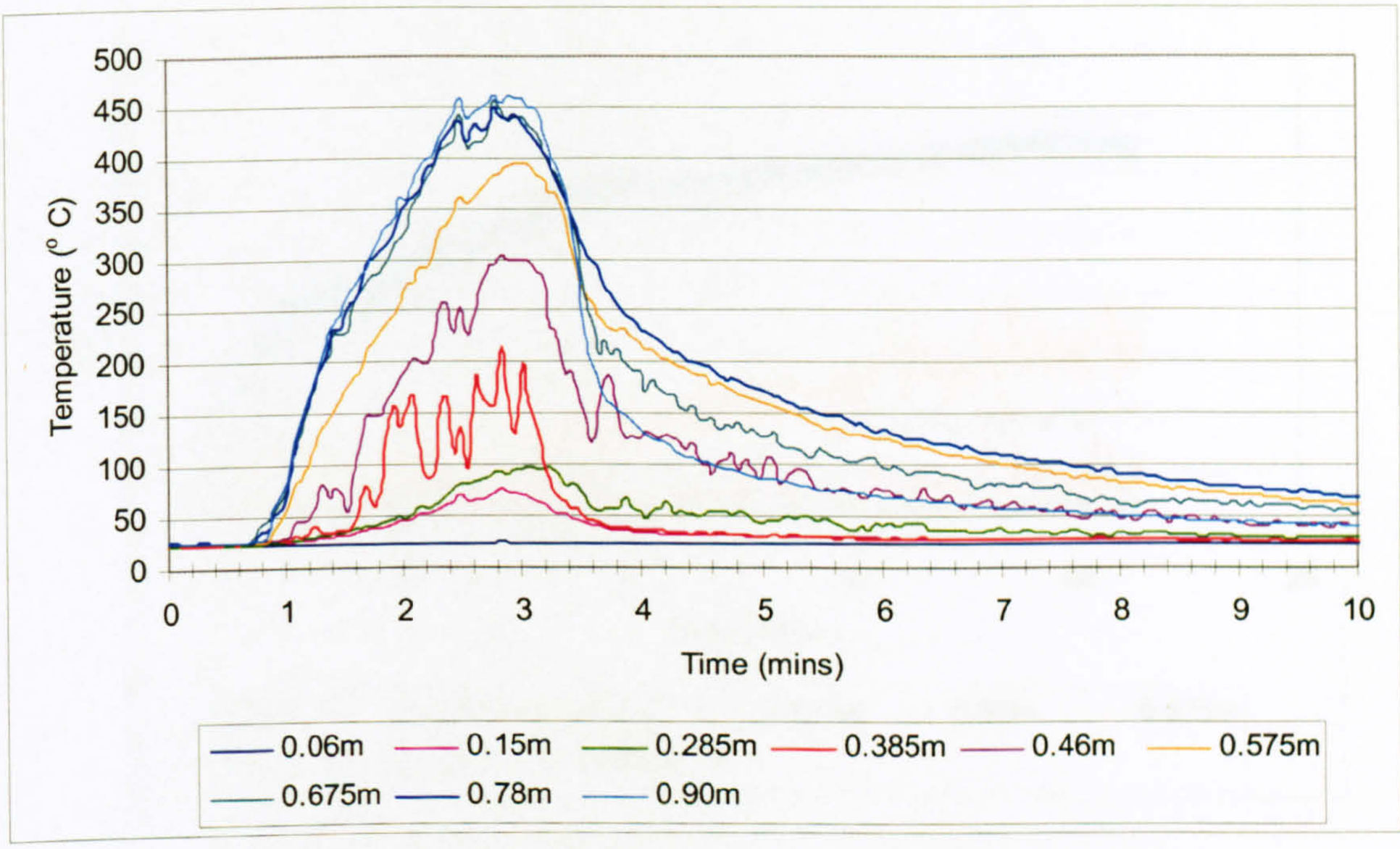

(a) Doorway temperature profile; 0.23m burner; **0.36m doorwidth**

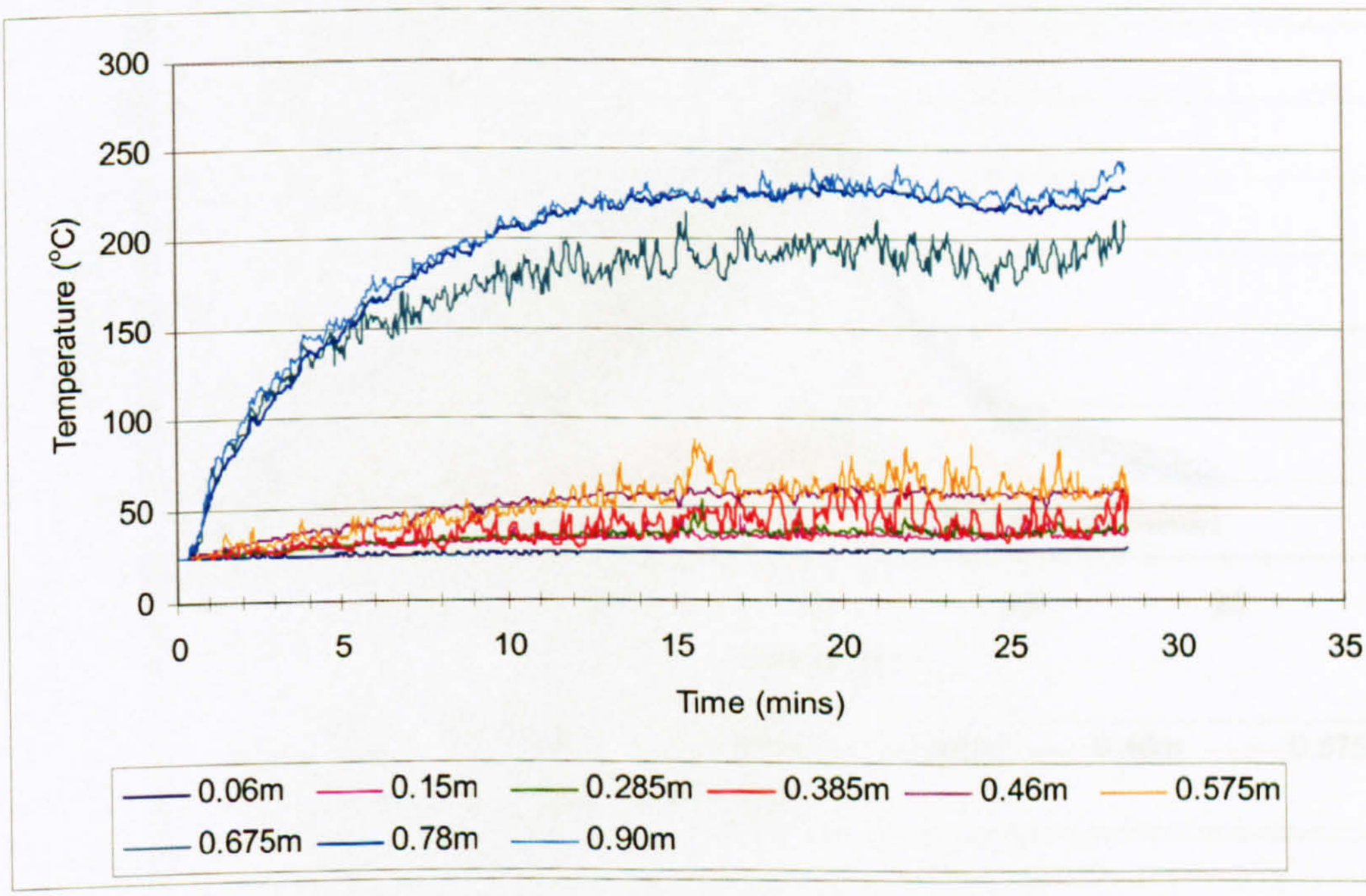

(b) Doorway temperature profile; 0.17m burner; **0.36m doorwidth**

Figure 3.10: Doorway temperature profiles; 0.23m burner, 0.36m doorwidth and 0.17m burner, 0.36m doorwidth

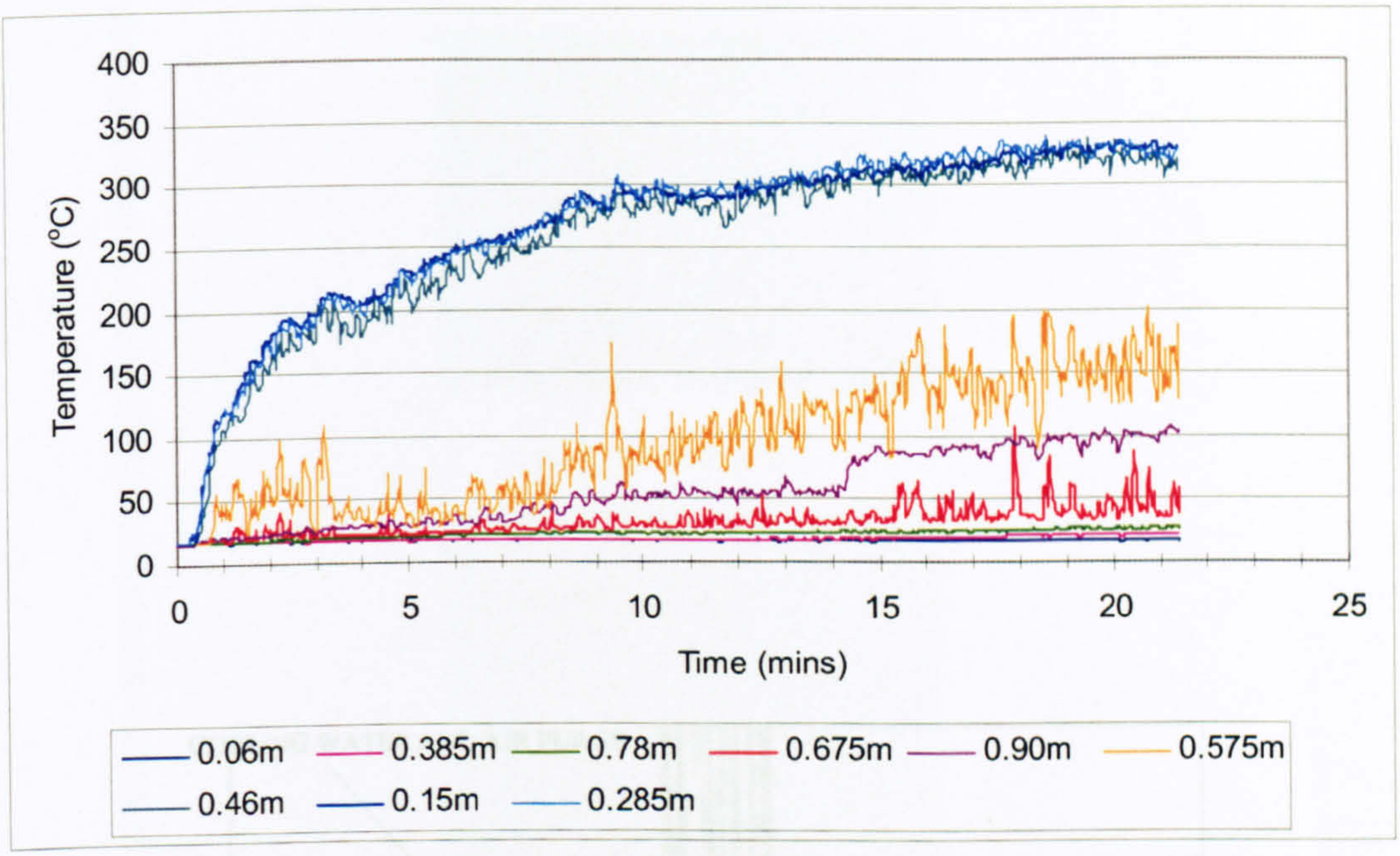

(a) Doorway temperature profile; 0.17m burner; **0.25m doorwidth**

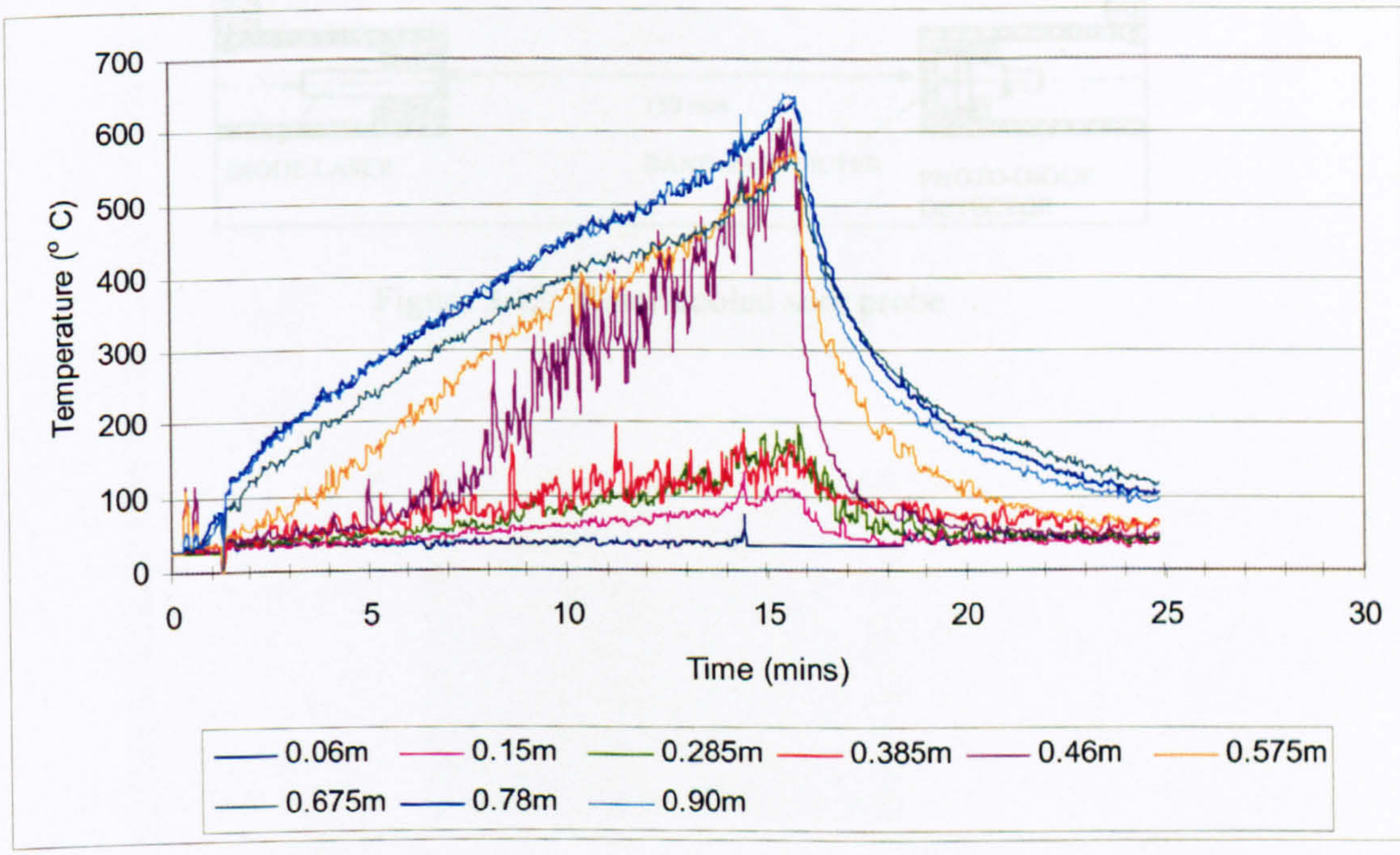

(b) Doorway temperature profile; 0.17m burner; **0.15m doorwidth**

Figure 3.11: Doorway temperature profiles; 0.17m burner; 0.25m doorwidth and 0.15m doorwidth

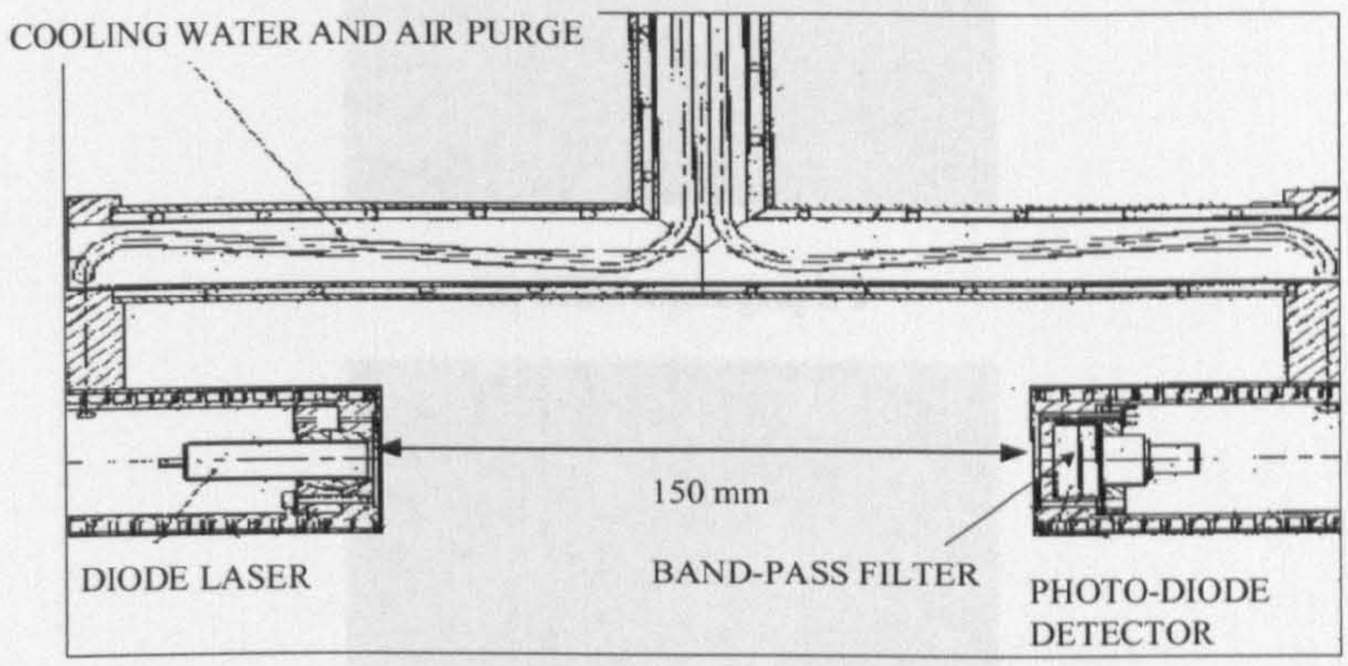

Figure 3.12: Water-cooled soot probe

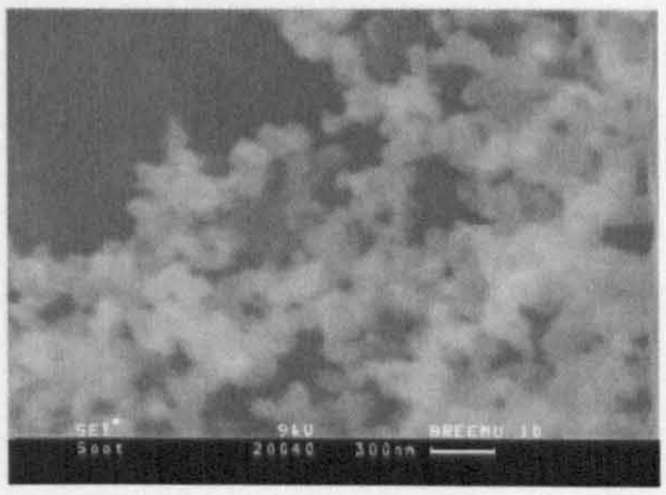

(a) SEM Micrograph 1

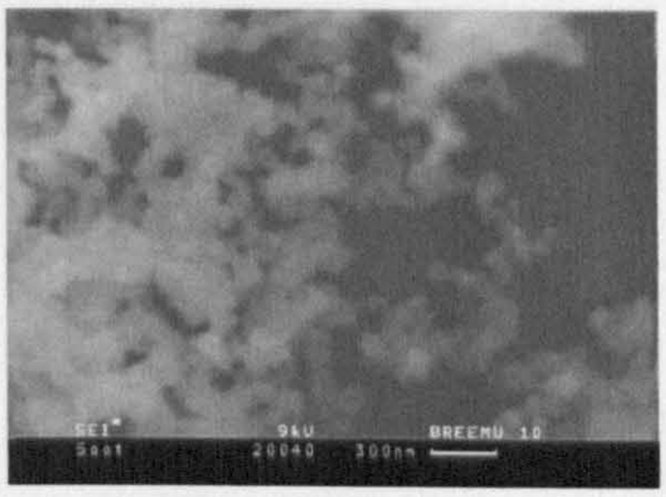

(b) SEM micrograph 2

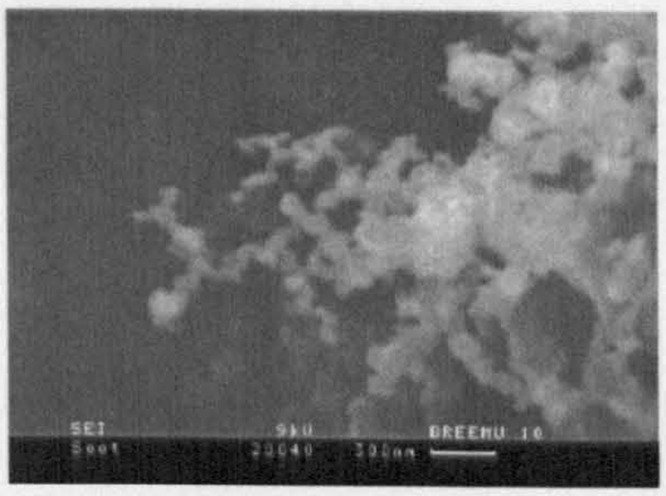

(c) SEM micrograph 3

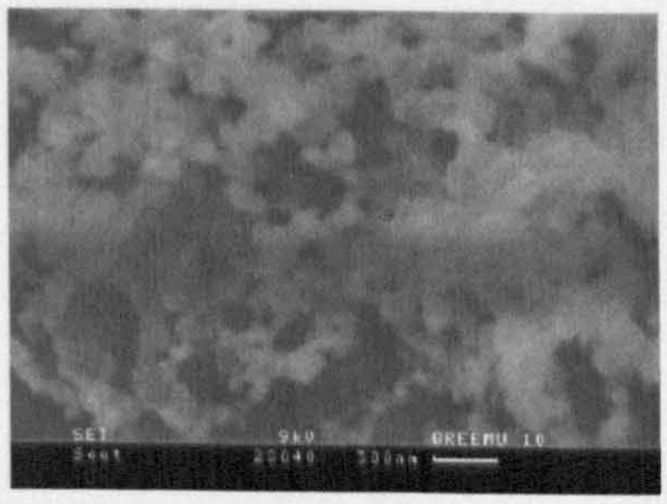

(d) SEM micrograph 4

Figure 3.13: First set of SEM micrographs of compartment fire soot

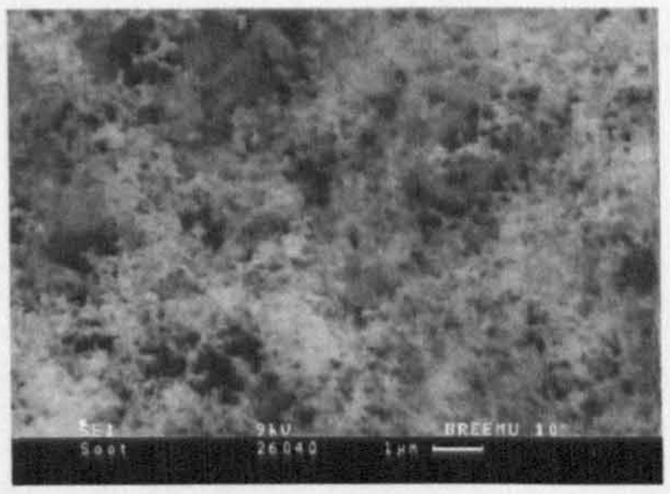

(a) SEM micrograph 5

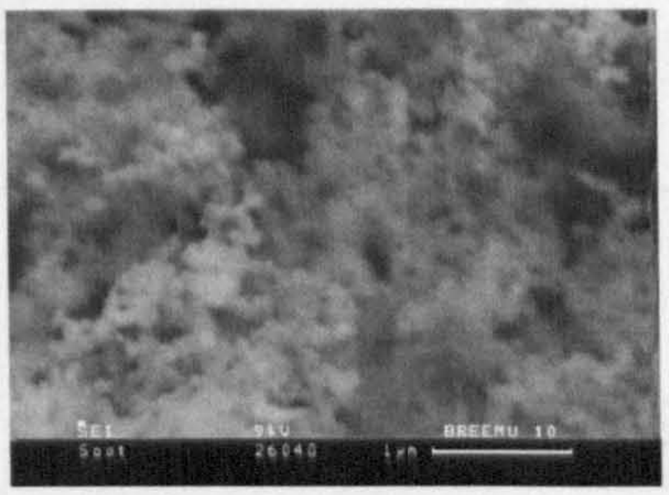

(b) SEM micrograph 6

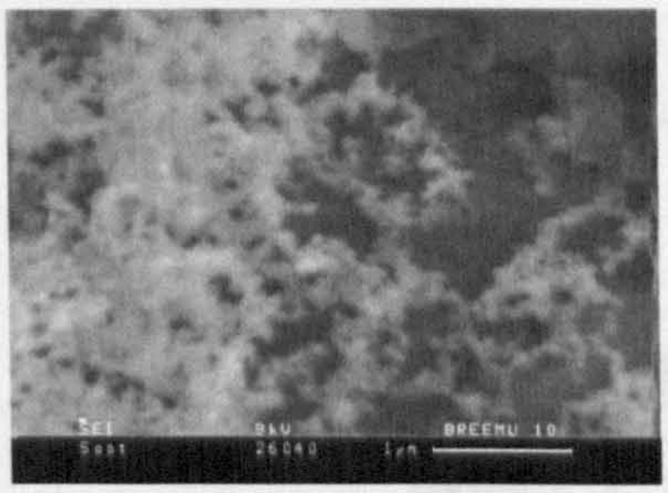

(c) SEM micrograph 7

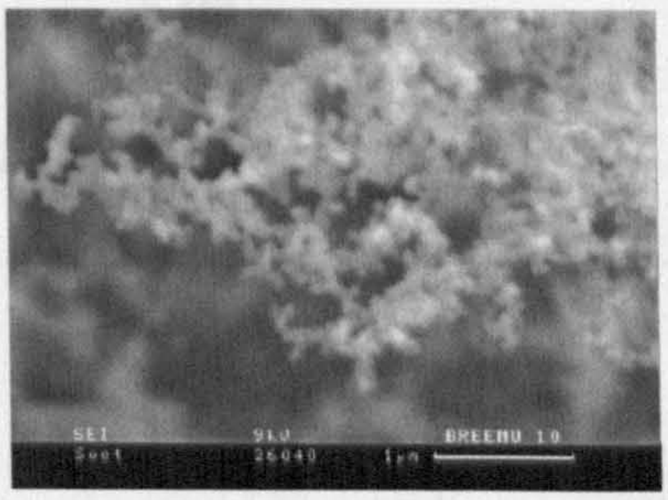

(d) SEM micrograph 8

Figure 3.14: Second set of SEM micrographs of compartment fire soot

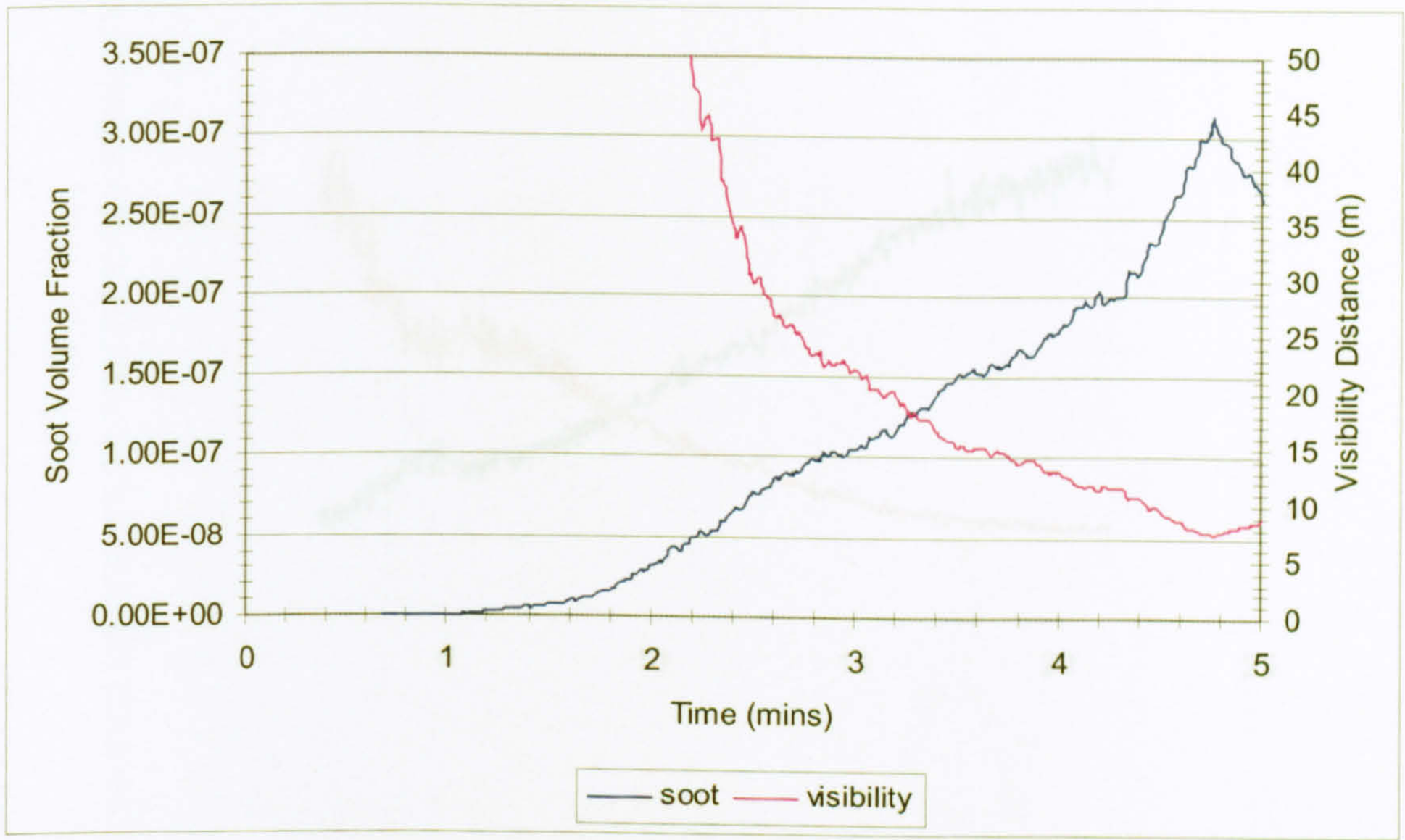

(a) Doorway soot profile; 0.23m burner; **0.36m doorwidth**

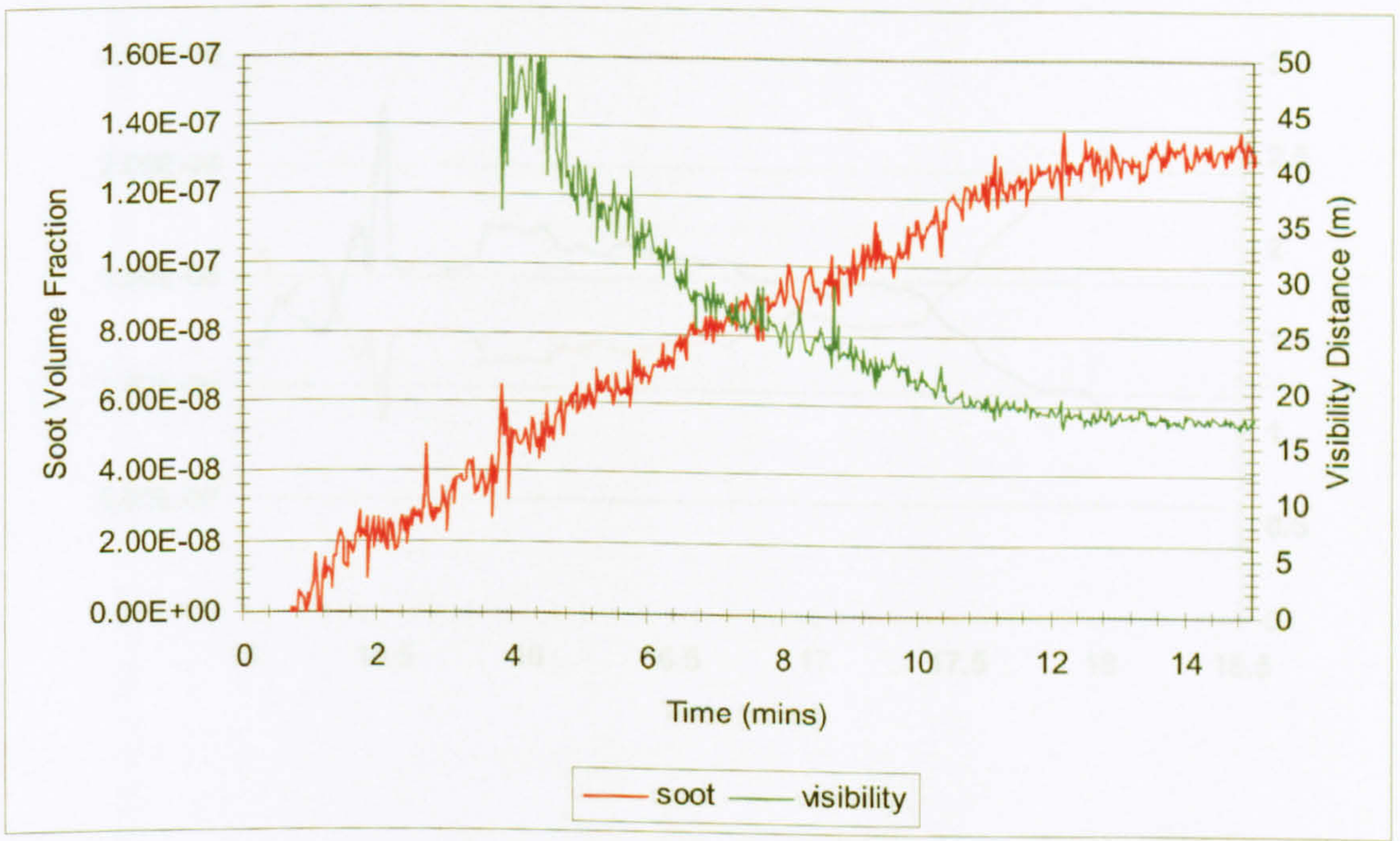

(b) Doorway soot profile; 0.17m burner; **0.36m doorwidth**

Figure 3.15: Doorway soot profiles; 0.23m burner, 0.36m doorwidth and 0.17m burner, 0.36m doorwidth

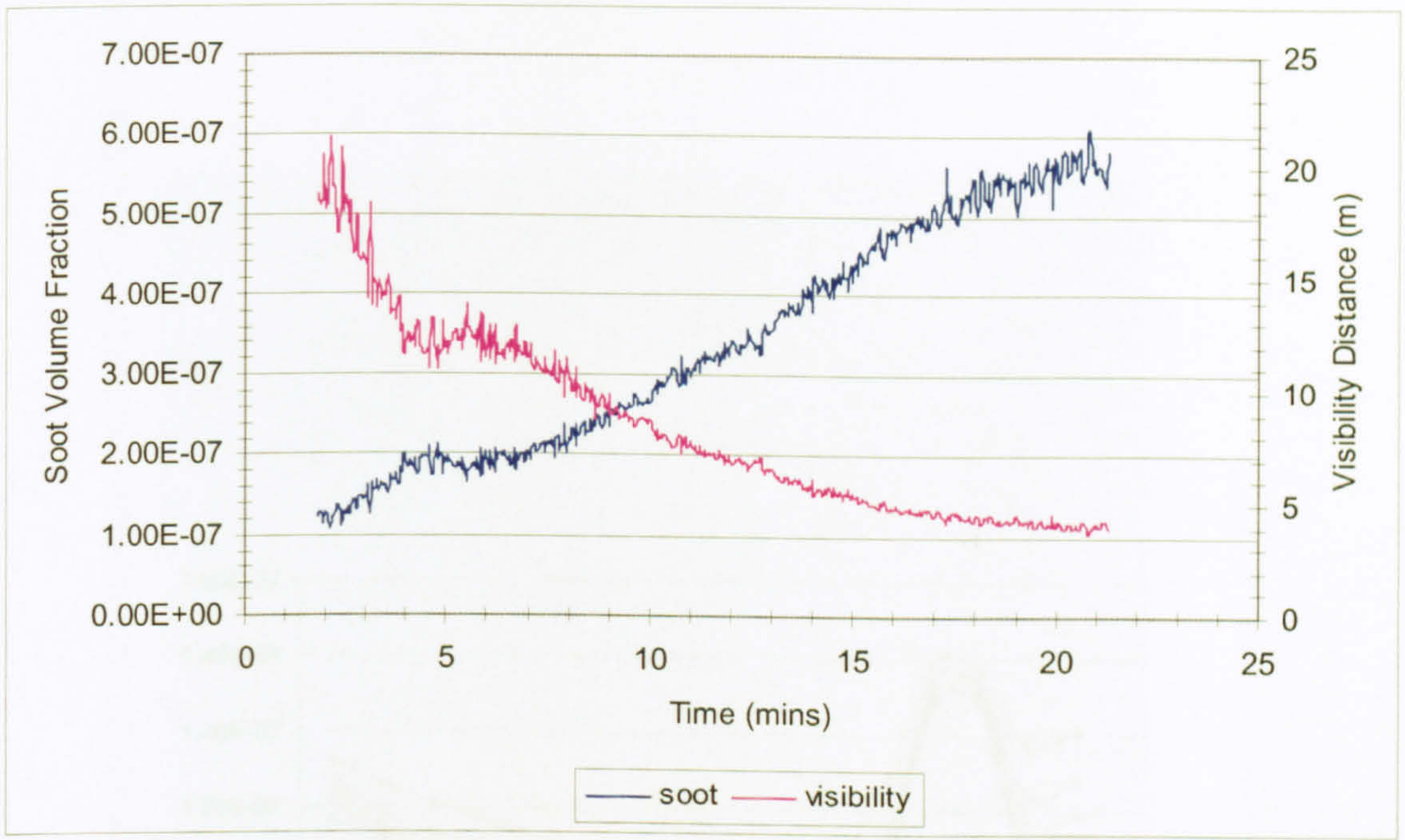

(a) Doorway soot profile; 0.17m burner; **0.25m doorwidth**

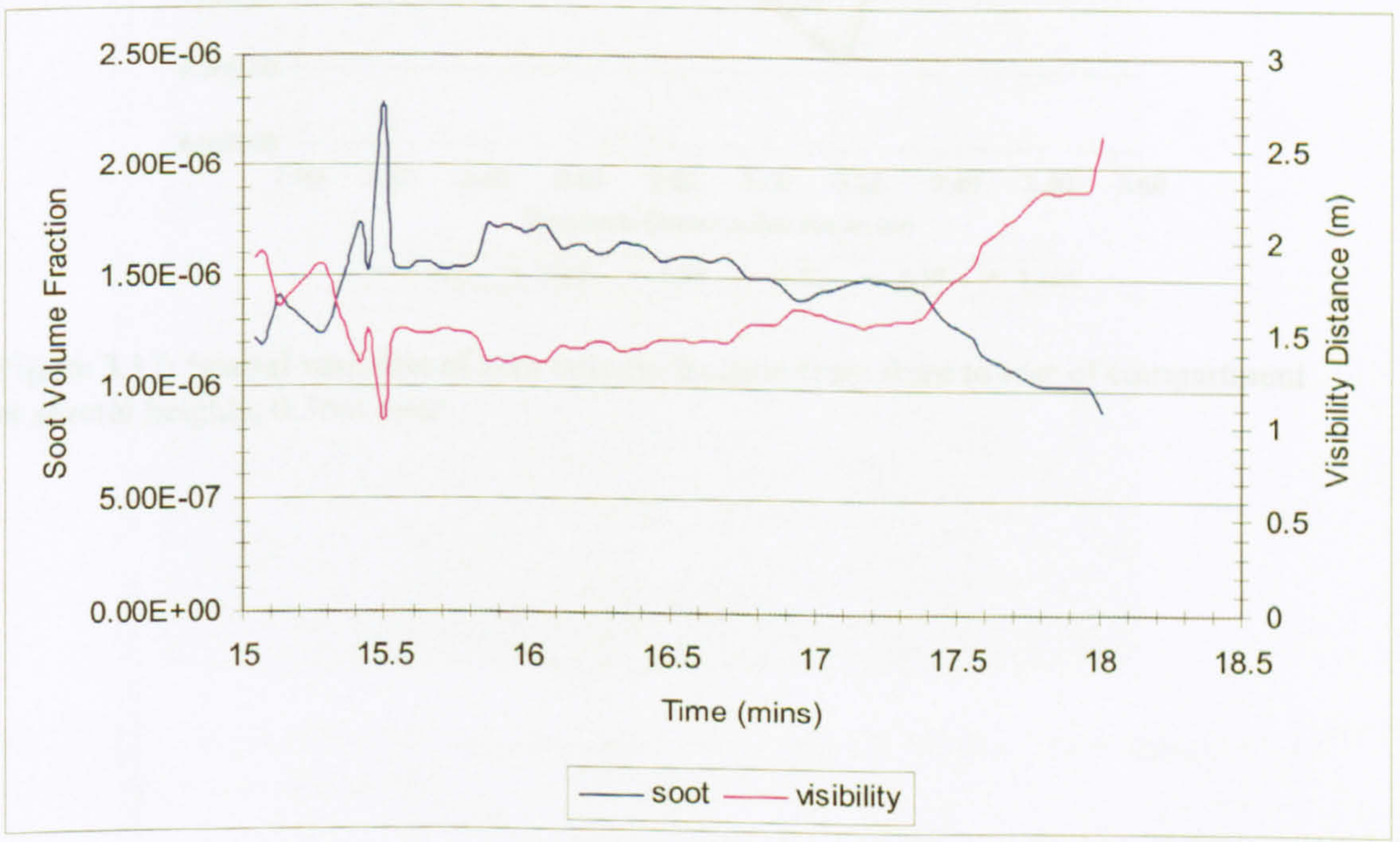

(b) Doorway soot profile; 0.17m burner; **0.15m doorwidth**

Figure 3.16: Doorway soot profiles; 0.17m burner; 0.25m doorwidth and 0.15m doorwidth

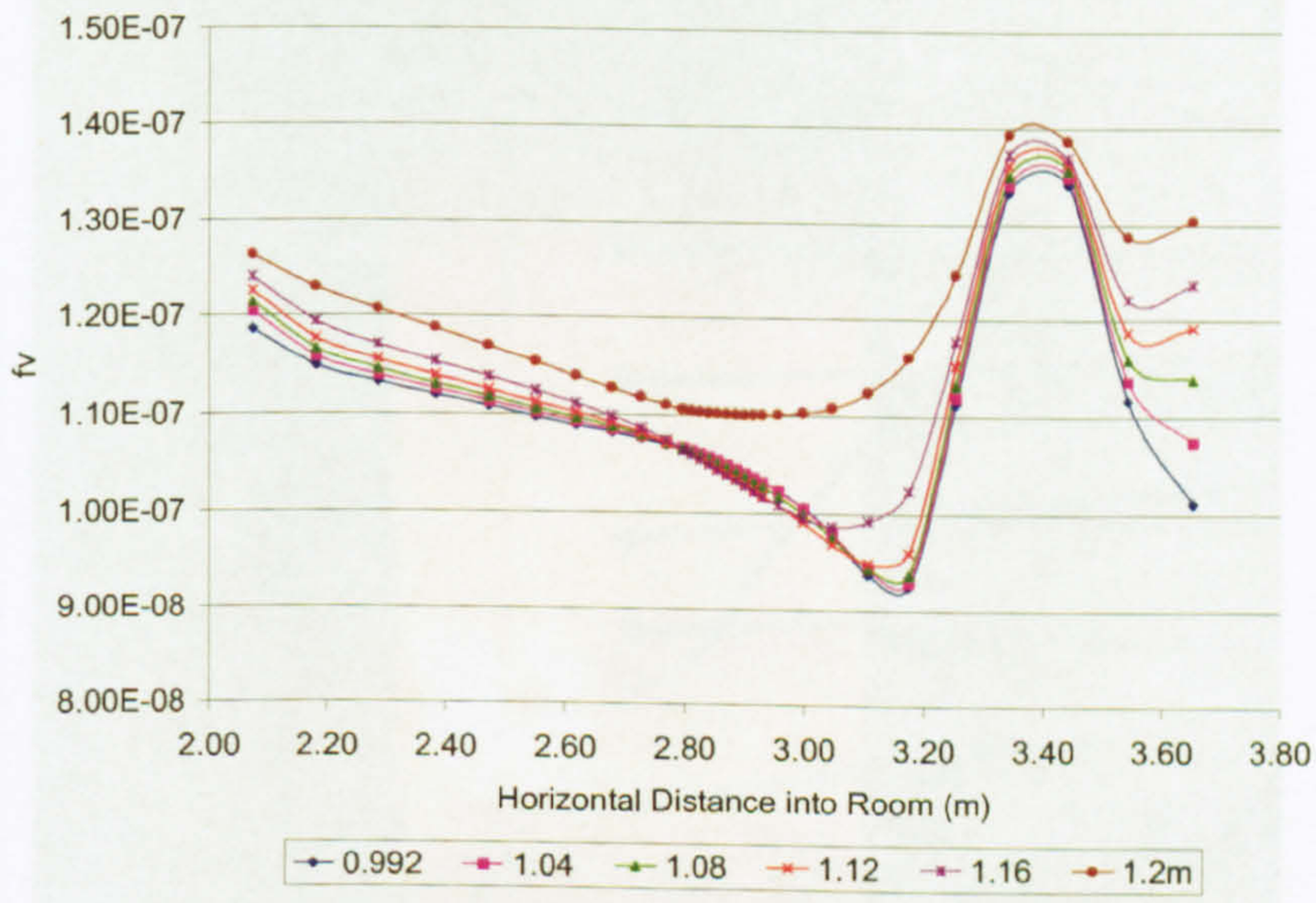

Figure 3.17: Spatial variation of soot volume fraction from front to rear of compartment at several heights; 0.36m door

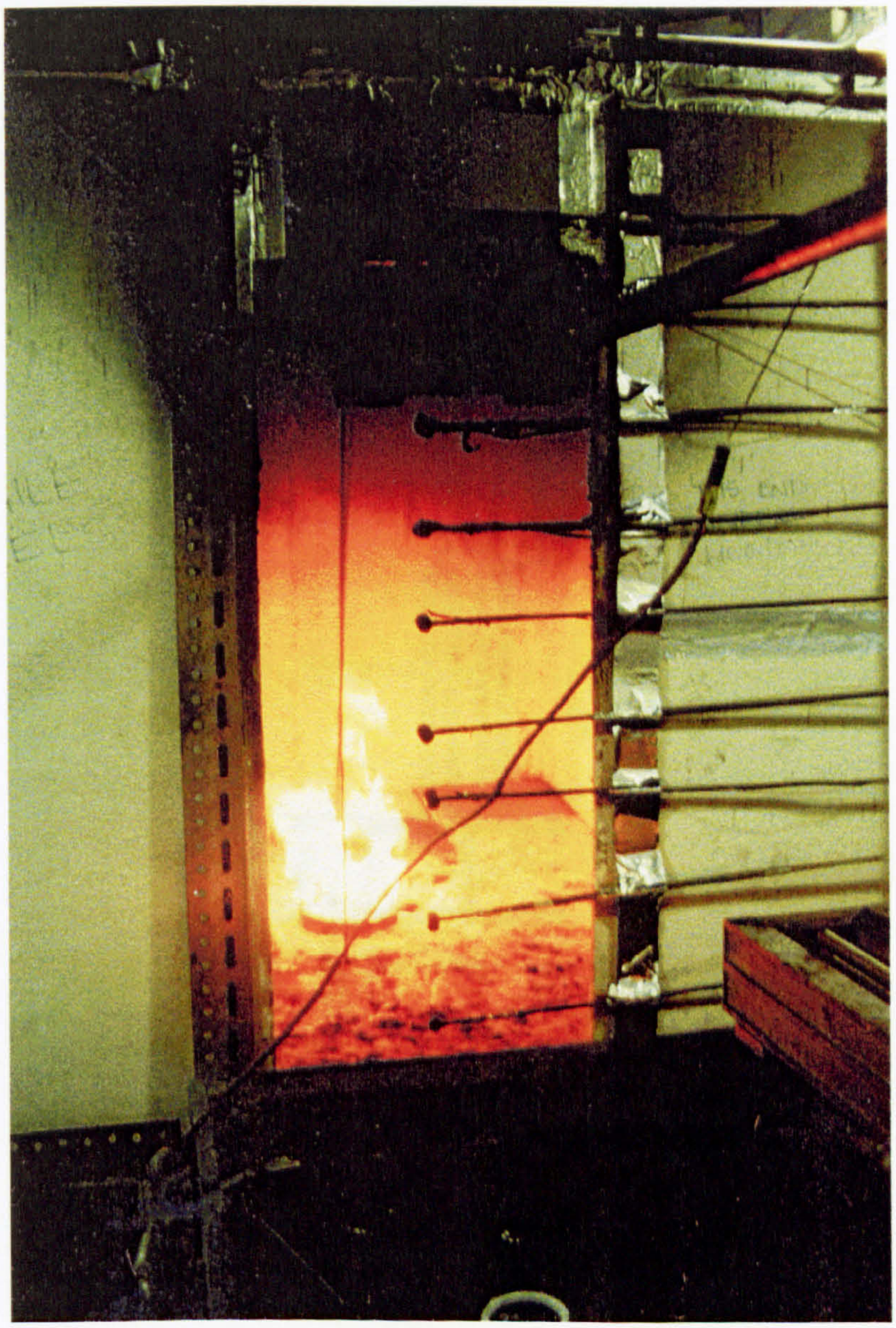

Figure 3.18: Enclosure door showing location of velocity probes; water-cooled soot probe at the top of the doorway

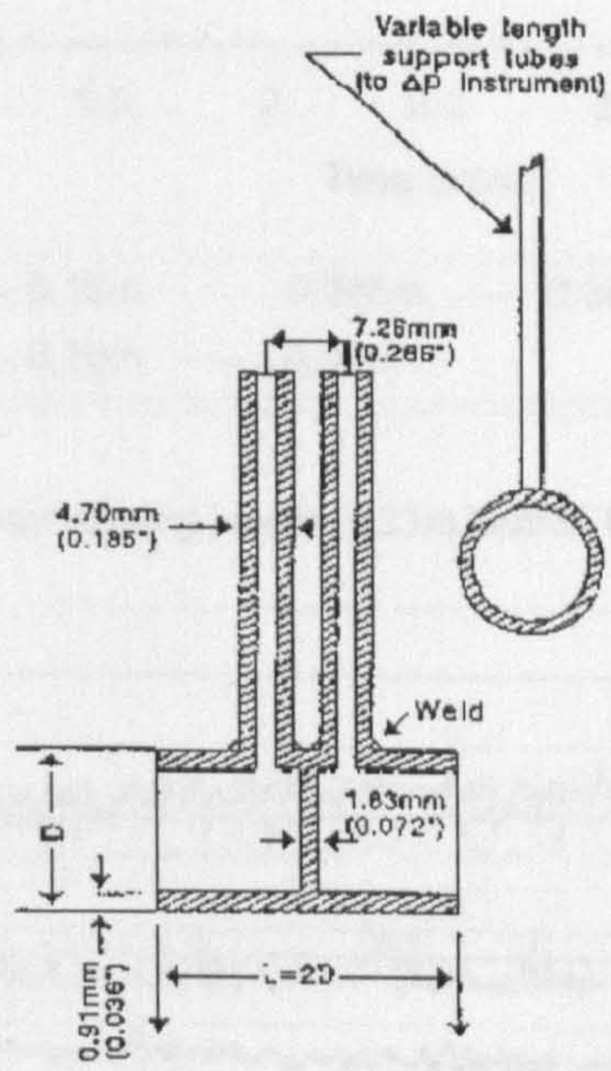

Figure 3.19: Bi-directional velocity probe schematic

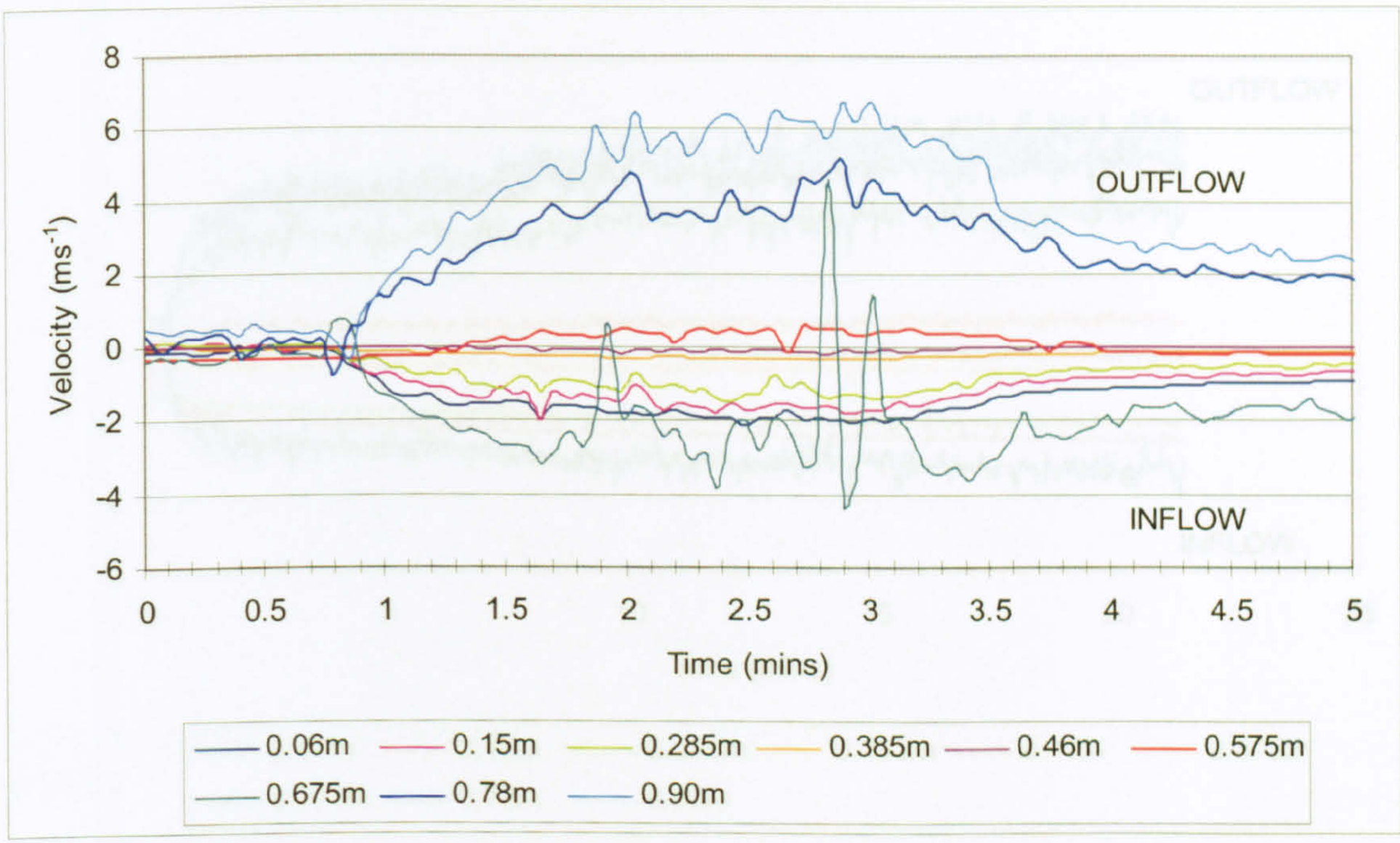

(a) Doorway velocity profile; 0.23m burner; **0.36m doorwidth**

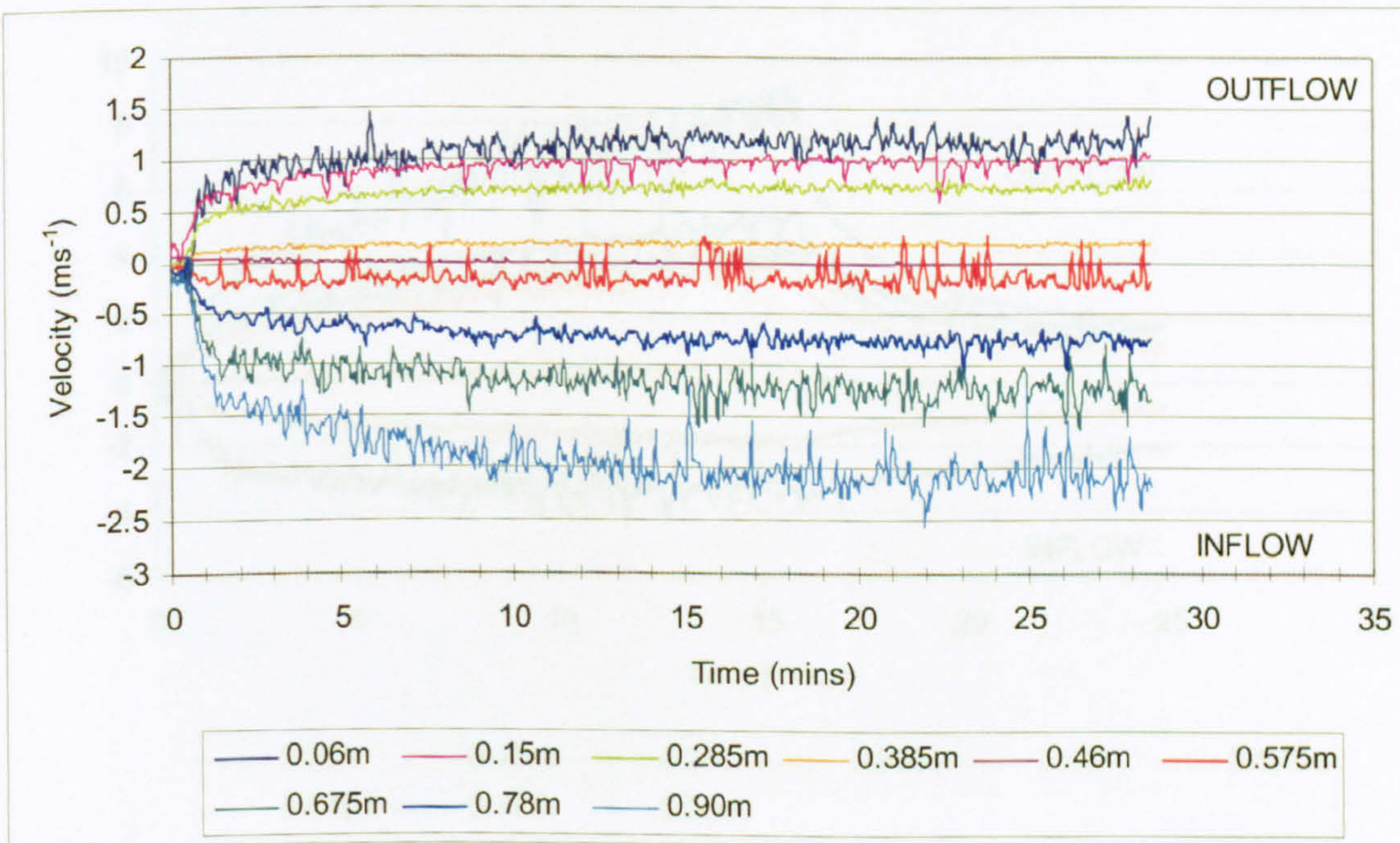

(b) Doorway velocity profile; 0.17m burner; **0.36m doorwidth**

Figure 3.20: Doorway velocity profiles; 0.23m burner, 0.36m doorwidth and 0.17m burner, 0.36m doorwidth

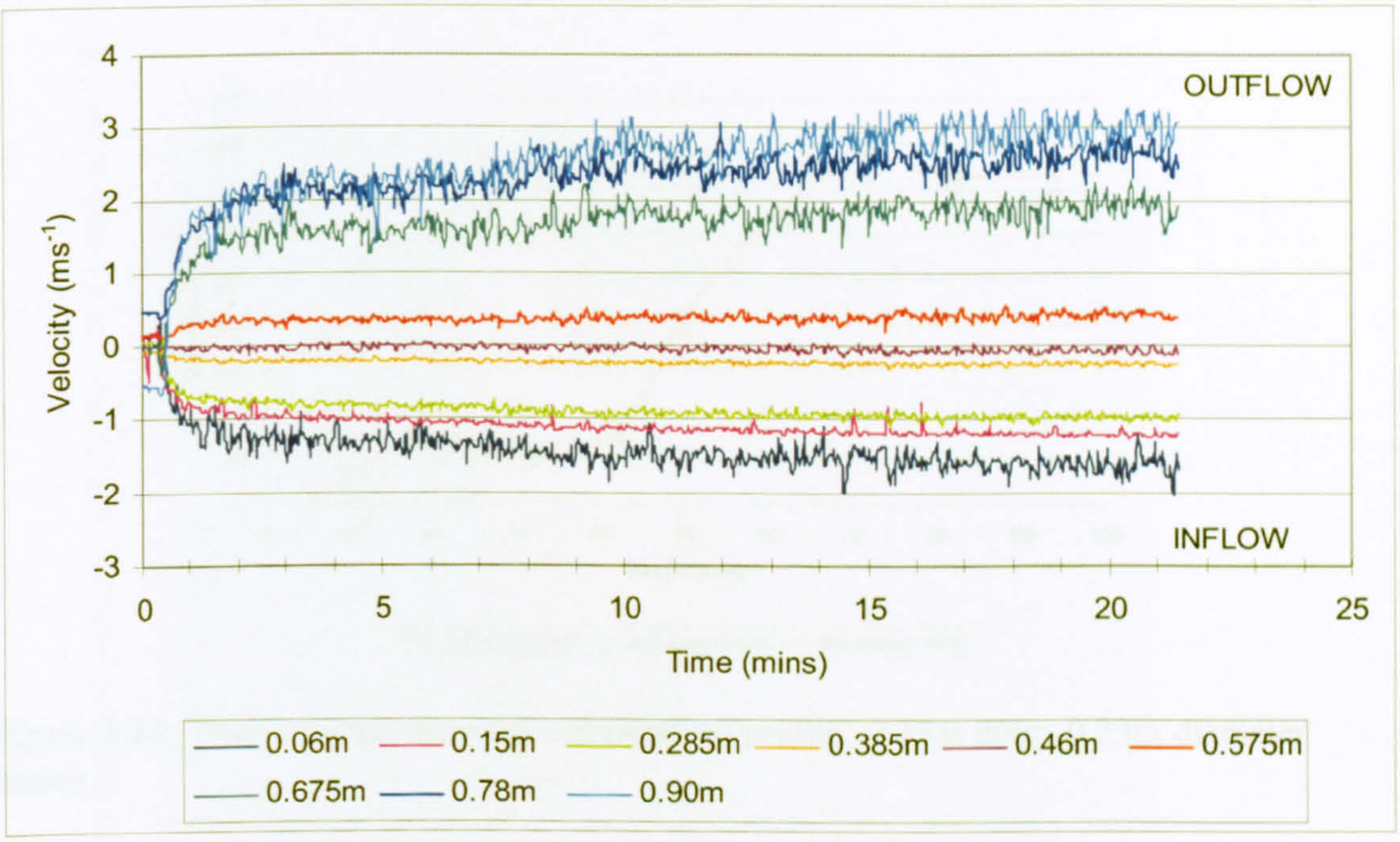

(a) Doorway velocity profile; 0.17m burner; **0.25m doorwidth**

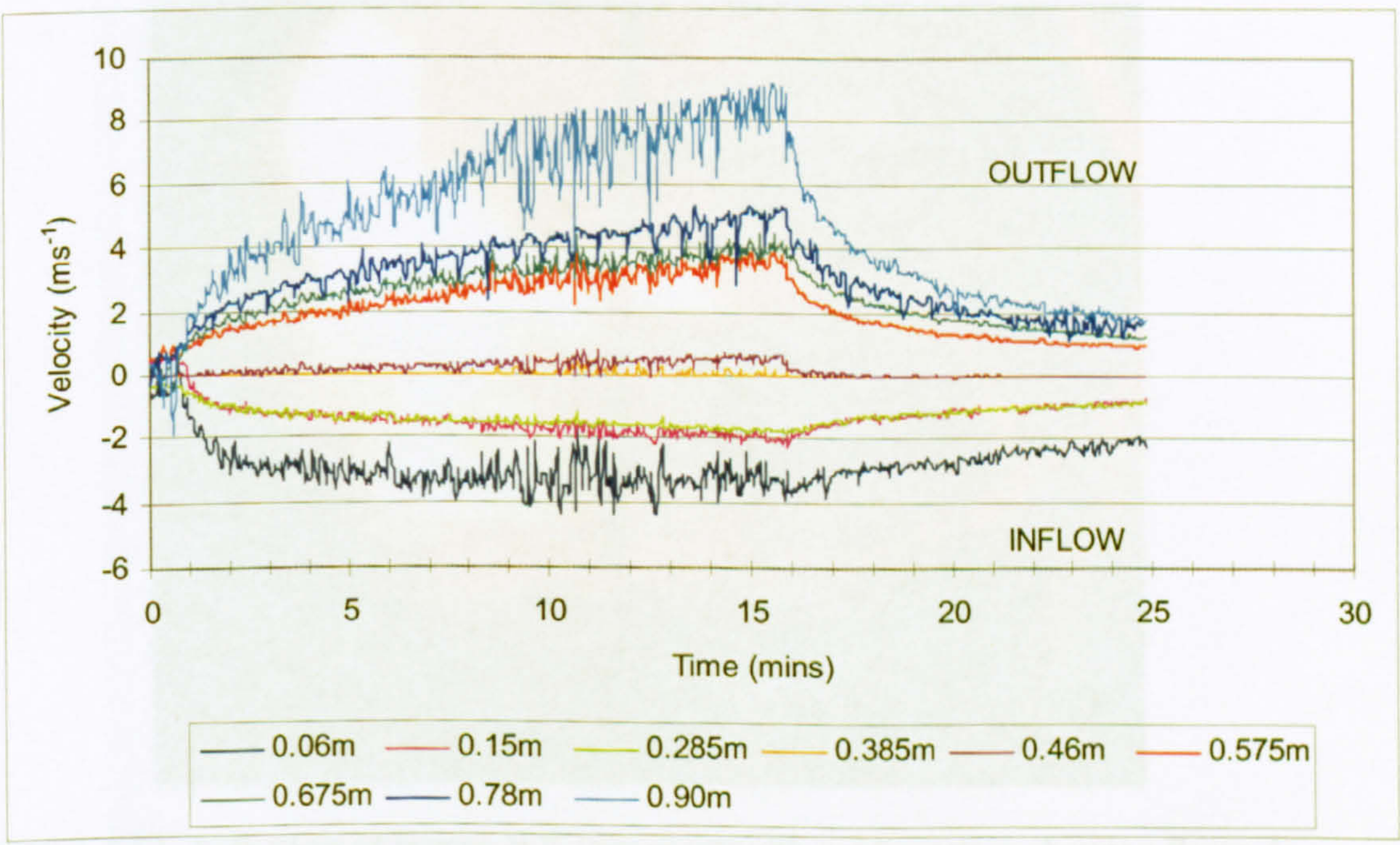

(b) Doorway velocity profile; 0.17m burner; **0.15m doorwidth**

Figure 3.21: Doorway velocity profiles; 0.17m burner; 0.25m doorwidth and 0.15m doorwidth

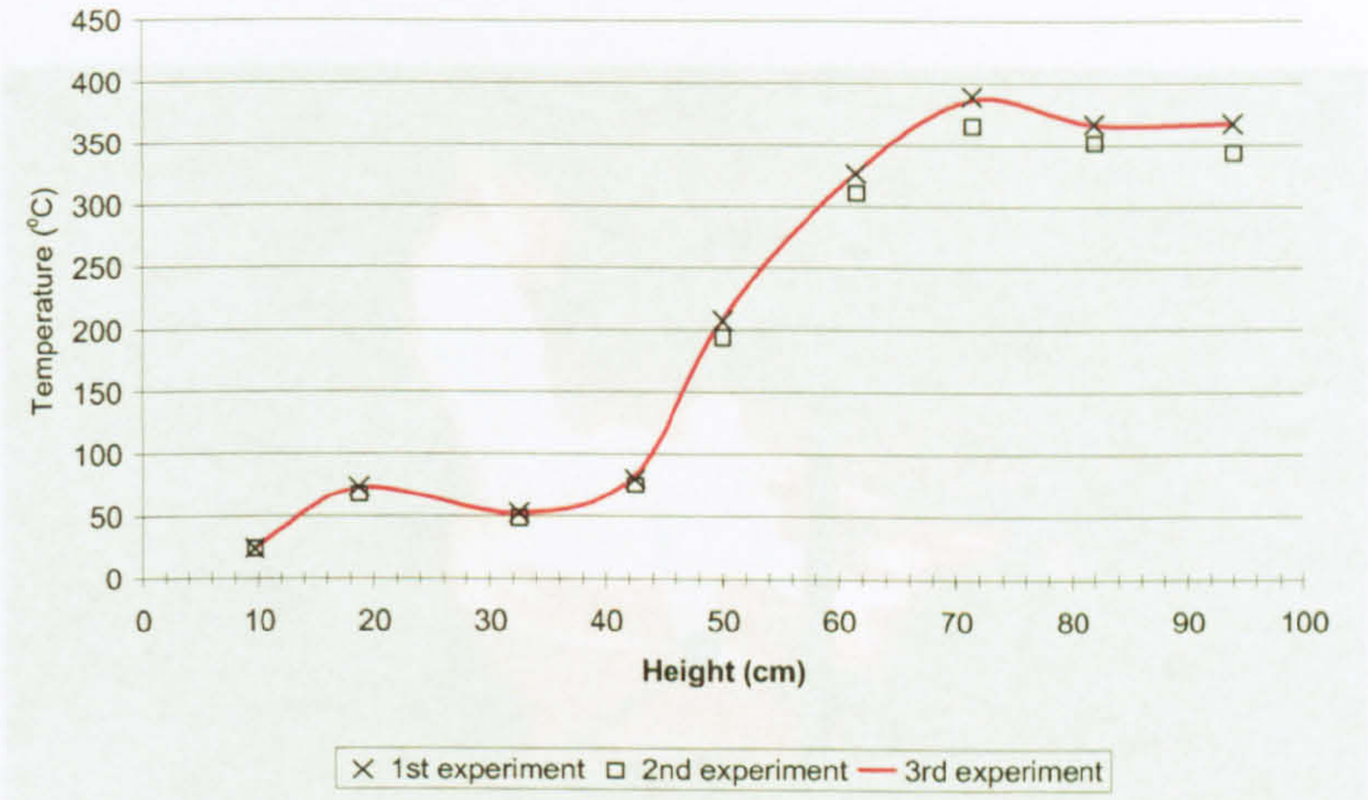

Figure 3.22: Peak average doorway temperature profile; 0.25m door; 0.23m diameter burner

Figure 3.23: Side-view of burner in 0.15m doorwidth configuration showing flame detachment

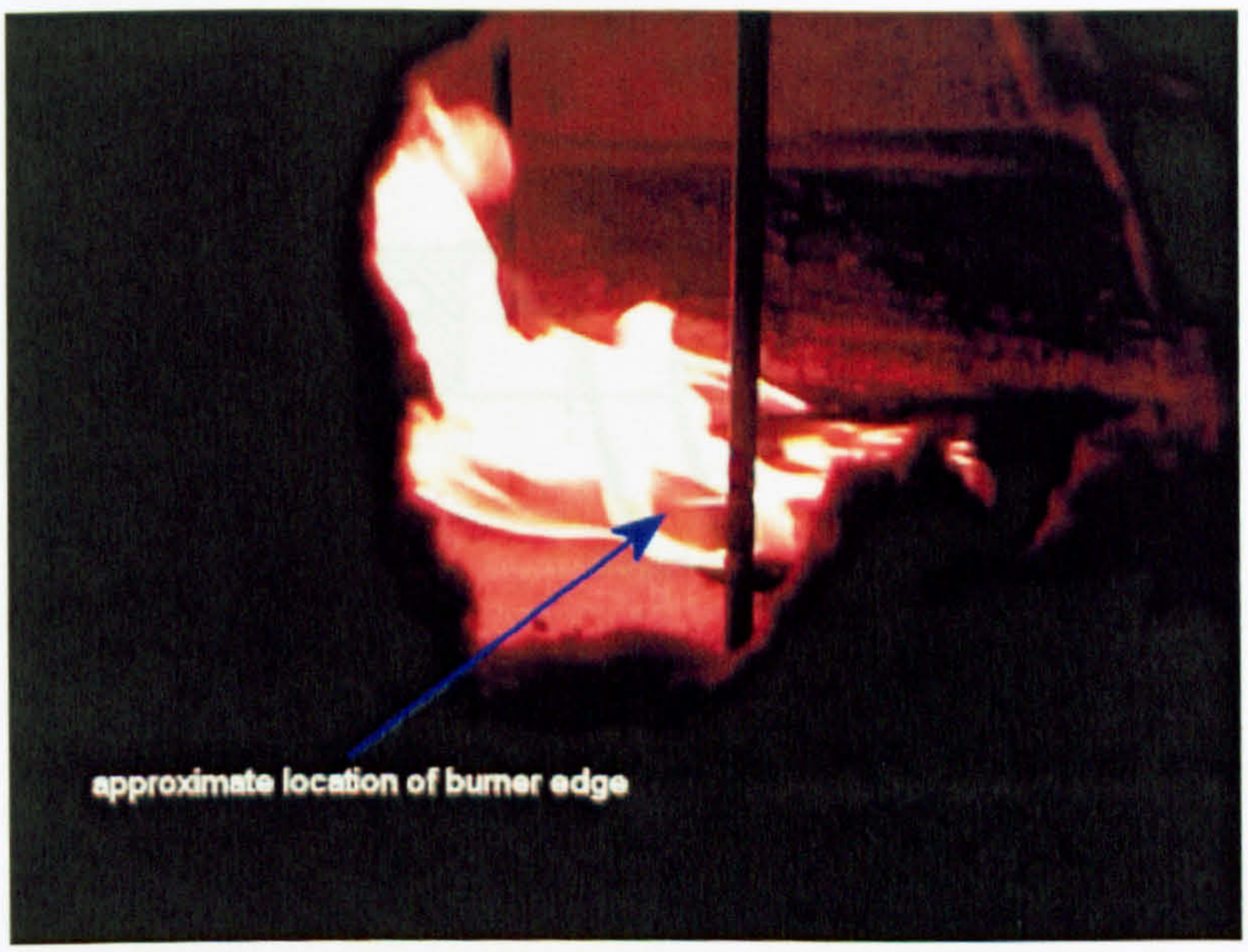

Figure 3.24: Vortex formation in burner of 0.36m door enclosure fire

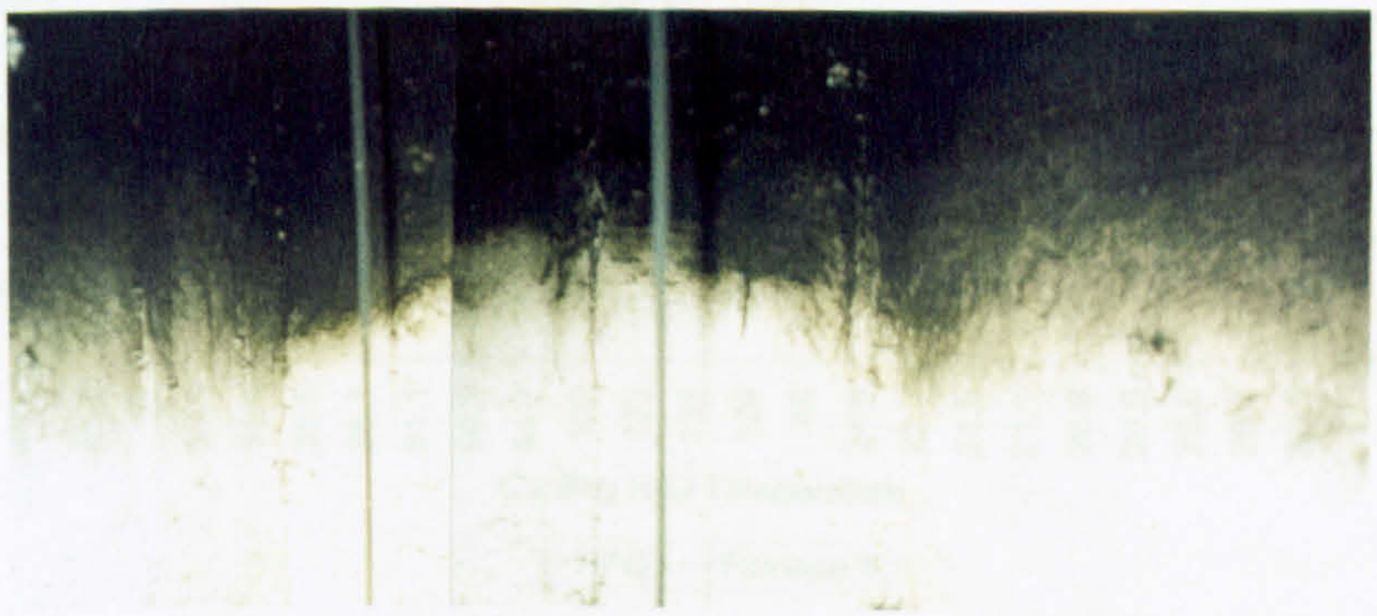

Figure 3.25: Compartment interior showing convex profile of hot upper layer

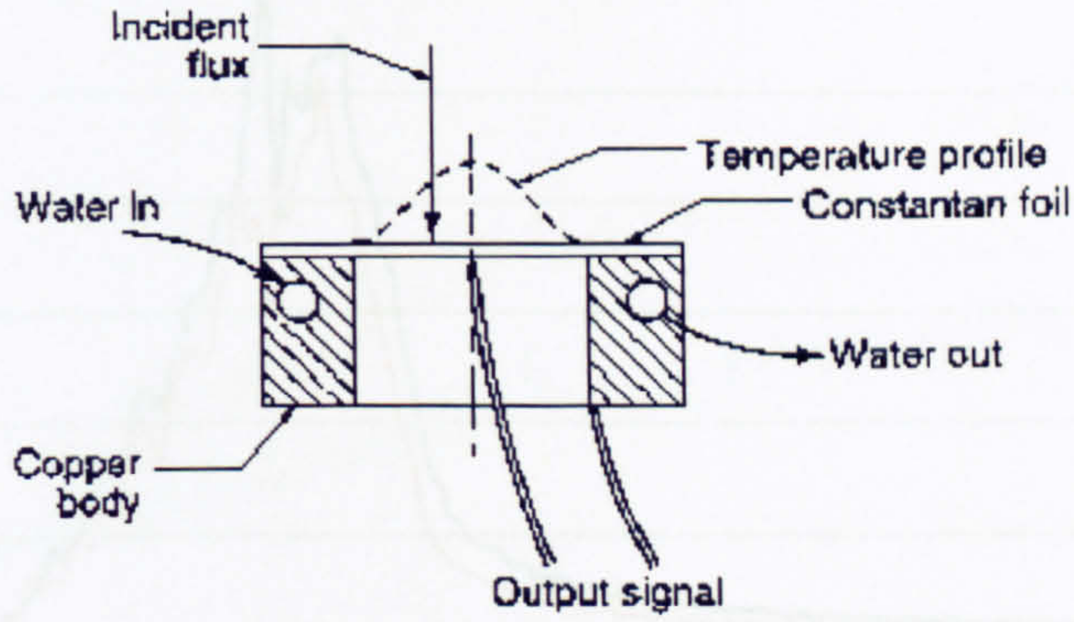

Figure 3.26: Gardon type heat flux gauge schematic

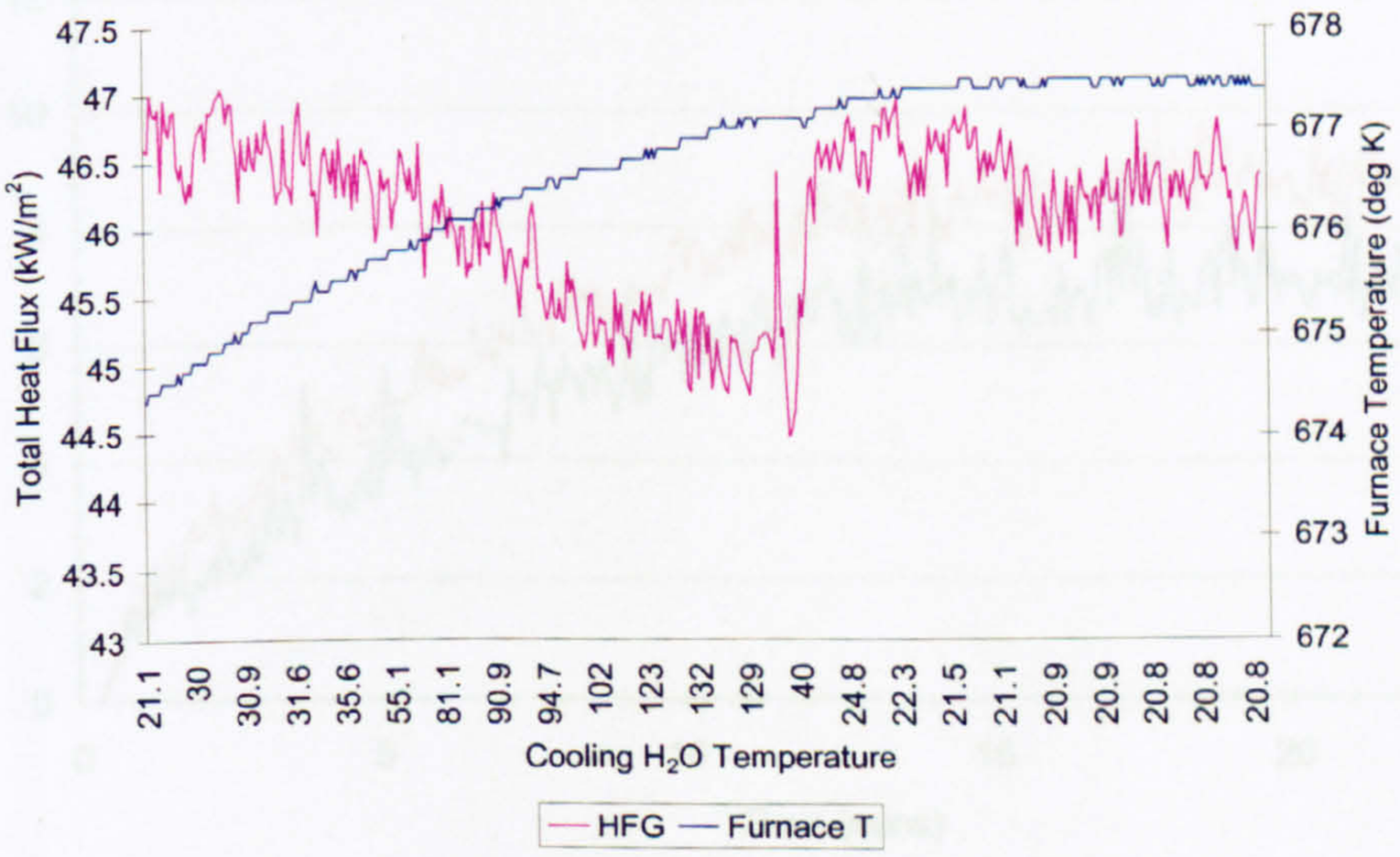

Figure 3.27: Effect of cooling water temperature on measured heat flux

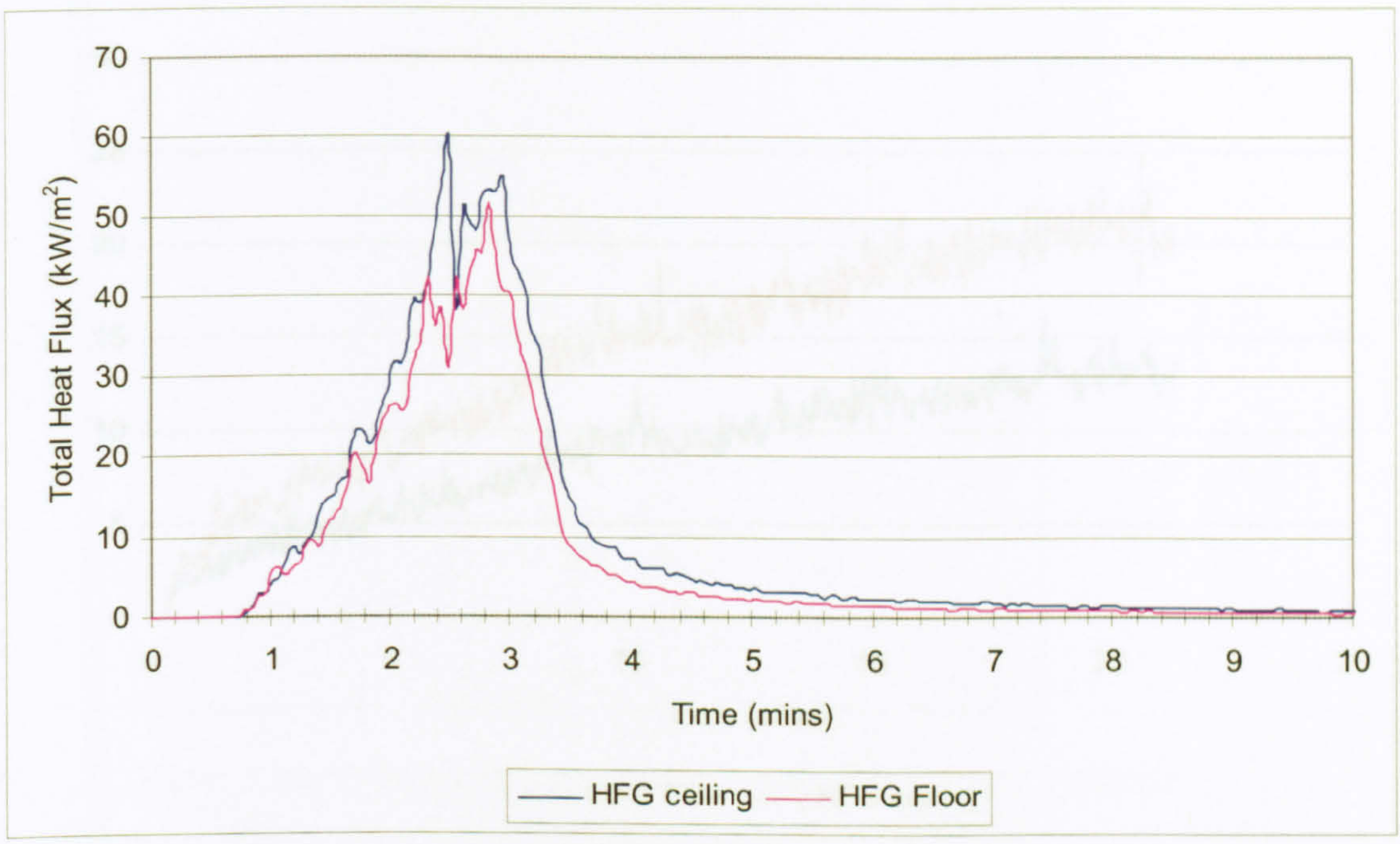

(a) Total heat flux to compartment side wall and floor; 0.23m burner; **0.36m doorwidth**

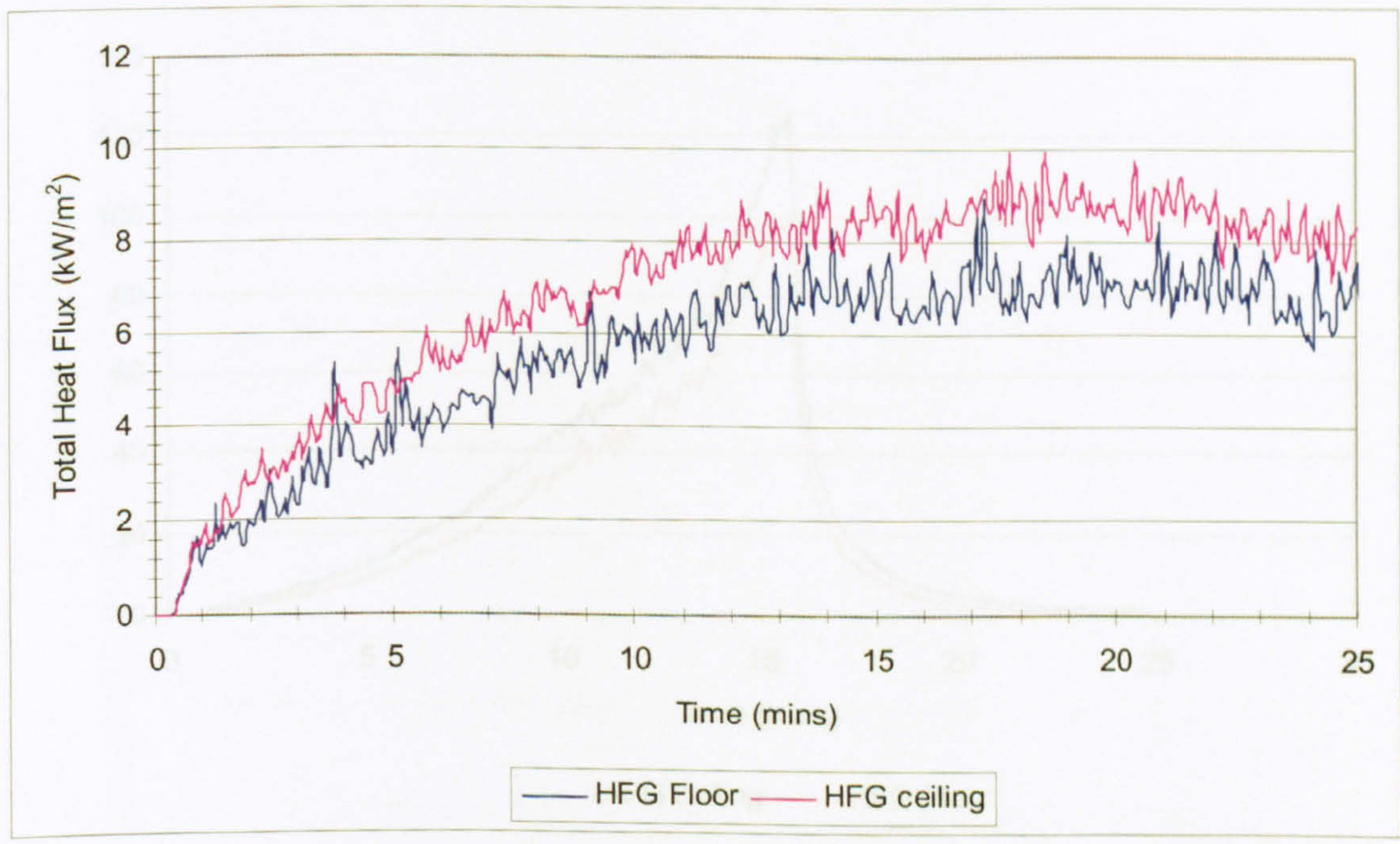

(b) Total heat flux to compartment side wall and floor; 0.17m burner; **0.36m doorwidth**

Figure 3.28: Total heat flux to compartment side wall and floor; 0.23m burner, 0.36m doorwidth and 0.17m burner, 0.36m doorwidth

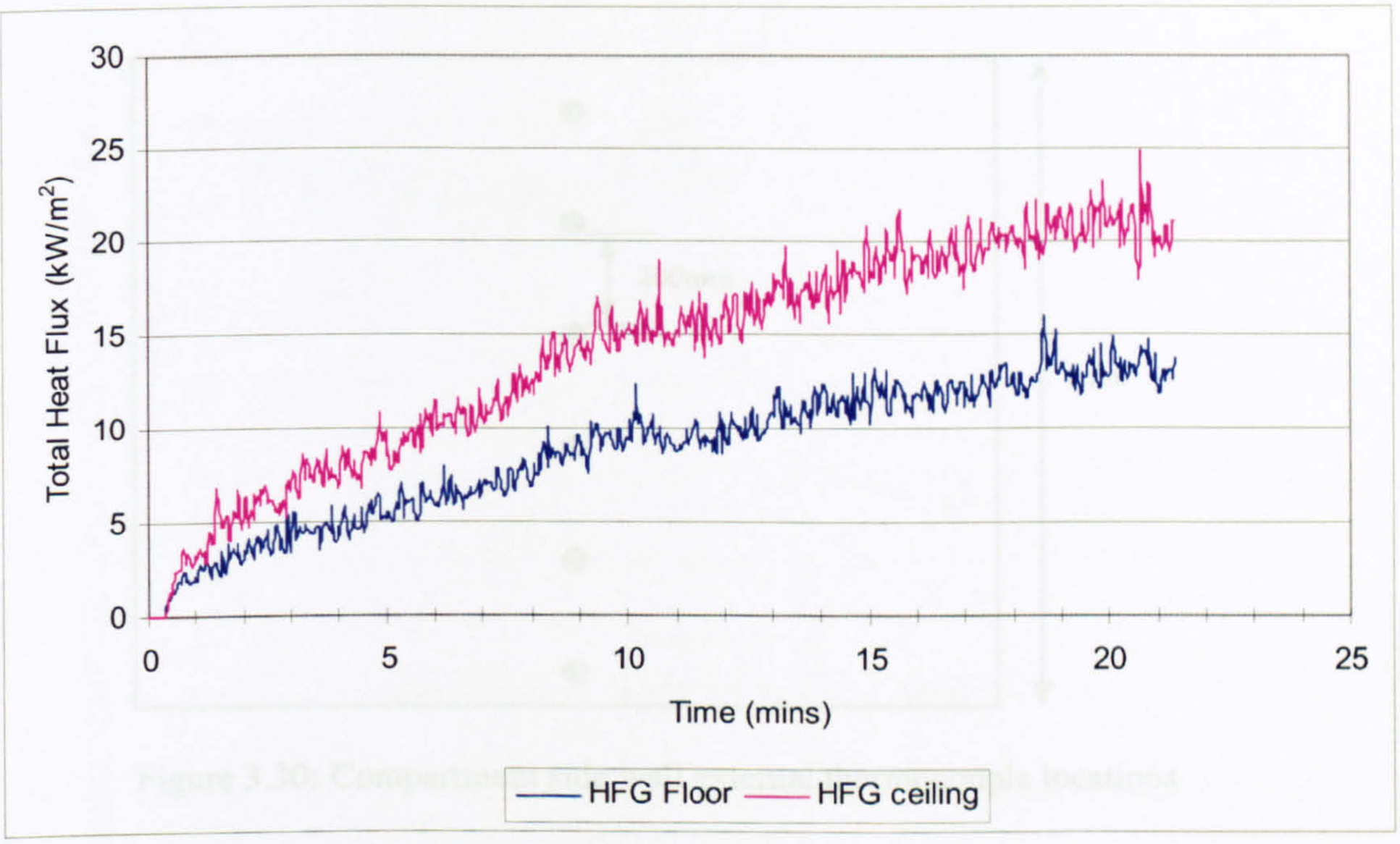

(a) Total heat flux to compartment side wall and floor; 0.17m burner; **0.25m doorwidth**

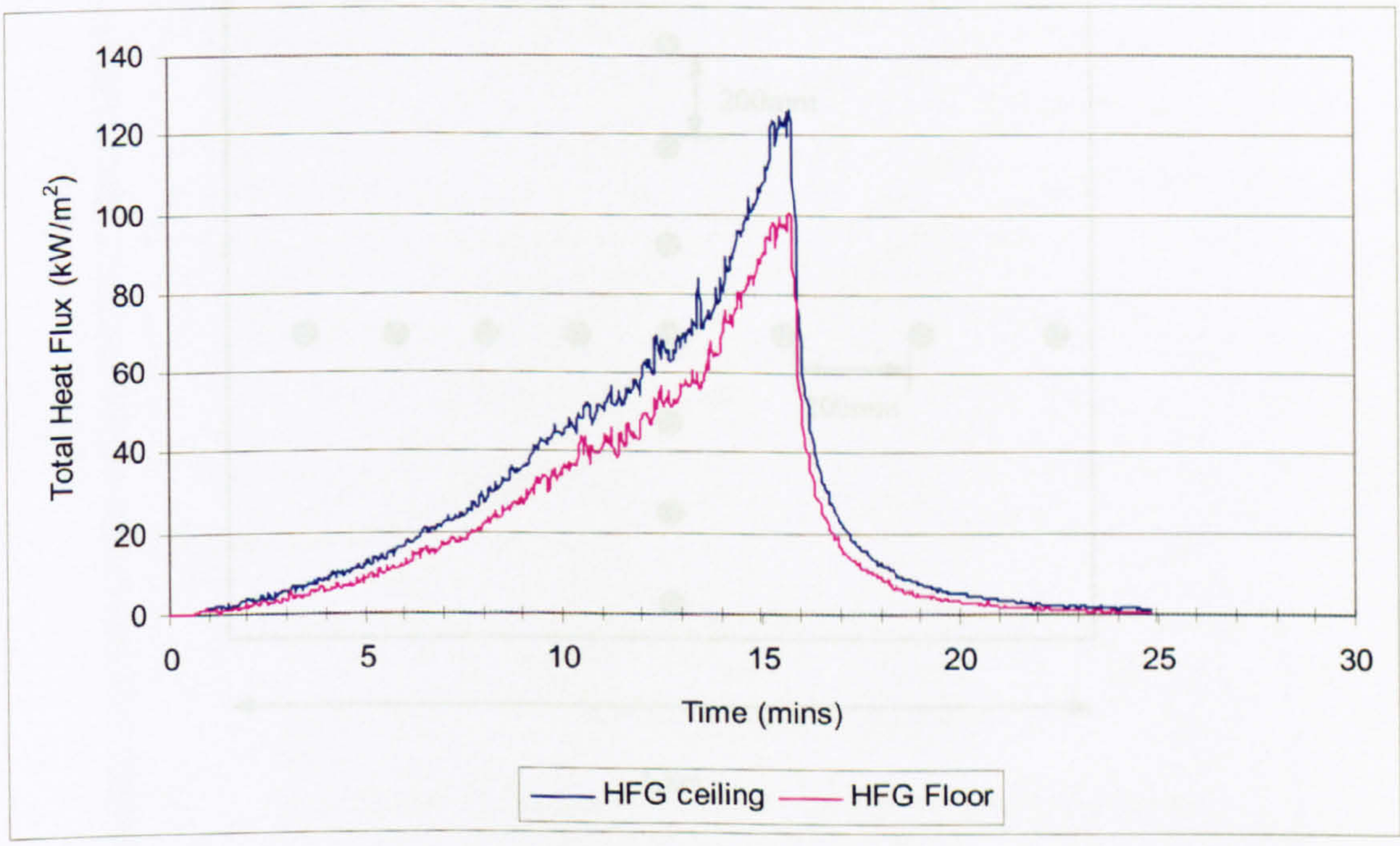

(b) Total heat flux to compartment side wall and floor; 0.17m burner; **0.15m doorwidth**

Figure 3.29: Total heat flux to compartment side wall and floor; 0.17m burner; 0.25m doorwidth and 0.15m doorwidth

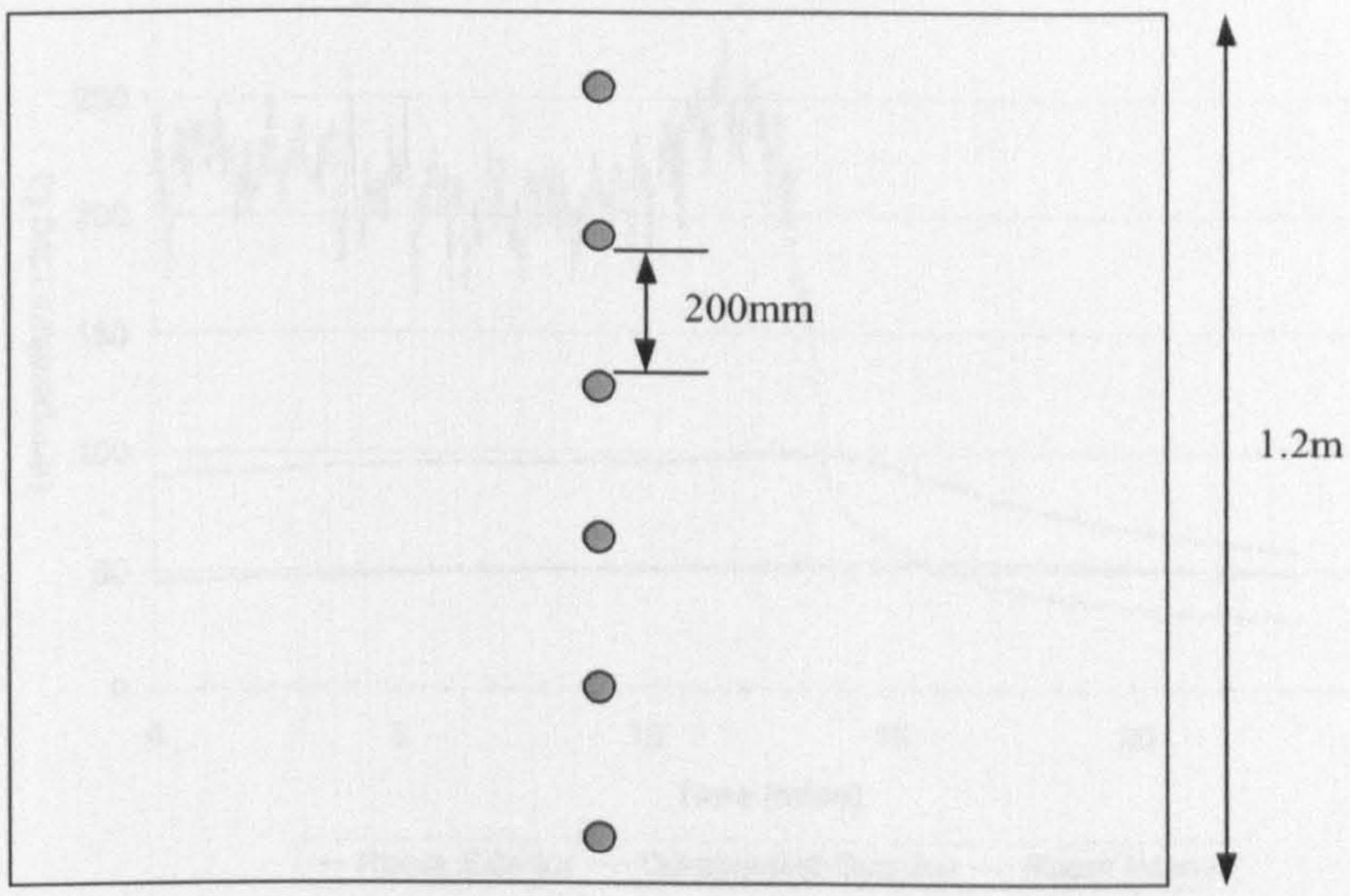

Figure 3.30: Compartment side wall external thermocouple locations

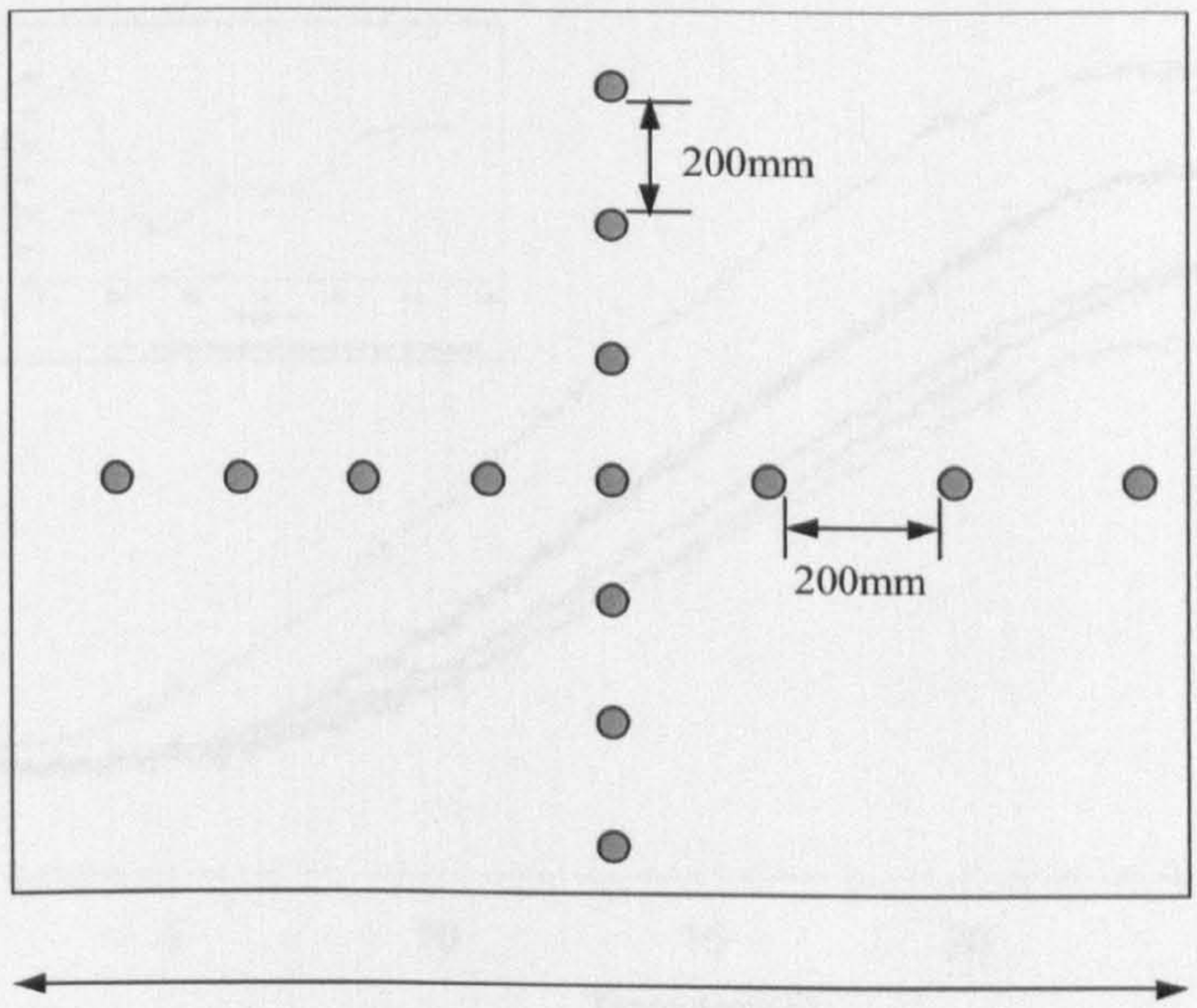

Figure 3.31: Compartment ceiling external thermocouple locations

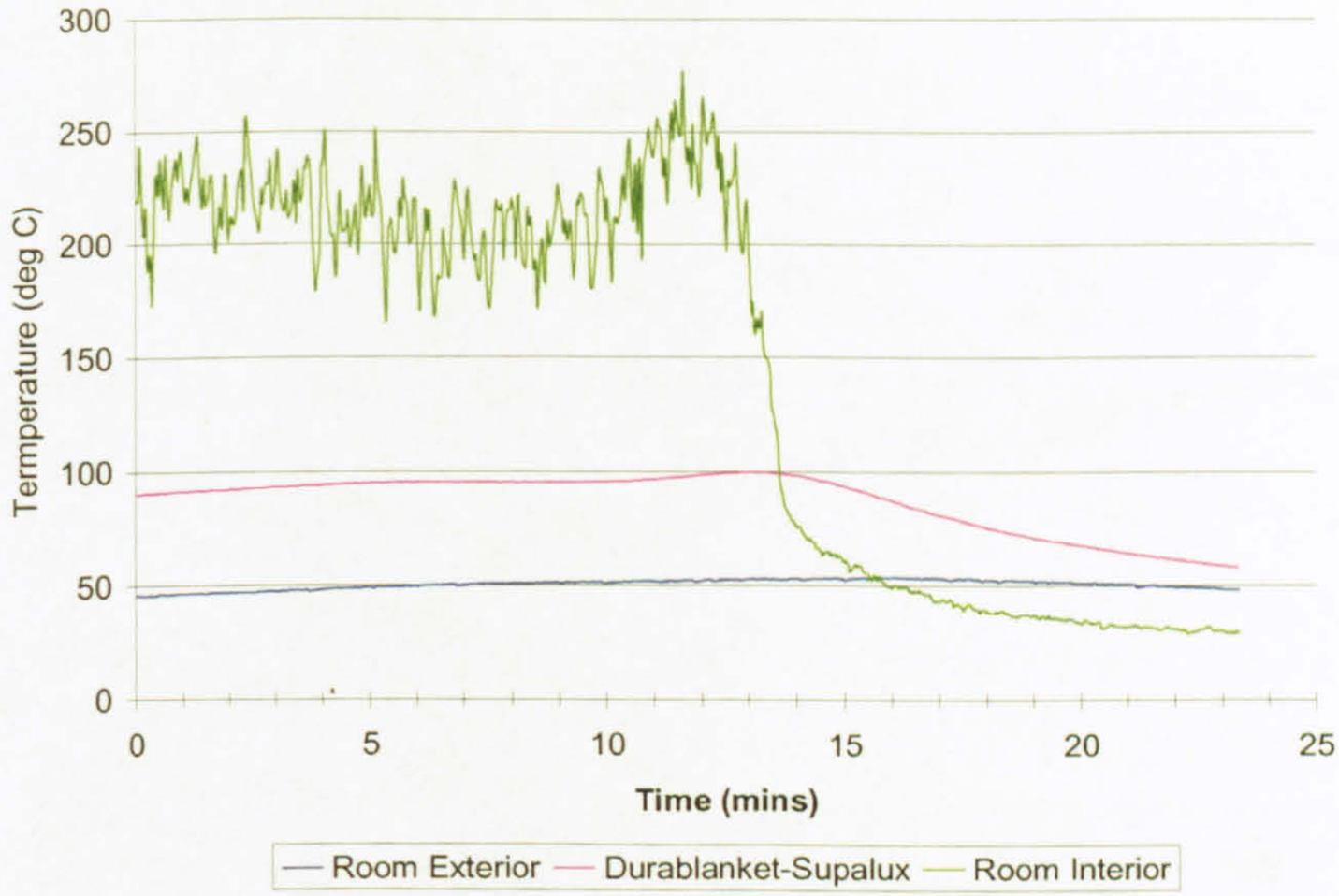

Figure 3.32: Side wall layer temperature showing benefit of insulation on compartment heat loss; 0.17m diameter burner; 0.36m doorwidth

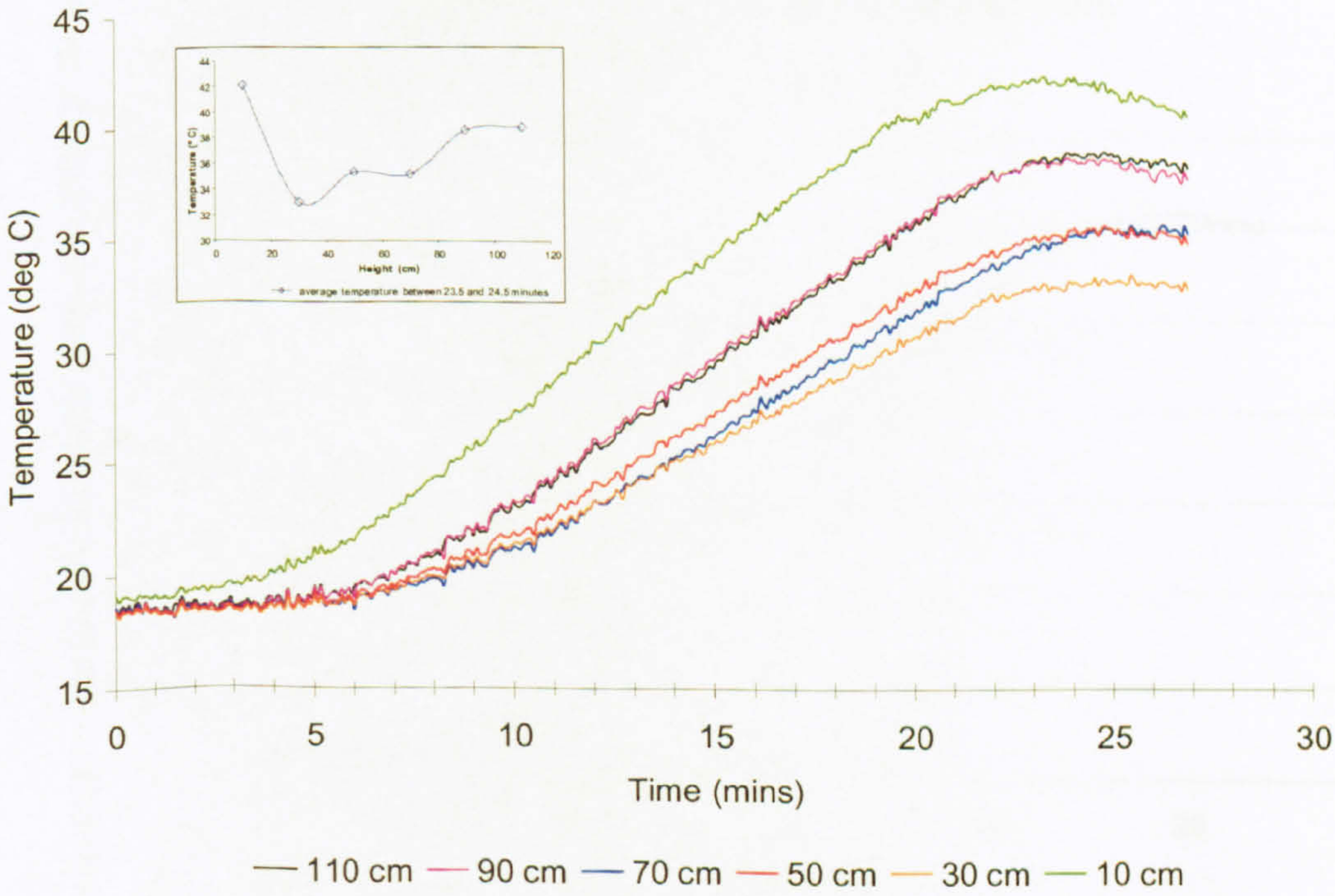

Figure 3.33: Time evolution and peak average external surface thermocouple temperature of compartment side wall; 0.17m diameter burner; 0.36m door width

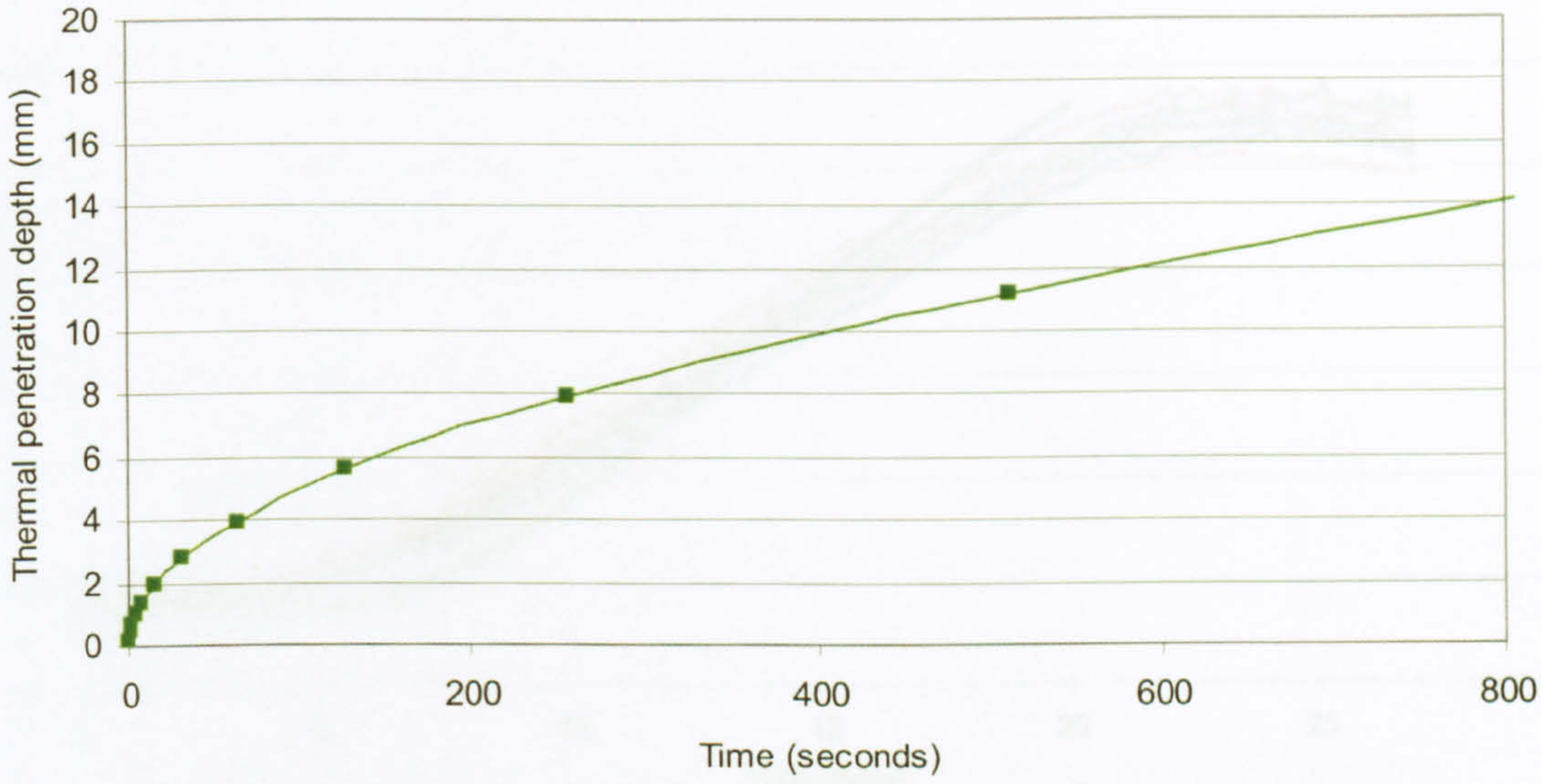

Figure 3.34: Thermal depth in compartment supalux walls;

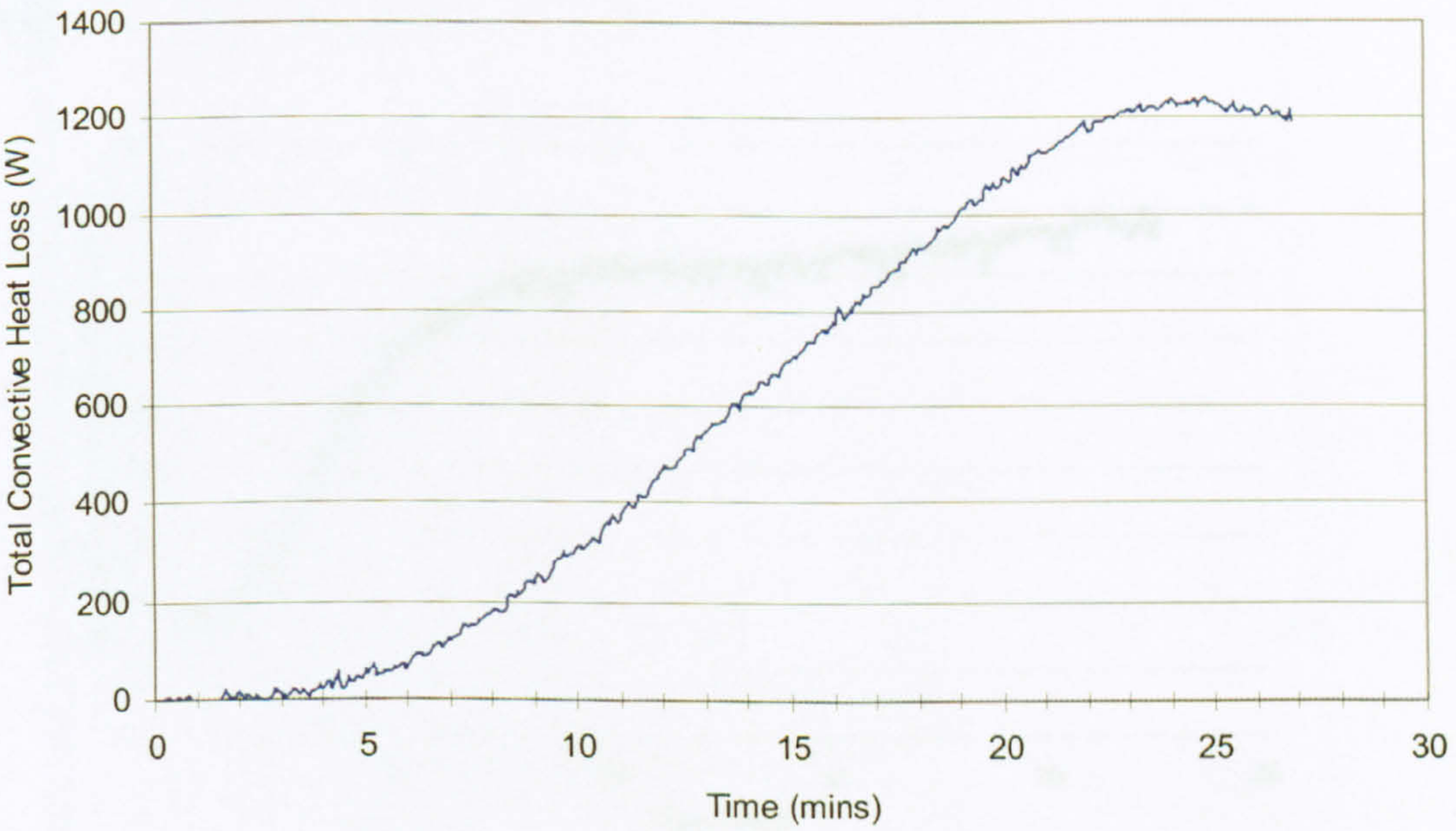

Figure 3.35: Compartment wall heat loss; 0.17m diameter burner; 0.36m doorwidth

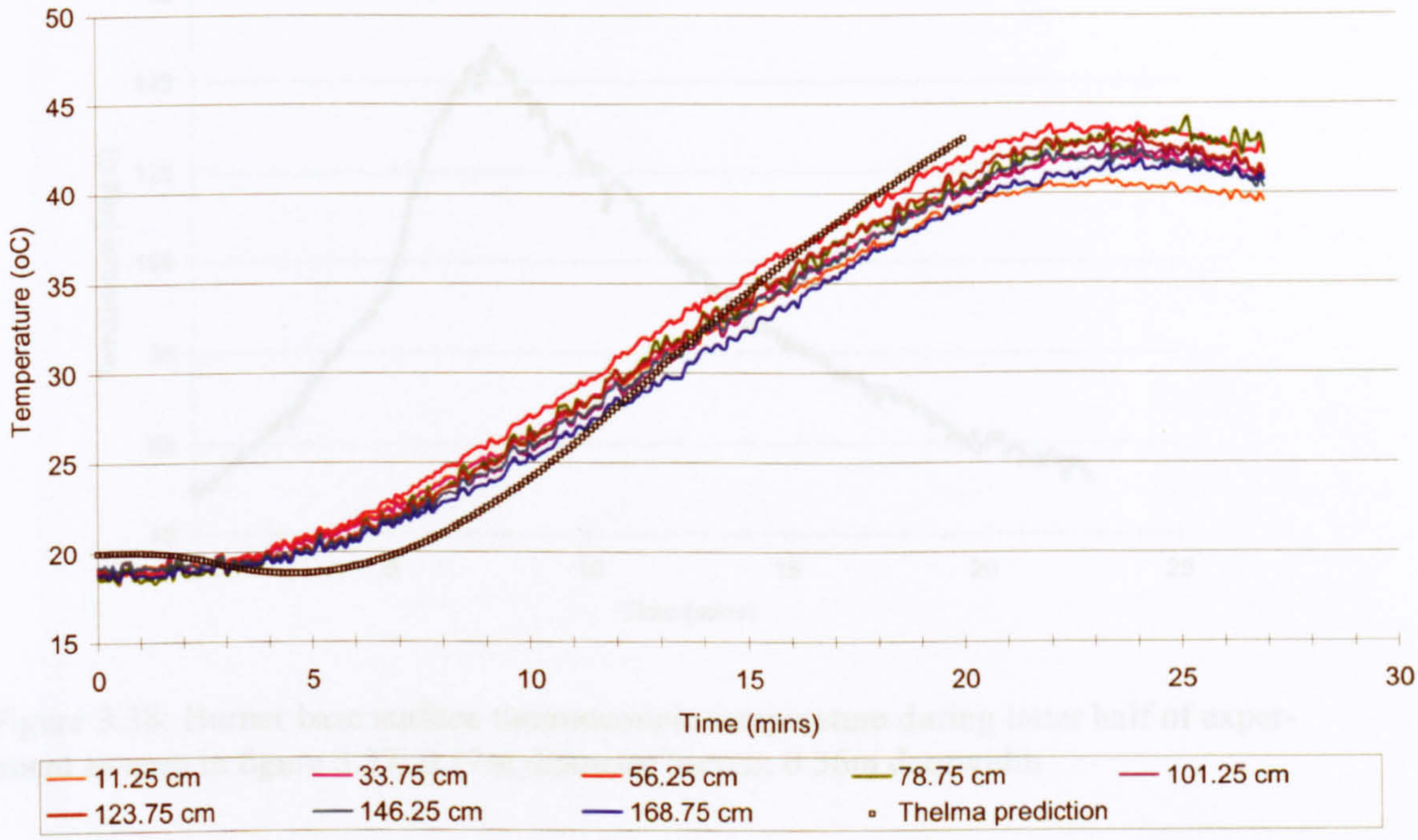

Figure 3.36: Transient profile of experimental ceiling external surface temperature compared to predicted temperature using THELMA; 0.17m diameter burner; 0.36m door-width

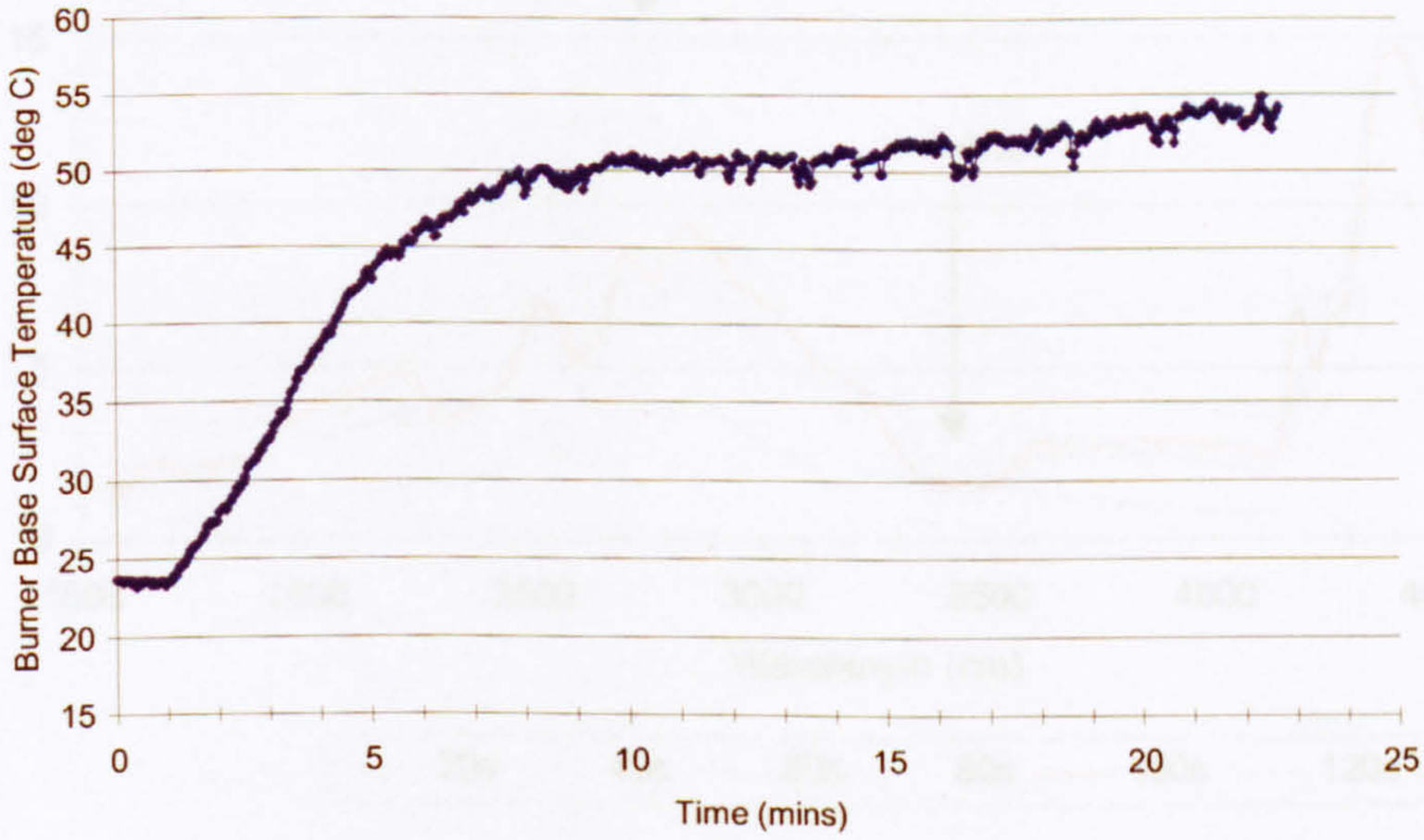

Figure 3.37: Burner base surface thermocouple temperature; 0.17m diameter pan

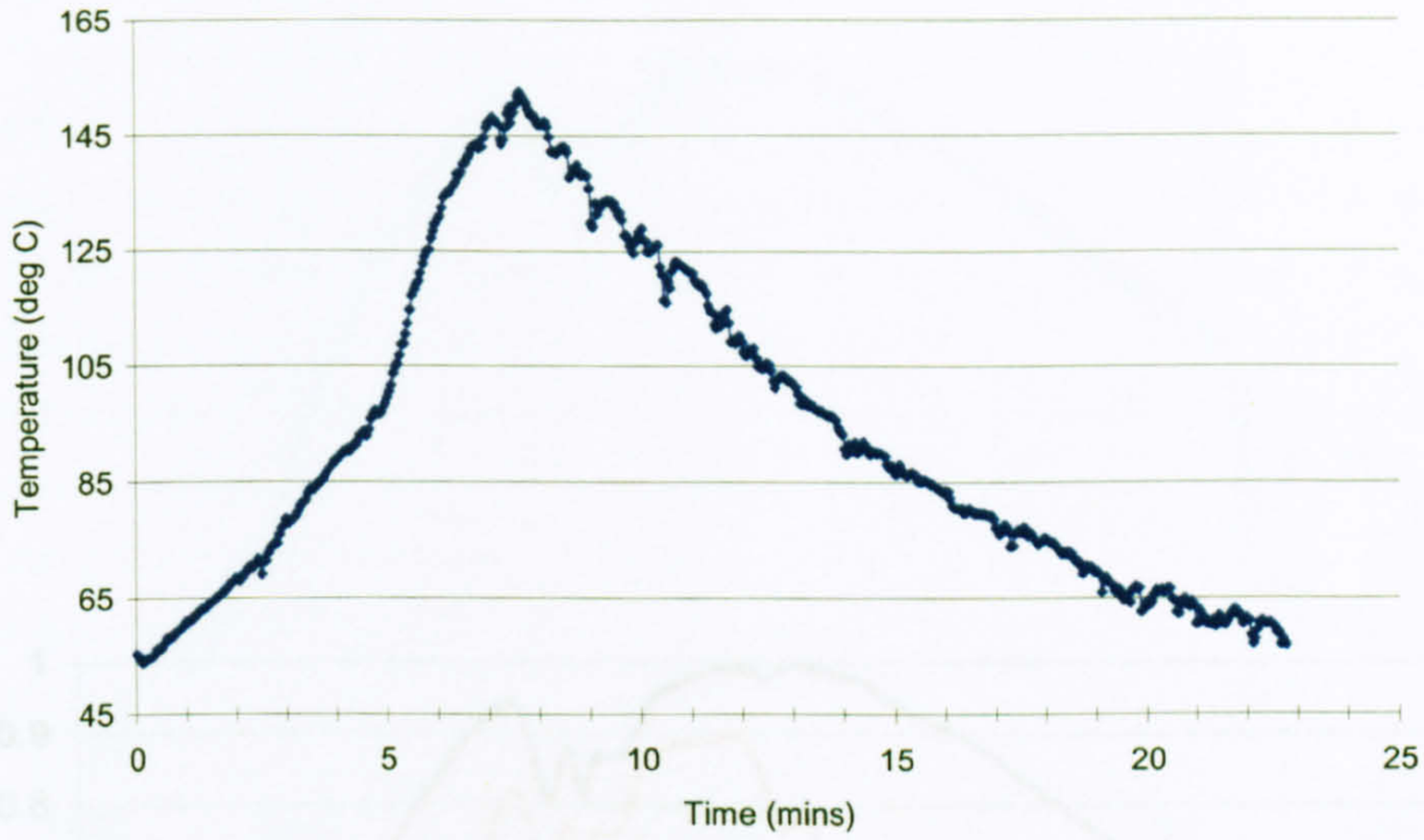

Figure 3.38: Burner base surface thermocouple temperature during latter half of experiment as seen in figure 3.37; 0.17m diameter burner; 0.36m doorwidth

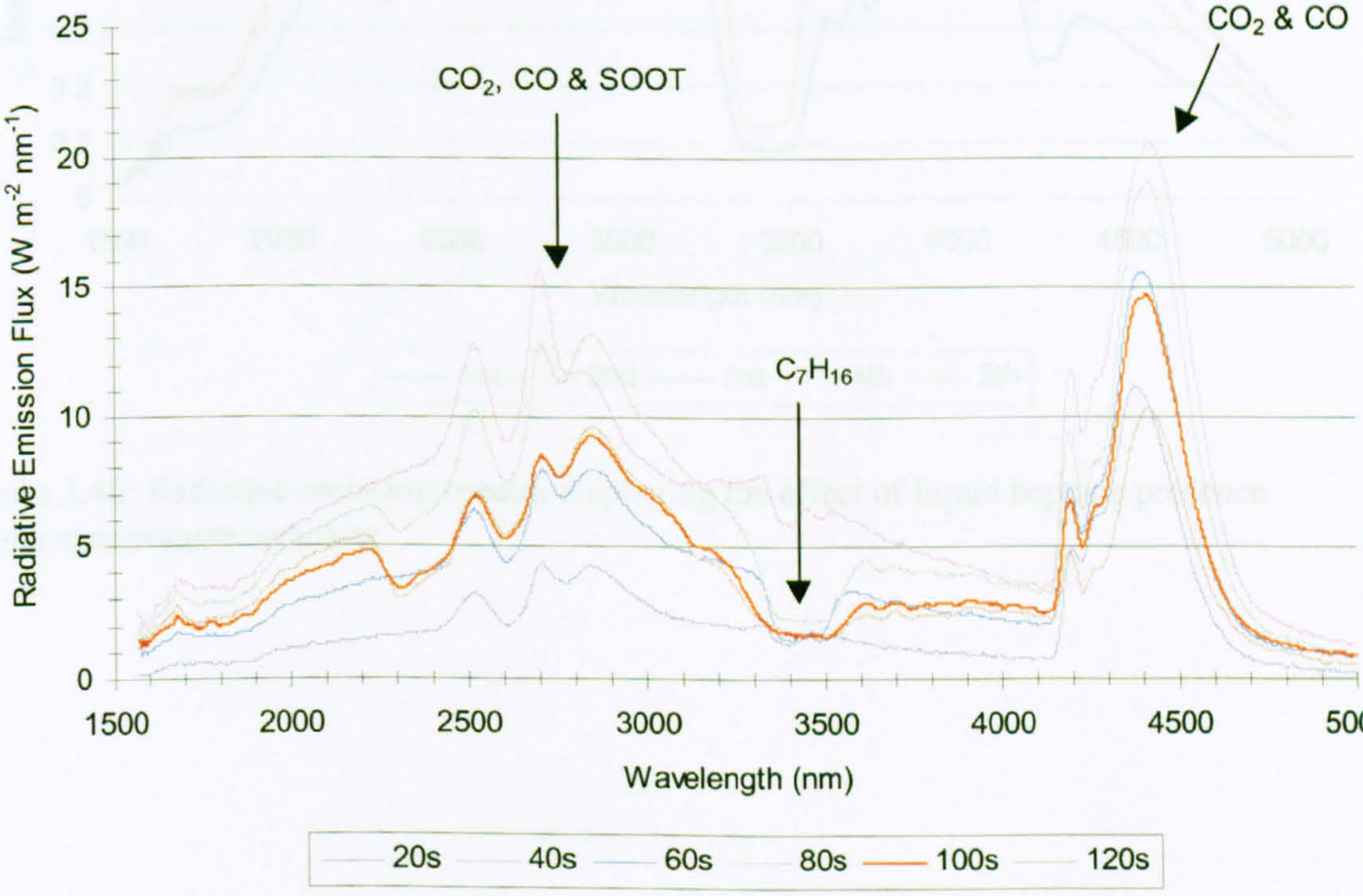

Figure 3.39: Radiative emission spectra showing heat flux to the fuel surface; 0.23m diameter burner; 0.36m doorwidth

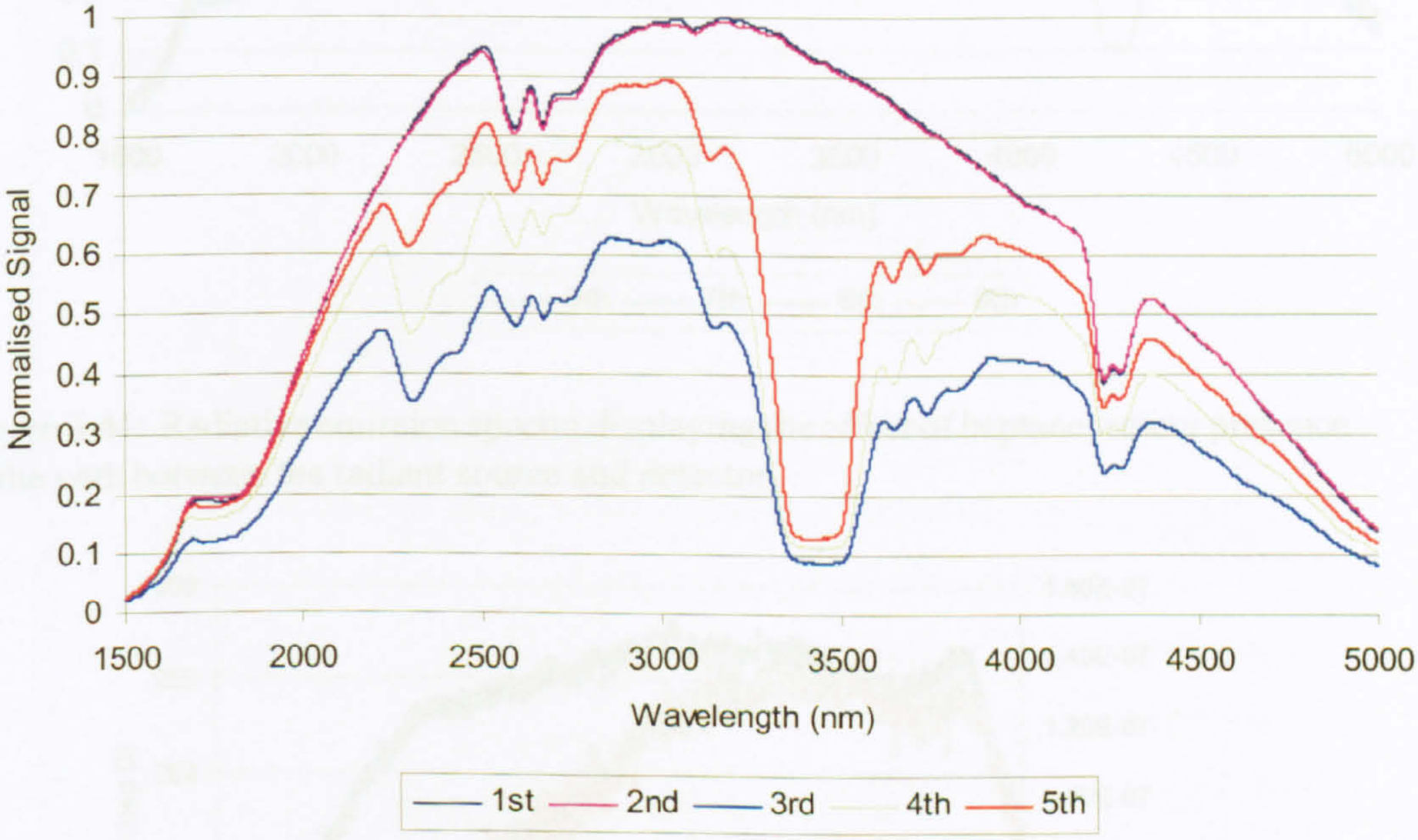

Figure 3.40: Radiative emission spectra displaying the effect of liquid heptane presence on the spectrometer window

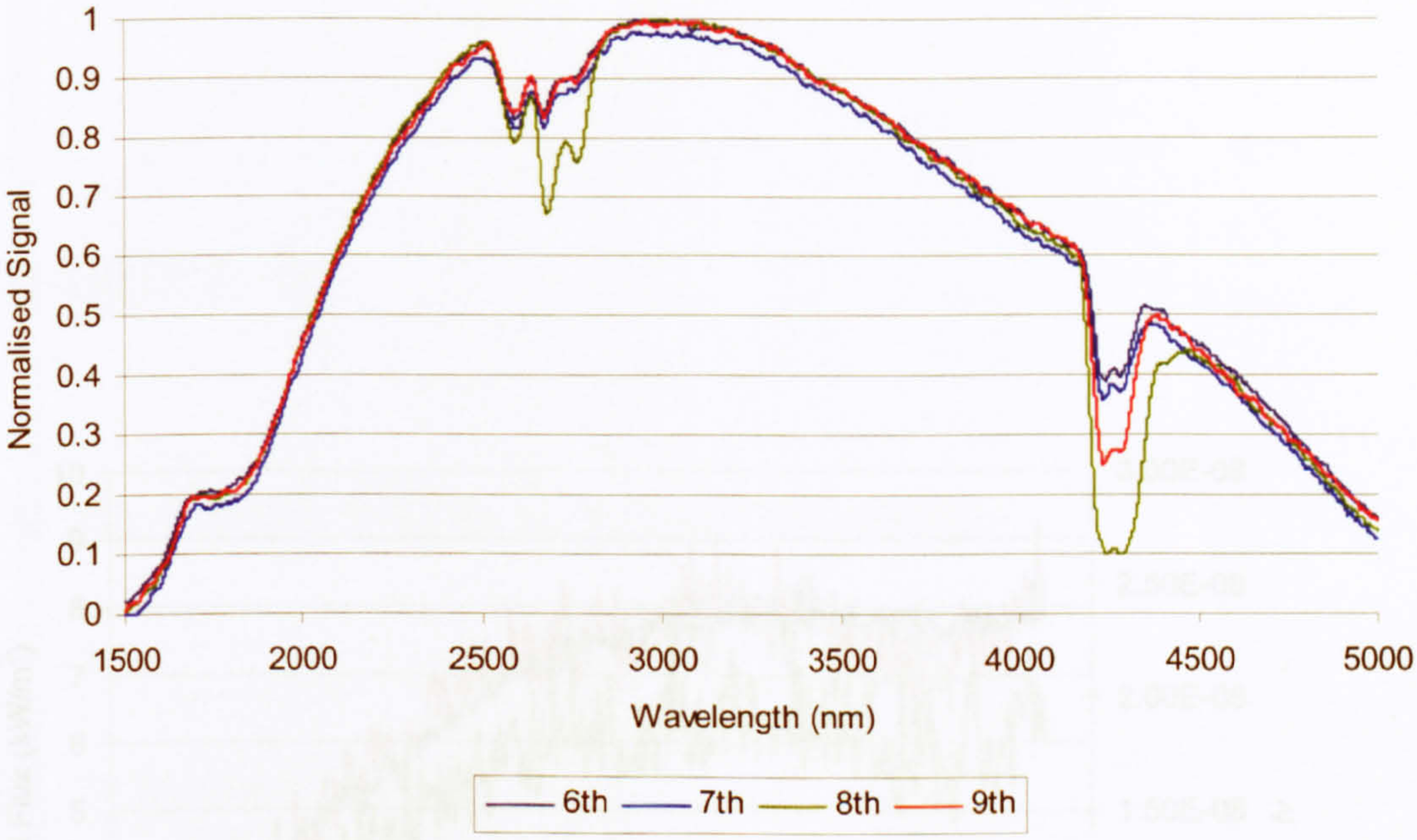

Figure 3.41: Radiative emission spectra displaying the effect of heptane vapour presence in the path between the radiant source and detector

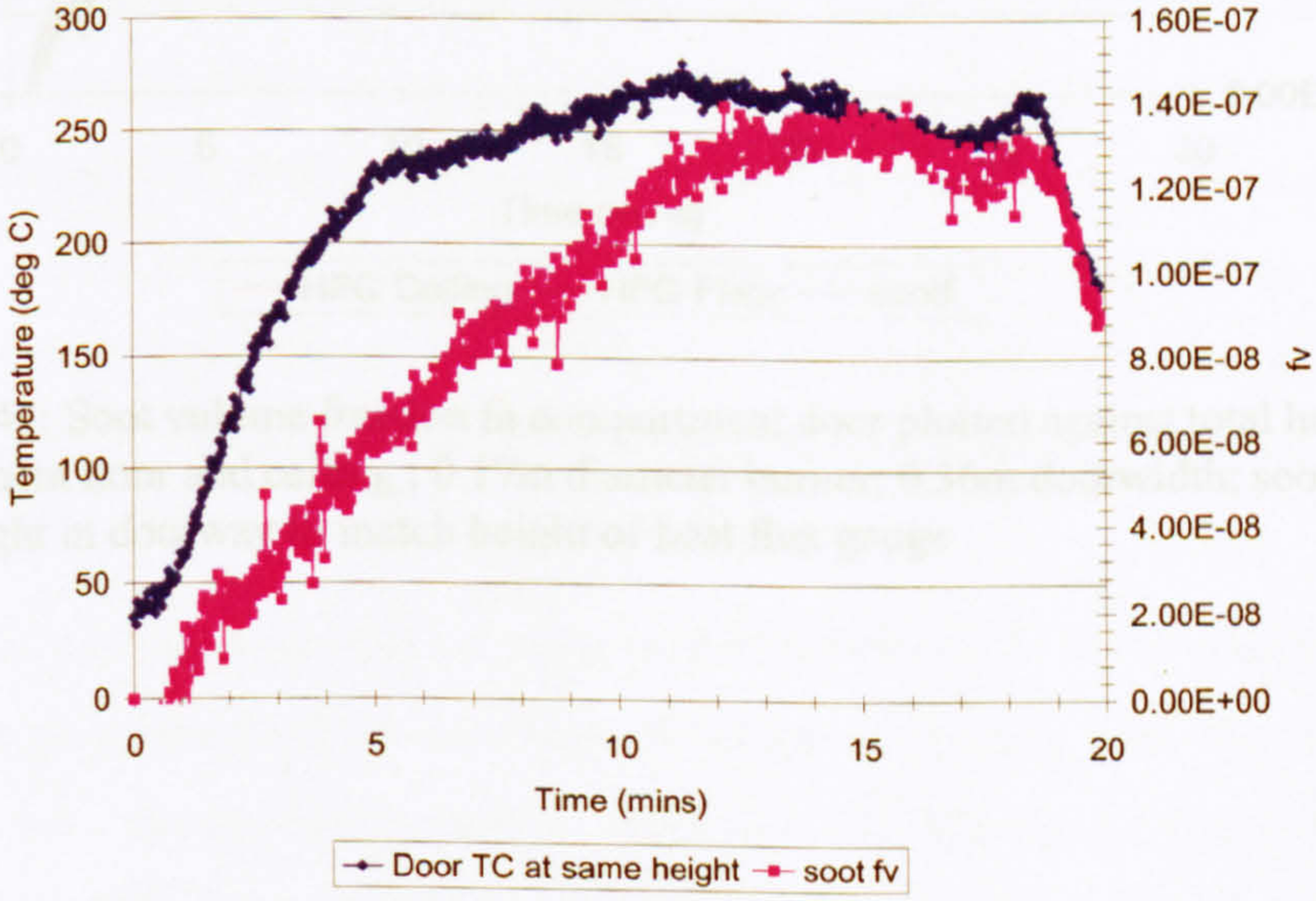

Figure 3.42: Soot volume fraction in compartment door showing approach to steady-state - comparison with corresponding thermocouple temperature; 0.17m diameter burner; full doorwidth

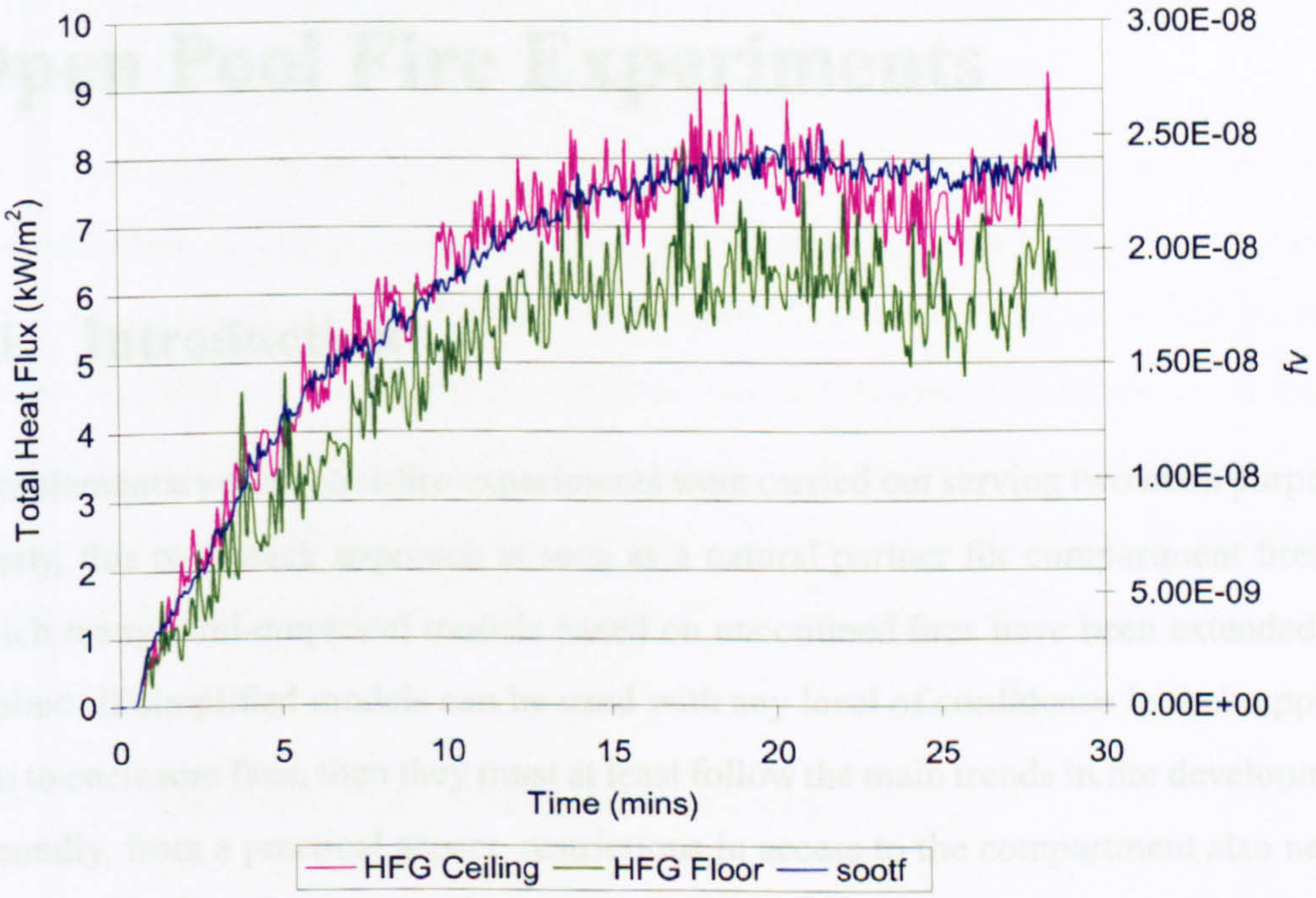

Figure 3.43: Soot volume fraction in compartment door plotted against total heat flux to compartment floor and ceiling ; 0.17m diameter burner; 0.36m doorwidth; soot probe at 0.6m height in doorway to match height of heat flux gauge

Chapter 4

Open Pool Fire Experiments

4.1 Introduction

Complementary open pool-fire experiments were carried out serving two main purposes. Firstly, this twin-track approach is seen as a natural partner for compartment fires for which many semi-empirical models based on unconfined fires have been extended and applied. If simplified models can be used with any level of confidence in their application to enclosure fires, then they must at least follow the main trends in fire development. Secondly, from a practical aspect, restrictions in access to the compartment also necessitated pursuit of a more finely resolved data-set, which simultaneously enabled further probing of other fire characteristics that were difficult to quantify in the compartment, such as the level of turbulent fluctuations and its intensity.

Where relevant, measurements are compared with those made in the compartment and results are presented for both experimental scenarios. Results from this series of experiments have already been presented publically [89]. The three different liquid fuels namely IMS, Heptane and Kerosene have been chosen due to their significantly different sooting propensities and generatation of fuel vapours with substantially different molecular weights (46, 100, 175 respectively).

4.2 Experimental Design

Figure 4.1 depicts the main geometry of the apparatus used in the open pool-fire experiments. The larger burner of 0.23m diameter, formerly used in the compartment fire experiments, is utilised throughout due to its provision for instrumental access at its base and to provide consistency. A conical shaped fire-resistant smoke hood was attached to the rim of a chimney extract directly above the burner, in order to provide the necessary means of natural ventilation extract, whilst importantly ensuring that this was arranged at a suitable distance to prevent any disruption on entrained air-flow.

The measurements made in this configuration are identical to those made in the enclosure. However, additional instrumentation included that of a load cell with a resolution of 2g, which was mounted centrally to the base of the burner and an in-line heater to elevate the water cooling temperature for the heat flux gauges. The burner itself was capable of being rotated through 360° by means of a bearing arrangement, which initially provided an indication as to flame symmetry. Once this was satisfactorily established, the burner then remained in a fixed position for the duration of each experiment.

4.3 Experimental Measurements

The following subsections briefly describe the measurements which are made in the experiments, followed by a description of the parameters related to the measurement concerned.

4.3.1 Light extinction

The identical light extinction measurement technique to that carried out in the enclosure fire experiments, was employed to determine the concentration of soot in the over-fire region of the pool-fire. Once again, the concentration of soot is expressed as a soot

volume fraction for ease of comparison with results of other workers, such as that of Koylu [55]. Measurements were made employing the water-cooled soot probe previously described in section 3.3.4 (see figure 4.2). The same level of N_2 purging was used to prevent soot deposition by thermophoresis onto the optical surfaces of the probe.

In the case of the open pool-fires, two parameters could be discerned using this instrument. Firstly, the soot volume fraction time series may be established, in-line with the measurements made within the compartment and for which a comparison of time averaged steady-state absolute values is made. Secondly, intermittent fluctuations could be captured. The nature of these fluctuations may be split into two categories. Figure 4.3 and 4.4 illustrate two phenomena which are quite distinct. Firstly, by correlating the local external soot probe thermocouple temperature profile, which is taken immediately adjacent to the laser-beam housing orifice, we can suggest that at these relatively low temperatures, the fluctuations in measured soot concentration is caused by the pulsing emission of relatively cool soot caused by thermal quenching at or below the measurement height. Figure 4.3 further substantiates this assumption due to the slow waveforms of soot that correspond almost exactly with the pool-fire pulsation frequency, as determined by Fourier transformation of the vertical thermocouple rake signals.

Secondly, at roughly half the frequency of these slow pulsations, a secondary superimposed fluctuation is evident. The level of soot is roughly six times that of the lower frequency and lasting in duration for around an order of magnitude less. The explanation for this phenomenon is likely to be the intermittent instantaneous flame front elongation, extending into the line of sight of the laser-photo-diode arrangement of the soot probe.

The time frequency of both patterns of soot fluctuations start to increase upon cessation of fuel inflow to the pan. Again, this seems to relate to the influence of conduction from an uninsulated pan on the observed overshoot of all measured parameters in both the open pool-fire and compartment fire configurations.

4.3.2 Flame temperature

Six fine-wire Platinum-Platinum 87%/Rhodium 13% thermocouples (type R) were aligned vertically and attached to a traversable rake situated external to the burner (see figure 4.5). Each thermocouple was manufactured in-house, with a typical bead diameter of 250 microns, established by spark discharge in an inert environment. Figure 4.6 depicts the main lineaments of the thermocouple construction. The thermocouple wire was housed in twin-bore ceramic tube of 400 mm in length to provide insulation for the thermocouple wires against the high temperatures to which they would otherwise be exposed. At one end of the ceramic tube, the wires are connected to a miniature type R thermocouple connector. At the opposite end, the thermocouple wire is splayed outwards to form a closed triangular shape, extending to approximately 25 mm from the end of the ceramic tube. The widest part of the triangle is approximately 40 mm across. The thermocouple bead is situated central to the base of the triangle.

Figure 4.7 shows the average flame temperature with height above the burner, produced by burning heptane until a steady-state is reached.

4.3.3 Convective velocity

From the turbulent fluctuations inherent in pool fires of this diameter, the convective velocity of the fire plume may be discerned from time correlation techniques.

The application of this technique is not a new concept, but it has been used successfully to determine turbulence parameters and plume velocities from the cross correlation of thermocouple signals, for example [90].

The cross correlation is described by the following function:-

$$R(r, \tau xy) = \overline{x(t-\tau)y(t)} \tag{4.1}$$

which describes the similarity of two random signals x(t) and y(t) a distance, r, apart

as a function of the time shift between them (τ). This function will have a maximum value at $\tau = \tau_{mean}$, the mean transit time of the fluctuating property, x(t) and y(t) are the signals received at two measurement points through which the fluctuating pattern travels.

A typical temperature-time profile for Heptane, from which the convective velocity is calculated may be seen in figure 4.8. This figure describes the evolution of temperature from ignition by means of a pilot flame. An average velocity is calculated based on closer inspection of the thermocouple signals over a period of 2 seconds upon reaching steady-state (see figure 4.9 for example).

The availability of convective velocity component measurements also enables calculation of estimated soot residence times, assuming it to be proportional to the ratio of a characteristic length scale, L and a characteristic velocity.

The properties of highly buoyant turbulent diffusion flames are not strongly influenced by burner exit velocities and molecular transport properties, while the driving potential for buoyancy forces, $\Delta\rho/\rho\infty$, is essentially unity because densities within the flame are small in comparison to ambient densities. This implies that the characteristic velocity is a function of L and the ratio of volume flow rates of air and fuel for stoichiometric combustion.

4.3.4 Turbulent radiative emission fluctuations

Caution is required when using mean properties of for example, radiation heat transfer, to characterize turbulent fires, which inevitably can lead to significant differences between the predicted and measured fuel burning rates.

Markstein [91] investigated spatial and temporal variations of the emission intensity for pool fires and suggested the importance of turbulent fluctuations of temperature and soot volume fractions on the heat transfer mechanism. To perform direct integration of radiative heat transfer to an open-pool fire, requires knowledge of time-varying tem-

perature and emissivity of the combustion gases and soot at the flame-fuel interface. To better understand the process governing this important mechanism required detailed measurements that are difficult to perform within the confines of a compartment, due to the inability to separate the flame itself from heat transfer originating from the hot smoky layer and wall radiation.

To this end, the emission spectrometer was once more positioned beneath the burner, akin to the compartment fire configuration. Although the radial symmetry of the flame enables great simplification in establishing typical profiles of emission fluctuations, the measurements are still required to be performed within a relatively narrow window in time before fuel and pan heating effects become important, thus raising the question as to consistent measurement positions due to the flame lengthening and increased momentum that results.

Due to the use of two different data acquisition hardware and software for this set of experiments, the question arises as to the uncertainty in formulating correlations from instantaneous measurements in which the data are not necessarily acquired simultaneously.

In order to correlate different data sets taken non-simultaneously, a distinct pattern repeated at regular intervals must be present, thus displaying self-correlation. Figure 4.10 shows the radiative emission signal taken at 4000nm and 4405nm. It is clearly seen, that the fluctuations in emission are regular and appear identical to the pulsation frequency observed from the thermocouple and soot volume fraction data. This is in contradiction with other workers [46], who found that auto-correlating their emission data from a heptane pool fire showed a maximum at 0, suggesting that the low correlation values are indicative of no dominant pattern present that is repeated in time. Despite the inability to directly compare the data from this research with that of Choi [46], it was demonstrated in their experiments, that a difference of only 1% in the apparent emission was achieved using:-

- zero time shift

- random time shift for every other data set and a
- random time shift for each data set

for 19 non-simultaneous measurements of temperature and soot volume fraction.

4.3.5 Total heat flux and mass loss rate

As previously mentioned, the calculation of heat flux to the fuel surface requires a detailed description of temporal and spatial distributions for both temperature and soot volume fraction.

Clearly, the trajectory of the flame under ventilation controlled conditions where the flame sits closer to the fuel surface, is different to that of an open environment. The influence of the compartment is immediately apparent when we compare figures 4.11 to 4.12 where we can see that the level of heat flux to the fuel surface experienced in the compartment fire experiments is around twice that of the open pool fire. In addition, two total heat flux gauges were placed one at the centre, the other at a 5 cm radius as an indication of the total heat flux distribution over the fuel surface. The results suggest that the heat flux is evenly distributed. Heat transfer to the gauge is initially high due to rapid evolution of fuel, with the flame sitting close to the liquid surface engulfing the sensor. This phenomenon is repeated just prior to ignition when the flame is observed to shorten and once again engulf the sensors. Figure 4.13 illustrates the fluctuations in heat flux for the open pool fire over a period of 60s at steady-state.

Concerns were first raised in section 3.3.7 as to the effect of a condensed layer of heptane which formed on the upper surfaces of the Gardon gauges. As such an in-line heater was used to elevate the cooling water temperature of the sensors above the dew-point of heptane. The effect on the steady-state signal was to reduce the absolute steady-state heat flux by just under 5% for both the compartment and open pool-fire experiments.

The mass loss rate of fuel was determined from load cell measurements at a resolution of 2g, from continuous mass loss profiles such as may be seen in figure 4.14. Towards

the end of the experiment, it can be seen that the mass loss rate of fuel is enhanced due to conduction from the burner when the level of fuel is low.

The signal from load cells is notoriously noisy. The spectral range from 0.1 to 10Hz is dominated by electronic circuitry noise, the magnitude of which is inversely proportional to frequency. The range 10Hz to 1kHz is dominated by hum at the line frequency (60Hz) and harmonics of the line frequency, by electrostatic or magnetic coupling with external fields such as solenoids or electric motors, or by ground loop hum. The high-frequency end of the spectrum is white noise having a flat spectral density over the full bandwidth. This noise arises from thermal vibration of charged particles in solids and is often referred to as resistor of Johnson noise. It was found that significant fluctuations in the load cell signal occurred at around 50-60Hz due to mains interference. Therefore, noise of frequencies higher than the expected turbulent flow signal is filtered out with a low-pass filter card as supplied by IOTECH. The filter card was configured as a 3-pole active Butterworth type filter (optimized for gain flatness in the pass band, with an attenuation of -3db at the cutoff frequency). The cut-off frequency for the load cell data acquisition was conveniently chosen to be 10Hz.

Table 4.1 compares the enthalpy required for gasification, $\dot{m}\triangle H_g$, with that implied by the measured heat flux under steady state conditions, assuming the flux to be uniform over the entire surface. In the case of kerosene, with the relatively dense vapour burning inside the burner and closer to the centre-line, the mismatch in effective area for the mass loss computation is particularly large. The influence of heat flux distribution and the variation with fuel type are clearly demonstrated.

The comparable experiment in the compartment, fuelled by heptane, produces a different energy balance. Figure 4.12 shows that the total heat flux as measured by the Gardon gauge would lead to an overestimate of the fuel vapour generation rate.

	IMS [open]	Heptane [open]	Kerosene [open]	Heptane [compartment (0.36m door)]
Mass generation rate $\dot{m}$ (g/min)	37	76	32	100
Gasification enthalpy flux $\dot{m}\triangle H_g$ (kW)	0.6	0.61	0.31	0.80
Total incident heat flux $\dot{Q}A_{burner}$ (kW)	1.25	0.42	2.49	1.04

Table 4.1: Fuel vapour generation rate for the three fuels (0.23m diameter burner)

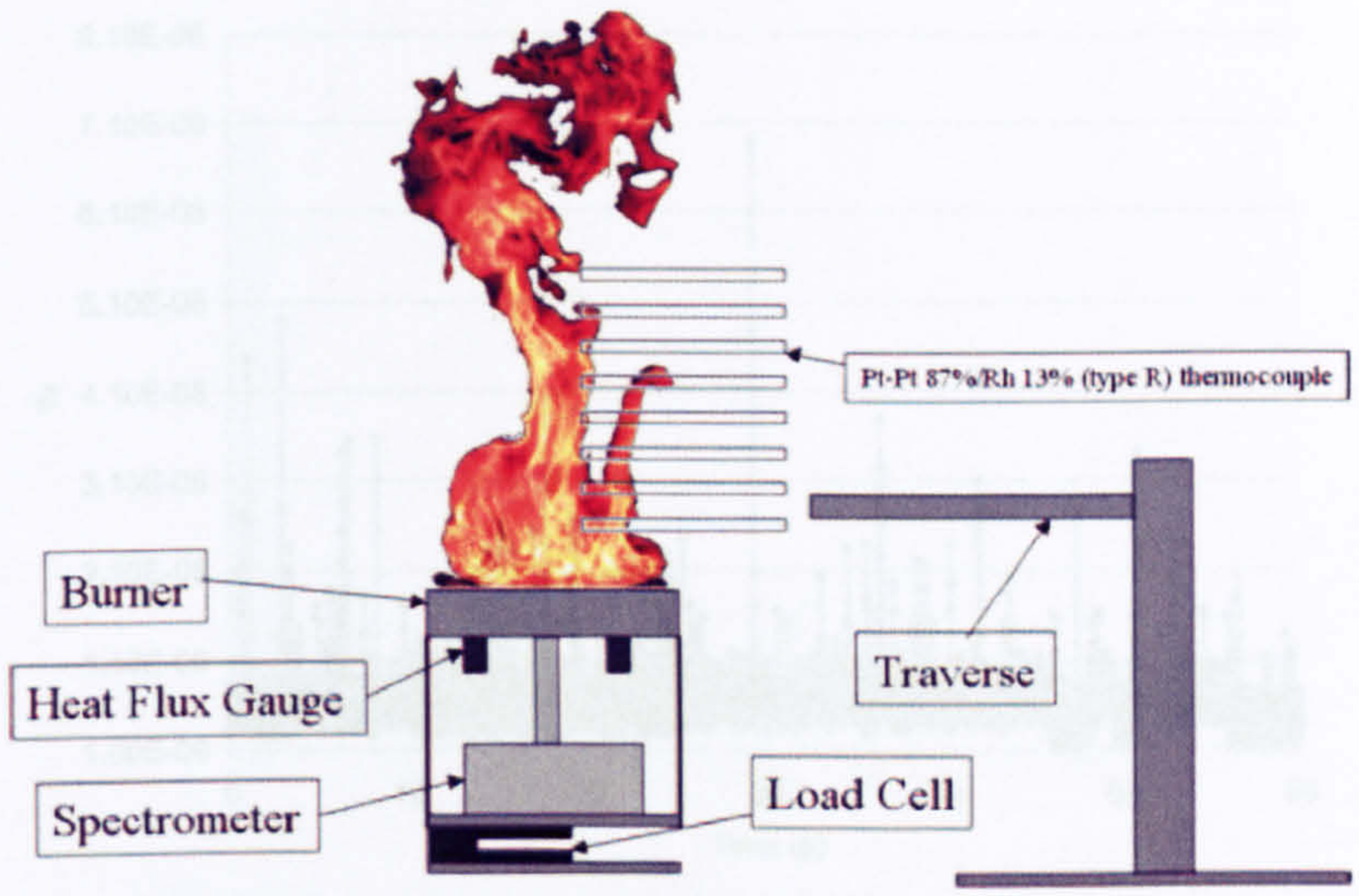

Figure 4.1: Schematic of open pool-fire experimental setup

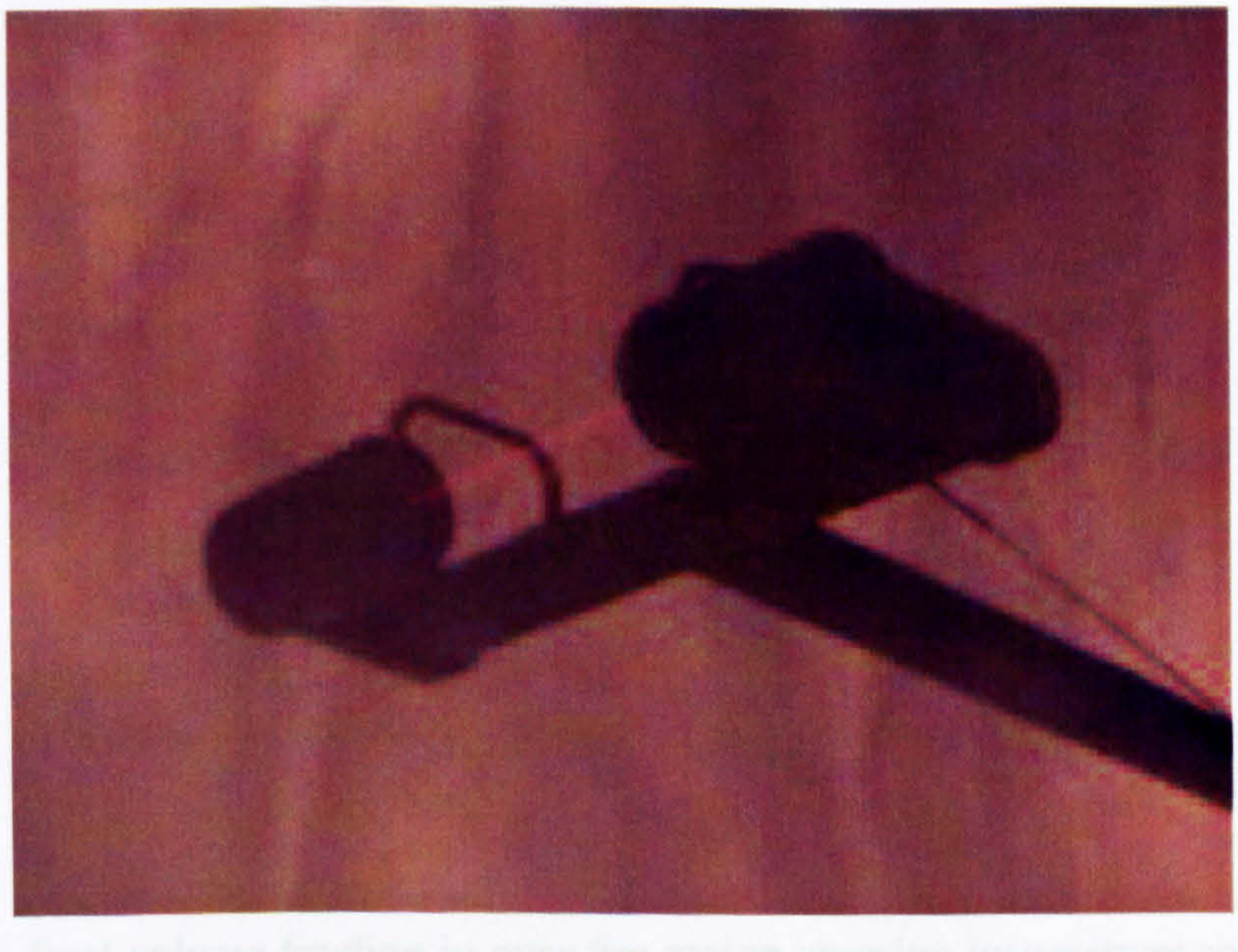

Figure 4.2: Soot probe showing laser beam scatter during open pool fire experiments

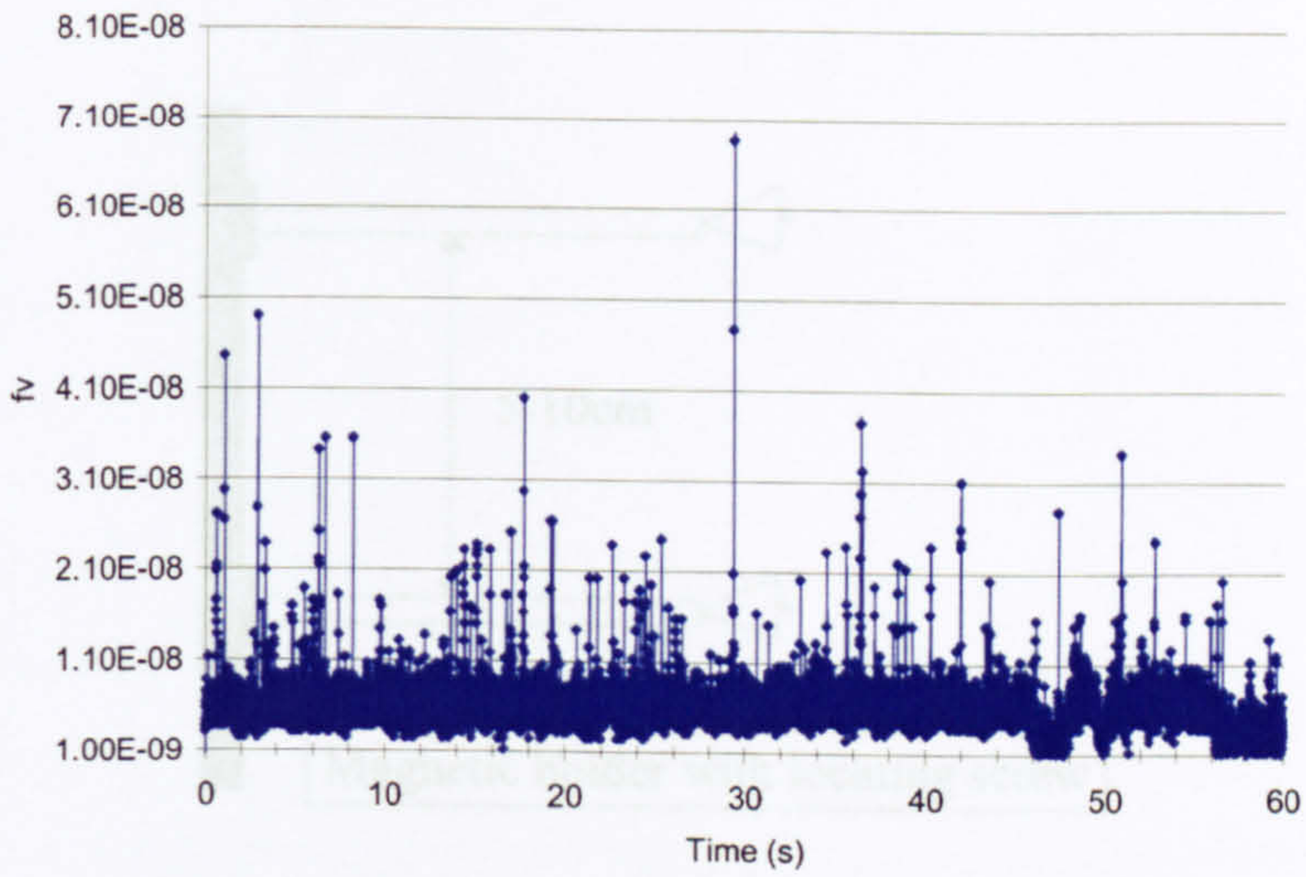

Figure 4.3: Soot volume fraction in over-fire region showing intermittent soot fluctuations; heptane; 0.23m diameter pan; open pool-fire

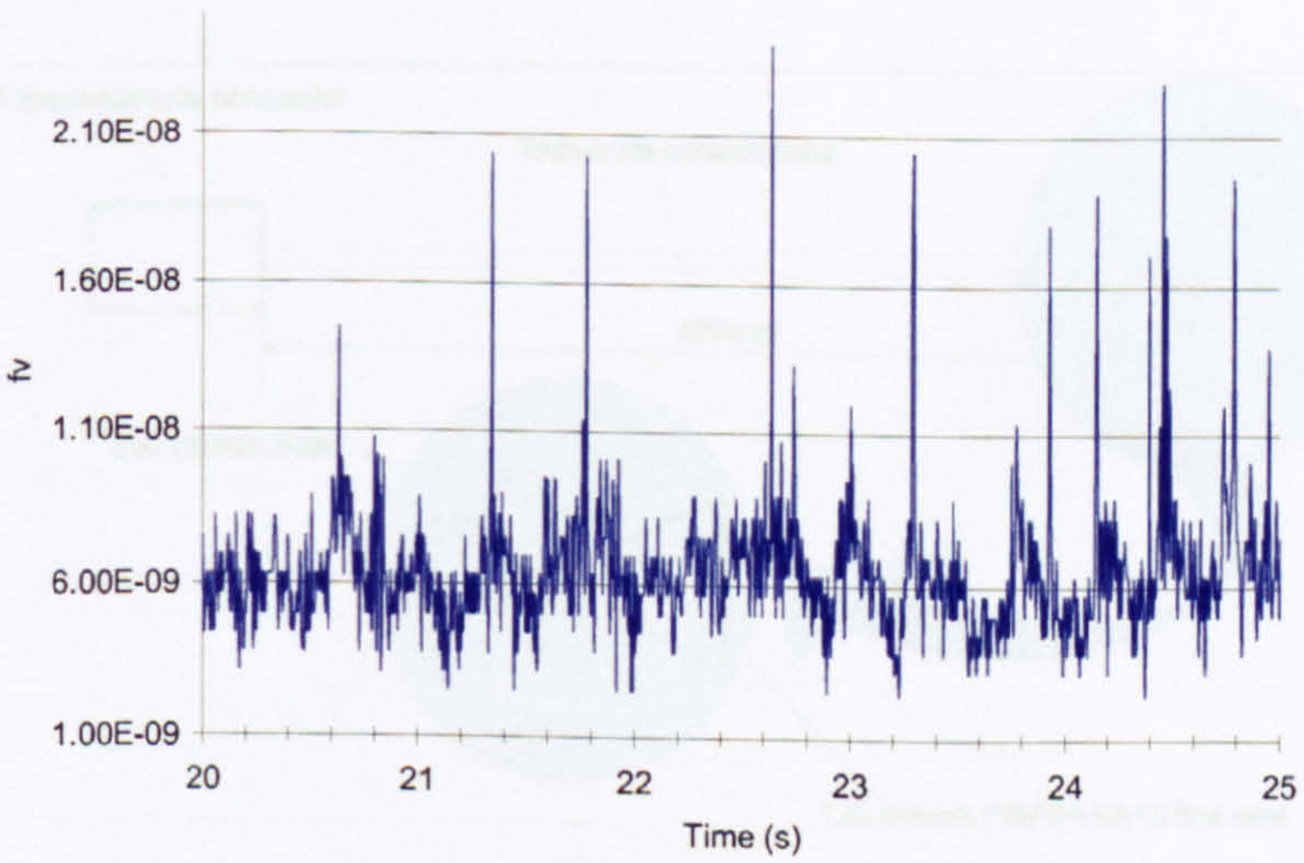

Figure 4.4: Soot volume fraction in over-fire region showing intermittent soot fluctuations over 5s interval; heptane; 0.23m diameter pan; open pool-fire

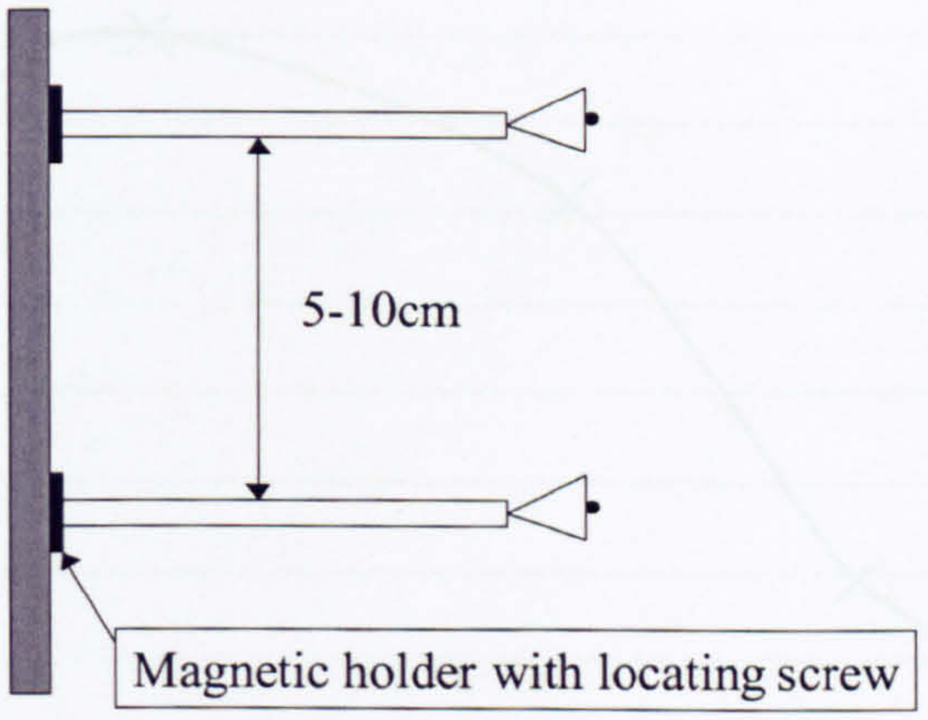

Figure 4.5: Vertical rake thermocouple arrangment

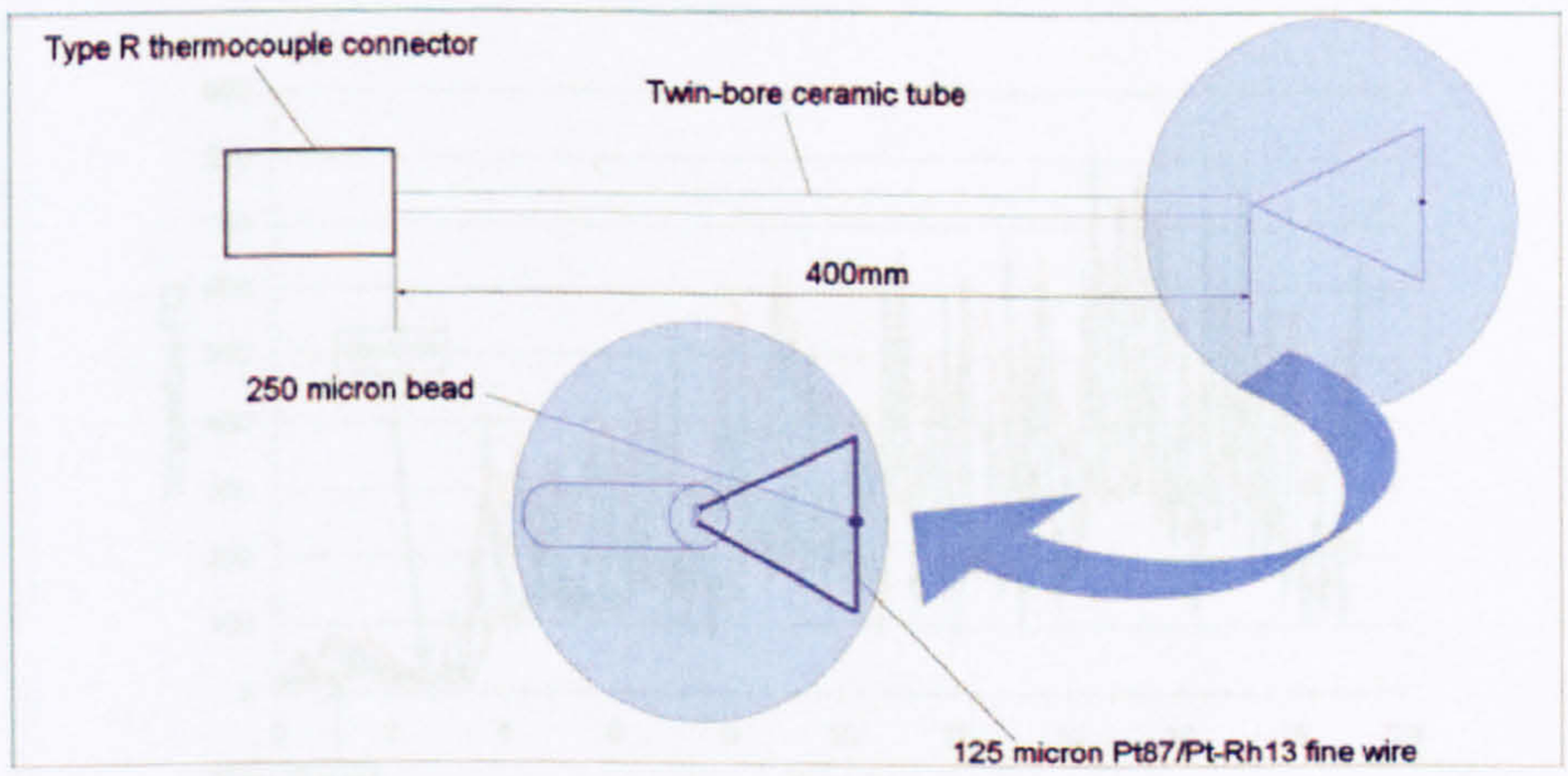

Figure 4.6: Platinum/Platinum-Rhodium13 thermocouple schematic

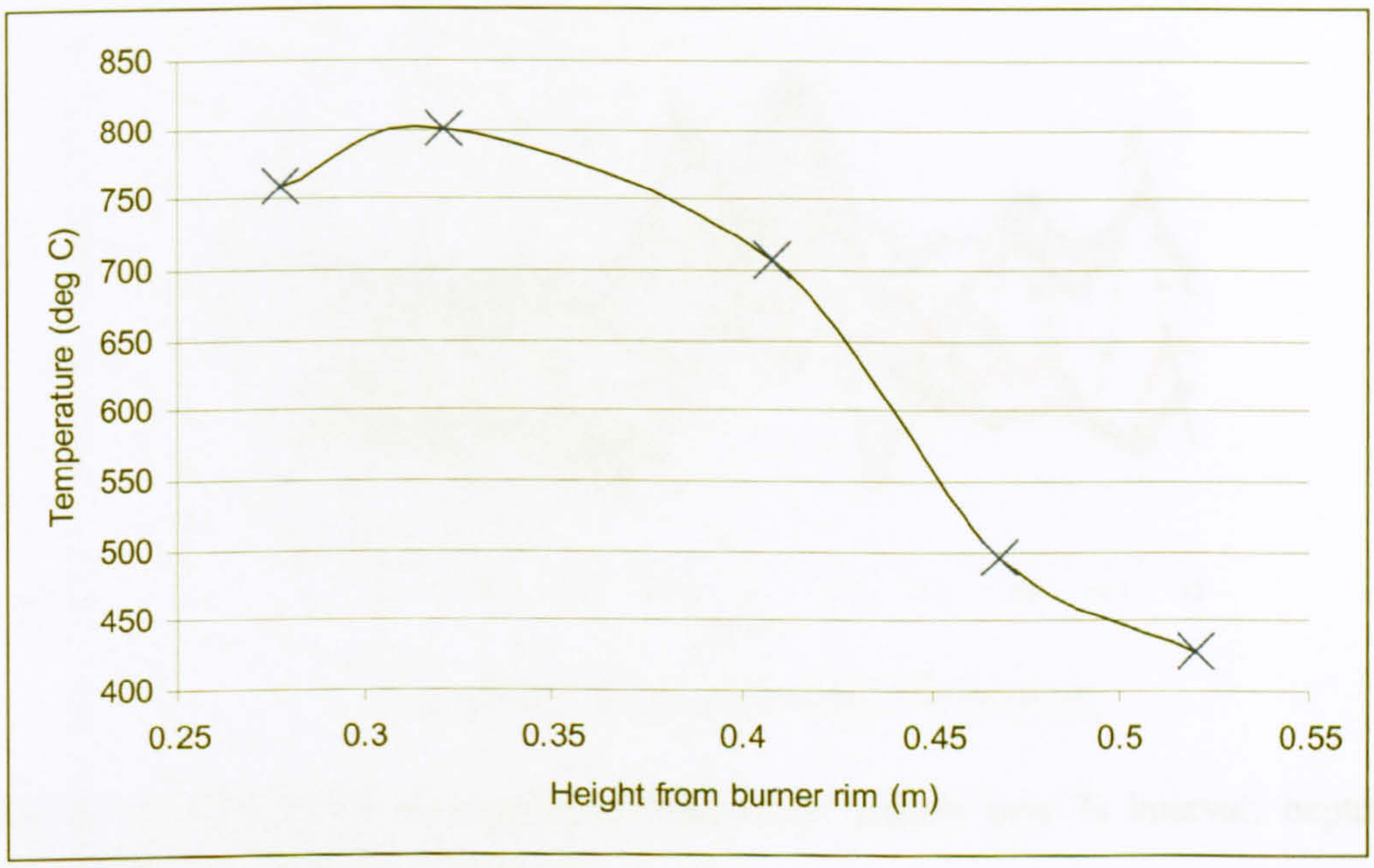

Figure 4.7: Vertical thermocouple temperature; heptane; 0.23m diameter pan; open pool fire

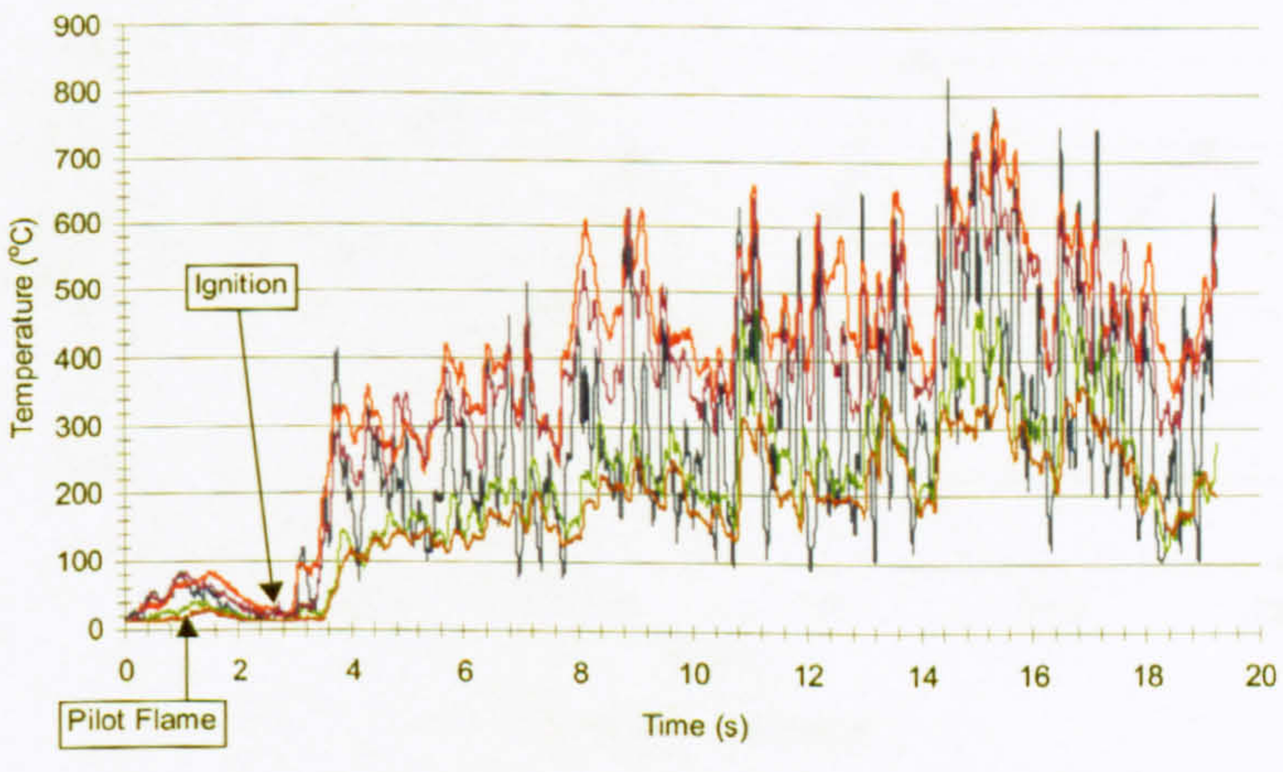

Figure 4.8: Individual thermocouple temperature signals from ignition; heptane; 0.23m diameter pan; open pool-fire

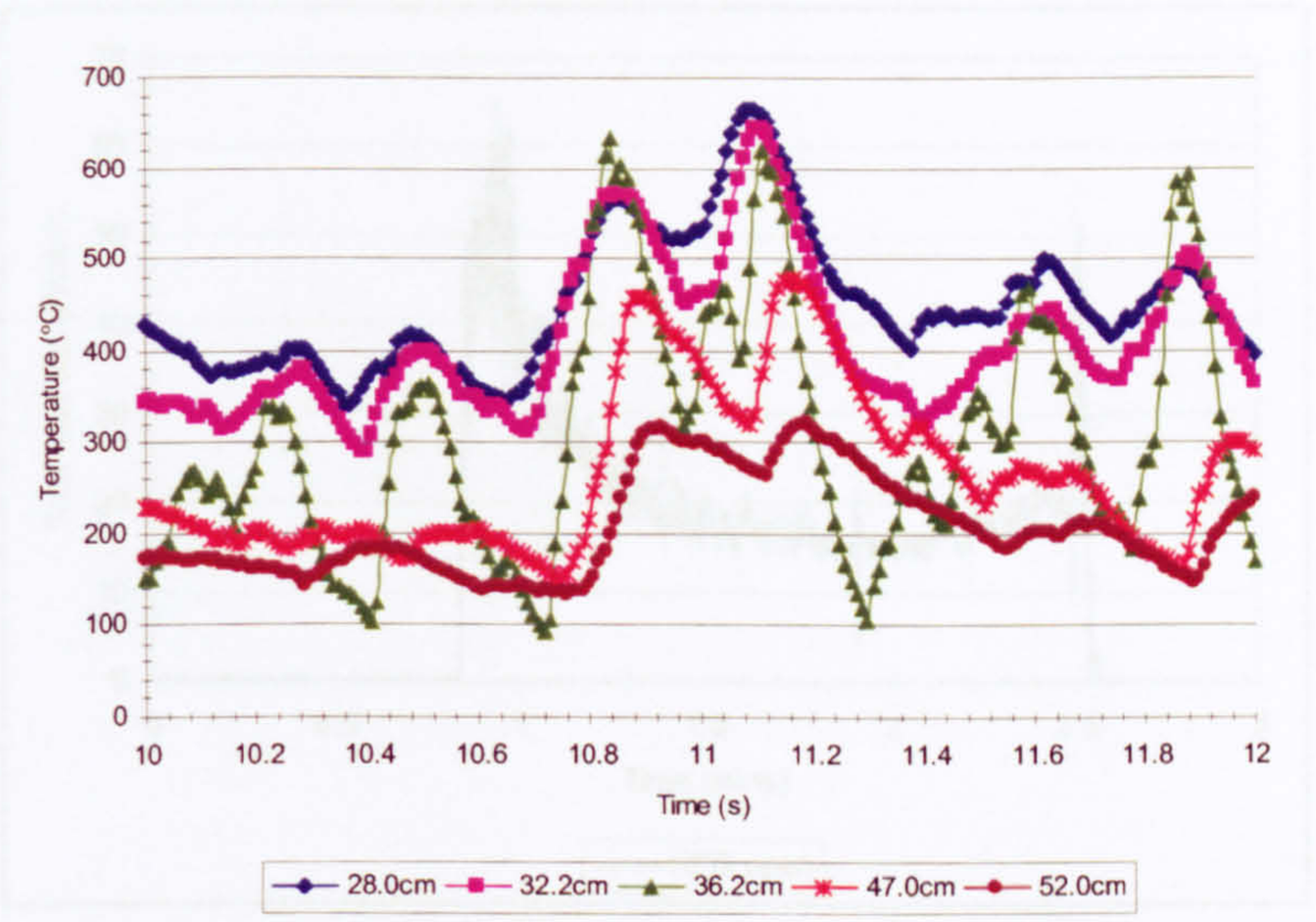

Figure 4.9: Individual thermocouple temperature signals over 2s interval; heptane; 0.23m diameter pan; open pool-fire

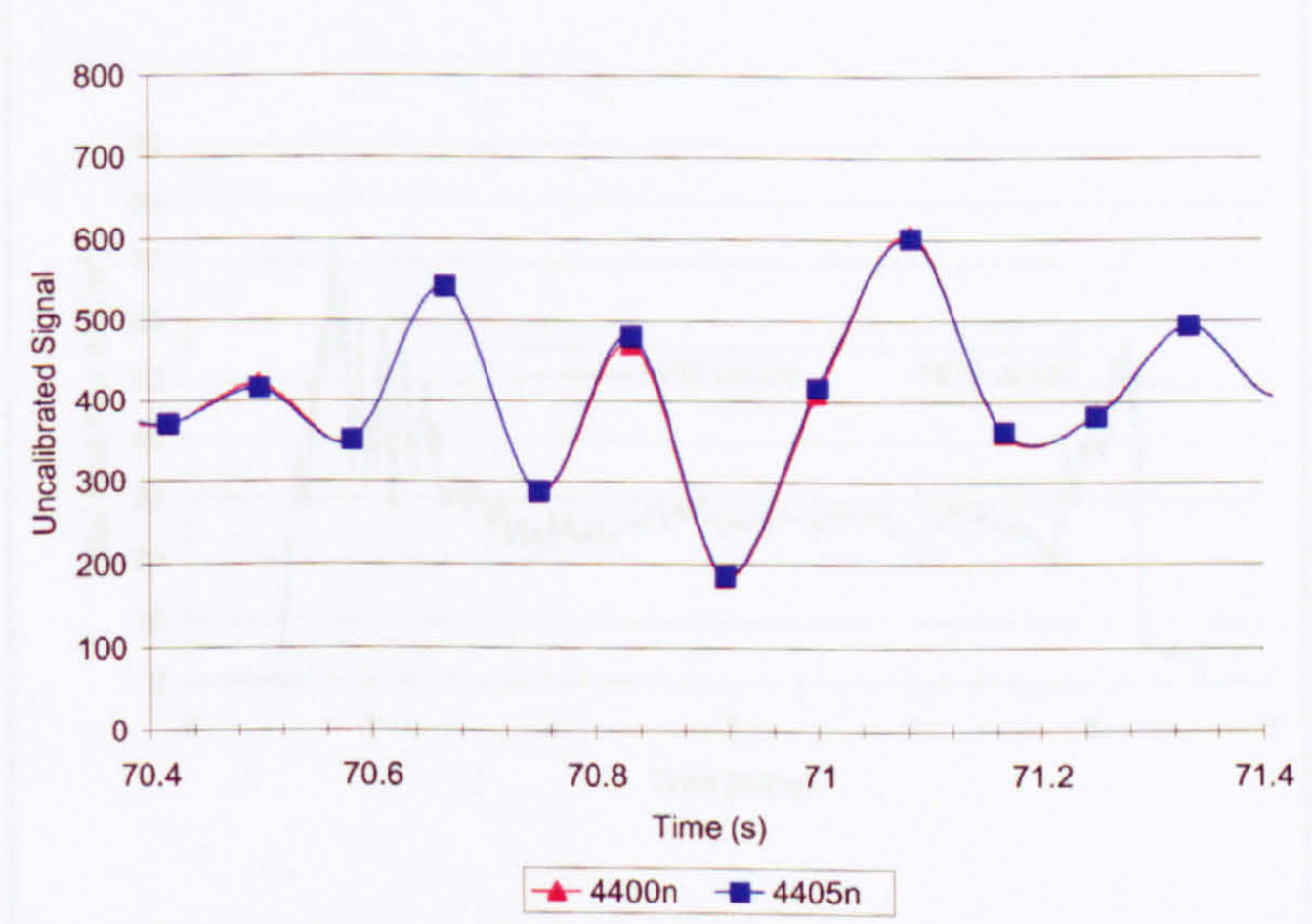

Figure 4.10: Radiative emission fluctuations over 1s interval; heptane; 0.23m diameter pan; open pool-fire

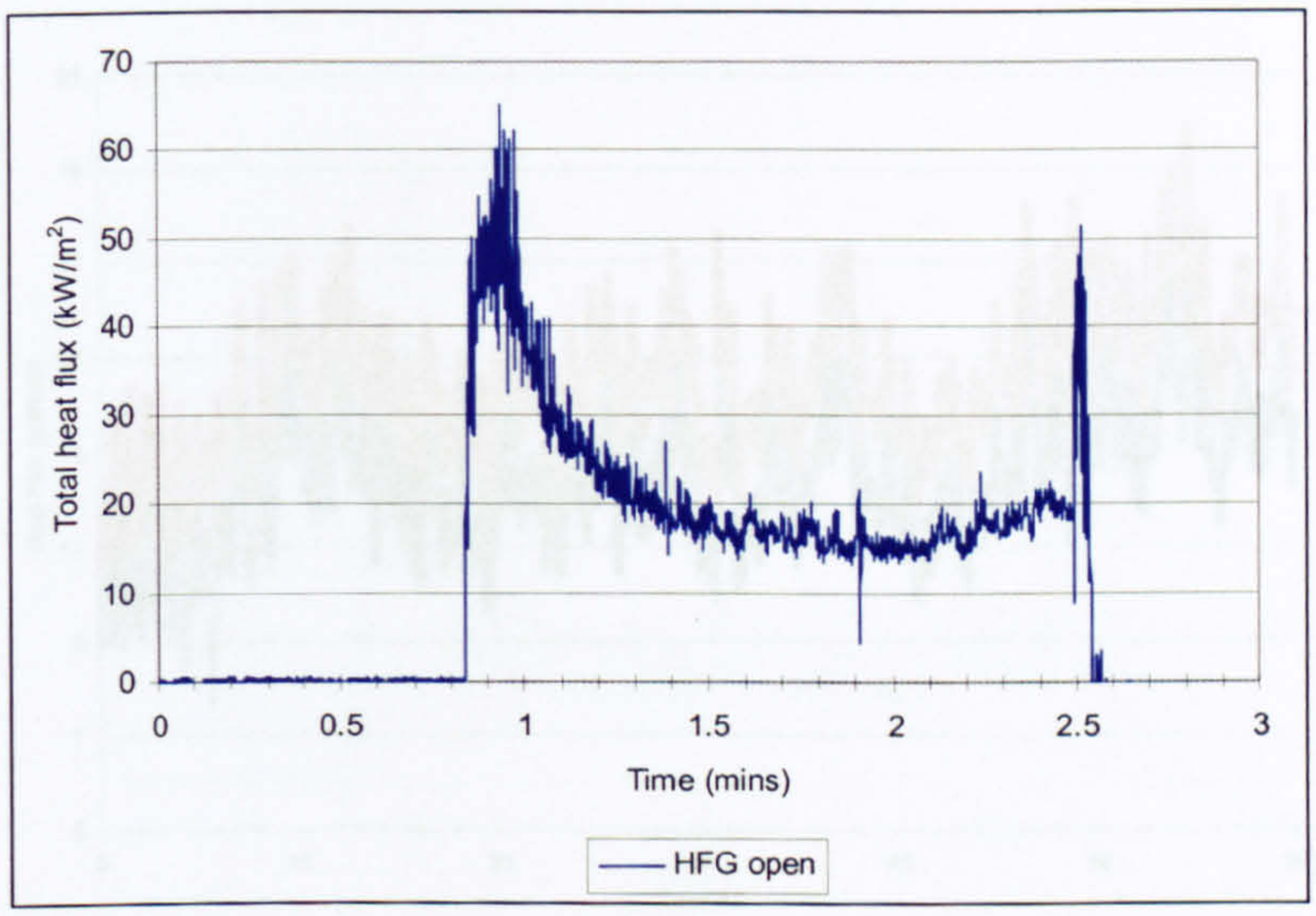

Figure 4.11: Transient profile of total heat flux to fuel surface; heptane; 0.23m diameter pan; open pool fire

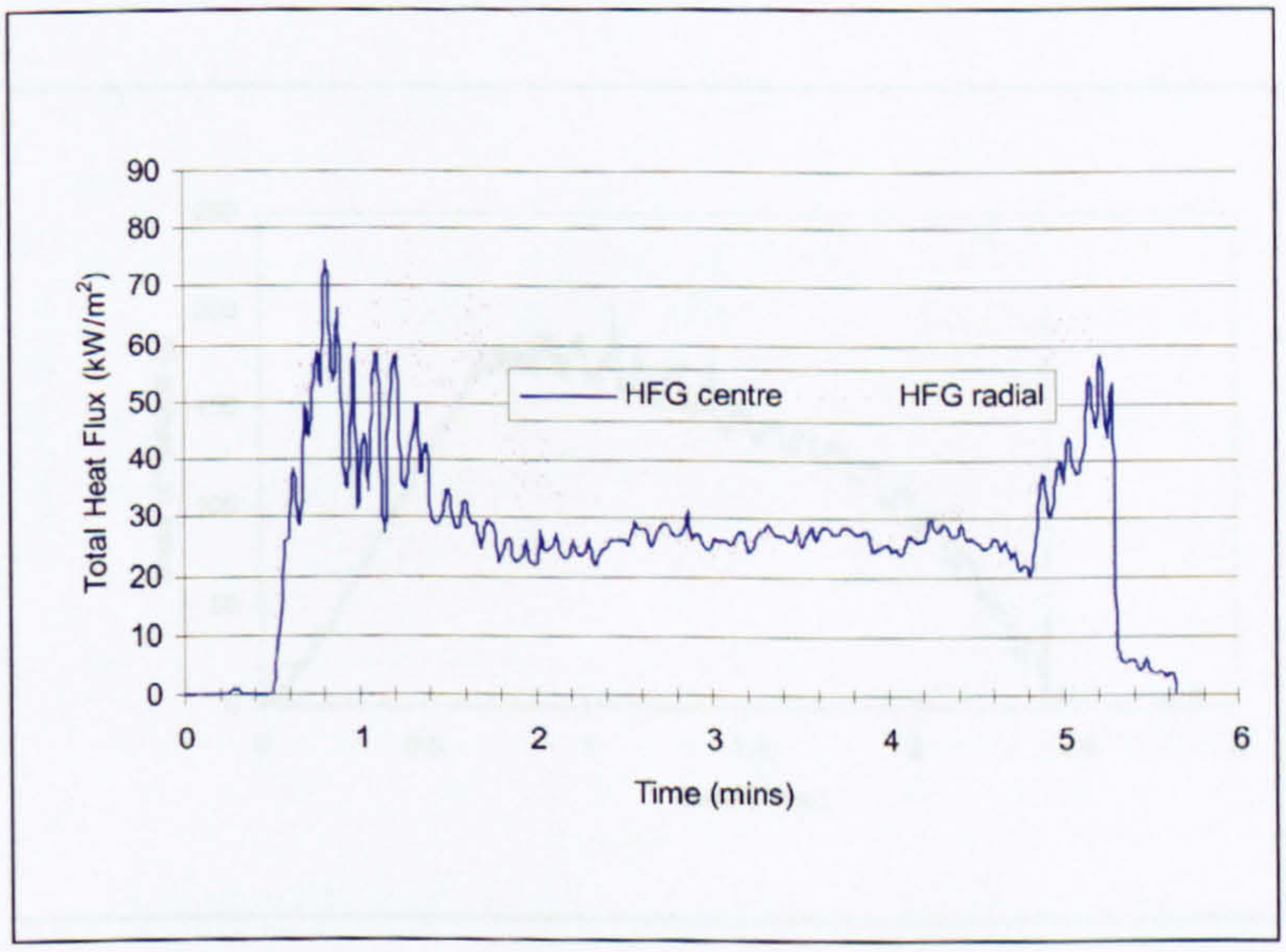

Figure 4.12: Transient total heat flux to fuel surface at steady-state; heptane; 0.23m diameter pan; compartment fire

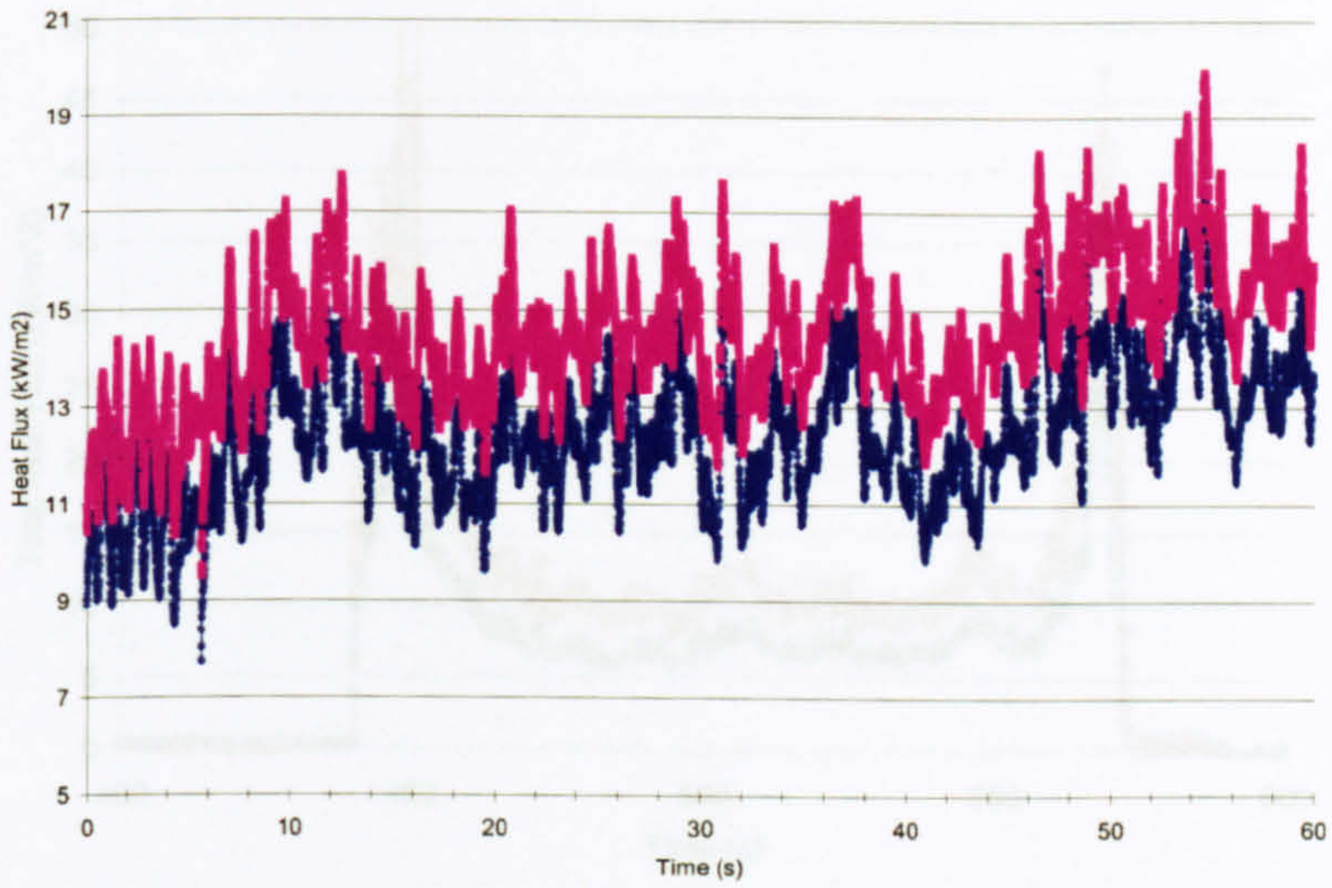

Figure 4.13: Total heat flux to fuel surface at steady-state; heptane; 0.23m diameter pan; open pool fire

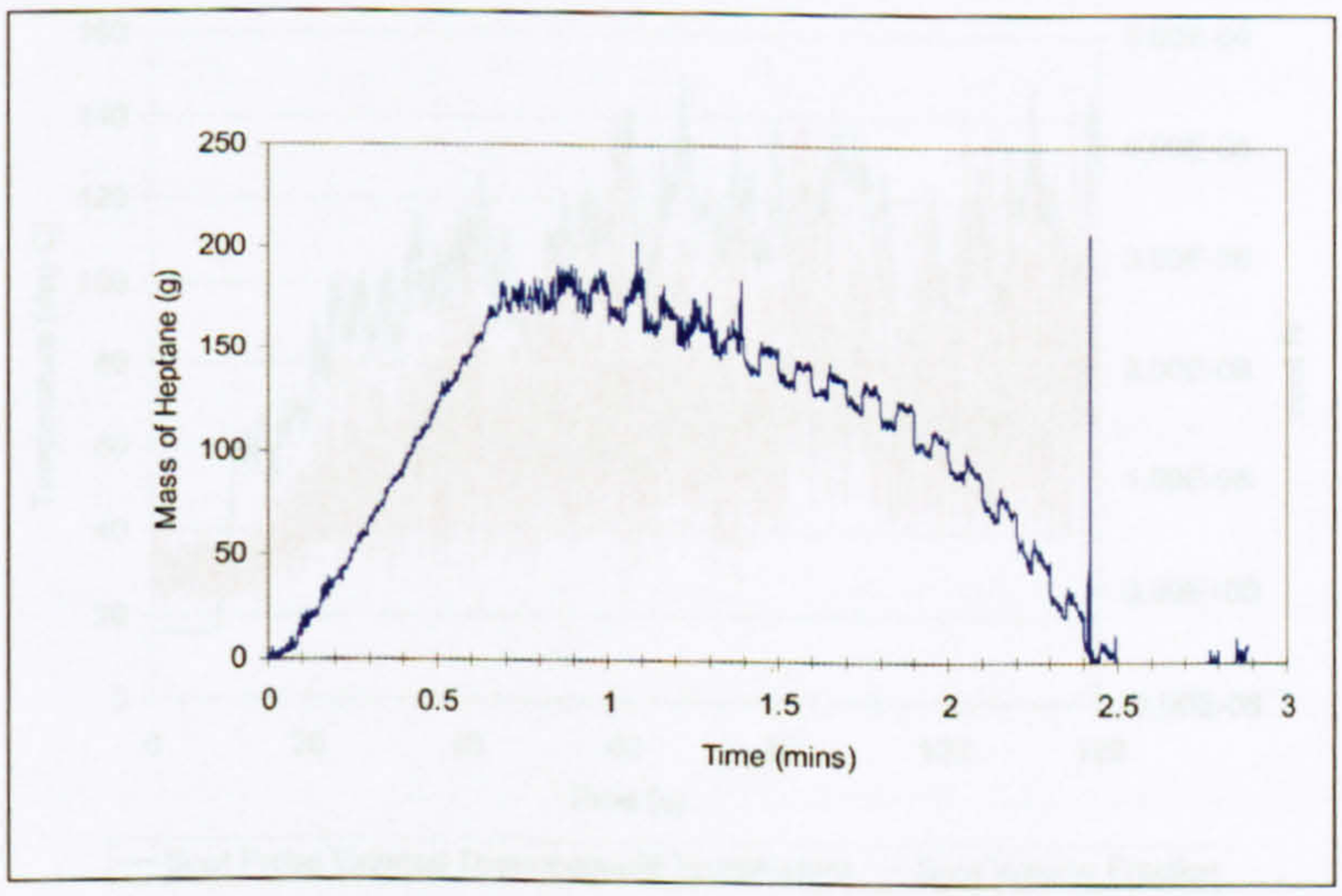

Figure 4.14: Continuous mass loss time history; heptane; 0.23m diameter pan; open pool fire

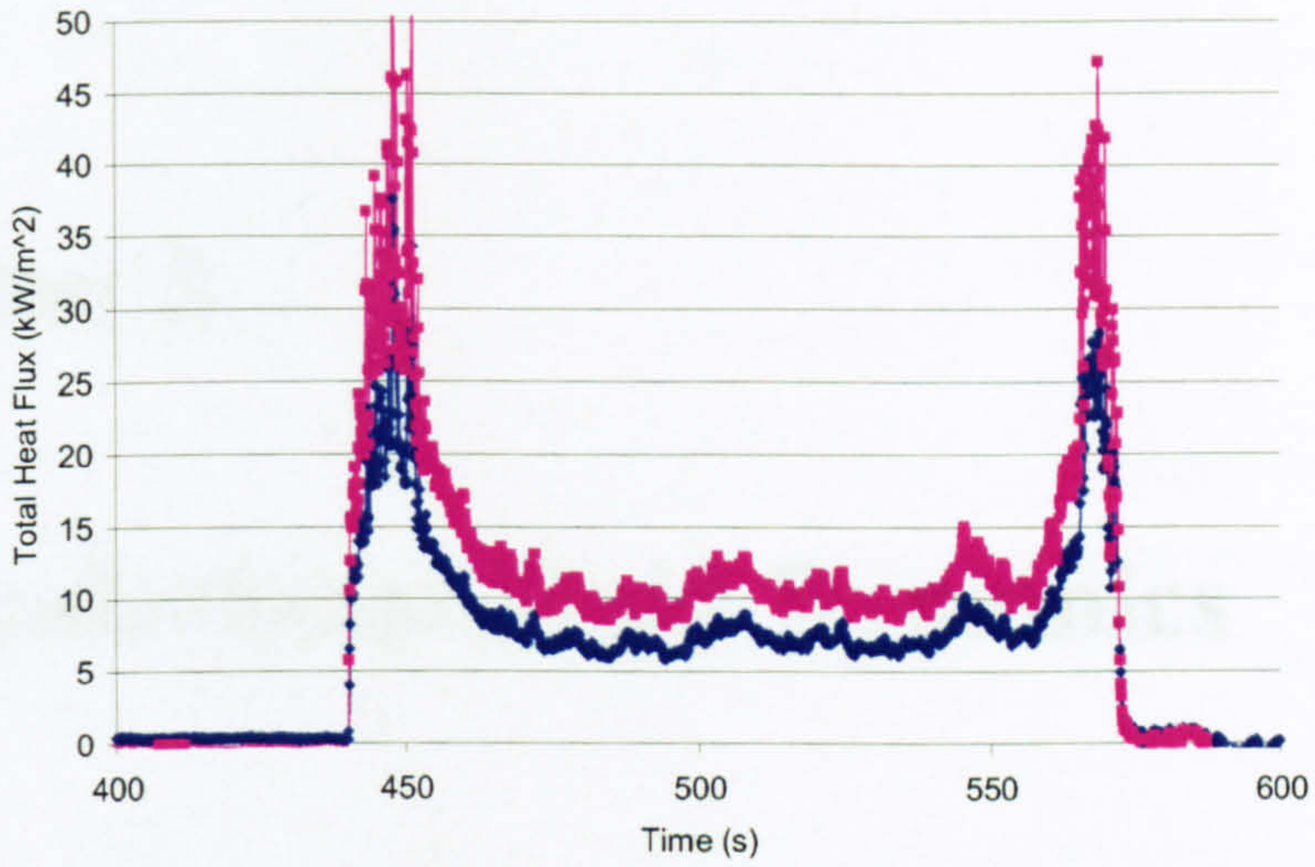

Figure 4.15: Total heat flux to fuel surface at steady-state; heptane; 0.23m diameter pan; open pool fire

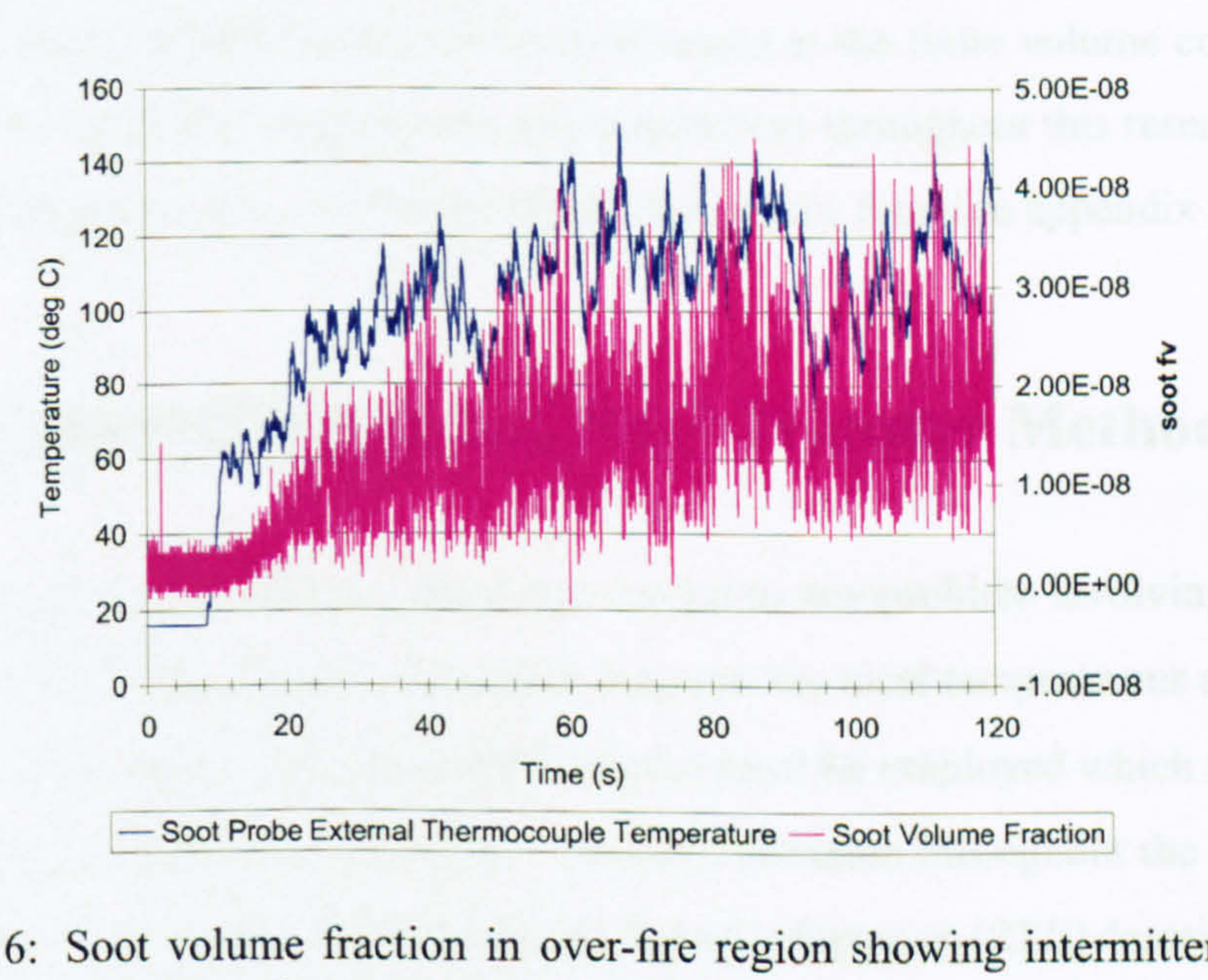

Figure 4.16: Soot volume fraction in over-fire region showing intermittent soot and temperature fluctuations; kerosene; 0.23m diameter pan; open pool-fire

Chapter 5

Computational Fluid Dynamics

5.1 Introduction

This section will highlight topics such as combustion, radiative heat transfer and the formation of soot in its application to CFD in the context of fires. It is not intended as a general review of CFD; instead focus is directed at the finite volume code - SOFIE, which is used in all the compartment fire simulations throughout this research. A more detailed description of the governing equations may be found in appendix C.

5.2 Numerical Radiative Heat Transfer Methods

The computation of radiative exchange is central to any problem involving the simulation of fires. In order to capture radiation transfer, the local temperatures and soot concentrations must be known. Secondly, a model must be employed which can calculate the emission, absorption and scatter of incident radiation throughout the domain. For the purposes of this research, the Radiation Transfer Equation (RTE) describes the transfer of radiation by absorption and emission only, based on the assumption of negligible scattering at incident wavelengths much larger than the particle size of participating gas

molecules and soot. Integration of the RTE results in an expression for the conservation of radiant energy, which provides the radiant energy source term for the energy equation. Discretization of the RTE is achieved using the Discrete Transfer Radiation Model (DTRM) in which radiation transfer is solved along rays selected *apriori*. Calculation of the radiative properties is then reliant on a suitable gas property model to evaluate the radiative emission and absorption.

The popular Weighted Sum of Gray Gases (WSGG) (De Ris discusses when it is appropriate to treat flames and smoke as gray [92]) model introduced by Hottel and Sarofim [58] was employed for the CFD simulations in this study, due to its widespread use in the combustion community. In addition, this approach has the advantage of being computationally efficient when compared to other methods, although it is acknowledged that alternative spectral methods, such as the narrow band method [93] offer improved predictions of radiative intensity [94]. The WSGG model requires a series of weighted absorption coefficients for a number of gray gases where "windows" in each spectrum is represented by a clear gas. Coefficients of Truelove [95] were used for each of the compartment fires simulations.

5.3 Stages of soot formation

The ability to encapsulate predictions of soot concentration is important, not solely in the context of "visibility in smoke". As previously suggested, enhancement of radiative transfer and flame spread is also effected by the presence of soot. The close coupling of radiative heat transfer for instance, with the evaporation model required in the determination of heat release, therefore places the distribution of soot as central to the simulations performed.

The stages of formation of soot which are considered in this research can be classified by: nucleation, coagulation, surface growth and oxidation. Each of these stages are briefly described below for clarification. Further, more detailed descriptions of soot

formation may be found in the literature review.

Nucleation

In diffusion flames, particle inception occurs on the fuel rich side of the flame whereby the first condensed phase material arises from the fuel molecules via their oxidation and/or pyrolysis products [96]. Such products typically include various unsaturated hydrocarbons, particularly Acetylene and PAH's. Condensation reactions of gas phase species such as these lead to the appearance of the first recognisable soot particles, with diameters of the order 1nm with a mass of around 1000 amu. Flame temperature also plays an important role in soot formation as the rates of fuel pyrolysis and PAH production depend crucially on temperature [97].

It has also been speculated that positively charged hydrocarbon ions act as nucleation sites that attract other hydrocarbons to form soot particles. Arguments for this are based on the appearance of ions prior to the appearance of soot. However, as a predictive tool, this mechanism has not been implemented in a soot model which has met with wide acceptance.

Coagulation

Coagulation is defined as growth of particles by collisions among particles. It is usually associated with dense, three-dimensional growth, in contrast to aggregation which leads to low dimension, branched structures. The process of coagulation is usually associated with sintering and coalescence of particles by Gibbs-Thompson maturing and through strong Van der Waals bonding of the particles. The result of coagulation is then usually considered to be a solid three-dimensional particle. Agglomeration of a particle is similar in concept to coagulation, but does not usually consider coalescence of the particles, so that an agglomerate may be broken down into the units from which it made. Conversely, a coagulated particle can not be broken down exactly into the sub-particles from

which it originated. The time rate of change of particle size distribution is of primary interest to soot and other gas phase growth. To generalise, we can consider two particles, with volumes, v_i and v_j. The rate of collision between i and j particles is N_{ij}. For spherical particles, each diameter of particles has a unique volume. The collision of two particles leads immediately to the growth of a new particle with the summed volume of the two contributing particles. The concentration of particles "i" is n_i and that of "j" is n_j. We can define the collision frequency function, β_{ij}, by:-

$$N_{ij} = \beta_{ij}(v_i, v_j, T, P, etc.)n_i n_j \tag{5.1}$$

For one such collision, a new particle, "k", is formed of volume $v_k = v_i + v_j$. The rate of formation of "k" particles is therefore:-

$$\frac{1}{2}\sum_{i+j=k} N_{ij} \tag{5.2}$$

The rate of loss of particles "k" due to collision with other particles is:-

$$\sum_{i=1}^{\infty} N_{ik} \tag{5.3}$$

resulting in:-

$$\frac{dn_k}{dt} = \frac{1}{2}\sum_{i+j=k} N_{ij} - \sum_{i=1}^{\infty} N_{ik} = \frac{1}{2}\sum_{i+j=k} \beta(v_i, v_j)n_i n_j - n_k \sum_{i=1}^{\infty} \beta(v_i, v_k)n_i \tag{5.4}$$

Coagulation of soot is considered here in its simplest form by thermal coagulation of monodisperse spherical particles. The assumption is made that particles adhere at every collision and initially the particle size changes slowly. This theory is better known eponymously as "Smoluchowski Coagulation" [48] after the person who developed the original theory.

Surface Growth

Once soot particles are formed through the inception process, they grow by collision coagulation and surface growth. Of greatest significance to the final soot mass is the surface growth mechanism. This is where deposition of hydrocarbon compounds occurs at the surface of the soot particle.

Oxidation

Soot oxidation takes place in the reaction zone, when the formation processes are largely complete. Oxidation of soot leads to to visible radiative emission from the incandescent particles. The most widely used model for soot oxidation is that of Nagle and Strickland [98]. However, criticisms of this approach include applicability - their investigations were concerned with pyrographite which differs in composition to soot, also with their neglect of oxidation via OH attack to which Fenimore and Jones concluded from their experiments as being the most important.

5.4 Soot formation modelling

Perhaps the simplest approach would be to incorporate an assumed conversion of fuel carbon to soot, for which the production rate of the soot mass concentration M_s may be calculated from the one equation form:

$$\frac{dM_s}{dt} = A\kappa \tag{5.5}$$

where κ is the rate of combustion and A is the prescribed conversion factor.

This approach has the advantage of being relatively simple to implement, although the shortcomings are obvious due to the inability to infer dependencies on other processes which occur in a compartment fire.

The soot formation model used in this research is based on a two-equation model of soot production which is described by two parameters, namely the number density of soot particles and the soot volume fraction. This type of model has been developed by Moss and co-workers for both laminar and turbulent diffusion flames [99], [100], [101] et al. The general approach has been presented in [100]. The models consider the processes which occur during the formation of soot, that is particle nucleation, coagulation, surface growth and oxidation as described previously. The mean production rate of particle number density is described by:

$$\frac{d}{dt}\left(\frac{N}{N_A}\right) = C_\alpha \rho^2 X_{HC} T^{0.5} e^{\frac{-T_\alpha}{T}} - C_\beta T^{0.5}\left(\frac{N}{N_A}\right)^2 \tag{5.6}$$

where N_A is Avogadro's number, C_α and C_β are model constants, X_{HC} is the mole fraction of a hydrocarbon pre-cursor - taken in this case to be Acetylene (see figure 5.1 for state relationship plot), and T_α is the activation temperature of the nucleation reaction. The first term on the right hand side represents the creation of particles by nucleation and the second term the reduction in number density due to coagulation.

The formation of additional soot mass is assumed to take place through heterogeneous surface growth processes. Soot nuclei are assigned an initial mass 144 kg $kmol^{-1}$, corresponding to 12 atoms. The level is not dependent on this initial mass, but a non-negative number is required in order to initiate the process of nucleation.

The balance equation for soot mass concentration is:-

$$\frac{d}{dt}\left(\rho_{soot} f_v\right) = 144 C_\alpha \rho^2 X_{HC} T^{\frac{1}{2}} e^{\frac{-T_\alpha}{T}} + C_\gamma \rho X_{HC} T^{\frac{1}{2}} e^{\frac{-T_\gamma}{T}} N \tag{5.7}$$

The first term on the right hand side of this expression represents the creation of particles due to nucleation, the second term represents the addition of mass due to the processes of surface growth. The soot particle diameter can then be estimated by:

$$d_p = \left(\frac{6f_v}{N\pi}\right)^{\frac{1}{3}} \tag{5.8}$$

The particle diameter of soot allows a surface area dependent term for oxidation to be incorporated. The rate of destruction of soot mass is then given by:

$$\frac{d}{dt}(\rho_{soot} f_v) = -\left(\frac{36\pi}{\rho_{soot}^2}\right)^{\frac{1}{3}} n^{\frac{1}{3}} (\rho_{soot} f_v)^{\frac{2}{3}} \omega_{ox} \tag{5.9}$$

where ω_{ox} is the specific oxidation rate given by Fenimore and Jones [102]:

$$\omega_{ox} = 1.27 \times 10^3 \Gamma p_{OH} T^{-\frac{1}{2}} \tag{5.10}$$

p_{OH} is the partial pressure of the OH radical and Γ is the collisional efficiency which is taken to be 0.2 in line with the value suggested in reference [103].

Figures 5.2 to 5.13 clearly show the sensitivity of each stage in the formation of soot to the parameters of mixture fraction, mixture fraction variance - and to temperature.

5.5 Combustion

Two combustion models are available in SOFIE, the popular "industrial standard" Eddy-Break-up (EBU) model, originating from the works of Spalding [104],[105] and subsequently developed by Magnussen and Hjertager [106] and the relatively more detailed laminar flamelet combustion model, which views a turbulent flame as an ensemble of thin locally one-dimensional structures embedded within the turbulent flow-field.

The Eddy break-up model assumes combustion is fast and therefore turbulent mixing is rate controlling, together with a one-step description of stoichiometric hydrocarbon combustion.

A single transport equation for fuel mass fraction is solved with the source term taking the slowest rate of fuel, oxygen and product dissipation as the reaction rate of fuel, R_f:-

$$\overline{R}_f = C_{r1}\overline{\rho}\frac{\varepsilon}{k}\min(\tilde{Y}_f, \frac{\tilde{Y}_o}{s}, C_{r2}\frac{\tilde{Y}_p}{1+s}) \tag{5.11}$$

Where k is the turbulent kinetic energy and ε is the rate of dissipation of k. The EBU constants C_{r1} and C_{r2} usually take the values of 4.0 and 0.5 respectively. Y_f, Y_o and Y_p are mass fractions of fuel, oxygen and products respectively.

One of the major disadvantages to the use of the eddy-breakup model is the inability to consider chemical reaction rates, which vary considerably with temperature through Arrhenius expressions. In addition, linear relationships are assumed between mixture fraction, mass fractions and temperature. This assumption may be adequate for methane which has a somewhat unique linear enthalpy relationship, but for other hydrocarbon fuels of interest to this study, this may lead to significant errors.

From an experimental point of view, Bilger [107] investigated the applicability of using this type of global mechanism to reproduce experimental data for both methane and heptane laminar diffusion flames. It was shown that the species composition measurements in the heptane flame were far from equilibrium, particularly on the rich side of the flame.

One of the main obstacles in employing detailed chemical kinetics in the modelling and simulation of turbulent reacting flows is the additional difficulty and computational expense involved in solving the reacting species transport equations. In particular, the stiffness inherent in the chemical source terms and the uncertainties in the assumed chemical mechanism used, whether reduced or full, pose serious challenges. The laminar flamelet state relationship approach counteracts these difficulties with measurements of major gaseous species concentrations, albeit in a laminar flame, and the effects of turbulence are relegated to the determination of the instantaneous mixture fraction. Simplification is therefore introduced through reducing the problem to that of turbulent mixing. Experimental observations have shown that measurements of scalar properties in laminar diffusion flames result in universal correlations as a function of mixture fraction (which is a normalized fraction of the fuel to oxygen ratio), in regions remote from

flame extinction [108], [109]. The mixture fraction correlation for heptane being particularly good for the major species of O_2, C_7H_{16} and CO_2. These state relationships have been shown to be independent of local length scales and low flame stretch situations (of which fire is an example), even for non-equilibrium conditions. This then provides validity for the use of the alternative laminar flamelet combustion model, although it is recognized that some workers [110] have found prediction of both major and minor species to be poor using this model.

The following chapter seeks to make a representation of the underlying chemical aspect of heptane combustion in a well/under ventilated compartment fire in reference to the flamelet library created specifically for this study.

5.6 Time averaging, closure, and turbulence modelling

Favre (density weighted) averaging is superior to Reynolds averaging in calculations involving variable density flows [111] and it is the prediction of Favre mixture fraction mean and variance that permits a presumed pdf to be computed via a beta function.

$$\widetilde{P}(\xi) = \frac{\xi^{\alpha-1}(1-\xi)^{\beta-1}}{\int_0^1 \xi^{\alpha-1}(1-\xi)^{\beta-1}d\xi}$$

where the parameters α and β are defined in terms of the mean mixture fraction and variance,

$$\alpha = \left[\widetilde{\xi}\frac{\widetilde{\xi}(1-\widetilde{\xi})}{\widetilde{\xi''^2} - 1}\right)$$

and

$$\beta = (1-\widetilde{\xi})\left[\frac{\widetilde{\xi}(1-\widetilde{\xi})}{\widetilde{\xi''^2} - 1)}\right]$$

The mean species composition (m_i) can therefore be evaluated as:

$$\widetilde{m}_i = \overline{\rho} \int_0^1 \frac{m_i(\xi)}{\rho(\xi)} \widetilde{P}(\xi) d\xi$$

Among the principal difficulties in modelling the structure and dynamics of fluid turbulence is the wide range of length and time scales over which variations occur. This is the case in the velocity field as well as in the concentration fields of dynamically passive conserved scalar quantities mixed in the flow. Attempts to simplify the description of these turbulence fields on the basis of dynamical self-similarity assumptions date back as far as Kolmogorov [112], Taylor [113] and Richardson [114].

Because the distance between grid points in finite-volume approximation is generally not sufficient to resolve all the turbulent length scales and because of the steady-state assumption often used in flow simulations, auxiliary relationships are required to account for the effects of turbulence on the transport processes. These relationships are developed by dividing the instantaneous properties in the conservation equations into mean and fluctuating components.

Richardson [114] succinctly summarized the idea of an energy cascade in turbulent free shear flows:

"Big whorls have little whorls,

Which feed on their velocity;

And little whorls have lesser whorls,

And so on to viscosity"

(in the molecular sense)

The notion behind the above poetic licence is that large eddies are unstable and disintegrate, transferring their energy to somewhat smaller eddies. The process continues and the energy is transferred to successively smaller eddies until the Reynolds number $Re(l) \equiv \frac{u(l)l}{\nu}$ is sufficiently small that the eddy motion is stable and the molecular vis-

cosity is effective in dissipating the kinetic energy. One of the main reasons that this hypothesis is important in the area of turbulence is that it places dissipation at the end of a sequence of processes. The *rate* of dissipation ε is determined, therefore, by the first process in the sequence, which is the transfer of energy from the largest eddies. Kolmogorov furthered this theory and introduced the smallest scales of turbulence to which his name is ascribed.

Turbulence is arguably one of the most difficult to replicate in non-linear physics. In turbulent combustion, the difficulties are further compounded by the complexities of chemical kinetics and the strong non-linear coupling of the turbulence and the chemistry. These *turbulence-chemistry* interactions arise from the fact that in most combustion systems, mixing is not fast compared with rates of chemical reaction, and large spatial and temporal variations in species composition and temperature are present. Chemical reaction rates cannot be evaluated from spatial or temporal mean values and are strongly coupled to molecular diffusion at the smallest scales of the turbulence. Furthermore, the heat release associated with combustion affects both the turbulent flow, by causing variations in the mean density field, and local expansion.

5.7 CHEMKIN

The laminar flamelet library used in the compartment fire simulations were computed using OPPDIF, which is part of the CHEMKIN package and computes the diffusion flame between two opposing nozzles (see figure 5.14). Assuming that the radial component of velocity is linear in radius, then the dependent variables become functions of the axial direction only. OPPDIF solves (amongst others) for temperature, and species mass fractions. The two-point boundary value problem for the steady-state form of the discretized equations are solved using a combination of Newtons method and time evolution to produce a converged solution.

The semi-empirical reaction mechanism employed in this research for n-Heptane oxi-

H	O	OH	H_2	O_2	H_2O	HO_2
H_2O_2	CO	CO_2	CH	HCO	CH_2	CH_2O
CH_3	CH_3O	CH_4	$HCCO$	CH_2CO	CH_3CO	CH_3HCO
C_2H	C_2H_2	C_2H_3	C_2H_4	C_2H_5	C_2H_6	C_3H_3
C_2H_3HCO	C_3H_4	C_3H_5	C_3H_6	C_4H_6	C_4H_8-1	C_5H_{10}
C_6H_6	C_6H_{10}	C_6H_{12}	C_7H_{16}	N_2	AR	

Table 5.1: Species contained in the Held reaction mechanism

dation and pyrolysis is that of Held *et al* [80]. The rationale behind the use of this mechanism is in its author's focus on quantitively capturing transient phenomena and, more importantly, intermediate species distributions. The mechanism involves 41 species (see table 5.1) and 274 reactions and although it has no direct relevance to the modelling approach used in this research, it does mean that it is sufficiently compact to be used in combined fluid-mechanical/ chemical kinetic computational studies. Validation of the mechanism is by comparisons with literature stirred reactor data and for higher temperature regimes (>1150K) with shock tube ignition delay and premixed laminar flame speed values. Its development is also supported by a series of variable-pressure flow reactor experiments.

The transformation from physical space to mixture fraction space eliminates the convection terms in the balance equations under the conditions that the Lewis numbers of all species are unity. This assumption is valid for hydrocarbon flames. Furthermore, if the boundary conditions are independent of the velocity field, the scalar flame structure may be analysed in mixture fraction space independently of the specific flow configuration. A counter-flow diffusion flame can therefore be entirely mapped onto mixture fraction space.

State relationships for species concentration of C_7H_{16}, CO_2, CO, O_2 and H_2O (see figure 5.15 for state relationship plot - the adiabatic flamelet has been chosen, merely because the species mole fraction is independent of the radiative loss term), total enthalpy, temperature, density and soot source terms are calculated using OPPDIF. These are then integrated directly in SOFIE - prior to the field model solution, to compute

look-up tables (collectively known as the flamelet library) of the integrand in terms of mean mixture fraction and variance. Favre averaging requires each parameter identified in the look-up tables to be divided by density, thus necessitating the inclusion of mixture density look-up values to aid consistency.

Figure 5.16 is taken from Yang, Hamins and Kashiwagi [1], which shows the effect of scale on radiative heat loss and combustion efficiency. The figure shows that a radiative loss of between 30% and 40% is reasonable for the burner diameters used in this research. Therefore, in order to account for this radiative loss, a fraction of sensible enthalpy is subtracted from the total enthalpy to provide an equivalent radiative loss in the range from adiabatic to 40% loss in increments of 5%.

Together, figures 5.17 and 5.18 and 5.19 show plots of flamelet temperature divided by density against mixture fraction and mixture fraction variance. The figures show that temperature peaks at a mixture fraction close to stoichiometric, although the absolute temperature value is somewhat lower than that predicted from equilibrium calculations. It can also be clearly seen that the temperature drops with an increase in variance as a result of a higher level of unmixedness.

Figure 5.20 illustrates the effect of the introduction of the radiative loss constraint on enthalpy - each constituent part representing a particular radiative loss, which converges as the mixture fraction limit of 1 representing 'pure' fuel is approached.

The pool-fire was fixed at its liquid boiling point (371K for C_7H_{16}) and therefore for the density to be consistent at the fuel inlet, it was necessary to incorporate a secondary flamelet library explicitly setting the initial mixture fraction of 1 to correspond with the enforced elevated temperature of 371K.

For each flamelet it would be possible to include an additional dimension, i.e that which is not necessarily confined only to the level of radiative loss. One approach could be the adoption of vitiation level as a second additional degree of freedom. However, this is an unnecessary elaboration in this research, as the compartment fires investigated through experimental and computational means pertain to well-ventilated fires only. That is,

with the exception of a very small number of experiments with a severely restricted doorwidth.

5.8 Plug flow calculations

Plug flow reactions were performed using the "PLUG" program from the Chemkin suite. PLUG simulates the non-dispersive one-dimensional flow of a chemically reacting ideal gas mixture in a conduit of essentially arbitrary geometry (a plug flow chemical reactor.)

The reaction mechanism used was identical to that used in the flamelet calculations using SOFIE. The temperatures and species distributions for the plug flow calculations chosen were based on the relatively narrow sooting range for hydrocarbon fuels. Therefore, three initial temperatures of 1000K, 1178K and 1480K and the relevant species concentrations at that temperature were used as the initial conditions. These temperatures are also representative of upper layer temperatures in compartment fires as reported in the literature. The temperature at 1480K corresponded to the maximum yield of C_2H_2 as determined in the laminar flamelet calculations and as such represents the worst case scenario.

These simulations are representative of upper layer dynamics, where the flame plume is quenched upon entry to the upper layer, which is largely isothermal, and further reaction continues in a premixed mode, in the absence of additional mixing with oxidizer. Results for species mole fraction of C_2H_2 and OH are shown due to their integral role in the soot model used in the CFD prediction, shown over a time period typical of flame soot residence times. The summary of the results of these simulations can be seen in Figures 5.21-5.23. In addition, due to the close coupling of soot and CO formation, results are also presented in figure 5.24 for mole fraction of CO at all three temperatures, demonstrating that the rate of CO production is enhanced at temperatures greater than 1178K.

It is interesting to note the differences in behaviour of the parameters that influence

the competing processes that occur in soot formation, namely nucleation and surface growth against oxidation, at the three given temperatures. These calculations once again highlight the sensitivity of soot production to temperature.

Table 5.2 shows the peak species mole fraction of C_2H_2 and OH and the time taken to decrease to 50% of the peak concentration (T50). Here we can see that at 1000K there is a sharp fall off rate for OH, whereas C_2H_2 declines steadily reaching its T50 after 0.68s. At 1178K we can see a dramatic increase in the peak level of OH of order 15 times that of the level at 1000K. The time taken to decrease to 50% of the initial concentration has correspondingly increased and is greater than the time-scale considered here. The level of C_2H_2 at 1178K remains similar to that achieved at 1000K, although the T50 has also increased and once again is greater than the time-scale considered here.

As anticipated, the largest impact of temperature on the levels of both C_2H_2 and OH occurs at 1480K. At this temperature the peak level of OH has increased by three orders of magnitude and is actually seen to increase with time. The peak mole fraction C_2H_2 which is also seen to rise initially has increased by nearly 90% from the peak value at 1000K.

Temperature (K)	Peak C2H2	T50 C2H2 (s)	Peak OH	T50 OH (s)
1000	3.15E-02	0.68	1.12E-10	0.02
1178	3.15E-02	>1.83	1.69E-09	>1.83
1480	5.88E-02	>1.83	3.77E-07	0.03

Table 5.2: Peak Mole Fraction and T50 of C_2H_2 and OH from plug-flow calculations

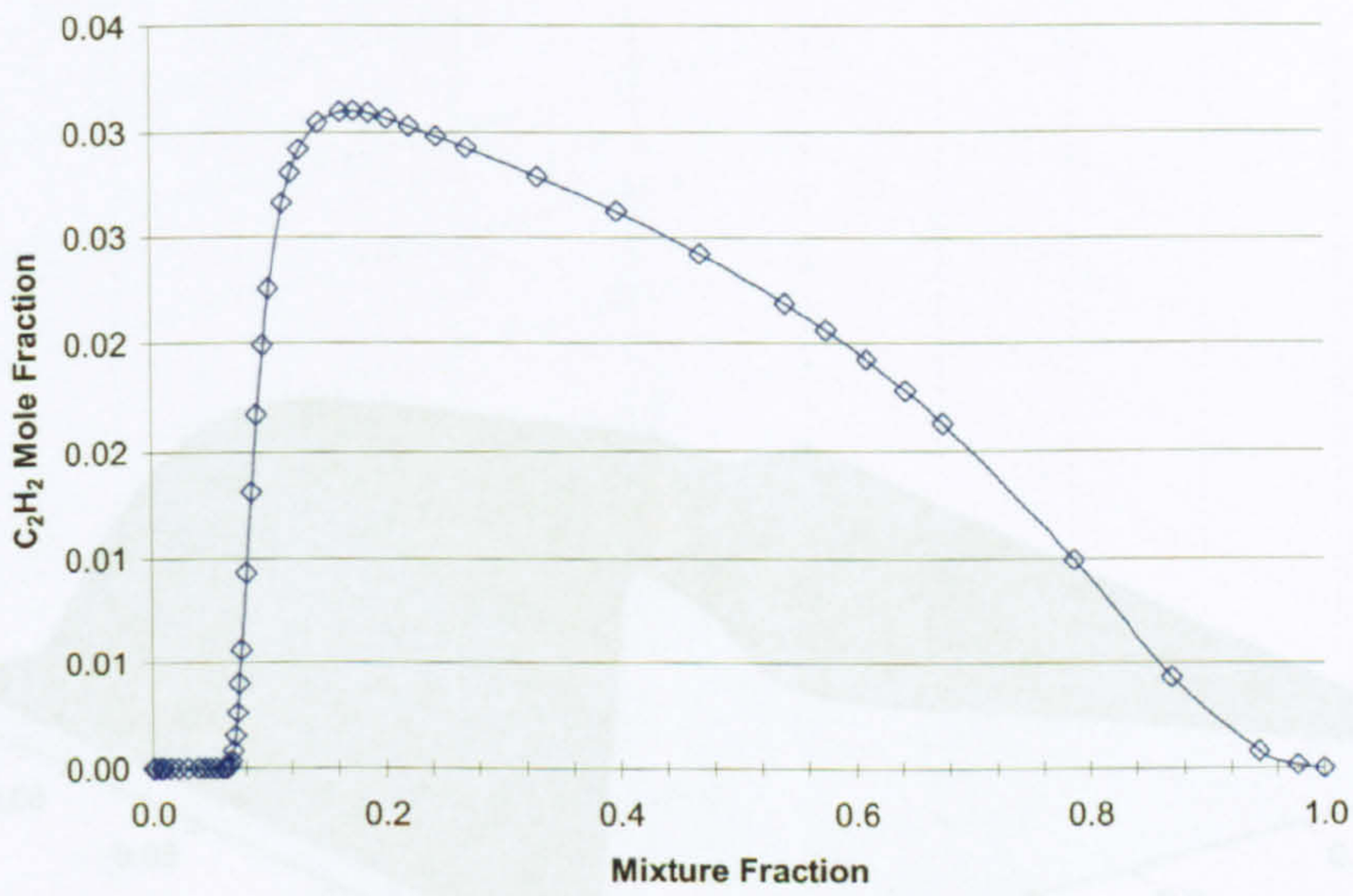

Figure 5.1: C_2H_2 mole fraction versus mixture fraction flamelet lookup 2-d plot.

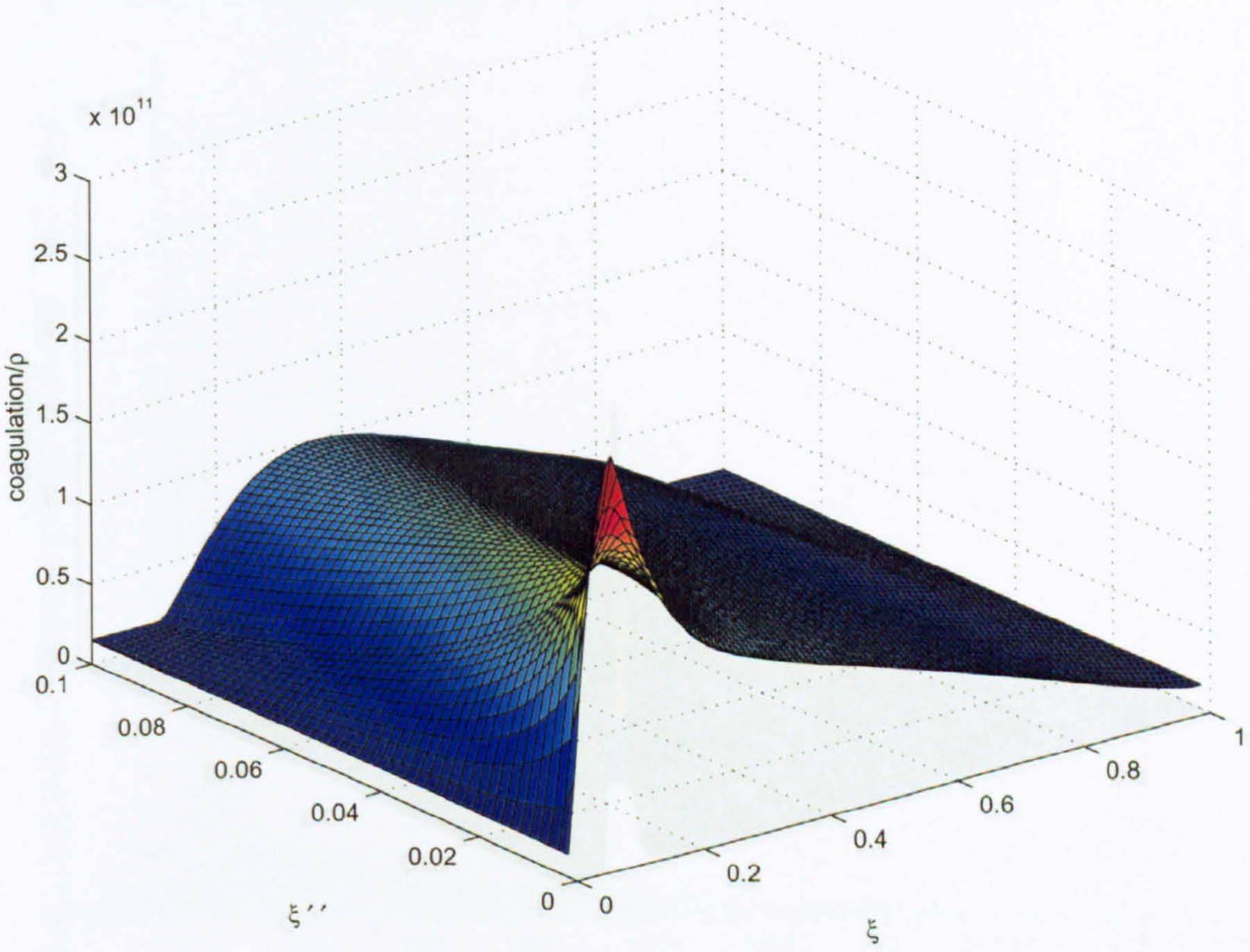

Figure 5.2: $\frac{Coagulation}{\rho}$ flamelet look-up 3-d surface plot; values integrated over mixture fraction and mixture fraction variance space.

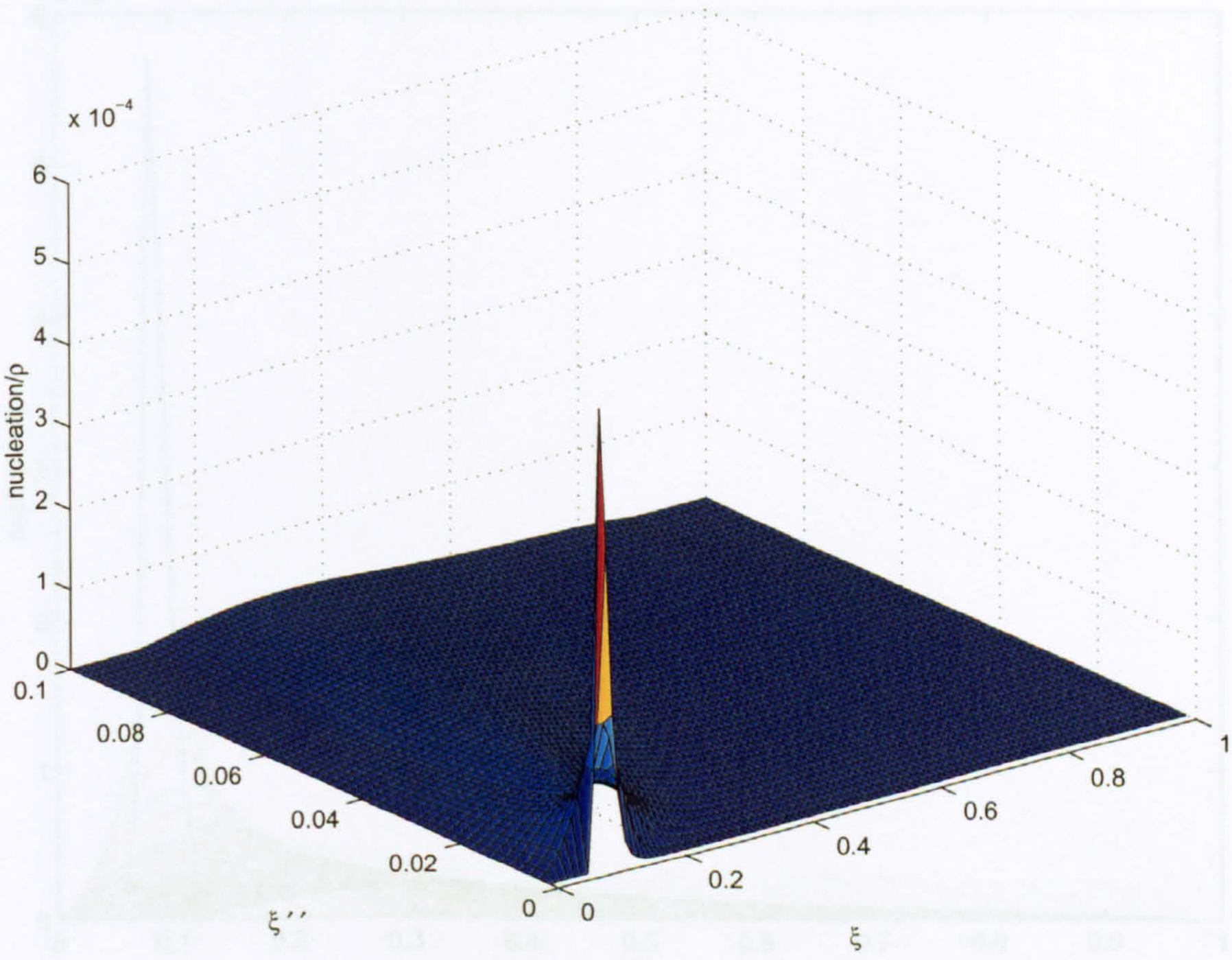

Figure 5.3: $\frac{Nucleation}{\rho}$ flamelet look-up 3-d surface plot; values integrated over mixture fraction and mixture fraction variance space.

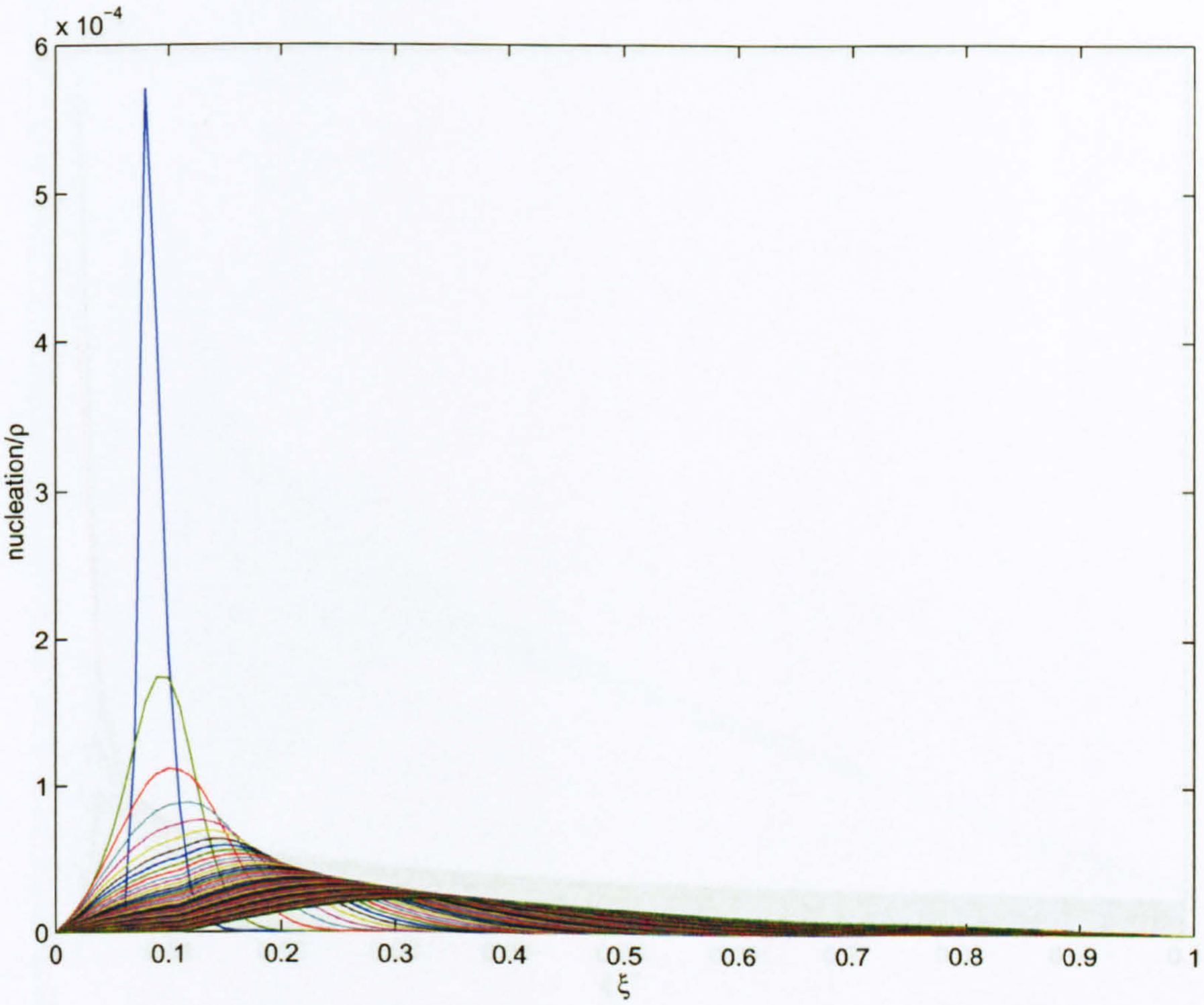

Figure 5.4: $\frac{Nucleation}{\rho}$ versus mixture fraction flamelet look-up 2d plot;

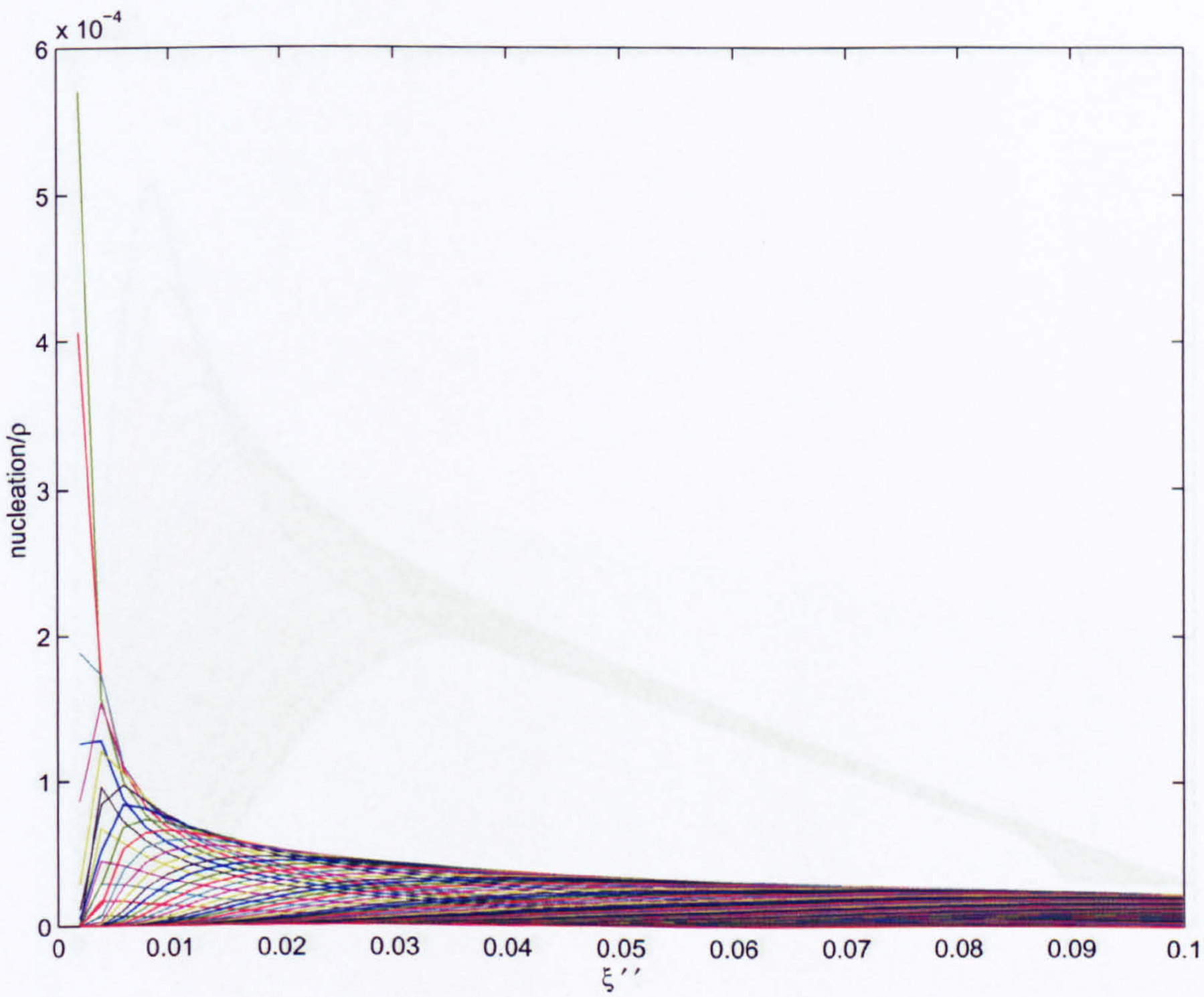

Figure 5.5: $\frac{Nucleation}{\rho}$ versus mixture fraction variance flamelet look-up 2d plot;

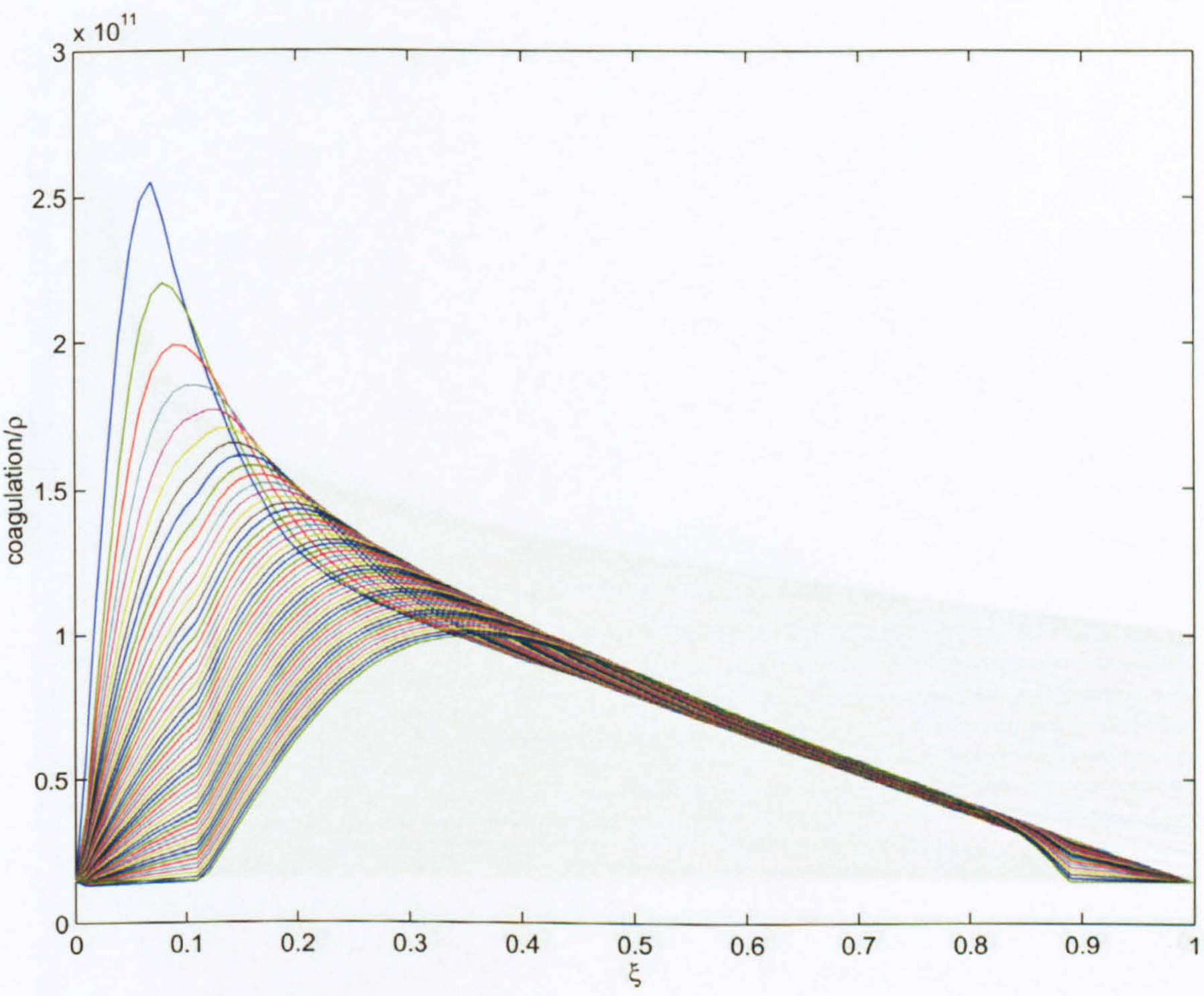

Figure 5.6: $\frac{Coagulation}{\rho}$ versus mixture fraction flamelet look-up 2d plot;

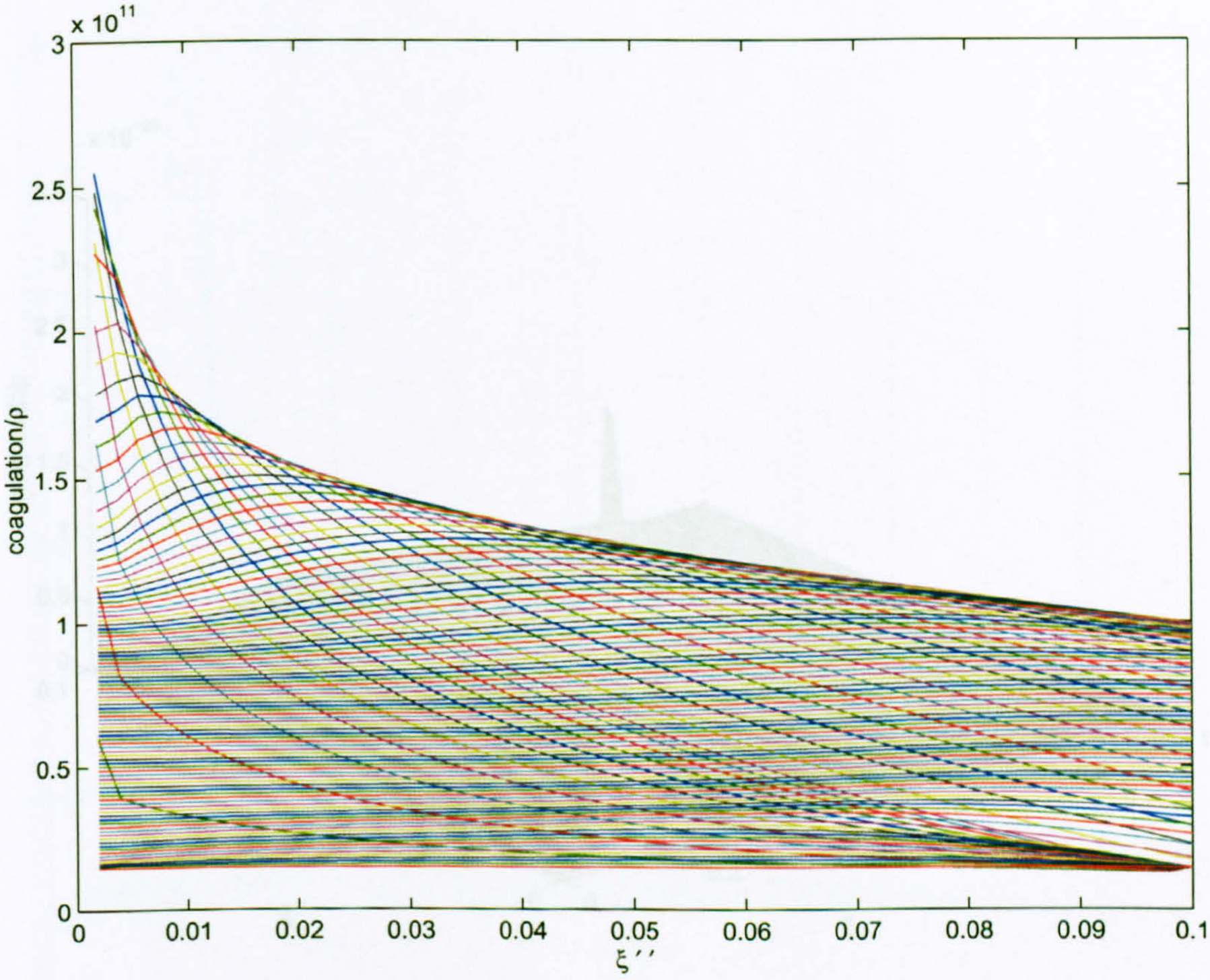

Figure 5.7: $\frac{Coagulation}{\rho}$ versus mixture fraction variance flamelet look-up 2d plot;

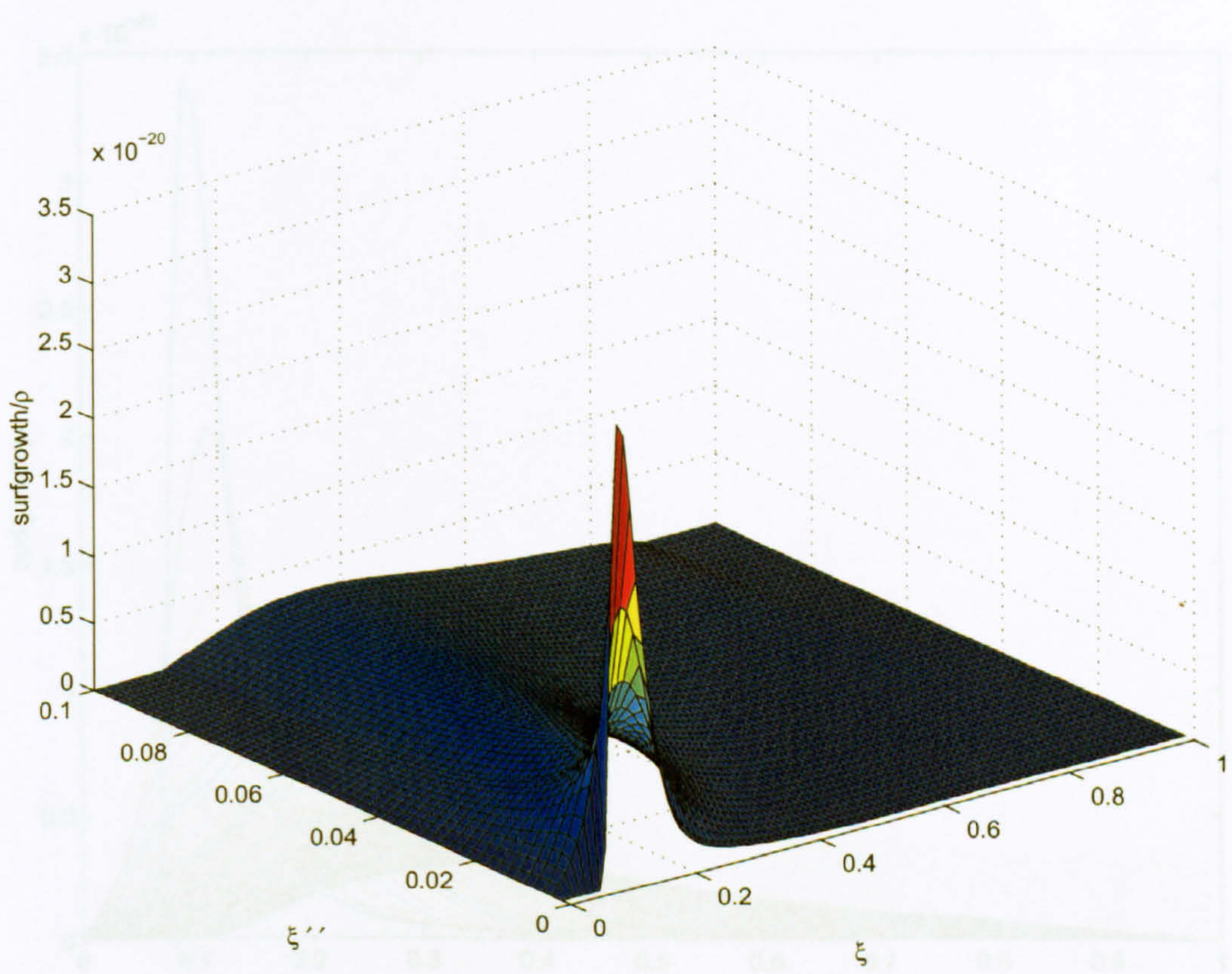

Figure 5.8: $\frac{SurfaceGrowth}{\rho}$ flamelet look-up 3-d surface plot; values integrated over mixture fraction and mixture fraction variance space.

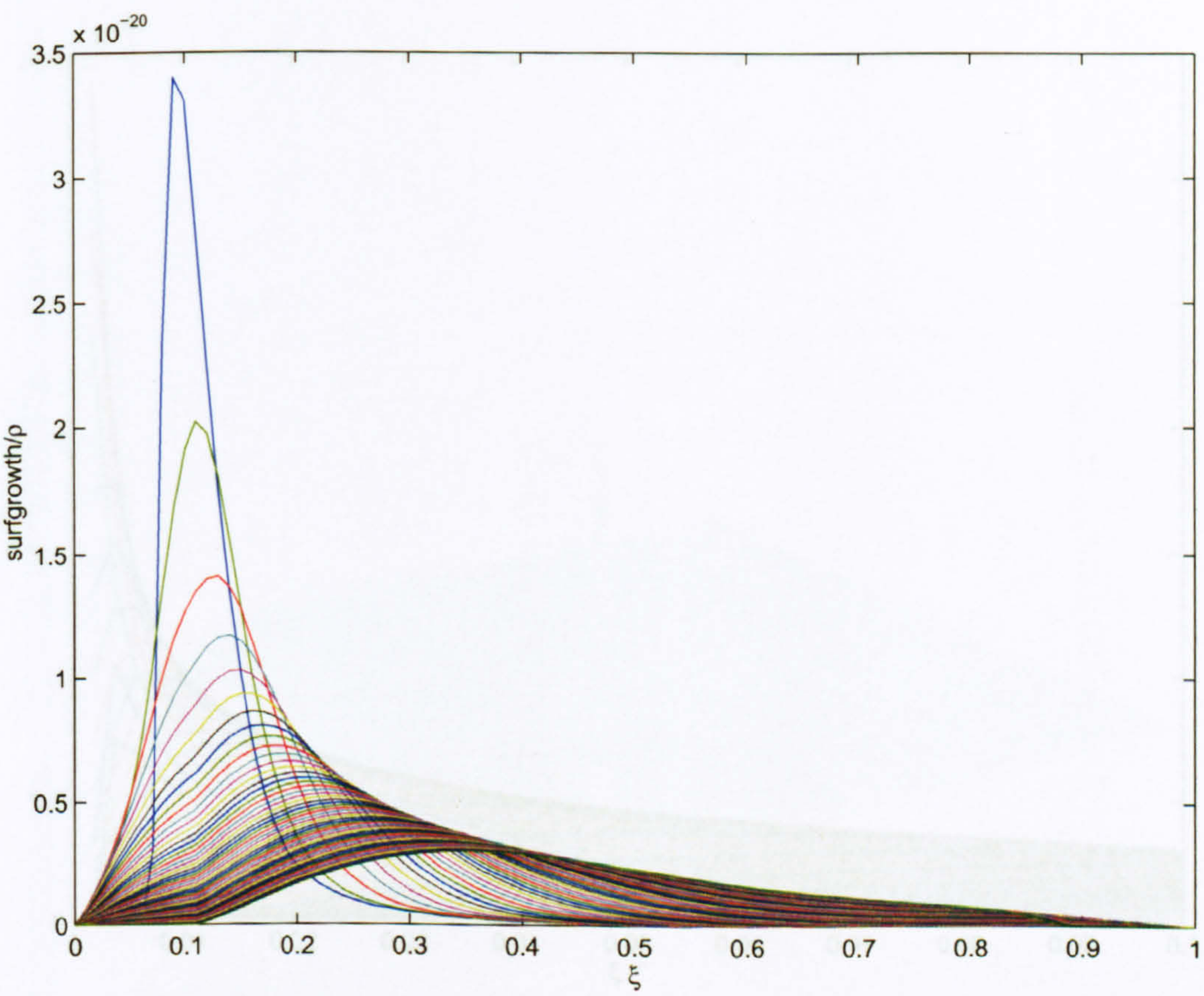

Figure 5.9: $\frac{SurfaceGrowth}{\rho}$ versus mixture fraction flamelet look-up 2d plot;

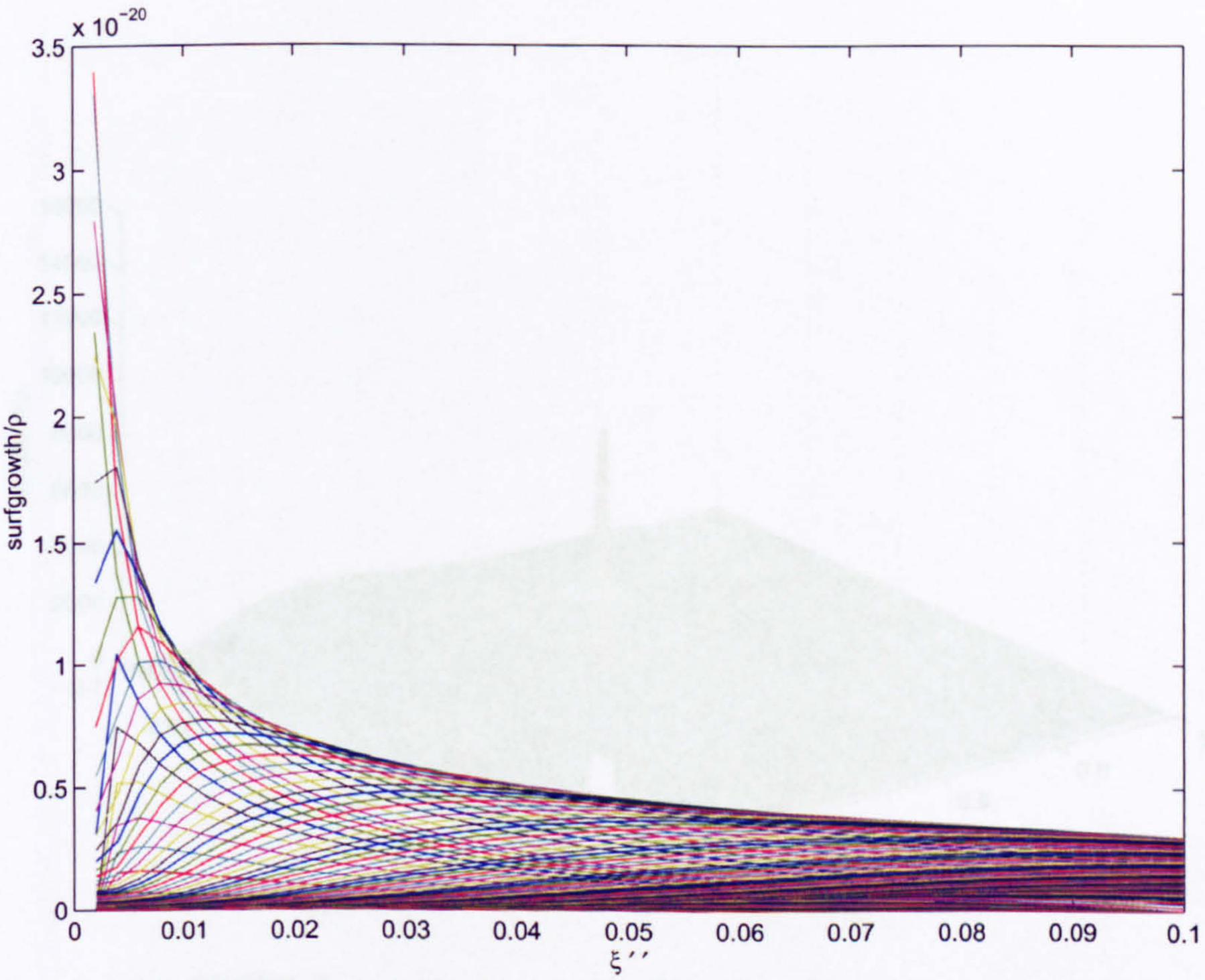

Figure 5.10: $\frac{SurfaceGrowth}{\rho}$ versus mixture fraction variance flamelet look-up 2d plot;

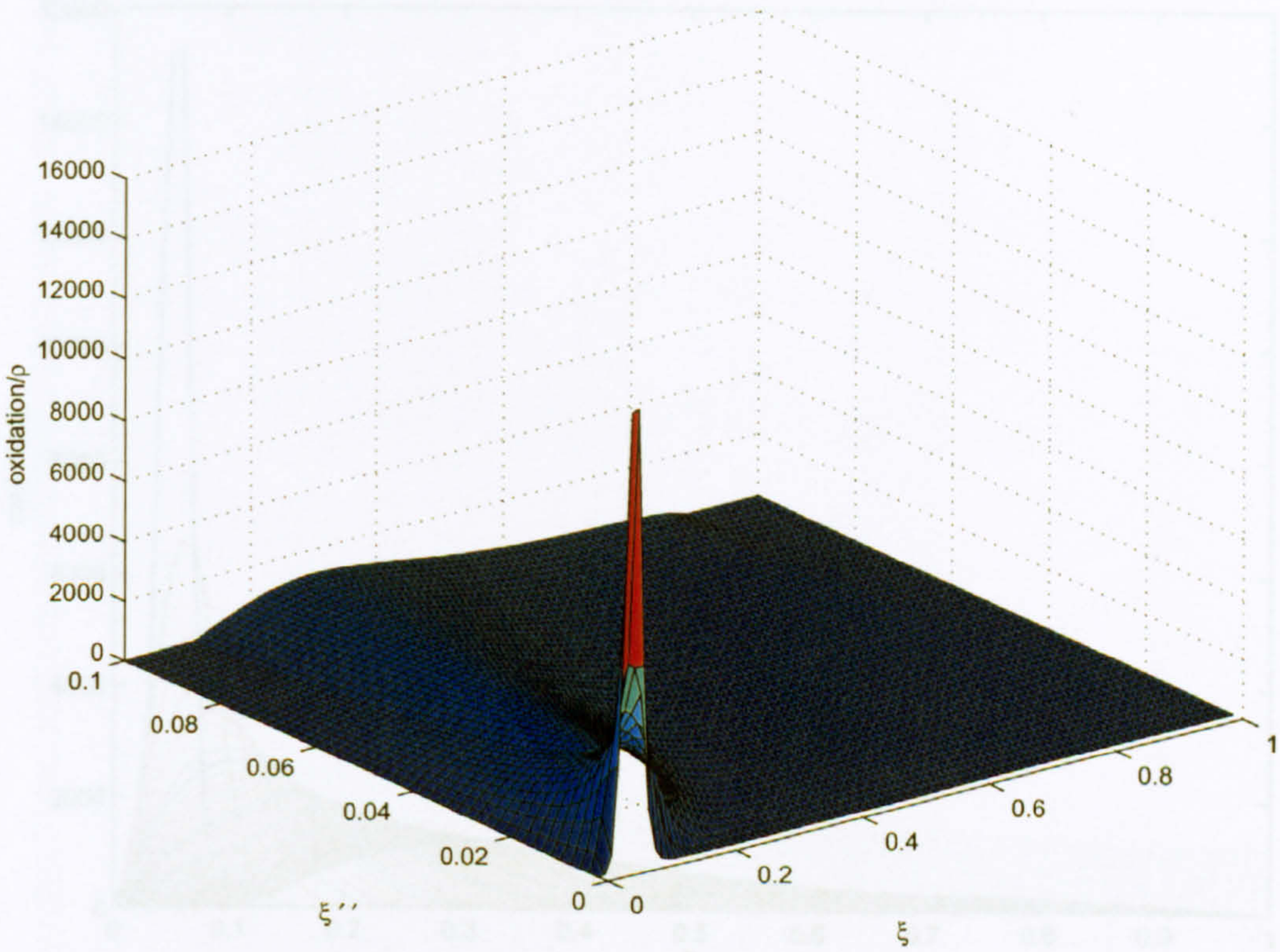

Figure 5.11: $\frac{Oxidation}{\rho}$ flamelet look-up 3-d surface plot; values integrated over mixture fraction and mixture fraction variance space.

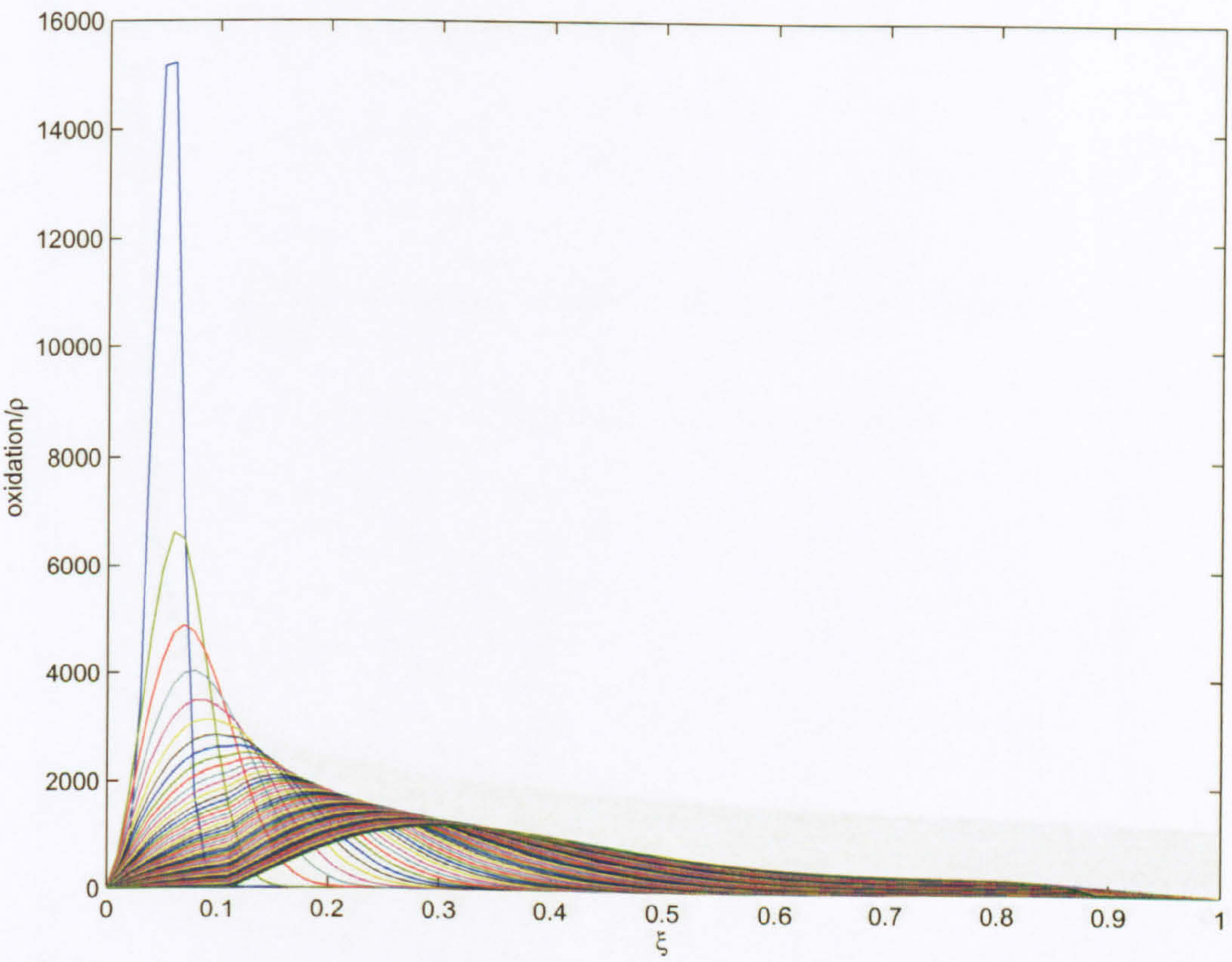

Figure 5.12: $\frac{Oxidation}{\rho}$ versus mixture fraction flamelet look-up 2d plot;

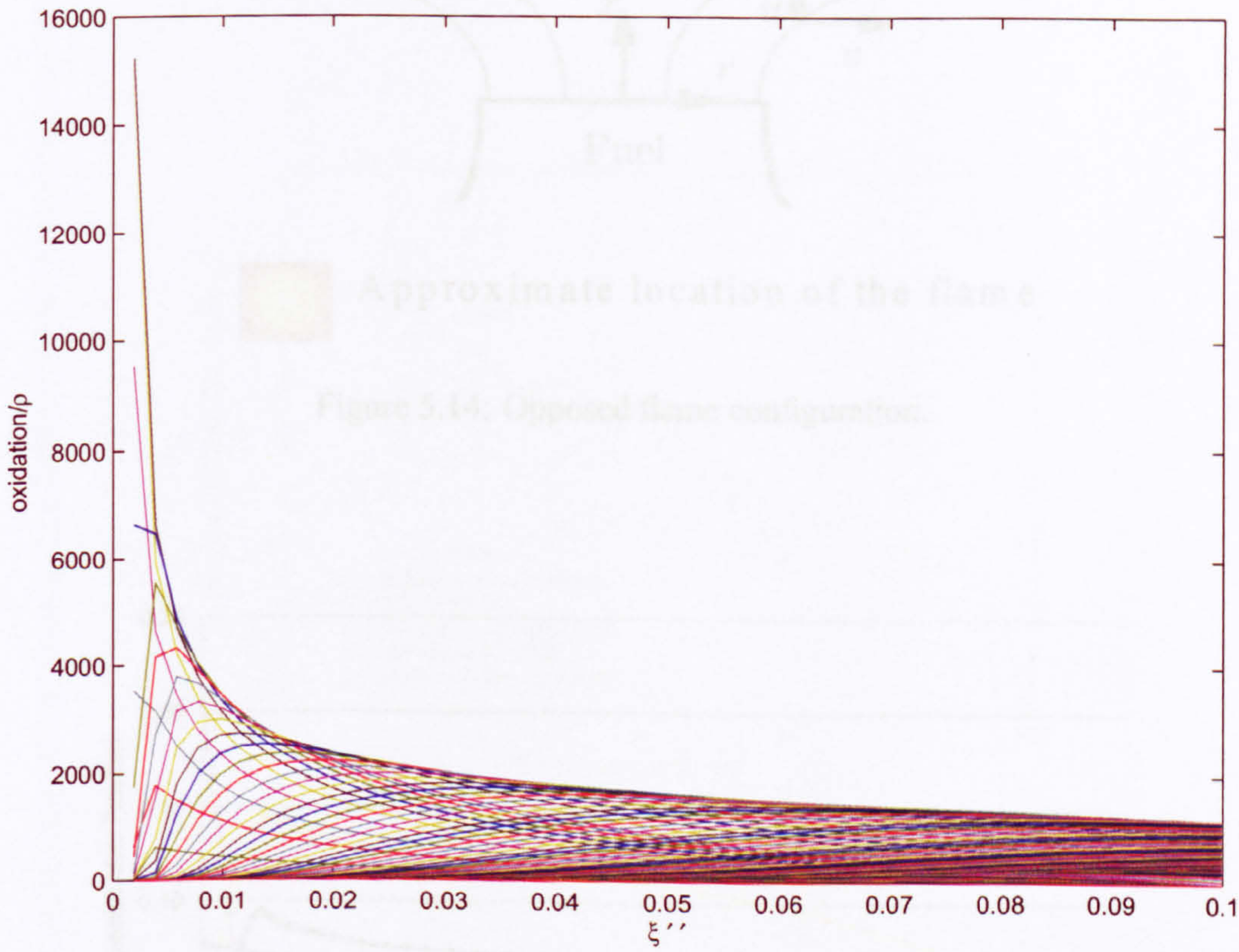

Figure 5.13: $\frac{Oxidation}{\rho}$ versus mixture fraction variance flamelet look-up 2d plot;

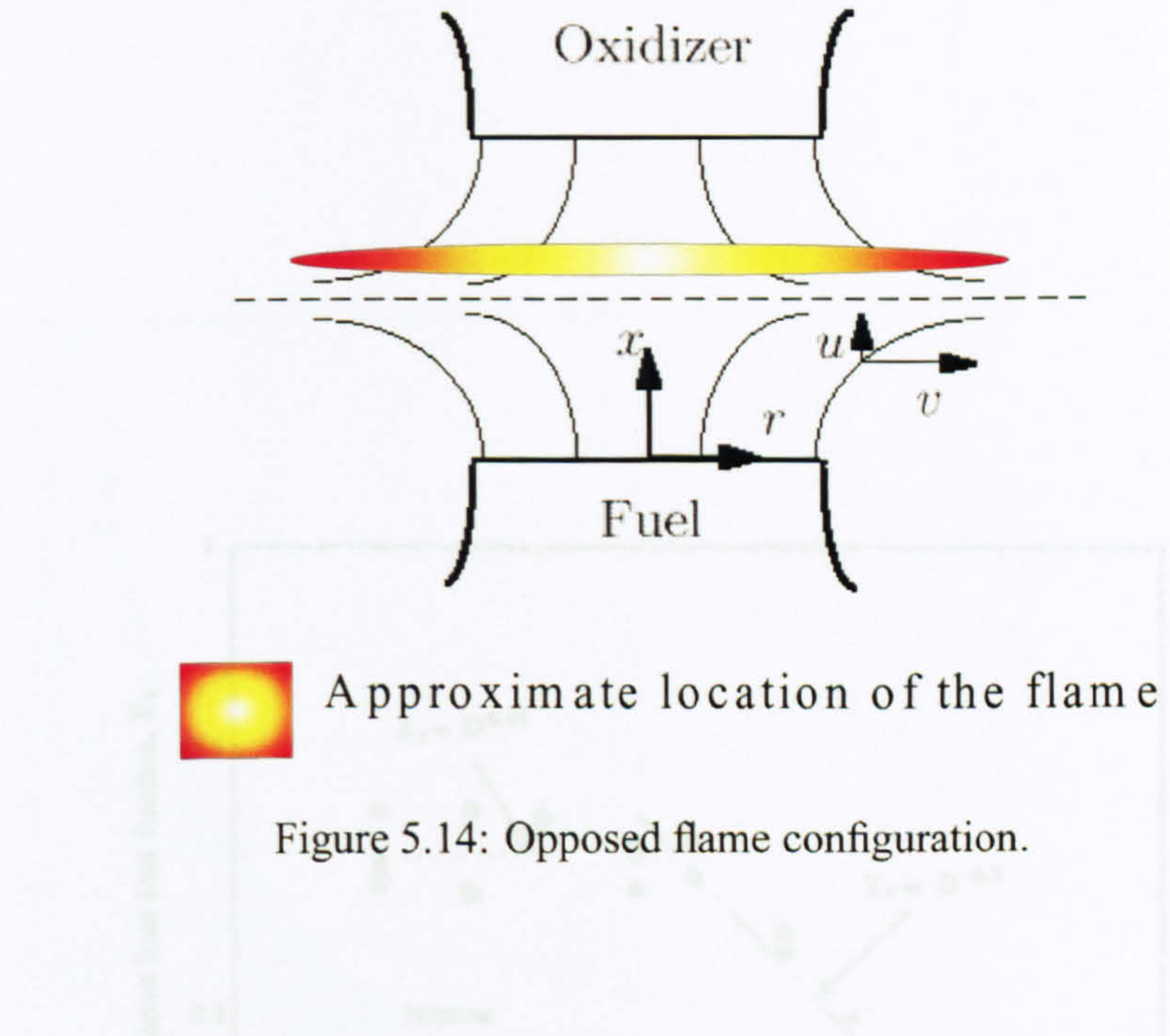

Figure 5.14: Opposed flame configuration.

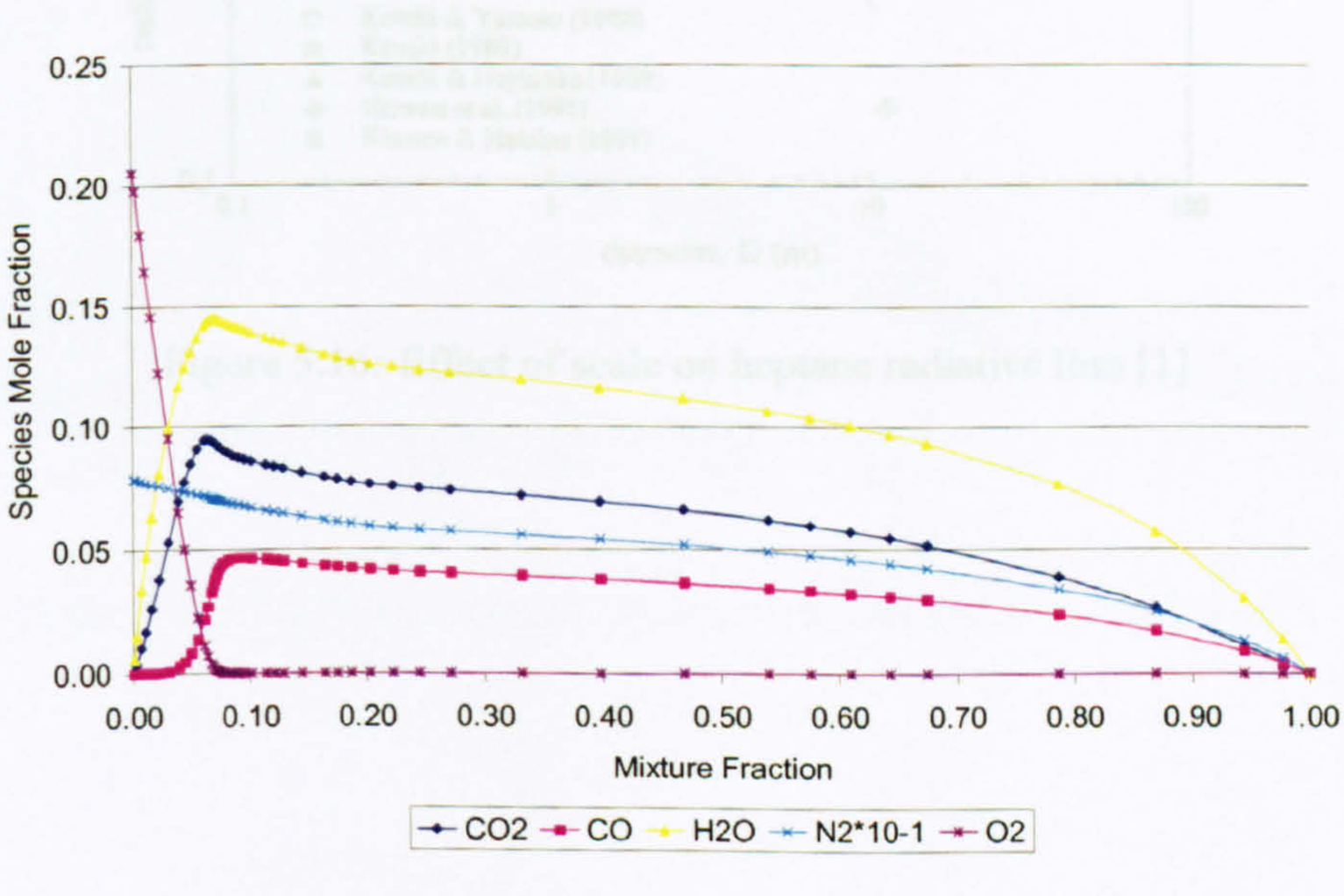

Figure 5.15: Species mole fraction versus mixture fraction flamelet look-up 2d plot; N_2 scaled for visualisation

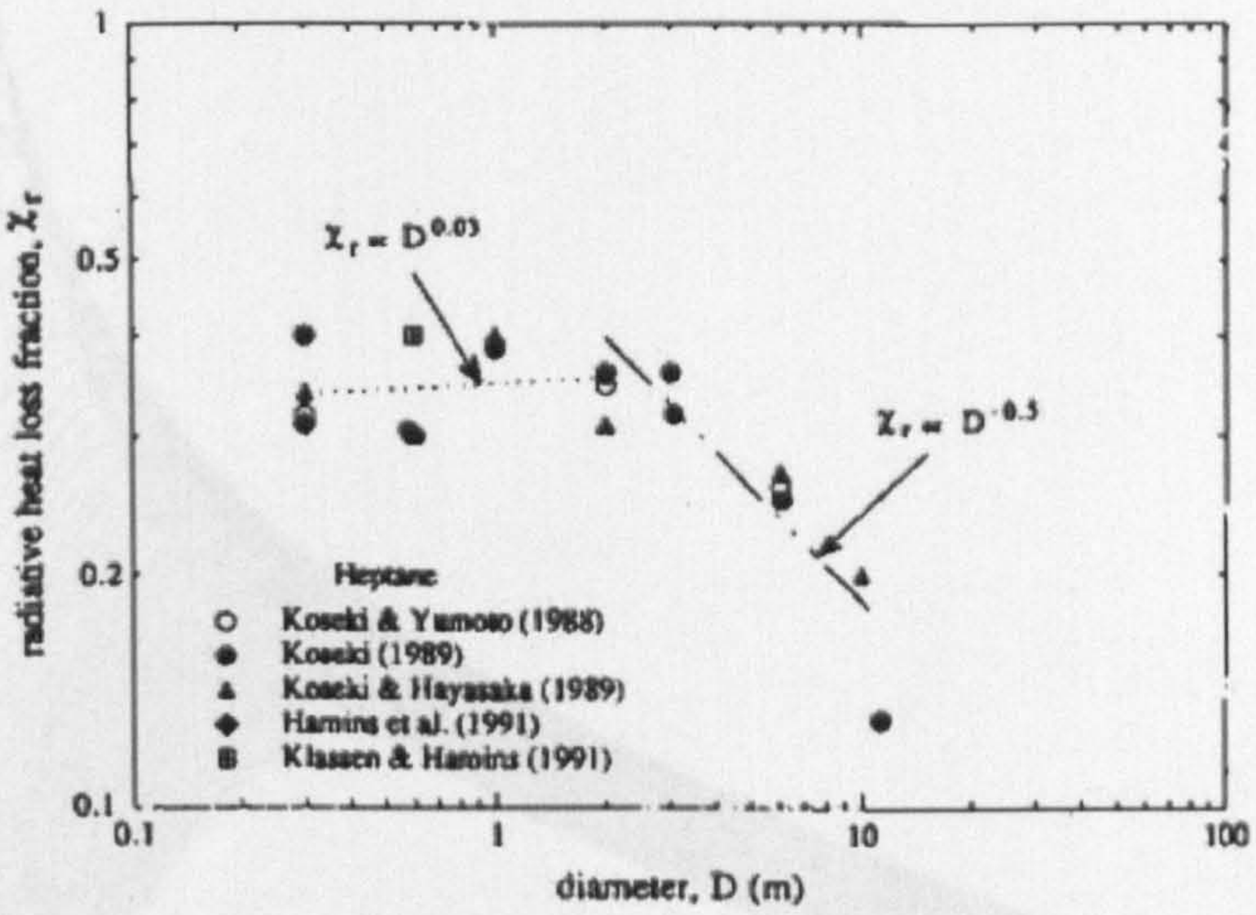

Figure 5.16: Effect of scale on heptane radiative loss [1]

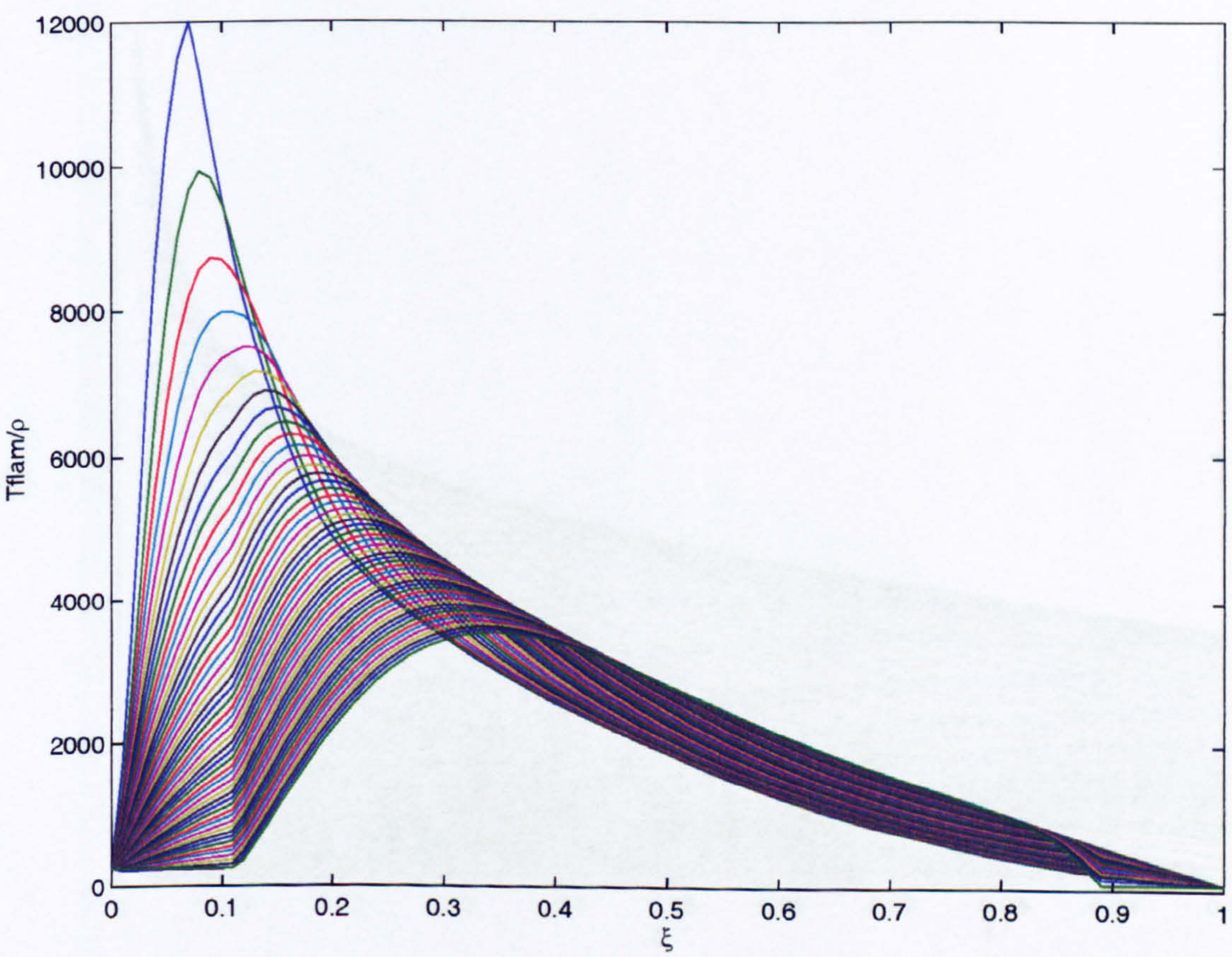

Figure 5.17: $\frac{Tflam}{\rho}$ versus mixture fraction flamelet look-up 2d plot;

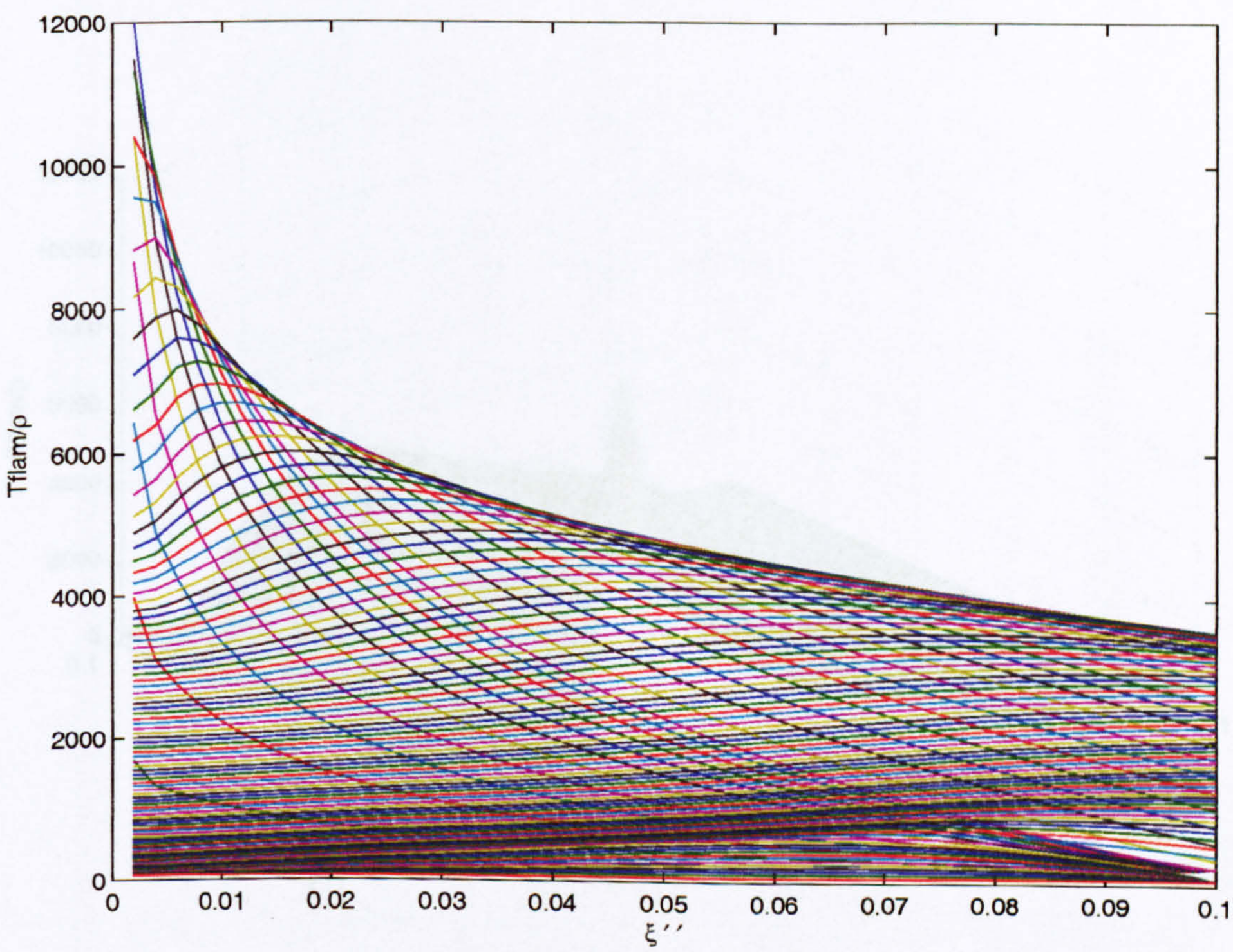

Figure 5.18: $\frac{Tflam}{\rho}$ versus mixture fraction variance flamelet look-up 2d plot;

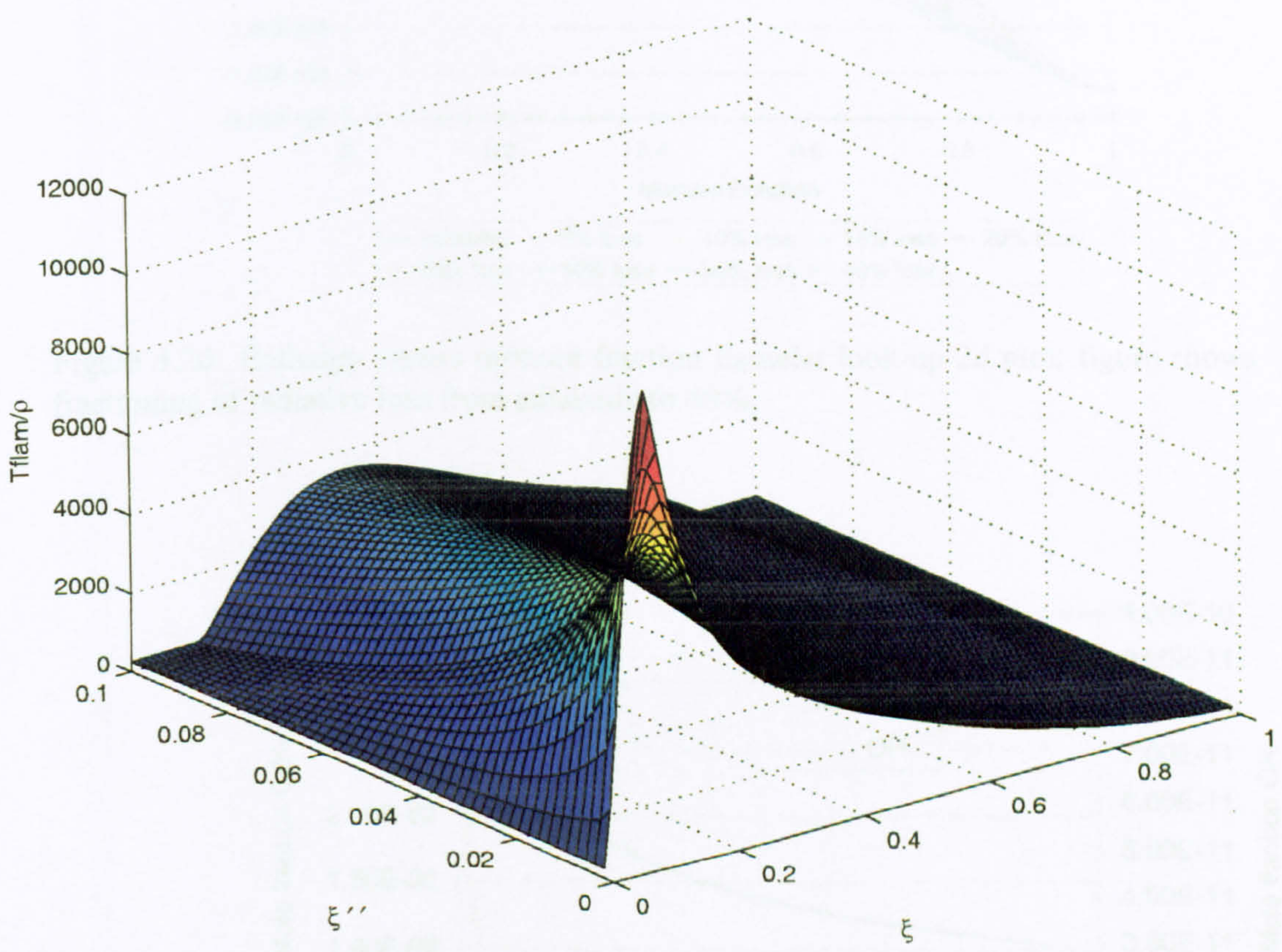

Figure 5.19: $\frac{Tflam}{\rho}$ flamelet look-up 3-d surface plot; values integrated over mixture fraction and mixture fraction variance space.

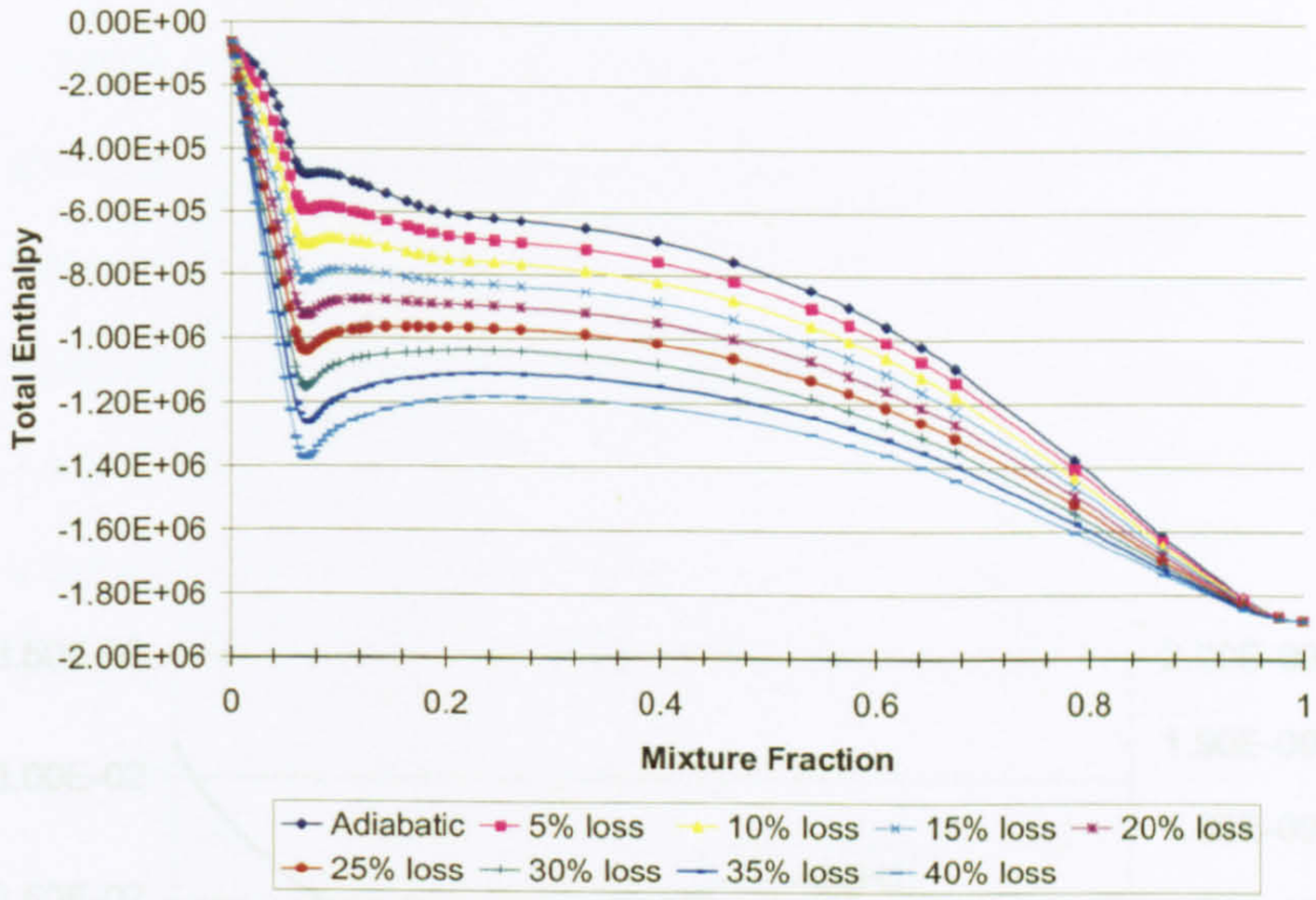

Figure 5.20: Enthalpy versus mixture fraction flamelet look-up 2d plot; figure shows fractioning of radiative loss from adiabatic to 40%.

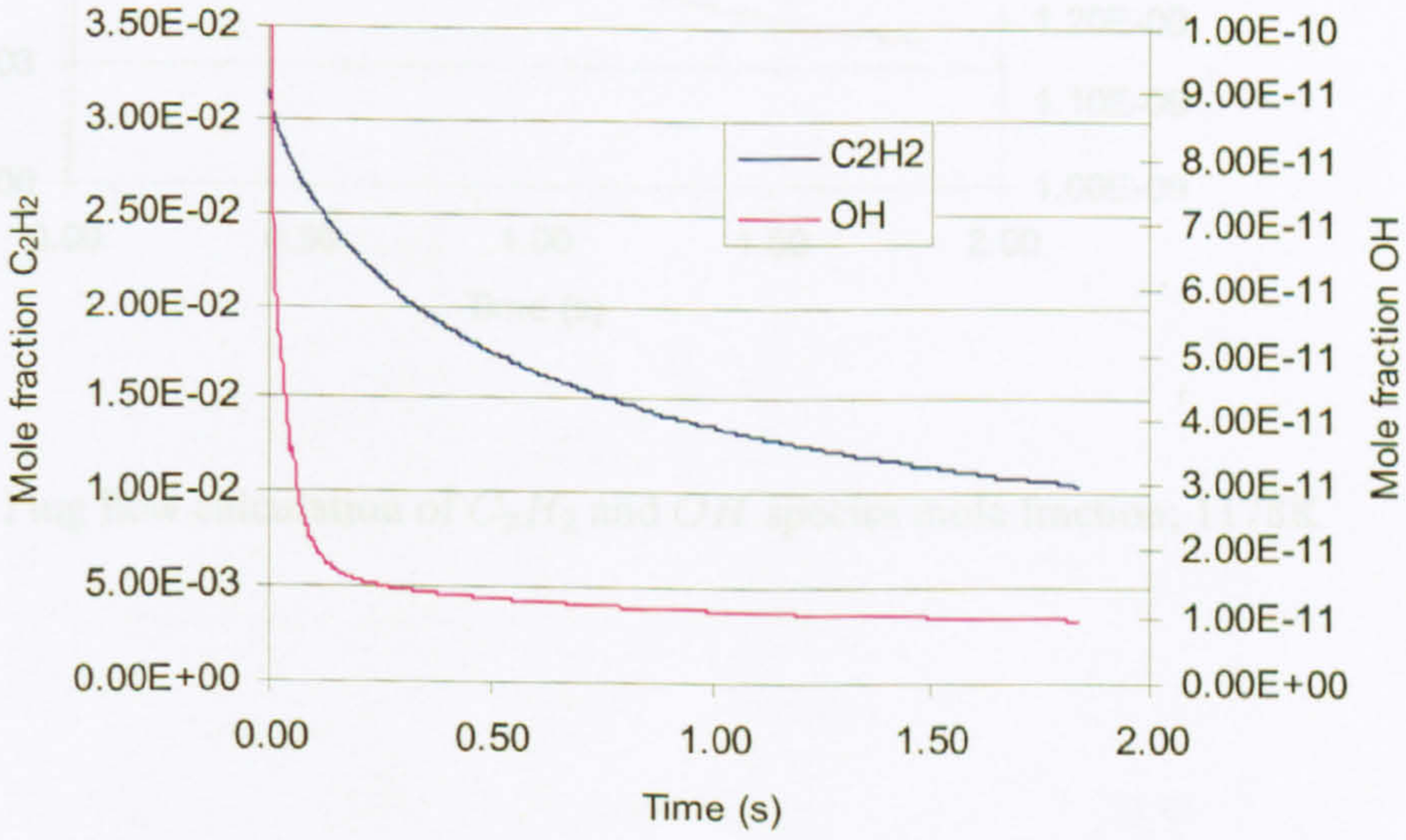

Figure 5.21: Plug flow calculation of C_2H_2 and OH species mole fraction; 1000K

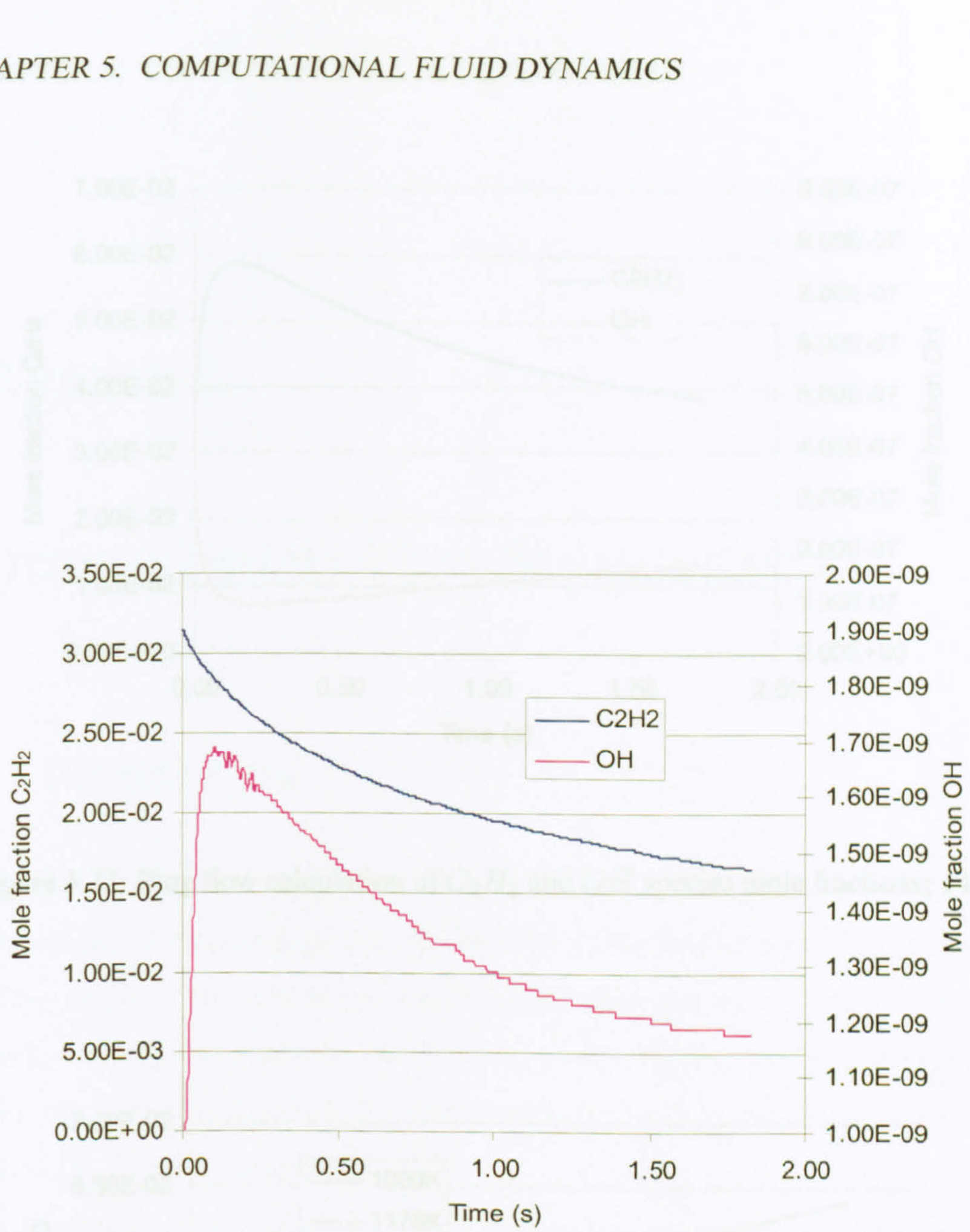

Figure 5.22: Plug flow calculation of C_2H_2 and OH species mole fraction; 1178K

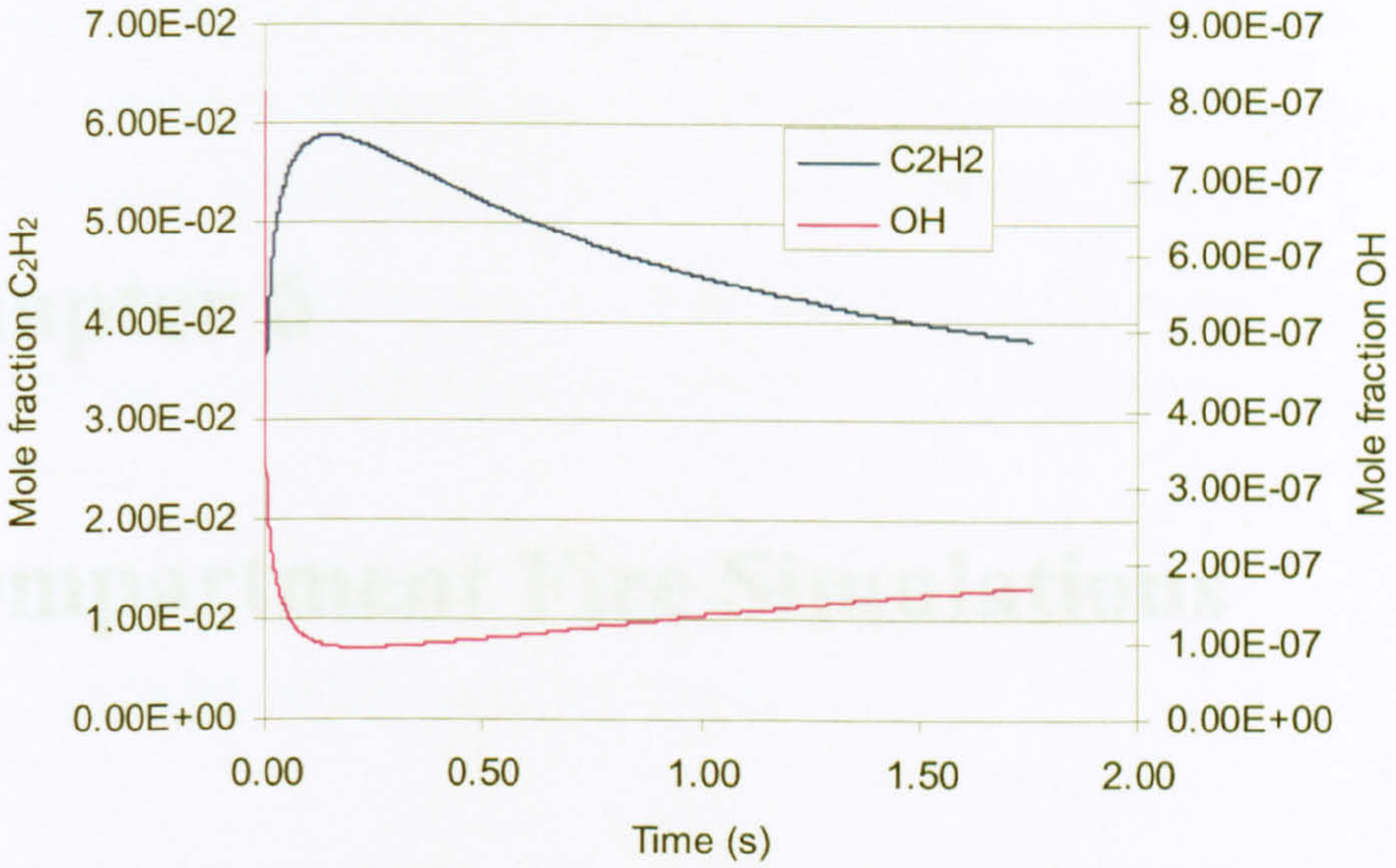

Figure 5.23: Plug flow calculation of C_2H_2 and OH species mole fractions; 1480K

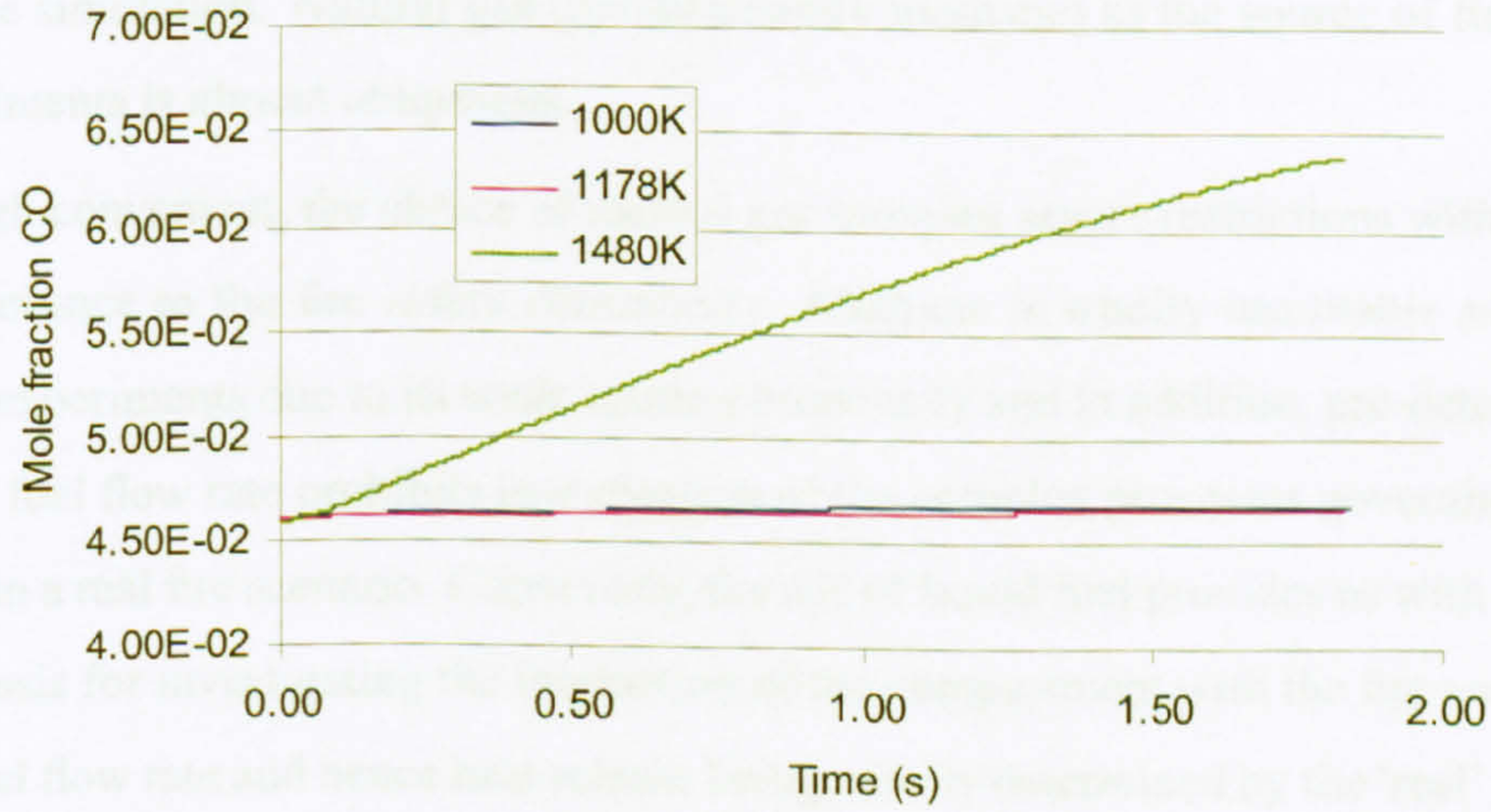

Figure 5.24: Plug flow calculation of CO species mole fraction; 1000K, 1178K, 1480K

Chapter 6

Compartment Fire Simulations

6.1 Introduction

Experience of compartment fire simulations at Cranfield has previously been restricted to simpler Steckler room type configurations [115, 6], in which the heat release is determined *apriori*. The attraction of this methodology lies in the simple experimental geometry and ease to which the effects of the various models can be characterised during the simulation. Natural gas (predominantly methane) as the source of fuel in such experiments is almost ubiquitous.

Though convenient, the choice of natural gas imposes severe restrictions with regard to its relevance to the fire safety community. Methane is wholly unsuitable as a fuel in these experiments due to its weak sooting propensity and in addition, pre-determination of the fuel flow rate prohibits investigation of the complex processes governing heat release in a real fire scenario. Conversely, the use of liquid fuel provides us with an important basis for investigating the interaction of the compartment with the fire source, with the fuel flow rate and hence heat release being wholly determined by the 'real' processes occurring inside the compartment. Heptane provides a good level of sooting propensity *apropos* the newly developed 'soot probe', which, along with its well established chemistry defines it as a suitable fuel. The half-scale ASTM experimental compartment used

in this research is broadly similar to that of the Steckler room. However, additional parameters are examined in in this research, such as external wall temperature profiles, which are considered shortcomings of the Steckler experiment in forcing the imposition of 'best guessed' boundary conditions in the corresponding simulations.

This chapter seeks to demonstrate the application of the models implemented in SOFIE to describe the experiments carried out in the half-scale ASTM room in order to validate the CFD code.

6.2 ASTM room model setup

6.2.1 Physical and Numerical Models

The physical and numerical models used in the simulations using SOFIE are summarised in the following tables:-

Combustion model	EBU, Laminar flamelet
Turbulence model	High Reynolds number k-ϵ model, with buoyancy corrections via the single gradient diffusion hypothesis
Radiation model	Discrete transfer, $2\theta \times 8\psi$ rays, polar + original discretisation
RTE solution method	Discrete band weighted sum of grey gases (WSGG)
WSGG model	Truelove's methane + soot coefficient set, Truelove's oil+soot coefficient set
Soot model	Moss general soot model with coefficients for C_2H_4
Flamelet options	Multiple radiative loss flamelet, using 8 heat loss fractions
Heat Transfer	Conjugate heat transfer to solid boundaries

Table 6.1: Physical parameters used in the SOFIE simulations

Numerical grid	• 23 cells for room width including 5 cells for 0.17m diameter burner • 28 cells for room height • 45 cells for room length • total number of cells in domain = 23×28×45 = 28,980 cells
Solid boundaries	Light-weight ceramic walls of 12mm width, with each wall represented by two numerical grid cells
Interpolation scheme	Hybrid
Solver	Stone's implicit 3D (sip3d)
Number of iterations	5000

Table 6.2: Numerical parameters used in the SOFIE simulations

In addition to tables 6.1 and 6.2, variations were also introduced into the models that were included in order to perform a sensitivity analysis. These variations are as follows and summarised in table 6.3:-

- Eddy break-up combustion model. Fuel flow rate, thus HRR is pre-determined based on experimental results.
- Laminar flamelet combustion model. Fuel flow rate is pre-determined based on experimental results. Fixed radiative loss flamelet (0% and 40% radiative loss)
- Laminar flamelet combustion model. Fuel flow rate is pre-determined based on experimental results. Interpolated radiative loss flamelet. Calculated transported enthalpy is compared to flamelet enthalpy at adiabatic to determine appropriate level of flamelet radiative loss [116].
- Laminar flamelet combustion model. Fuel flow rate is driven by the mass-loss rate of fuel based on simple evaporation model. Multiple flamelet choice dependent

upon corresponding local transported enthalpy.

	Eddy break-up	Laminar flamelet	Evaporation model
Fixed fuel flow rate	√	√	×
Multiple flamelet	×	√	×
Multiple flamelet	×	√	√
Fixed loss flamelet	×	√	√

Table 6.3: Summary of Combustion Models Used in SOFIE

In line with the compartment fire experiments, the door-width of the compartment was correspondingly reduced in the simulations in order to capture the effects of under-ventilation.

6.2.2 Numerical Mesh

The room geometry is shown in Figure 6.1 and the mesh used is shown in Figure 6.2. The burner is in the centre of the room and the symmetry of the room has been exploited to minimise the number of nodes by using a mirror boundary on the computational mesh. The simulations are run transiently in 10s time-steps for 600s which corresponds to the time taken to reach steady-state using the smaller diameter burner with the largest doorwidth.

Figure 6.3 depicts a steady-state simulation for the full doorwidth configuration. The flame trajectory can be clearly seen to bend away from the doorway under ventilation controlled conditions, ultimately forming a ceiling jet with sufficient heat release. This simulated profile is typical of that observed in a compartment fire.

During the course of each computation, variables were monitored in the doorway and were found to remain stable. To aid computational expense, initially, a coarse grid was used. Because the mesh density was not high enough to ensure full grid independence, further simulations were run doubling the grid density in all dimensions throughout the compartment domain. What dependence there is, manifests itself at the interfaces between the two layers. The interfacial heights vary a little as do the local scalar profiles.

6.2.3 Boundary Conditions

There are two alternative fluid boundary conditions attached to the burner in the compartment; an inflow of fuel whose flow rate and therefore heat release rate is either pre-determined, or it is calculated during the course of the simulation by modification of the standard wall function to include transpiration from the surface of the pool-fire. The transpiring boundary approach is more commonly ascribed to the steady-state burning of a solid. The simple evaporation model used here calculates the mass loss rate of fuel, which determines the heat release rate of the compartment fire, by assuming the following simple relationship between the net heat flux to the fuel surface and heat of gasification of heptane:

$$\dot{m} = \frac{\dot{q}''_{net}}{\triangle H_g} \tag{6.1}$$

where $\dot{q}''_{net}$ is the net total incident heat flux to the fuel surface and $\triangle H_g$ is the effective heat of gasification of heptane. The above equation assumes that all heat to the pool surface goes to vapourise the fuel, i.e heat losses for these relatively deep pools with a depth of ~30mm, increases in the sensible heat of the liquid fuel and conduction through the burner walls are negligible.

An ignition criteria was attached to the burner at 371K which is the boiling point of heptane. Although the fire-point temperature of heptane is much lower than this at 269K, the boiling point temperature is considered to be representative of the actual burning fuel surface temperature. The temperature of the solid face in the model was explicitly set to this temperature so that mass flux from the surface was immediate. However, despite this ready release of fuel, difficulty was still encountered with ignition. Various approaches were adopted, including artificially elevating the ambient temperature, forced flow injection at high temperatures and situating a radiant panel close to the upper surface of the fuel. In the majority of cases, ignition was initially achieved but the flame extinguished rapidly. Previous experience at Cranfield held the ignitable solid in

a vertical configuration only. This posed a significant advantage unavailable in the first few minutes of a well-ventilated compartment fire with a burner in a horizontal orientation, due to flame propagation being in the same direction as the buoyancy induced gas flow.

The solution to the problem lay in an alternative approach whereby a pilot flame was ignited directly in front of the pool fire in the compartment, at a heat release rate of 10kW. When the compartment became ventilation controlled the pilot flame directly impinged on the surface of the pool-fire causing it to ignite. The pilot flame remained ignited for a further 200s at which point the simulation was interrupted and the mixture fraction at the pilot flame inlet was re-set to zero, resulting in flame extinguishment. No 'memory effect' of the pilot flame on the main burner was apparent in subsequent time-steps.

A constant pressure boundary some distance from the front of the compartment is chosen to represent a quiescent condition. For those simulations that require heat transfer calculations, active walls of light-weight ceramic are included, with conjugate heat transfer conditions on the fluid side of the wall and isothermal boundary conditions applied to the far side.

6.3 ASTM room fire results

The following sections make comparisons - where applicable - of numerical prediction using SOFIE, against experimental measurements made in the compartment.

Where possible, the results are presented in such a way that comparisons may be made with experiments published in the literature and to aid consistency. A typical example would be the inclusion of doorway profiles, in which the results are presented on the line of room symmetry which passes through the centre of the doorway and burner. The principal scalars reported here are, soot volume fraction, visibility distance, temperature, air flow velocity and mass flow.

In light of somewhat controversial results in the literature, profiles across the doorway were also investigated. Figure 6.4 presents results for the 0.23m diameter burner and 0.36m doorwidth configuration illustrating 'door edge effects' in which the velocity is seen to decrease locally adjacent to the door edges. Results from other workers in this area such as Kumar [117] for example, employed the CFD code JASMINE and predicted that higher velocities occur at the centre of the doorway which is in agreement with the trend found in this research, conversely, others (e.g [118] and [119]) have predicted complex flows dependent upon the level of mesh refinement in and around the whole of the door area.

6.3.1 Heat Release Rate/Mass Loss Rate

The evaporation model provides determination of the rate of heat release, for which the critical component needed to be modelled accurately is the net heat flux to the fuel surface. The correct prediction of heat release is of course of paramount importance due to the consequential effects on the remaining parameters being simulated in the compartment. A plot of the total net heat flux to the entire fuel surface in the 0.36m doorwidth and 0.17m diameter burner configuration is illustrated in figure 6.5, which is further split into components of radiative and convective fluxes in figures 6.6 and 6.7 respectively. The results show that heat transfer to the fuel surface is dominated by radiation. The heat flux profile in figure 6.5 shows significant variation across the entire fuel surface; in particular a higher incident flux may be seen towards the rear of the burner; this is anticipated because here the flame front lies closer to the fuel surface. What is also noticeable is a pronounced peak towards the edge of the burner of order 25kW. Increasing the number of rays in the radiation model to 32+1 does not improve the distribution, as we can see in figure 6.8. It should however be noted that the coarse grid used in these simulations obviates a detailed analysis of the fire source and its comparison with experimental measurements. The mean values of predicted heat flux over the entire fuel surface and the corresponding fuel mass release rate do however

closely match those found experimentally under steady-state conditions.

Diameter Burner (m)	Doorwidth (m)	HRR based on MLR (kW)	
		Expt	SOFIE
0.23	0.36	74.3	53.0
0.17	0.36	30.7	31.6
0.17	0.25	44.1	46.6
0.17	0.15	74.3	64.1

Table 6.4: Heat Release Rate Predicted using SOFIE

Table 6.4 Heat release rates predicted using the simple fire-spread model implemented in SOFIE for all three doorwidth configurations in the compartment.

6.3.2 Mass Air Flow Rate

Mass flow into and out of the compartment are calculated based on the the peak steady-state average velocity and temperature profiles described in section 3.3.5. Results from which are presented in table 6.5.

Diameter Burner (m)	Doorwidth (m)	Mass Air Flow in (kg/s)		Mass Air Flow Out (kg/s)	
		Expt	SOFIE	Expt	SOFIE
0.23	0.36	0.32	0.31	0.43	0.31
0.17	0.36	0.19	0.15	0.20	0.16
0.17	0.25	0.26	0.26	0.29	0.26
0.17	0.15	0.42	0.39	0.54	0.4

Table 6.5: Mass Air Flow Rate Predicted using SOFIE

From continuity, the mass flow entering the compartment - including that of fuel, must equal that leaving the compartment. Differences between the predicted and experimental results can be explained largely by the location of the bi-directional probes used the measure the local air flow velocity at the compartment door and would require a much greater density in order to improve the comparison. Setting the probes closer together would however introduce an undesirable influence on the flow.

6.3.3 Temperature

Doorway temperatures are compared in figure 6.9 for the 0.25m doorwidth configuration using the smallest 0.17m diameter burner. This configuration represents the most demanding steady-state calculation for model validation. A comparison is made with both the Non-Adiabatic Flamelet (NAF) combustion model which extends the use of the multiple flamelet strategy first introduced by Young and Moss [120] for which the relevant flamelet set is chosen based upon the transported enthalpy and the Eddy-Break-Up (EBU) model in which the fuel flow rate and hence heat release is established *apriori*. From the experiments conducted in the half-scale room, we expect the upper layer temperature to be in the region of 650K-670K for the 0.25m doorwidth configuration. It is shown that results eluding to the Eddy Break-up simulations that the temperature is over-predicted by around 50K. It must although be noted that the EBU model constants (see appendix A) are optimised for a buoyant jet flame. However, the temperature predicted using the NAF model is in good agreement with both the experimental measurements and that calculated based on transported enthalpy.

The steep rise in temperature at 0.44 m height indicates the start of the hot layer. The EBU and NAF model predictions agree well with the height of the neutral layer in the experiment calculated from velocity measurements as previously described in Chapter 3 and summarised in table 3.3. The experimental velocity profile is shown alongside for visualisation.

6.3.4 Total Heat Flux

As previously described in section 3.3.7, two total heat flux gauges were positioned in the floor adjacent to the burner and in one of the compartment side walls. Figures 3.28 and 3.29 shows experimental transient heat flux experienced by the Gardon gauges located in the both the compartment floor and ceiling for all three doorwidths. To aid visualisation, the results are split into each of the three different door widths. Table

6.6 lists the steady-state values achieved comparing predicted levels against those found experimentally. It may be seen that SOFIE generally underpredicts the total heat flux at these locations. The error increases with reduction in doorwidth with rather poor results for the smallest 0.15m doorwidth. Due to the close coupling with soot loading and the tendency to underpredict soot volume fraction with decreasing doorwidth, this result is unsurprising. However, the latter smallest doorwidth case is rather semantic in its comparison with experimental values due to the occurrence of flashover in the experiment.

Doorwidth (m)	Expt ceiling (kW/m^2)	SOFIE ceiling (kW/m^2)	Expt floor (kW/m^2)	SOFIE floor (kW/m^2)
0.36	6.9	5.9	8.5	7.2
0.25	12.1	8.7	20.9	15.6
0.15	97	37	122	55

Table 6.6: Total heat flux; experiment versus prediction; 0.17m diameter burner; 0.36m, 0.25m and 0.15m doorwidth

6.3.5 Gas Species

The ability of SOFIE to predict species concentrations under well ventilated conditions may be seen in figures 6.10, 6.11 and 6.12. These results relate to the 0.36m doorwidth case showing predicted versus experimental levels of O_2, CO_2 and CO respectively.

Results for the 0.36m doorwidth underpredict the levels found experimentally by as much as a factor of 2 for the CO_2 and CO levels.

6.3.6 Soot

Table 6.7 below presents a summary of both experimental and numerical results, in the context of visibility in smoke as described in Chapter 3. For each simulation, the absolute peak soot concentration is underpredicted. The time taken to reach 0.33 OD/m is also considered; this is the average optical density of smoke at which people would tend

to turn back rather than continue in terms of general visibility in smoke. This criteria has already been discussed in section 2.4. This limit was not reached experimentally for the 0.17m diameter burner at the full 0.36m doorwidth, even at steady-state. However, upon reducing the doorway to 0.25m, this limit was reached at 80.2s. Based on the minimum visibility distance achieved for the 0.15m doorwidth we can say that the limit has been reached even though the experiment had not reached a steady-state, but unfortunately information regarding the time taken to reach this limit is unavailable. For the largest diameter burner, the criteria had not been reached. However, once again the experiment has not reached a steady state and was of a much shorter duration than the 0.15m doorwidth case.

Burner (m)	Door (m)	Peak Expt Door Soot fv	Steady-state?	Min. Vis. Dist. (m)	Time to 0.33 OD/m (s)	Peak Door Soot fv NAF	Peak Door Soot fv FF	Peak Door Soot fv EBU
0.23	0.36	6.80E-07	No	3.8	limit not reached	2.68E-07	8.81E-08	9.2E-07
0.17	0.36	1.40E-07	Yes	16.6	limit not reached	1.19E-07	2.23E-08	2.42E-07
0.17	0.25	6.20E-07	Yes	3.70	80.2	2.44E-07	5.20E-08	8.84E-07
0.17	0.15	2.28E-06	No	1.01	no data	5.20E-07	3.08E-07	3.00E-06

Table 6.7: Predicted versus experimental single point peak soot volume fraction and visibility distance for each experimental configuration

Graphs plotting temperature and soot volume fraction pertaining to the 0.36m and 0.25m doorwidth case from table 6.7 predicted using the laminar flamelet and eddy-break-up model may be seen in figures 6.13 and 6.14 respectively.

The experimental soot volume fraction and visibility profiles for each case relating to the results shown in the table may be seen in figures 3.15 and 3.16.

Predicted versus experimental results for a vertical traverse in the doorway of the compartment may be seen in figure 6.15 for the 0.25m doorwidth. Two experiments are compared which are found to be in close agreement regarding their peak soot volume fraction at the top of the doorway. The first experimental traverse was initiated just prior

to reaching steady-state and does not reach the plateau which is achieved in the second experiment when the compartment *has* reached steady-state.

Figure 6.16 shows a soot volume fraction iso-surface. Visualising a 'single-value' soot volume fraction in this way helps demonstrate the complex flow-field within the compartment and highlights the existence of significant soot concentration gradients.

6.4 Convergence

Global residual values were typically 1×10^{-4} for the solved variables, and 1×10^{-3} for the mass error. However, for each simulation described in this chapter, a corresponding set of error residuals is also presented in table 6.8 as indicators of the level of convergence achieved. It can be seen that using the evaporation model to calculate the heat release during the course of computation results in a compromise regarding the accepted residual values, which in general represents a factor of almost two difference in absolute values compared to the use of a steady-state prescriptive rate of heat release with fixed fuel inlet conditions. Difficulty was encountered in setting the minimum residual below 1E-02, even with the aid of relaxation factors. The minimum error was found to be between 1% and 2% for each case compared with 0.01% for all other simulations. The time to convergence was in excess of 5000 iterations.

Simulation Type	MassErr	Floin	Flout	QfloErr	QbndErr	Enth
NAF, 371K flamelet, FS, 0.36m door	2.486E-02	1.520E-01	1.604E-01	5.019E-01	1.051E-03	3.023E-03
NAF, 371K flamelet, FS, 0.25m door	2.717E-02	2.613E-01	2.63E-01	2.437E-02	6.845E-04	1.848E-03
NAF, 371K flamelet, FS, 0.15m door	2.571E-02	3.906E-01	4.007E-01	2.121E-02	2.804E-04	2.220E-03
NAF, 300K flamelet, 0.36m door	1.815E-02	3.90E-01	4.002E-01	3.028E-02	9.993E-06	4.033E-04
NAF, 371K flamelet,FS, 32 rays, 0.36m door	3.189E-02	3.283E-01	3.286E-01	7.742E-01	1.108E-03	3.89E-03
FF(40%), 300K flamelet, FS, 0.36m door	2.336E-02	2.749E-01	2.752E-01	1.181E+00	2.219E-02	8.938E-04
FF(adiabatic), 300K flamelet, FS, 0.36m door	1.778E-02	3.339E-01	3.338E-01	1.685E+00	6.062E-04	1.019E-03

Table 6.8: Error residuals for each SOFIE simulation

The overall convergence criteria for each solution was chosen to be dependent on the mass error residual (**MassErr**), which represents the average mass error over the whole

of the solution domain, normalised by the total mass flow into the domain. The mass residual parameter is typically used in calculations of the type carried out in this research.

Apart from the mass error, SOFIE also computes residual values for all solved variables which are relevant to the particular problem. Of particular interest in simulations in which heat transfer plays an important part, is that of the enthalpy residual - **Enth**. This value pertains to the average enthalpy error, normalised by the total energy input. **Floin** and **Flout** are the total mass flows coming into and going out from the domain. Continuity requires that the values for these parameters should be nearly equal. **QfloErr** and **QbndErr** values provide a further check on convergence for enthalpy and radiation since the enthalpy residual relates only to the accuracy of its transport equation. **QfloErr** is the ratio of the heat flux imbalance to the total energy input in the fluid, whereas **QbndErr** represents a global imbalance in enthalpy flow, combustion energy and any other specified enthalpy sources.

6.5 Discussion

Significant advantage is made in the ability to perform room fire simulations simultaneously with the experiments. In general, the simulations of the compartment proved to be in broad agreement with the experiments. Grid independent solutions have shown that representation of global mechanisms are sufficient to predict macroscopic quantities in the compartment and that a high level of burner source detail is unnecessary for the parameters which are sought here. Varying the models included during the simulations allowed a sensitivity analysis to be undertaken. Model comparisons of doorway profiles indicate that the eddy break up description overpredicted the level of soot. This can be largely explained by the relatively high temperatures when compared to those predicted with the flamelet combustion model. The sensitivity of soot concentration to temperature has been emphasised throughout this work through both experimental and

numerical simulation; see section 5.8 for example.

The flamelet set which is chosen based upon the local calculation of enthalpy appears to be preferable in performing compartment fire simulations. Prediction of soot in the full doorwidth scenario shows good agreement, with the peak doorway soot volume fraction being underpredicted by around 15%. However, reduction of the doorwidth causes divergence between the numerical and experimental results for soot. Although, significant advantages in computational expense could be gained by using a fixed loss flamelet, the large underprediction of soot proves this approach pointless in the given exercise to produce adequate representation of visibility in smoke which is generally an order of magnitude or less than that found experimentally.

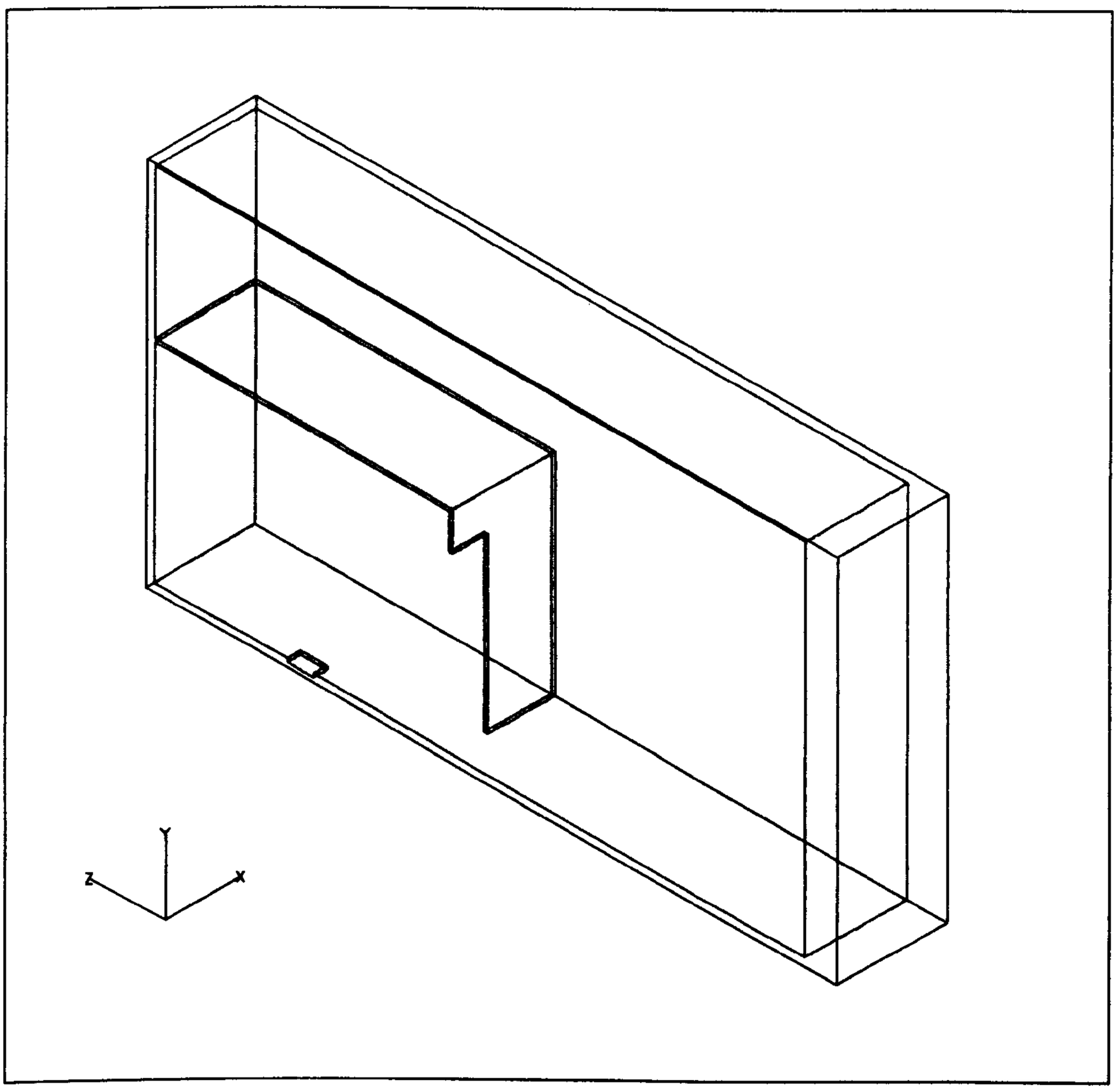

Figure 6.1: ASTM half-scale room geometry

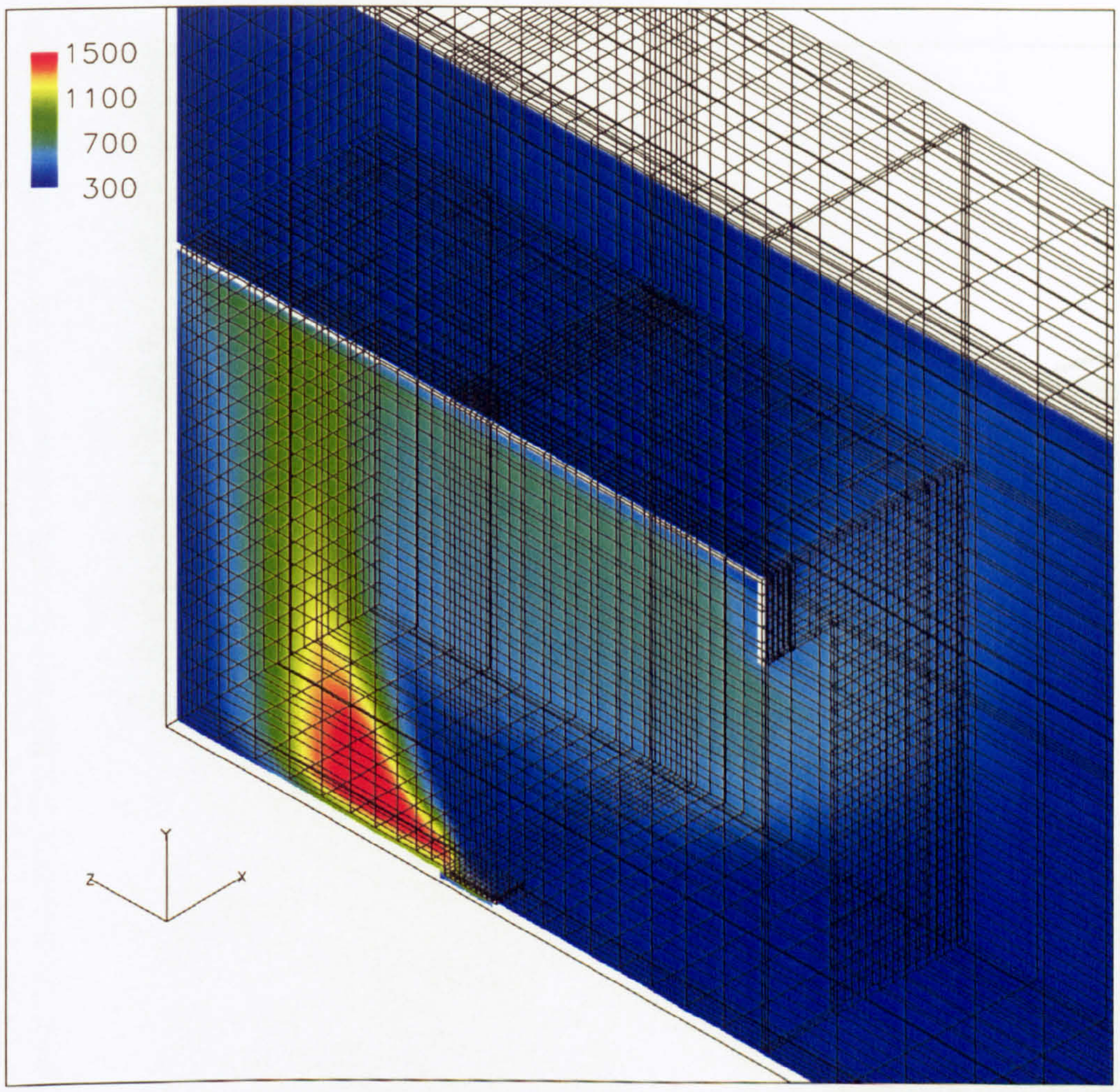

Figure 6.2: Mesh used for ASTM room; mirror boundary condition used on z-y plane through door centerline; burner at the center of the room highlighted by NAF temperature distribution; corridor at the end of the room; 21,252 nodes in the room; 44,505 nodes in total

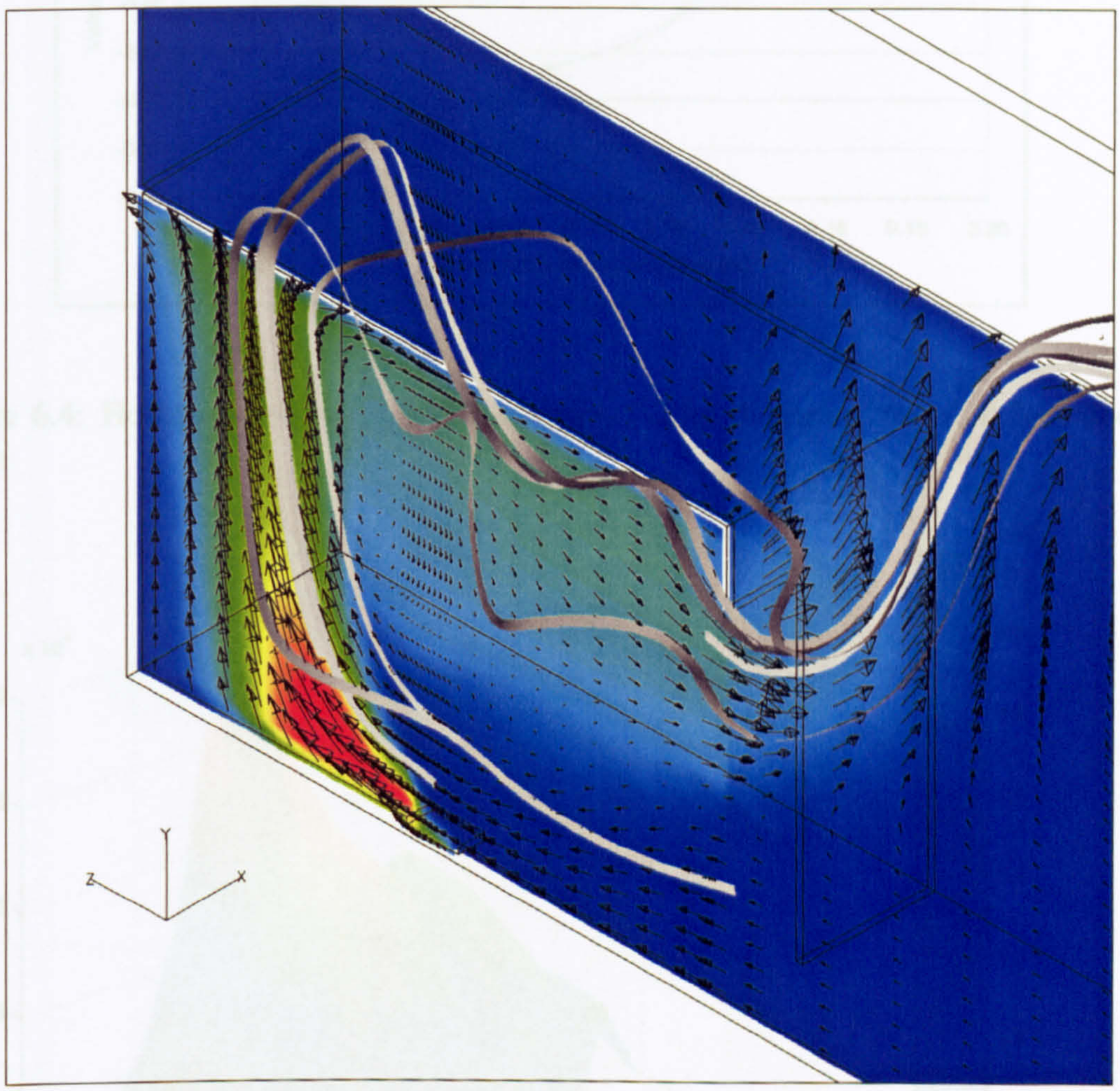

Figure 6.3: Results of multiple flamelet;ASTM room simulation; steady state; ambient temperature 300K; temperature distribution (K); streamlines; full doorwidth

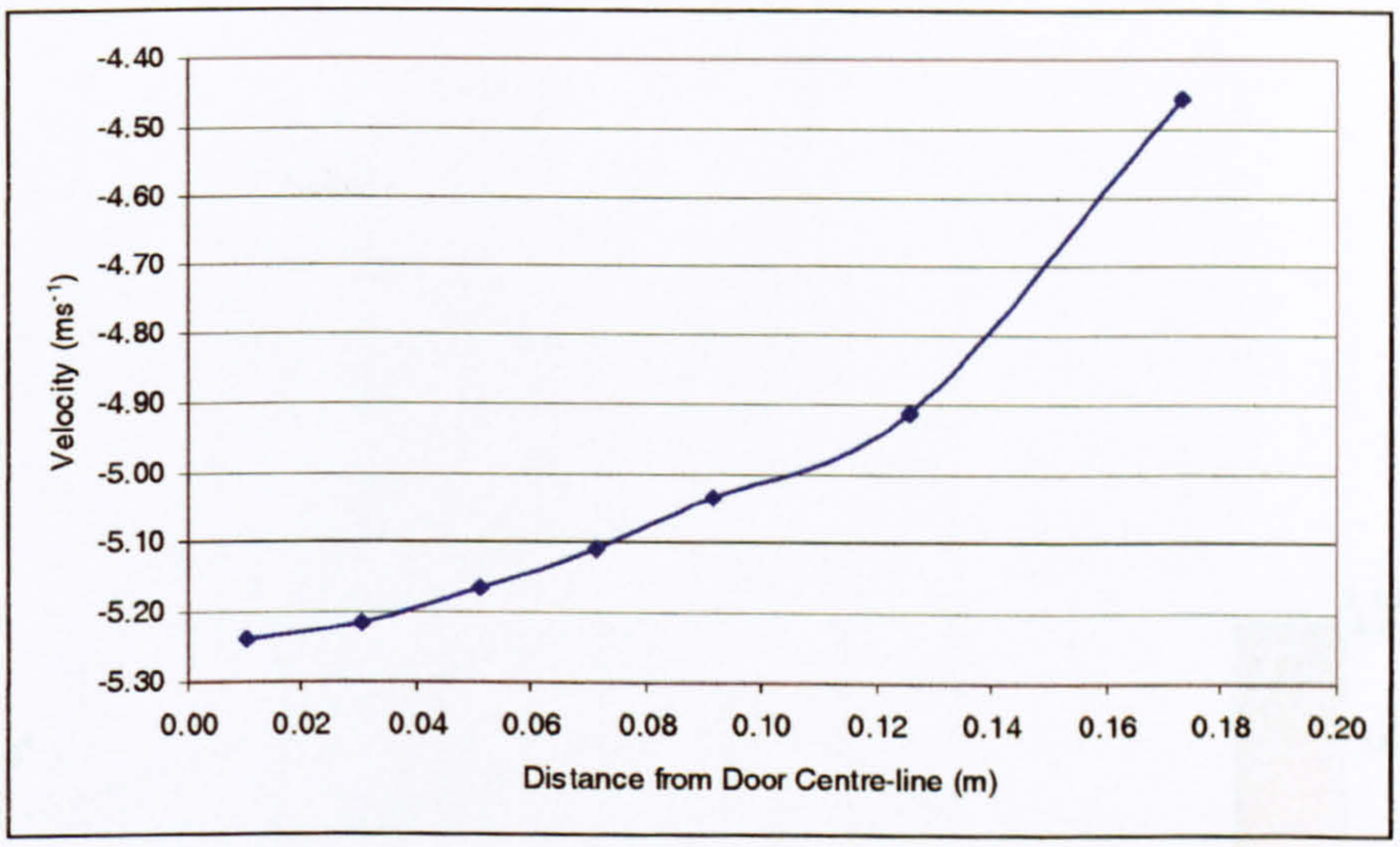

Figure 6.4: Horizontal velocity; 0.992m height; 0.23m diameter burner; 0.36m doorwidth

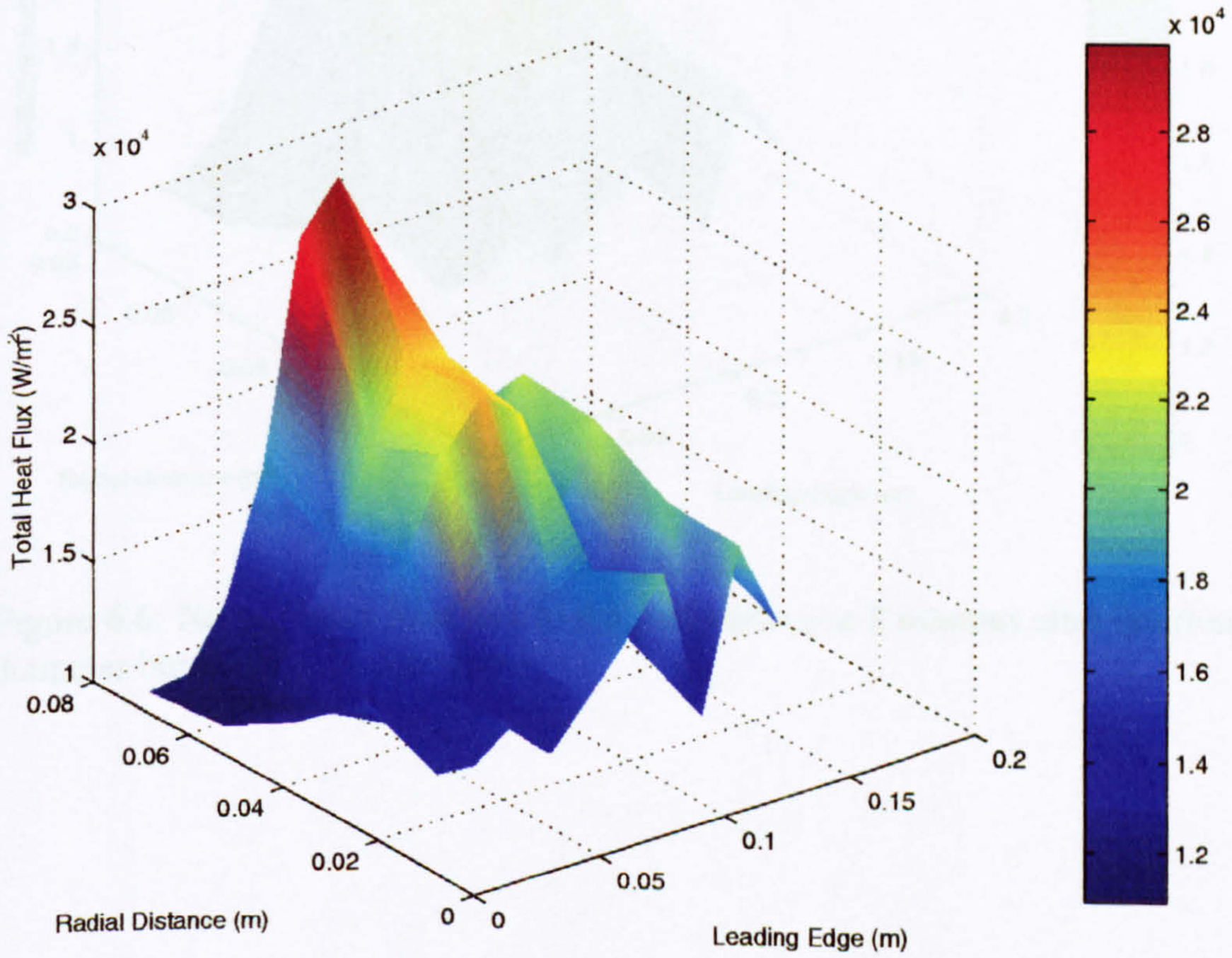

Figure 6.5: Total heat flux to the fuel surface at 8 minutes after ignition; 0.17m diameter burner; 0.36m doorwidth

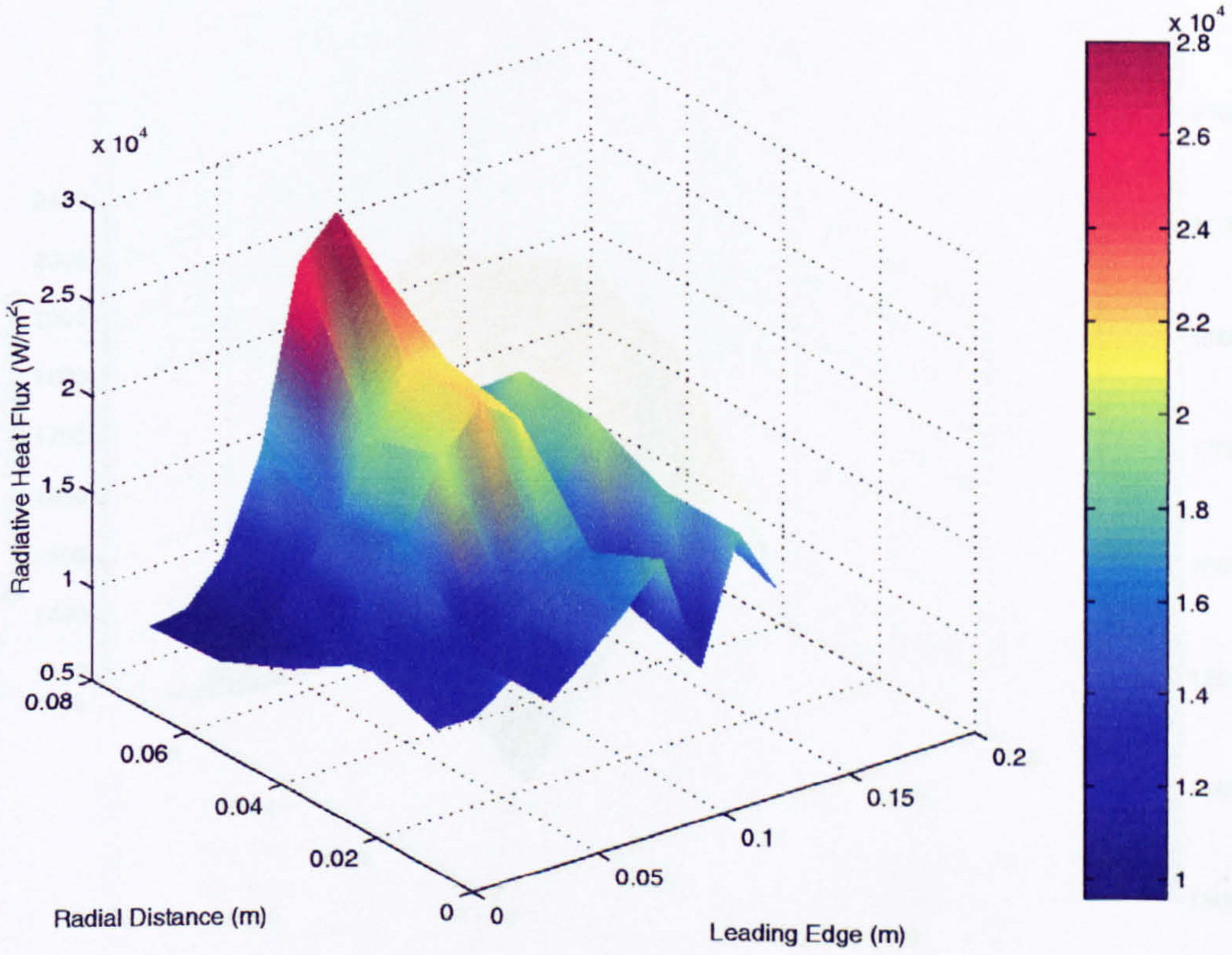

Figure 6.6: Net radiative heat flux to the fuel surface at 8 minutes after ignition; 0.17m diameter burner; 0.36m doorwidth

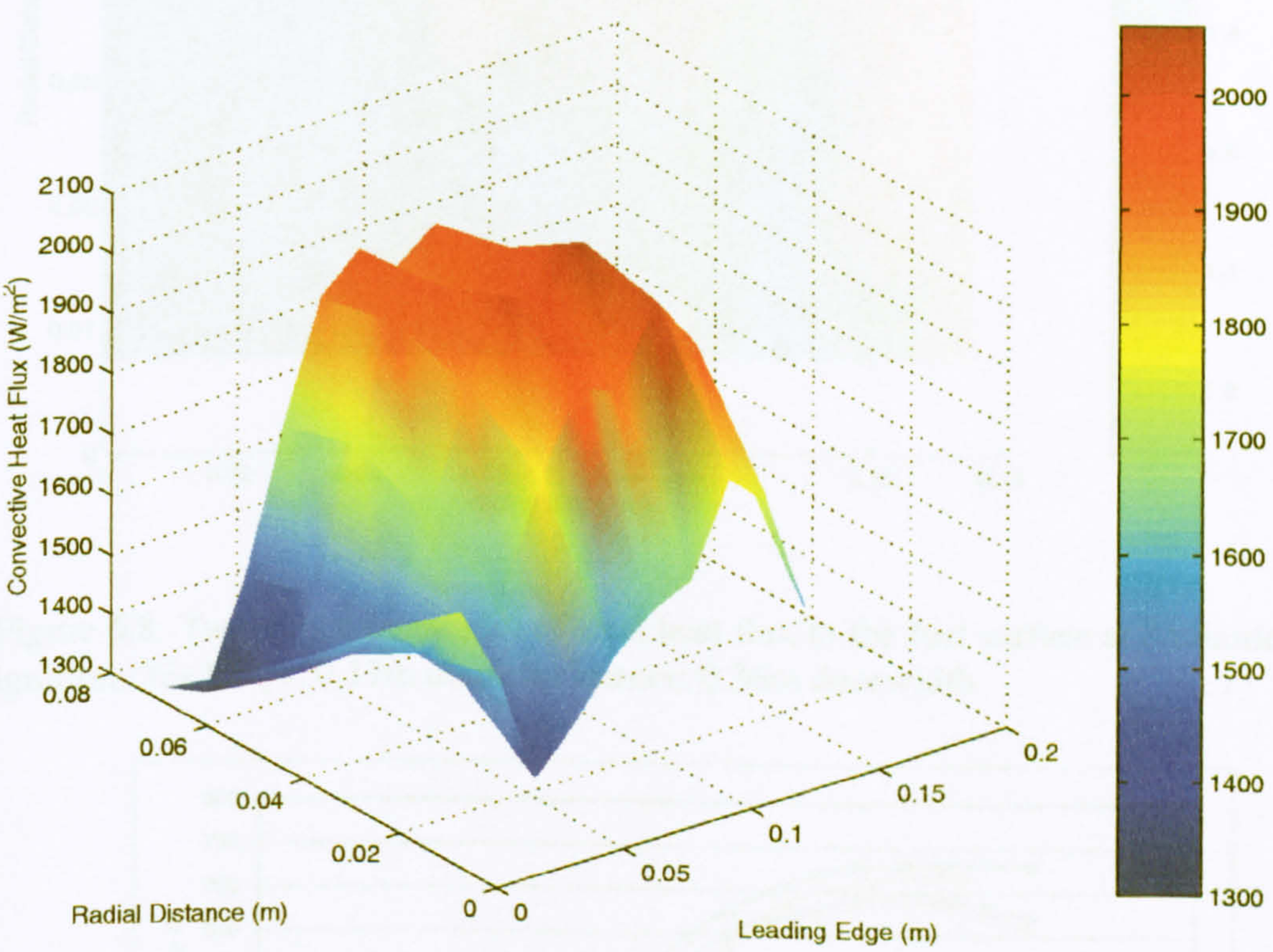

Figure 6.7: Convective heat flux to the fuel surface at 8 minutes after ignition; 0.17m diameter burner; 0.36m doorwidth

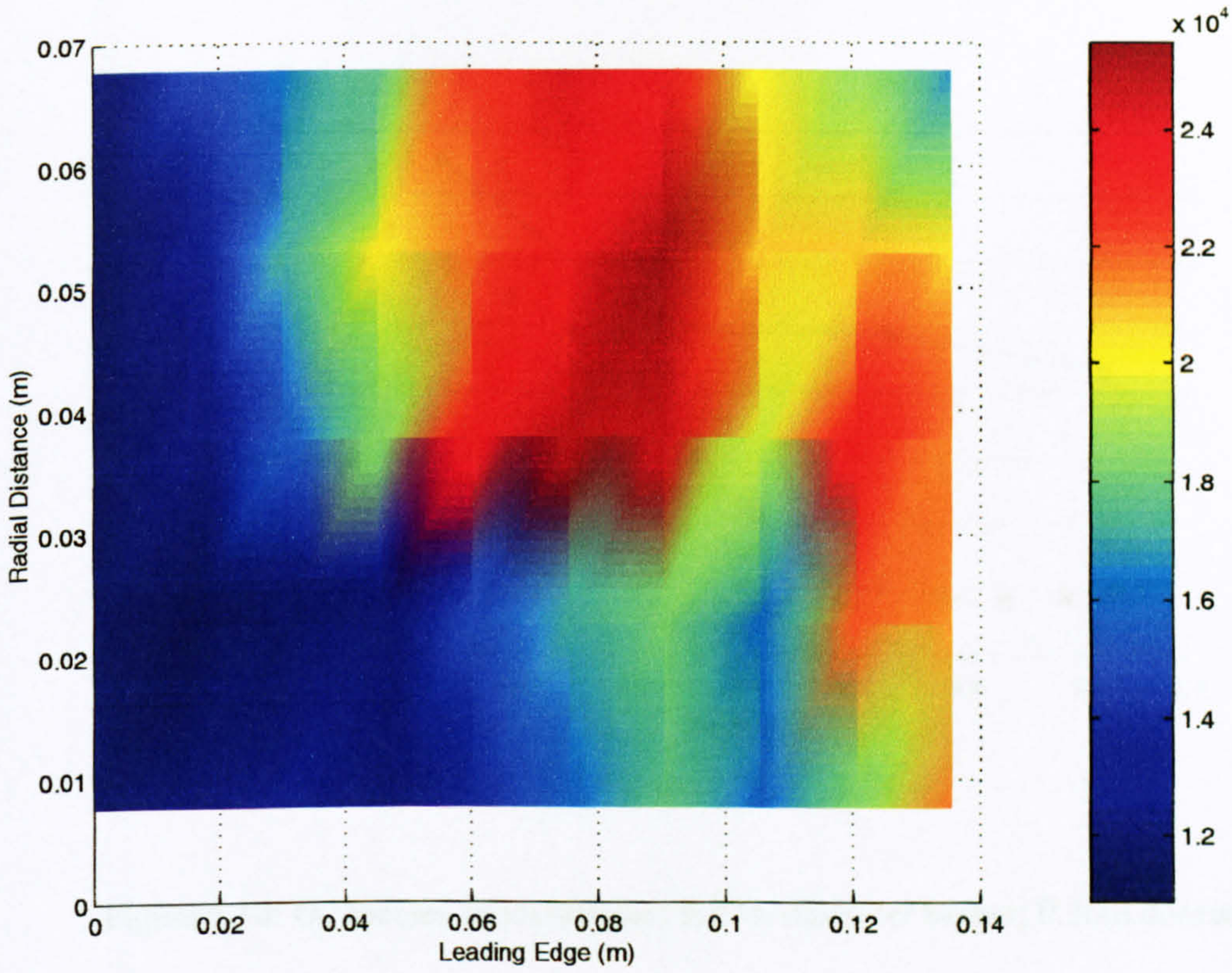

Figure 6.8: Two dimensional plot of total heat flux to the fuel surface at 8 minutes after ignition; 32+1 rays; 0.17m diameter burner; 0.36m doorwidth

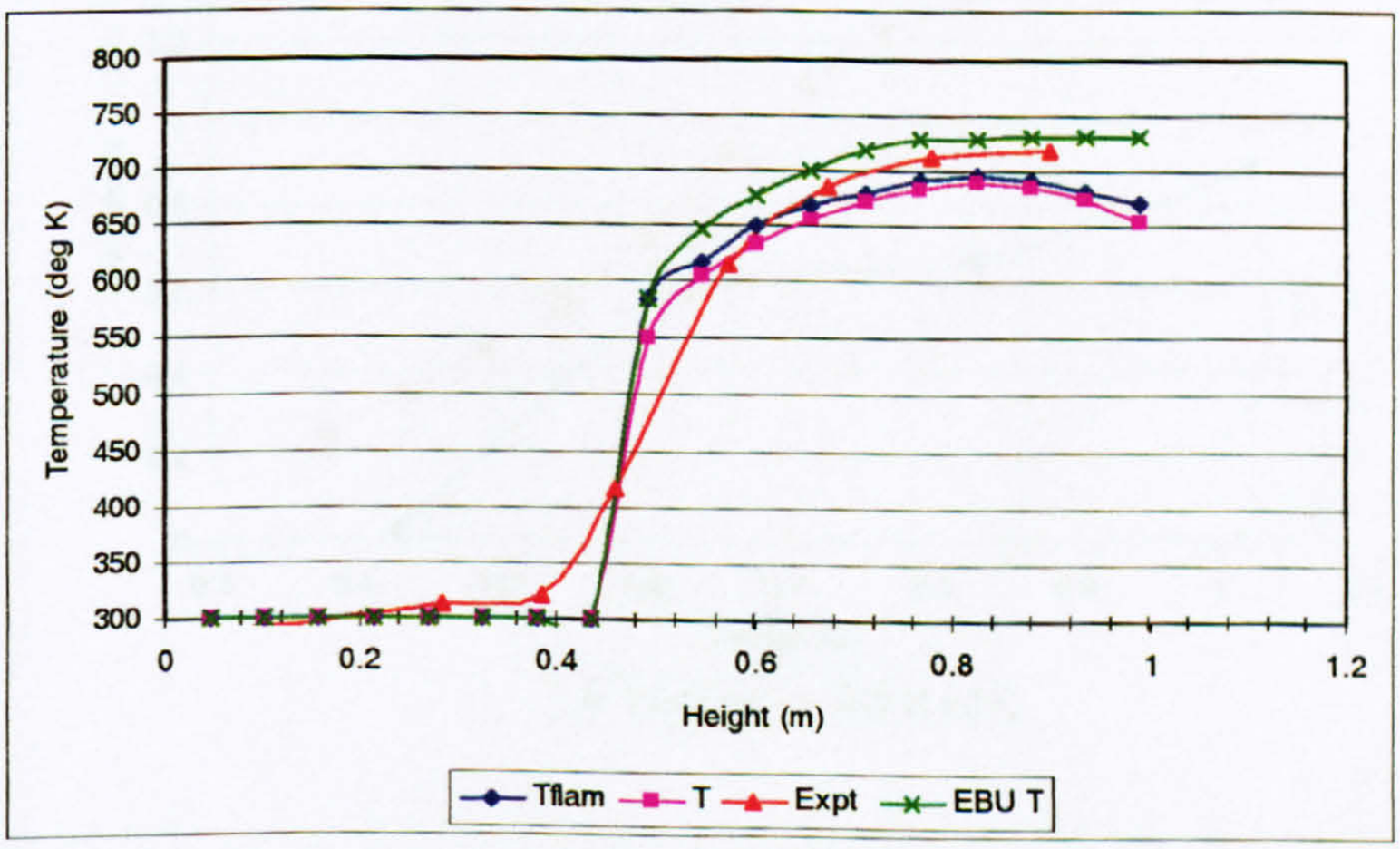

Figure 6.9: Doorway Temperature Profile; 0.17m diameter burner; 0.25m doorwidth.

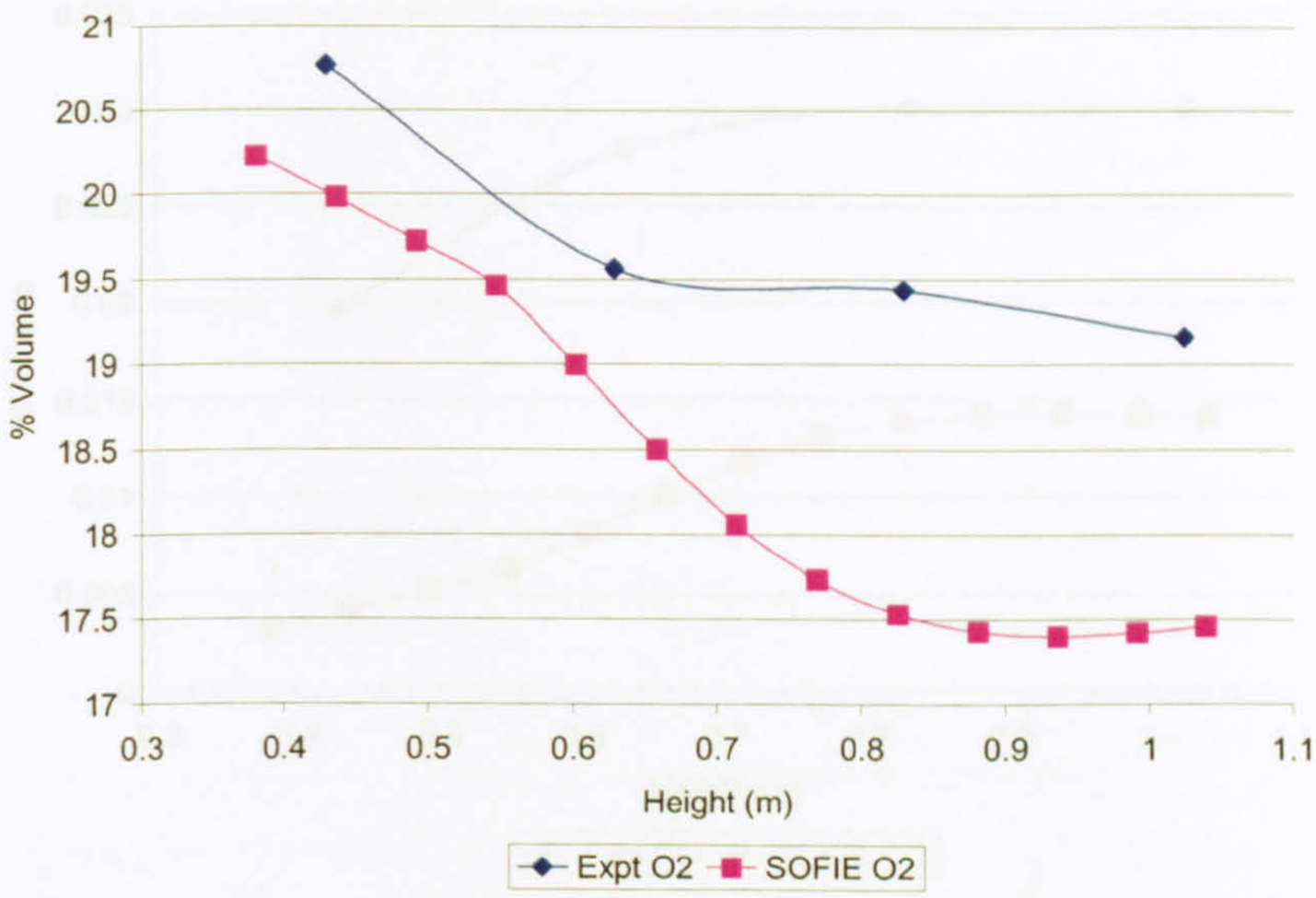

Figure 6.10: O_2 species concentration; 0.17m diameter burner; 0.36m doorwidth

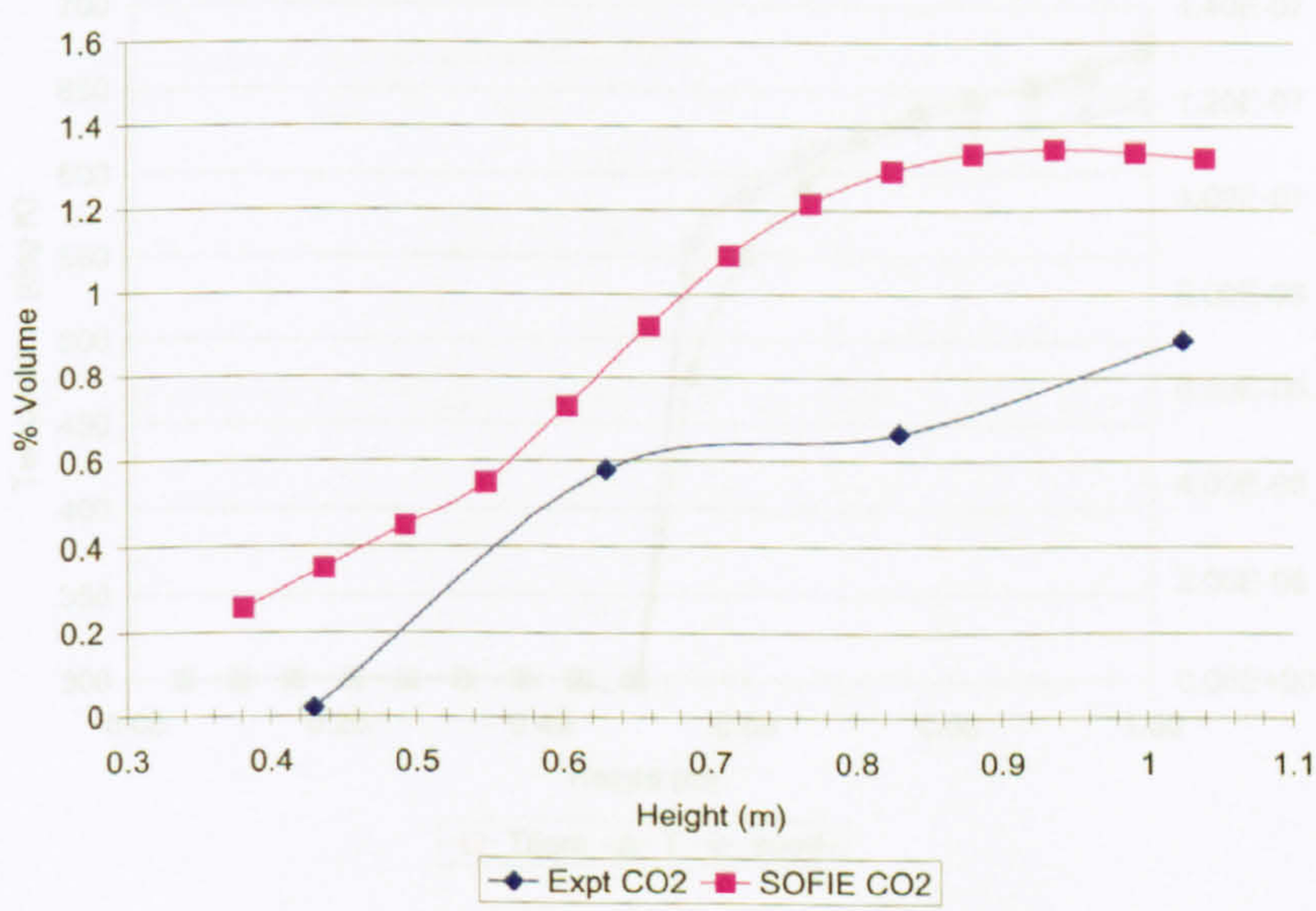

Figure 6.11: CO_2 species concentration; 0.17m diameter burner; 0.36m doorwidth

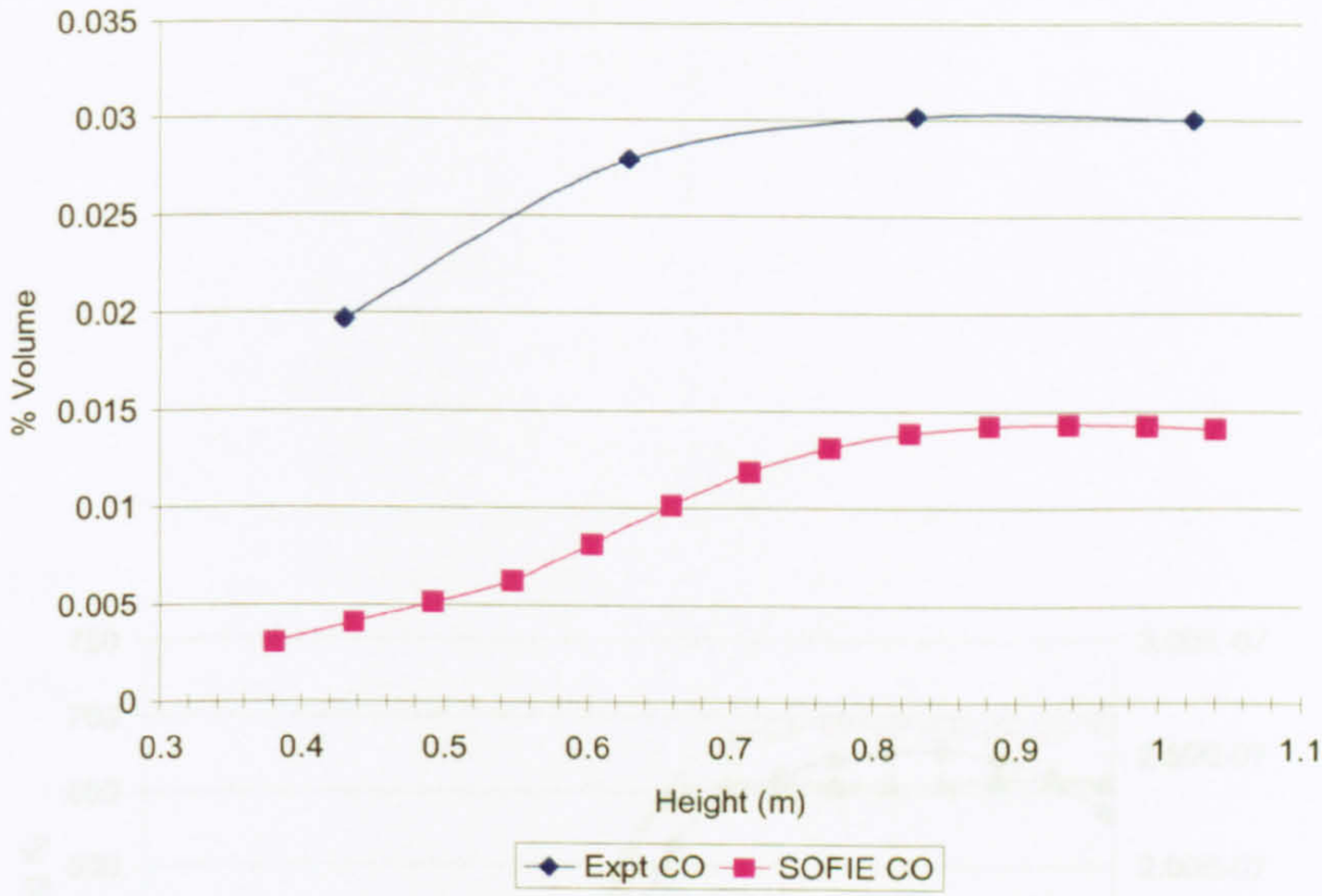

Figure 6.12: CO species concentration; 0.17m diameter burner; 0.36m doorwidth

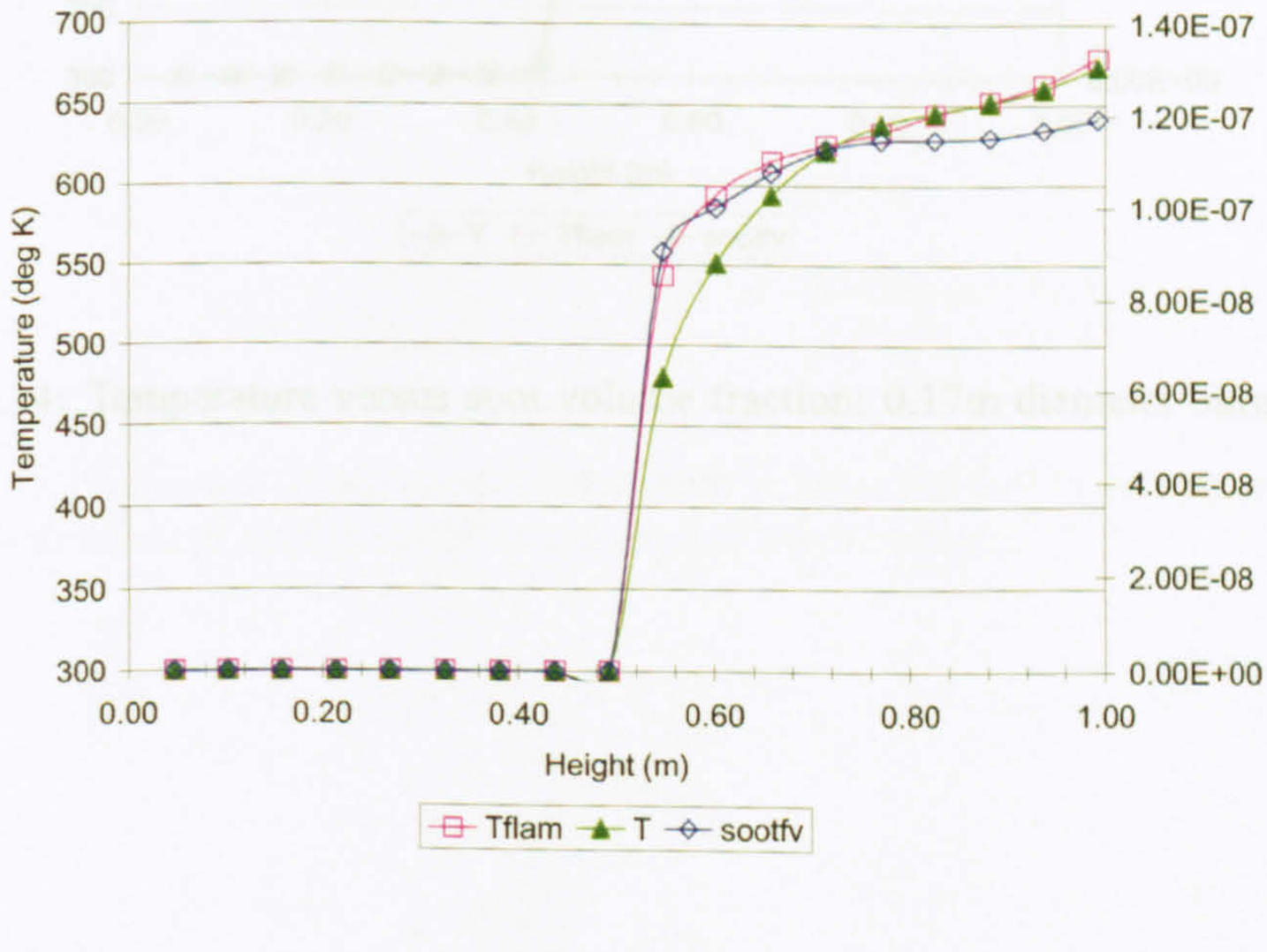

Figure 6.13: Temperature Versus Soot Volume Fraction; 0.17m diameter burner; 0.36m doorwidth

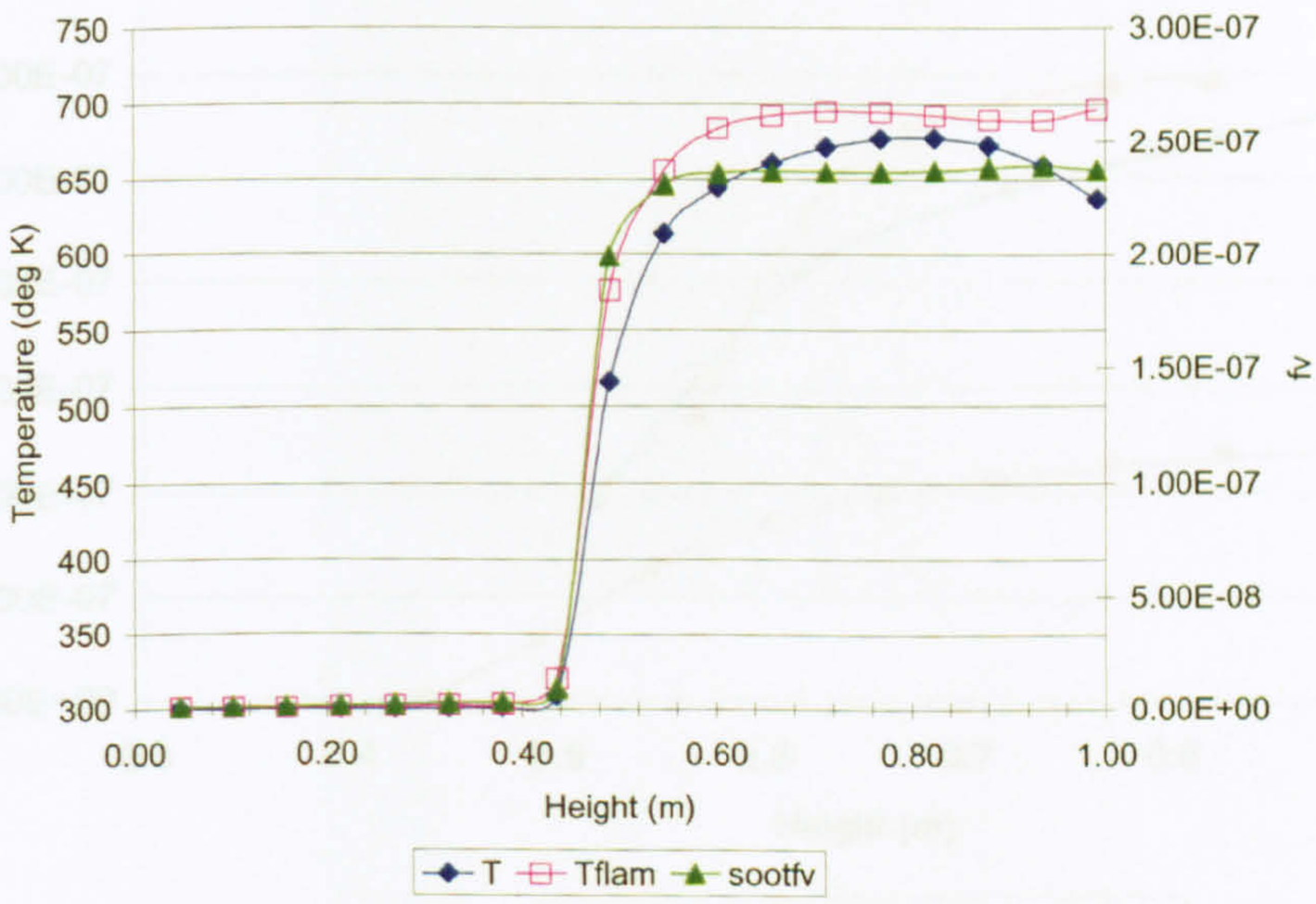

Figure 6.14: Temperature versus soot volume fraction; 0.17m diameter burner 0.25m door

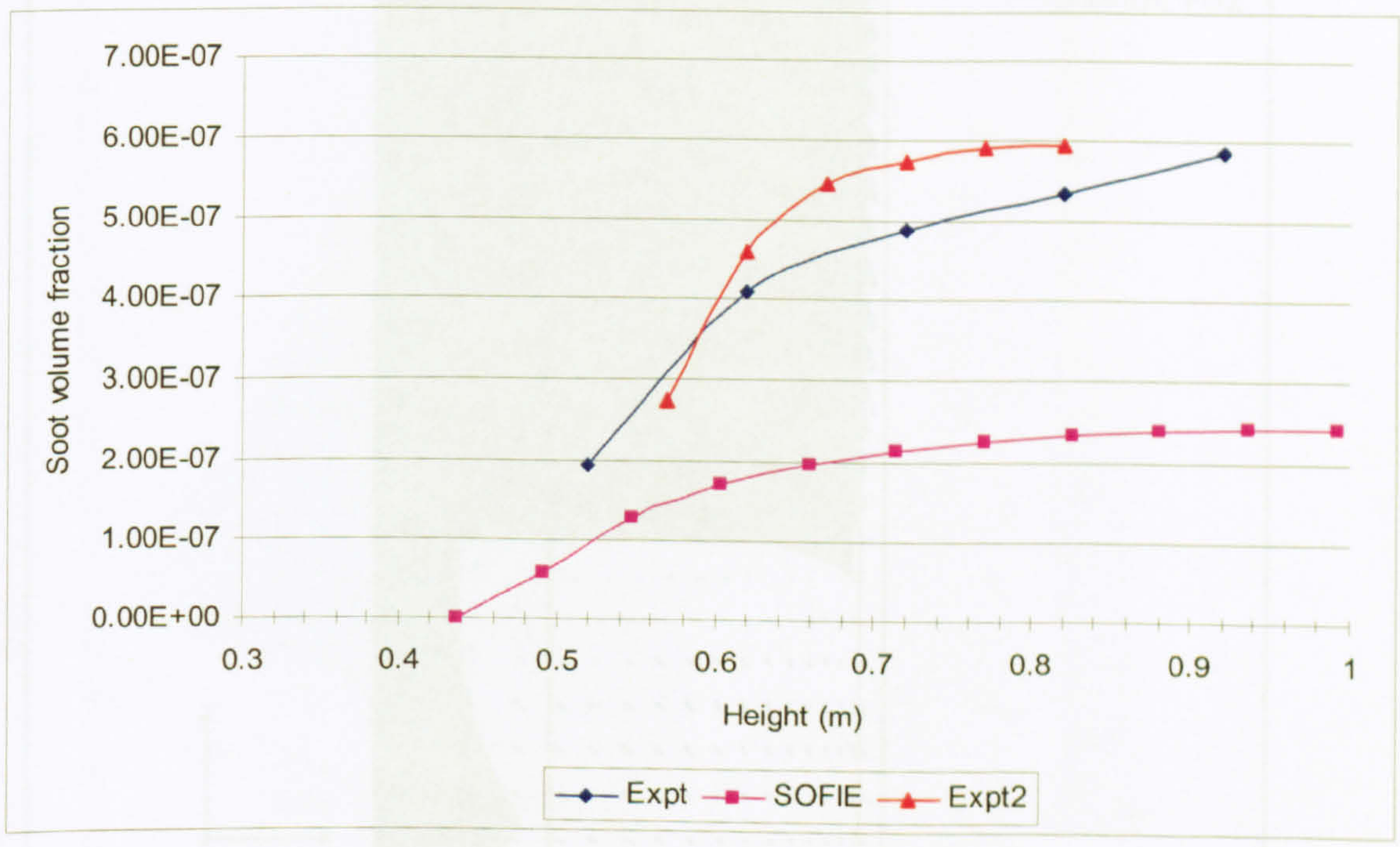

Figure 6.15: Predicted versus experimental soot volume fraction in compartment door with vertical traverse; 0.17m diameter burner; 0.25m doorwidth

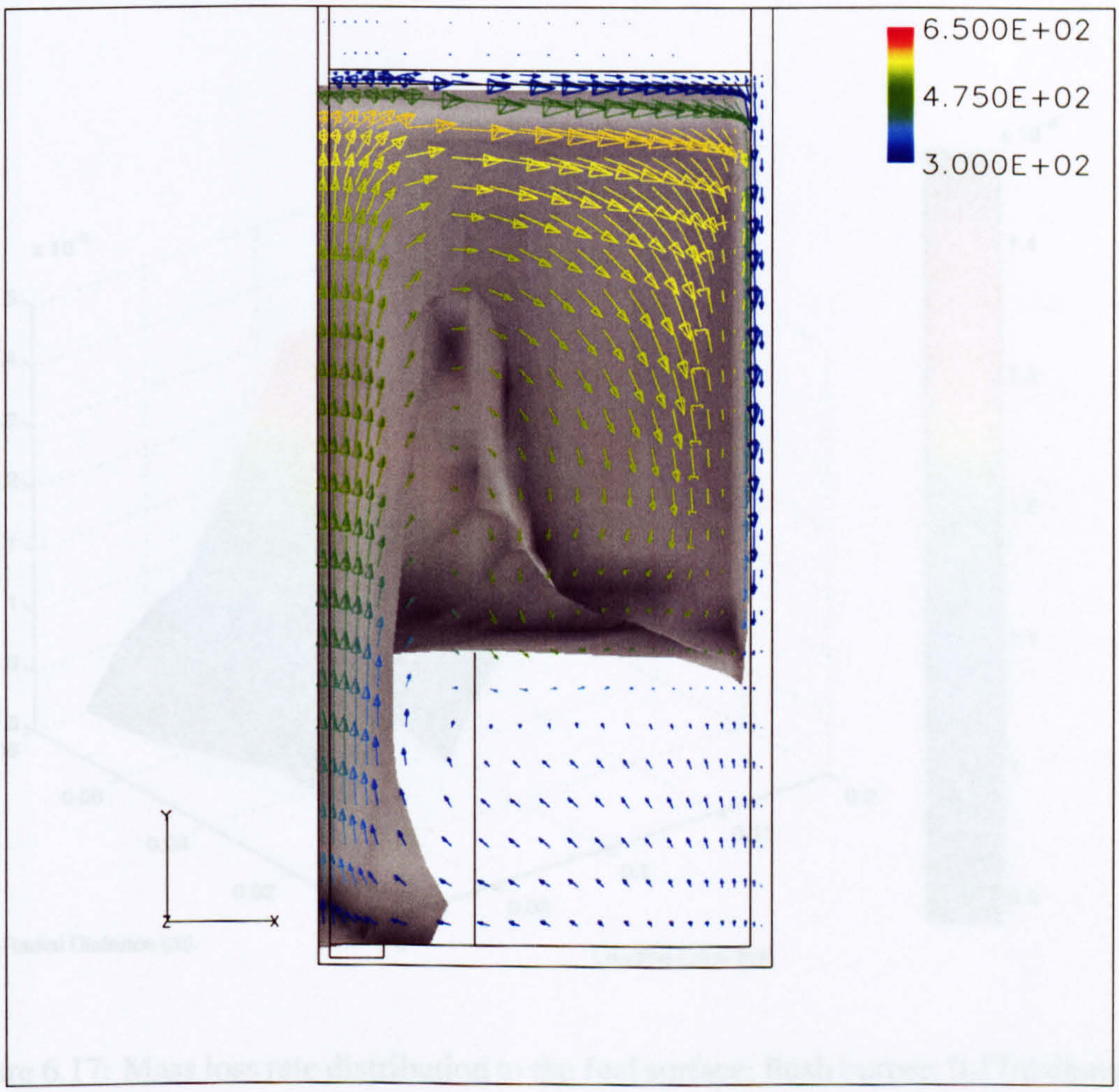

Figure 6.16: Soot volume fraction iso-surface at $1E-07$ with flamelet temperature velocity vectors; 0.36m doorwidth

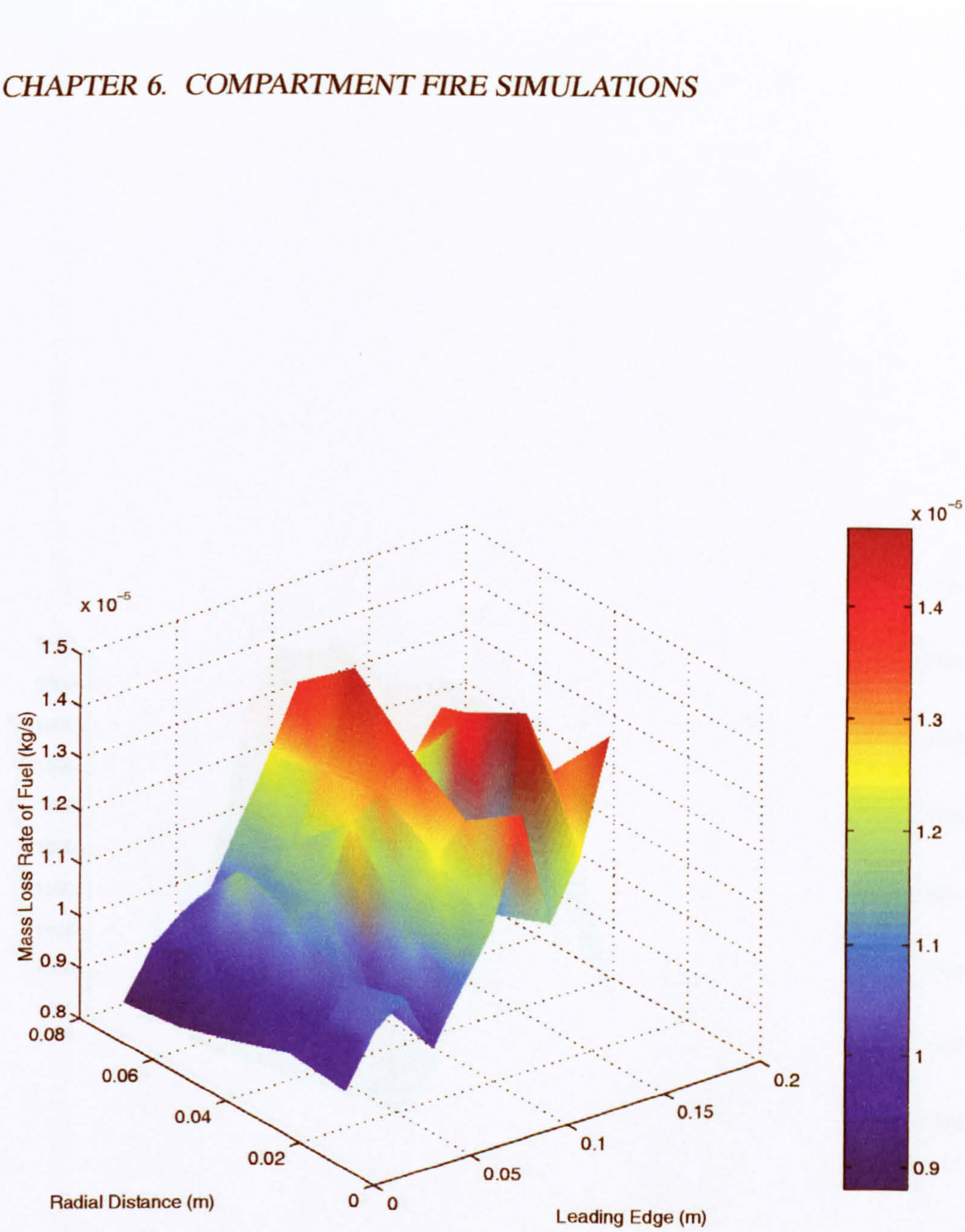

Figure 6.17: Mass loss rate distribution to the fuel surface; flush burner; 0.17m diameter burner; 0.36m doorwidth

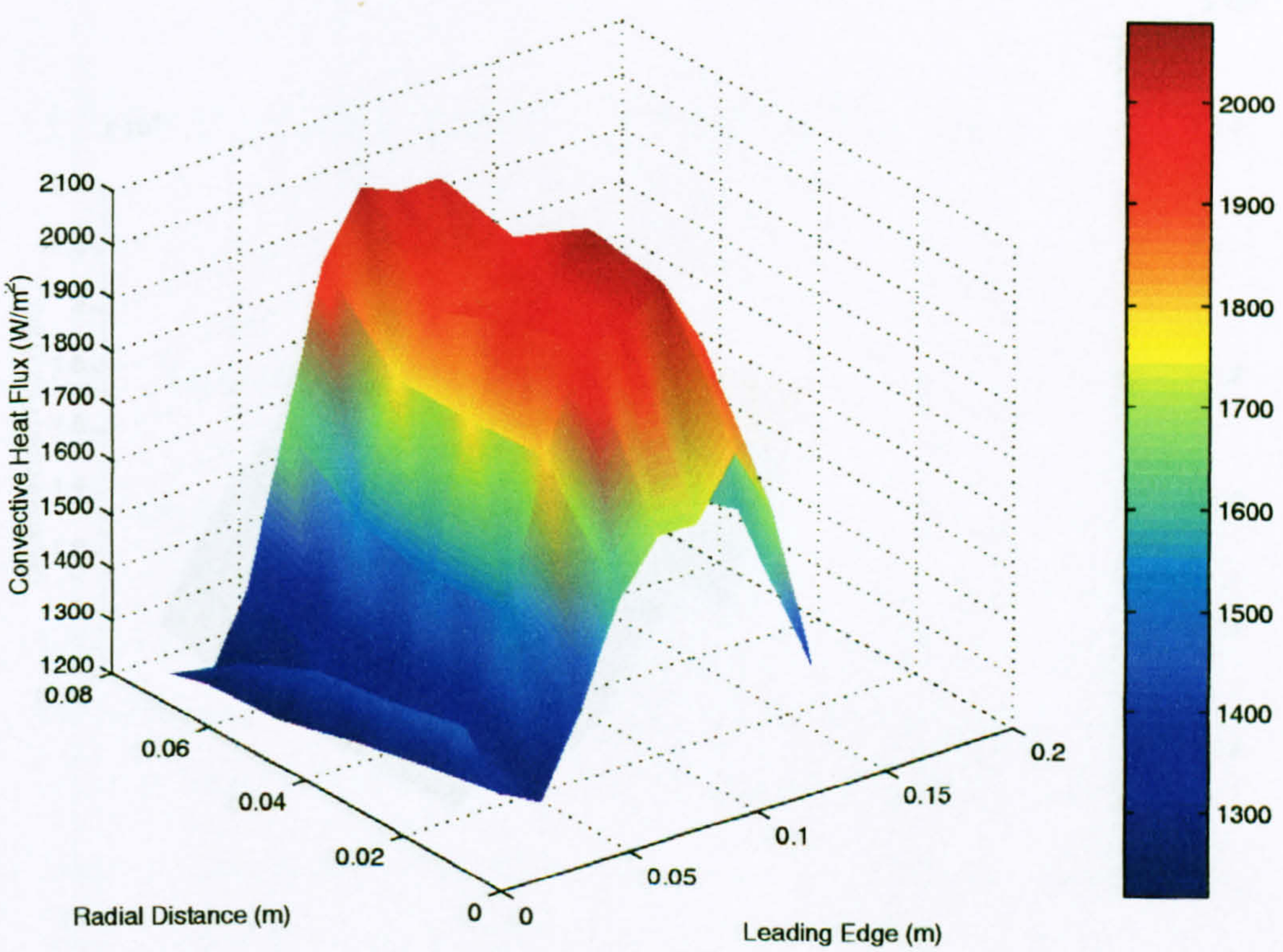

Figure 6.18: Convective heat flux to the fuel surface at 8 minutes after ignition; 32+1 rays; 0.36m doorwidth

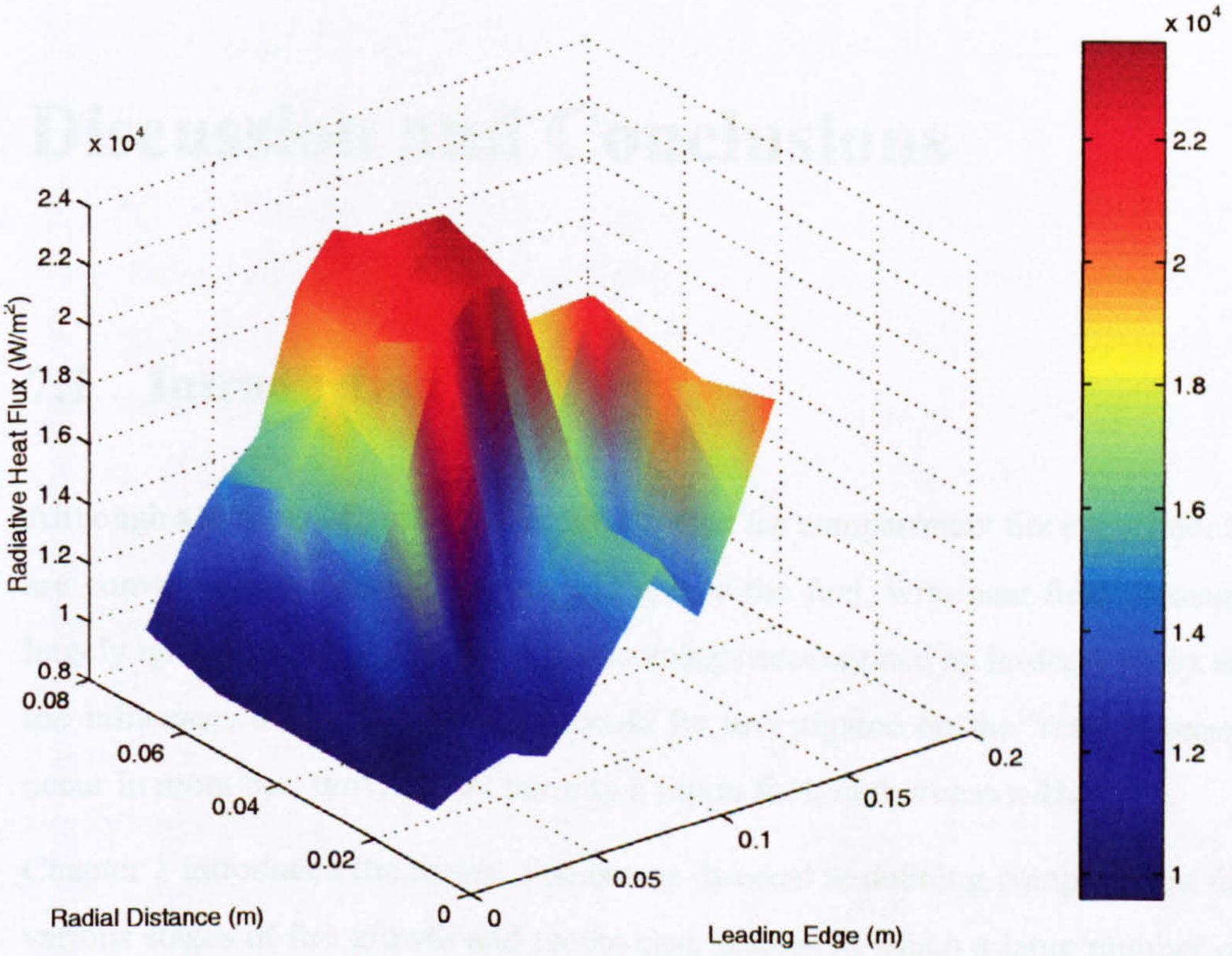

Figure 6.19: Net radiative heat flux to the fuel surface at 8 minutes after ignition; 32+1 rays; 0.36m doorwidth

Chapter 7

Discussion and Conclusions

7.1 Introduction

Although a number of published materials exist for compartment fire experiments, these are conventionally restricted to natural gas as the fuel, with near-field measurements largely ignored. Addressing these shortcomings necessitated an in-depth study in which the influences of the compartment could be investigated on the 'real' processes that occur in room fire, provided by burning a liquid fuel, in this case n-Heptane.

Chapter 1 introduced the thesis. Focus was directed at defining compartment fires, the various stages of fire growth and recent case studies in which a large number of casualties resulted either directly or indirectly from exposure to smoke. Fire statistics were also presented, including the location in which the fire first occurred and the likelihood of the fire spreading to other parts of the building.

Chapter 2 contained a literature review of compartment fires in general terms. A number of techniques were also highlighted that are available to measure the concentration of smoke. As far as the author is aware, previous to this research, no experimental data-set provided results representing the variation in soot concentration within the confines of a compartment fire; with reliance on observations made at bench-scale in an open

environment, or at points far removed from the fire source, where the products of combustion are well mixed and significant cooling has already occurred. Current techniques used to measure soot concentration were discussed.

7.2 Compartment fire and open pool fire experiments

Chapter 3 presented findings from a half-scale room in which liquid heptane was burnt as the fuel. The measurements made were designed to validate the CFD code SOFIE.

To a large extent, the methodological approach to the design of the enclosure fire experiments has closely followed those typically found in the literature. However, due to the need to validate the SOFIE CFD model predictions, the measurements made were extended to include a more rigorous investigation of the boundary conditions, which are not normally accounted for - e.g., the heat loss from the compartment walls.

Improved representation of soot was achieved by the design of a novel water-cooled probe, introduced in this chapter and capable of monitoring the concentration of soot immediately after ignition inside the compartment. The measurements made pertain to a pathlength of 150 mm, which is deemed an acceptable compromise between spatial resolution and signal to noise ratio. One important characteristic of the probe is its ability to be fully traversed during the course of the experiment, with the result of capturing soot profiles at multiple measurement points upon reaching steady-state *without* having to repeat experiments. Ultimately, the main motivation behind this work was to uniquely map soot distribution at a relatively high resolution. However, because no single dependant variable exists, a number of additional parameters were also investigated.

Somewhat transgressional behaviour of soot was observed in the compartment. The production of smoke was shown to be extremely sensitive to small changes in environmental conditions and as a result, large variations in the data may be seen in repeated experiments under supposedly identical conditions, as highlighted in section 3.3.11 and figures referenced within. At the design stage, one of the main additional advantages of

the soot-probe was seen to lie in its ability to traverse during the course of the experiment. By doing this it was able to mitigate the uncertainties introduced from these subtle changes in conditions in repeated experiments. In addition, the timing for the traverse of the soot probe itself proved rather critical due to the use of other convenient, more conventional markers as an indication of steady-state whereupon the probe was traversed. Initial results were poor showing in some instances that soot concentration actually decreased with increased layer height. By looking at the correlations between temperature, gas species concentration and the level of soot it appeared that two distinct processes were occurring in the compartment resulting in a mismatch between steady-state time scales for the soot compared with the other measurable quantities. The previous poorly described levels of soot concentration were indicative of a traverse made before the soot had reached its steady-state.

This phenomenon was particularly prevalent in regions displaying high levels of local spatial instability, such as close to the compartment door. As the probe was inserted deeper into the compartment or positioned higher in the hot upper layer where flow re-laminarisation may occur, the steady-state time-scales became more evenly matched. This research suggests that beyond the near-field region of the burner (in which one would anticipate a high degree of correlation between mixture fraction, temperature and soot), these mechanisms become de-coupled.

The location of a surface mounted thermocouple to the base of the burner was intended to establish the effects of fuel pre-heating on the level of smoke produced, but proved inconclusive. This is mainly due to the inability to separate the effects of room and burner pre-heating. It would also be expected that pre-heating of this nature would reduce the time for the compartment to reach thermal equilibrium. Future enclosure experiments would be best served by using an insulated burner in order to eradicate this influence, particularly if it is neglected in the CFD modelling.

In essence, the subtleties attached to the preferential transportation of soot highlights the importance of representing an accurate description of the flow-field, rather than simple

prescription by a temperature isotherm to mark its movement, as would be found in conventional empirically driven models. Instrument location is therefore critical. CFD techniques can provide information on the most suitable locations for making measurements using in-situ probing techniques outside the regions of large instabilities where steep scalar gradients occur.

The compartment fire experiments also revealed certain trends which were difficult to quantify within the confines of the compartment. As a result, open pool fire experiments were conducted in order to examine characteristics of the fire in more detail.

Two burners were used in the compartment fire experiments, the larger 0.23m diameter burner was employed in open pool fire experiments due to the requirement for instrumental access.

7.3 Field modelling

The simulations performed using SOFIE appear to capture at least the fundamental governing processes which occur in a compartment fire. The use of the simple evaporation model to predict the compartment fire heat release rate is in excellent agreement based on the measured mass loss rate in the compartment and the assumption of ideal combustion efficiency. The inclusion of this model and the coupling of gas and fuel phases is obviously more demanding of the CFD code SOFIE, than is realised using an alternative, more typical approach employing a prescriptive rate of heat release. However, localised sharp increases in radiation heat transfer to the fuel surface (endemic of the 'ray effect' in the radiation model) resulted in unequal mass flow release rates across the surface of the fuel. Increasing the number of rays did not increase the accuracy to a significant extent. However, the mean rate of fuel release rate did closely match that of the experiments and as such the overall heat release rate was found to be in excellent agreement. It must be also emphasised that the coarseness of the grid does not warrant detailed examination of the burner source - particularly if it is not the intention to cap-

ture finely resolved heat transfer mechanisms, such as the enthalpy losses from the pan which are neglected in this work. Doorway profiles of temperature and velocity profiles in the enclosure door, far removed from the source of heat release also showed good agreement using the non-adiabatic flamelet approach.

The spatial soot distribution trends appear to match that of the experiment, marked by complex flow fields which may be seen in figure 6.16 for example, although the absolute concentration level of soot is significantly under-predicted with the exception of the well-ventilated full-doorwidth case. These figures demonstrate the importance of correct siting of optical instruments for measuring soot concentration due to the large instantaneous variability over relatively short pathlengths. The effect of this is somewhat damped in other more conventional measurements, such as the integrated total heat flux, which would be expected to provide complementary measurements to that of soot concentration. As previously highlighted in section 5.4, the soot model constants are optimised for ethylene in the absence of data for heptane. Further work should include laminar flame measurements using heptane as the fuel to calibrate the soot model.

Bibliography

[1] J.C. Yang, A. Hamins, and T. Kashiwagi. Estimate of the effect of scale on radiative heat loss fraction and combustion efficiency. *Combustion Science and Technology*, 96(1-3):183–188, 1994.

[2] D.Roy. The cost of fires - a review of the information available. Technical Report 1, Home Office (UK), 1997.

[3] HMSO. Fires in the home in 1995: results from the british crime survey. Technical Report Report 9/97, Home Office (UK), 1997.

[4] T. Jin. Visibility through fire smoke. *Fire and Flammability*, 9:135, 1978.

[5] T. Jin and T. Yamada. Experimental-study on human emotional instability in smoke filled corridor. *Journal of Fire Sciences*, 8(2):124–134, 1990.

[6] K.D.Steckler, J.G.Quintiere, and W.J.Rinkinen. Flow induced by fire in a compartment. Technical Report NBSIR 82-2520, National Bureau of Standards, 1982.

[7] Williams C. *The Downward Movement of Smoke Due to a Sprinkler Spray*. PhD thesis, South Bank University, 1993.

[8] National Fire Protection Association. *Smoke Movement and Control in High Rise Buildings*. McGraw-Hill, 1994.

[9] A. Y. Snegirev, G. M. Makhviladze, and J. P. Roberts. The effect of particle coagulation and fractal structure on the optical properties and detection of smoke. *Fire Safety Journal*, 36(1):73–95, 2001.

[10] P.H.Thomas. The growth of fire-ignition to full involvement. In G.Cox, editor, *Combustion Fundamentals of Fire*, chapter 5. Academic press, 1995.

[11] S. R. Bishop, P. G. Holborn, and D. D. Drysdale. Experimental comparison with a compartment fire model. *International Communications in Heat and Mass Transfer*, 22(2):235–240, 1995.

[12] R.S.Levine and H.E.Nelson. Full scale simulation of a fatal fire and comparison of results with two multiroom models. Technical Report NISTIR 90-4268, National Institute of Standards and Technology, 1990.

[13] Summary fire statistics united kingdom 1996. Technical report, HMSO (UK), 1998.

[14] D. Fennell. *Investigation into the King's Cross Underground Fire*. HMSO, 1988.

[15] K. Satoh, J.R. Lloyd, and T.K. Yang. Ventilation and smoke layer thickness through a doorway of a cubic enclosure with central volumetric heat source. In *Proceedings of the Fall Meeting of the Eastern Section of the Combustion Institute*. The Combustion Institute, 1980.

[16] N. C. Markatos. The mathematical-modeling of turbulent flows. *Applied Mathematical Modelling*, 10(3):190–220, 1986.

[17] S. Simcox, N.S. Wilkes, and I.P. Jones. Computer simulation of the flow of hot gases from the fire at king's cross underground station. In *Proceedings of the Symposium on King's Cross Underground Fire*. Institute of Mechanical Engineers, 1989.

[18] K.Kawagoe. Fire behaviour in rooms. Technical Report Report 27, The Building Research Institute (Japan), 1958.

[19] D.D.Drysdale. *An introduction to fire dynamics*. John Wiley and sons, 1985.

[20] P.H.Thomas, H.J.M.Heselden, and M.Law. Fully developed compartment fires, two kinds of behaviour. Technical Report Technical Paper No. 183, Fire Research Station, 1967.

[21] C. K. Law and G. M. Faeth. Opportunities and challenges of combustion in microgravity. *Progress in Energy and Combustion Science*, 20(1):65–113, 1994.

[22] I. Thomas and I. Bennetts. Fires in enclosures with single ventilation openings - comparison of long and wide enclosures. In *Fire safety science - Proceedings of the 6th International Symposium*. Hemisphere Publishing Corporation, 1999.

[23] V. Babrauskas. Compf2 - a program for calculating post-flashover fire temperatures. Technical Report NBS Technical Note 991, National Bureau of Standards, 1979.

[24] M.M. Hirschler. The measurement of smoke in rate of heat release equipment in a manner related to fire hazard. *Fire safety journal*, 17:239–258, 1991.

[25] G.W. Mulholland, V. Henzel, and V. Babrauskas. The effect of scale on smoke emission. In *Fire safety science - Proceedings of the First International Symposium*. Hemisphere Publishing Corporation, 1988.

[26] M. Foley and D. Drysdale. Note: Smoke measurement and the cone calorimeter. *Fire and Materials*, 18:385–387, 1994.

[27] R. H. Whiteley. Short communication: Some comments concerning the measurement of smoke. *Fire and Materials*, 18:57–59, 1994.

[28] G. Porter. Carbon formation in the combustion wave. In *Fourth Symposium (International) on Combustion*, pages 248–252. The Combustion Institute, 1953.

[29] H.B. Palmer and C.F. Cullis. *Chemistry and Physics of Carbon*. Marcel Dekker, 1965.

[30] U. Bonne, K.H. Homann, and H.Gg. Wagner. Carbon formation in premixed flames. In *Tenth Symposium (International) on Combustion*. The Combustion Institute, 1965.

[31] A.D'Alessio, F.Beretta, and C.Venitozzi. Optical investigation on soot forming methane- oxygen flames. *Combustion Science and Technology*, 5, 1972.

[32] P.A.Tesner, T.D.Snegiriova, and V.G.Knorre. Kinetics of disperse carbon formation. *Combustion and Flame*, 17(2), 1971.

[33] A. V. Krestinin, M. B. Kislov, A. V. Raevskii, O. I. Kolesova, and L. N. Stesik. On the mechanism of soot particle formation. *Kinetics and Catalysis*, 41(1):90–98, 2000.

[34] M. Berthelot. *Ann Chim Phys*, 1866.

[35] I.Glassman. Soot formation in combustion processes. In *Twenty Second Symposium (International) on Combustion*, pages 295–311. The Combustion Institute, 1988.

[36] S.J. Harris and A.M. Weiner. Soot particle growth in premixed toluene/ethylene flames. *Combustion Science and Technology*, 38(1):75–87, 1984.

[37] J. H. Kent. Turbulent-diffusion flame sooting - relationship to smoke-point tests. *Combustion and Flame*, 67(3):223–233, 1987.

[38] Tewarson A. Generation of heat and chemical compounds in fires. In *The SFPE handbook of fire protection engineering, 1st Edition*. National Fire Protection Association, 1988.

[39] G.T Tamura. Effects of people movement and fire fighting on smoke movement and control. In *Smoke Movement and Control in High Rise Buildings*. McGraw-Hill, 1994.

[40] U. O. Koylu, C. S. Mcenally, D. E. Rosner, and L. D. Pfefferle. Simultaneous measurements of soot volume fraction and particle size/microstructure in flames using a thermophoretic sampling technique. *Combustion and Flame*, 110(4):494–507, 1997.

[41] H. Bockhorn, H. Geitlinger, B. Jungfleisch, T. Lehre, A. Schon, T. Streibel, and R. Suntz. Progress in characterization of soot formation by optical methods. *Physical Chemistry Chemical Physics*, 4(15):3780–3793, 2002.

[42] M. Y. Choi, G. W. Mulholland, A. Hamins, and T. Kashiwagi. Comparisons of the soot volume fraction using gravimetric and light extinction techniques. *Combustion and Flame*, 102(1-2):161–169, 1995.

[43] D. L. Black, M. Q. Mcquay, and M. P. Bonin. Laser-based techniques for particle-size measurement: a review of sizing methods and their industrial applications. *Progress in Energy and Combustion Science*, 22(3):267–306, 1996.

[44] SFPE. *SFPE Handbook of Fire Protection Engineering, 2nd Edition*. National Fire Protection Association, 1995.

[45] C. S. Mcenally, U. O. Koylu, L. D. Pfefferle, and D. E. Rosner. Soot volume fraction and temperature measurements in laminar nonpremixed flames using thermocouples. *Combustion and Flame*, 109(4):701–720, 1997.

[46] M.Y. Choi, F.L. Dryer, and J.B. Haggard. Simultaneous optical measurements of temperature, soot volume fraction and co_2 concentrations in a heptane pool fire. In *Twenty-Fifth Symposium (International) on Combustion*, pages 1471–1480, 1994.

[47] J.Mullins and A.Williams. The optical properties of soot: A comparison between experimental and theoretical values. *Fuel*, 66:277–280, 1987.

[48] M.Z. Smoluchowski. *Phys. Chem. Abt*, 92:129, 1917.

[49] D.J. Rasbash. Smoke and toxic products produced at fires. *Transactions and Journal of the Plastics Institute*, (2):55–62, 1967.

[50] V. Babrauskas. The cone calorimeter. In *The SFPE handbook of fire protection engineering, 2nd Edition*. National Fire Protection Association, 1995.

[51] T. Jin. Studies on human behaviour and tenability in fire smoke. In *Fifth International Symposium on Fire Safety Science*, pages 3–21. Hemisphere Publishing Corporation, 1997.

[52] Van de Hulst H.C. *Light Scattering by Small Particles*. Dover, 1981.

[53] Kerker M. *The Scattering of Light, and Other Electromagnetic Radiation*. Academic Press, 1969.

[54] C.F. Bohren and D.R. Huffman. *Absorption and Scattering of Light by Small Particles*. Wiley-Interscience, 1983.

[55] U. O. Koylu and G. M. Faeth. Optical-properties of overfire soot in buoyant turbulent- diffusion flames at long residence times. *Journal of Heat Transfer-transactions of the Asme*, 116(1):152–159, 1994.

[56] T. L. Farias, M. G. Carvalho, U. O. Koylu, and G. M. Faeth. Computational evaluation of approximate rayleigh-debye- gans/fractal-aggregate theory for the absorption and scattering properties of soot. *Journal of Heat Transfer-transactions of the Asme*, 117(1):152–159, 1995.

[57] S. H. Chan, J. Q. Yin, and B. J. Shi. Structure and extinction of methane-air flamelet with radiation and detailed chemical kinetic mechanism. *Combustion and Flame*, 112(3):445–456, 1998.

[58] Hottel H.C. and Sarofim A.F. *Radiative Transfer*. McGraw-Hill, 1967.

[59] D.Y. Svet. *Thermal Radiation: Metals, Semi-conductors, Ceramics, Partially Transparent Bodies, and Films*. Consultants Bureau, 1965.

[60] D.A Purser. Toxicity assessment of combustion products. In *The SFPE handbook of fire protection engineering, 2nd Edition*. National Fire Protection Association, 1995.

[61] D.A. Purser. Toxicity assessment of combustion products. In *The SFPE handbook of fire protection engineering, 2nd Edition*. National Fire Protection Association, 1988.

[62] Health and Safety Executive. *Occupational Exposure Limits, 2000*. 2001.

[63] World Health Organisation. *Air Quality Guidelines*. 1999.

[64] L. A. Gritzo, Y. R. Sivathanu, and W. Gill. Transient measurements of radiative properties, soot volume fraction and soot temperature in a large pool fire. *Combustion Science and Technology*, 139(1-6):113–136, 1998.

[65] M.F.Modest. The weighted-sum-of-gray-gases model for arbitrary solution methods in radiative transfer. *Journal of Heat Transfer*, 113:650–656, 1991.

[66] R.O. Buckius and C.L. Tien. Infrared flame radiation. *International Journal of Heat and Mass Transfer*, 20(2):93–106, 1977.

[67] L Orloff. In *Eighteenth Symposium (International) on Combustion*, page 549. The Combustion Institute, 1981.

[68] A. Shinotake, S. Koda, and K. Akita. An experimental-study of radiative properties of pool fires of an intermediate scale. *Combustion Science and Technology*, 43(1-2):85–97, 1985.

[69] L. Orloff, J. De Ris, and G.H. Markstein. Upward turbulent flame spread and burning of fuel surface. In *Fifteenth Symposium (International) on Combustion*, pages 183–182. The Combustion Institute, 1974.

[70] I.S. Wichman. Theory of opposed-flow flame spread. *Progress in Energy and Combustion Science*, 18:553–593, 1992.

[71] A.C. Fernandez-Pello. *Laminar Flame Spread over Flat Solid Surfaces*. PhD thesis, University of California, 1975.

[72] A.C. Fernandez-Pello and F.A. Williams. Laminar flame spread over pmma surfaces. In *Fifteenth Symposium (International) on Combustion*. The Combustion Institute, 1975.

[73] A.C. Fernandez-Pello and T. Hirano. Controlling mechanisms of flame spread. *Combustion Science and Technology*, 32:1–31, 1983.

[74] A. Ito and T. Kashiwagi. Temperature measurements in pmma dusing downward flame spread in air using holographic interferometry. In *Twenty-first Symposium (International) on Combustion*. The Combustion Institute, 1986.

[75] I.Glassman. *Combustion*. Academic press, 1987.

[76] J.G. Quintiere. Fire growth: An overview. *Fire Technology First Quarter*, pages 7–31, 1997.

[77] W.J. Parker. Flame spread model for cellulosic materials. *Fire and Flammability*, 3:254–269, 1972.

[78] T. Hirano, S. Noreikis, and T.E Waterman. Measured velocity and temperature profiles near flames spreading over a thin combustible solid. *Combustion and Flame*, 23:83–96, 1974.

[79] J.B.M. Pierce. Compartment and open pool fire experimental data - CFD prediction and validation. Technical Report 1, Cranfield University, 2002.

[80] Held T.J, Marchese A.J, and Dryer F.L. A semi-empirical reaction mechanism for n-heptane oxidation and pyrolysis. *Combustion Science and Technology*, 123(1), 1997.

[81] R. Seiser, H. Pitsch, K. Seshadri, W. J. Pitz, and H. J. Curran. Extinction and autoignition of n-heptane in counterflow configuration. *Proceedings of the Combustion Institute*, 28:2029–2037, 2000.

[82] International Organisation for Standardisation. BS476-33:1993, ISO9705:1993; fire tests on building materials and structures. full-scale room test for surface products, 1993.

[83] ASTM. Standard guide for room fire experiments astm e 603. Technical report, American Society for Testing and Materials, 1977.

[84] R. Gardon. An instrument for the direct measurement of intense thermal radiation. *Review of Scientific Instruments*, (5):366–370, 1953.

[85] S.M. Hyde. *Field Modelling of Carbon Monoxide Production in Vitiated Compartment Fires*. PhD thesis, Cranfield University, 2000.

[86] L. G. Blevins and W. M. Pitts. Modeling of bare and aspirated thermocouples in compartment fires. *Fire Safety Journal*, 33(4):239–259, 1999.

[87] B. McCaffrey and G. Heskestad. A robust bi-directional low-velocity probe for flame and fire application. *Combustion and Flame*, 26:125–127, 1976.

[88] A. F. Robertson and T. J. Ohlemiller. Low heat-flux measurements: Some precautions. *Fire Safety Journal*, 25(2):109–124, 1995.

[89] Devaud C.D. Moss J.B. Pierce, J.B.M. Mass loss rates and near-field open pool fire measurements - a comparison with compartment fires. In *Interflam 2001 - Conference Proceedings of the Ninth International Fire Science and Engineering Conference*, volume 2, pages 1349–1354, 2001.

[90] G. Cox. Gas velocity measurement in fires by the cross-correlation of random thermal fluctuations - a comparison with conventional techniques. *Combustion and Flame*, 28(2):155–163, 1977.

[91] G.H. Markstein. In *Eighteenth Symposium (International) on Combustion*, page 1055. The Combustion Institute, 1981.

[92] J. L. De Ris. Fire radiation - a review. In *Seventeenth Symposium (International) on Combustion*, pages 1003–1016, 1979.

[93] W.L. Grosshandler. Radiation from nonhomogenous fires. Technical Report Technical Report RC79-BT-9, Factory Mutual Research, 1979.

[94] J. L. De Ris, P. K. Wu, G. Heskestad, C. Fernandez-pello, L. D. Smoot, R. G. Gann, J. Gore, and M. Delichatsios. Radiation fire modeling. *Proceedings of the Combustion Institute*, 28(6):2751–2759, 2000.

[95] J.S. Truelove. Zone method for radiative heat transfer calculations. Technical Report Technical Report HTFS DR33, A.E.R.E.

[96] B. S. Haynes and H. G. Wagner. Soot formation. *Progress in Energy and Combustion Science*, 7(4):229–273, 1981.

[97] S.H. Kang, K.T. Hwang, and W.L Chung. Soot zone structure and sooting limit in diffusion flames: comparison of counterflow and co-flow flames. *Combustion and Flame*, 109:266–281, 1997.

[98] J. Nagle and R.F. Strickland-Constable. Oxidation of carbon between 1000-2000°c. In *Proceedings of the Fifth Carbon Conference*, volume 1, pages 154–164, 1962.

[99] S. J. Brookes and J. B. Moss. Predictions of soot and thermal radiation properties in confined turbulent jet diffusion flames. *Combustion and Flame*, 116(4):486–503, 1999.

[100] J. B. Moss and C. D. Stewart. Flamelet-based smoke properties for the field modelling of fires. *Fire Safety Journal*, 30(3):229–250, 1998.

[101] C. D. Stewart, K. J. Syed, and J. B. Moss. Modeling soot formation in non-premixed kerosene air flames. *Combustion Science and Technology*, 75(4-6):211–226, 1991.

[102] C.P. Fenimore and G.W. Jones. Oxidation of soot by hydroxyl radicals. *Journal of Physical Chemistry*, 71:593–597, 1967.

[103] K.G. Neoh, J.B Howard, and A.F. Sarofim. *Particulate Carbon Formation During Combustion*. Plenum, New York, 1981.

[104] D.B.Spalding. Concentration fluctuations in a round turbulent jet. *Chemical Engineering Science*, 26, 1971.

[105] B.E.Launder and D.B.Spalding. *Lectures in mathematical models of turbulence*. Academic press, 1972.

[106] B.F.Magnussen and B.H.Hjertager. On mathematical modeling of turbulent combustion with special emphasis on soot formation and combustion. In *Sixteenth Symposium (International) on Combustion*, pages 719–729, 1976.

[107] R. W. Bilger. Turbulent-diffusion flames. *Annual Review of Fluid Mechanics*, 21(4-6):101–135, 1989.

[108] R.W.Bilger. Reaction rates in diffusion flames. *Combustion and Flame*, 30(3):277.

[109] R. W. Bilger, L. R. Saetran, and L. V. Krishnamoorthy. Reaction in a scalar mixing layer. *Journal of Fluid Mechanics*, 233(3):211–242, 1991.

[110] N. Swaminathan and R. W. Bilger. Scalar dissipation, diffusion and dilatation in turbulent h-2- air premixed flames with complex chemistry. *Combustion Theory and Modelling*, 5(3):429–446, 2001.

[111] R. W. Bilger. Future progress in turbulent combustion research. *Progress in Energy and Combustion Science*, 26(4-6):367–380, 2000.

[112] A.N. Kolmogorov. Dissipation in energy in locally isotropic turbulence. *Dokl. Akad. Nauk SSSR*, 32:19–21, 1941.

[113] G.I Taylor. Statistical theory of turbulence. *Proc. R. Soc. London.*, pages 421–464, 1935.

[114] L.F. Richardson. *Weather prediction by numerical process*. Cambridge University Press, (republished by Dover, 1965), 1922.

[115] M.J.Lewis, J.B.Moss, and P.A.Rubini. CFD modelling of combustion heat transfer in compartment fires. In *Proceedings of the fifth international symposium on fire safety science*, pages 463–474, 1997.

[116] N.W.Bressloff. *CFD prediction of coupled radiation heat transfer and soot production in turbulent flames.* PhD thesis, Cranfield University, 1996.

[117] Gupta A.K. Kumar, S. and G. Cox. Effects of thermal radiation on the fluid dynamics of compartment fires. In *Third International Symposium on Fire Safety Science*, pages 345–354. Hemisphere Publishing Corporation, 1991.

[118] Galea E.R. Hoffman N. Mawhinney, R.N. and M.K. Patel. A critical comparison of a phoenics based fire model with experimental compartment fire data. *Journal of Fire Protection Engineering*, 6:137–152, 1994.

[119] Galea E.R. Hoffman N. Kerrison, L. and M.K. Patel. A comparison of a flow3d based fire model with experimental compartment fire. *Fire Safety Journal*, 23:387, 1994.

[120] K. J. Young and J. B. Moss. Modelling sooting turbulent jet flames using an extended flamelet technique. *Combustion Science and Technology*, 105(1-3):33–53, 1995.

[121] Hottel H.C. and Sarofim A.F. *Radiative Transfer*. McGraw-Hill, 1967.

[122] H.Schlichting. *Boundary Layer Theory*. McGraw-Hill, 1979.

Appendix A

Model Constants

A.1 k − ϵ turbulence model

$C_{1\epsilon} = 1.44$

$C_{2\epsilon} = 1.92$

$C_{3\epsilon} = 1$

$C_{\mu} = 0.09$

$\sigma_k = 1$

$\sigma_\epsilon = 1.3$

A.2 Mixture fraction variance

$C_{g1} = 2.8$

$C_{g2} = 1.25$

A.3 Eddy Break Up

$$cr_f = 4.0$$

$$cr_o = 4.0$$

$$cr_p = 2.0$$

$$cr_c = 6.0$$

$$cr_{oc} = 6.0$$

Appendix B

Soot Volume Fraction Determination

B.1 Extinction Measurements

The smoke properties of primary interest to the fire community are light extinction, visibility and detection. The most widely measured smoke property is the light extinction coefficient. The physical basis for light extinction measurements is Bouguer's law, which relates the intensity of the incident monochromatic light and the intensity of the light transmitted through the pathlength of the smoke by the following equation:

$$\frac{I}{I_0} = -\exp \int_0^L \kappa(l) dl \tag{B.1}$$

Where κ is the light extinction coefficient.

Visibility depends on many factors, including the scattering and the absorption coefficient of the smoke by the presence of particulates (soot), the illumination of the room, whether the sign is light-emitting or light-reflecting and the wavelength of the light.

Utilization of Bouguer's law for extinction estimates assumes that other certain simplifying assumptions are met. For example, it is assumed that the scattered light will have the same wavelength as the incident light. Although this is not precisely the case,

wavelength changes are so small that they can be neglected. A second assumption is that the particles act as independent scatterers, that is, the scattering of light by one particle does not influence the scattering by another. The third assumption is that of single scattering, which is another way of saying that a maximum of one scatter per photon is allowed. This assumption implies that Bouguer's law is valid only for thin clouds or low concentrations.

In these experiments a diode laser of $\lambda = 670 \times 10^{-9}m$ was used. The size criteria is cited as being (2π r / λ << 1). Here r is the mean particle diameter and in this case gives an upper limit on the particle size of 105nm.

Under the assumption that soot particles are spherical then the following relationship may be assumed:-

$$\kappa = \int_0^\infty N\pi r^2 Q_{Abs} dr \tag{B.2}$$

Another fundamental factor required for consideration of the optical properties of smoke aerosols is the particle refractive index, m. The refractive index of a material is defined as the ratio of the speed of light in the material to the speed of light in a vacuum. For aerosol particles where there is appreciable absorption of radiation as well as scattering it is necessary to express the refractive index of a material as a complex number of the form **m** = n -kj. For this research, the complex refractive index was chosen to be $m = 1.89 - 0.44j$ put forward by Mullins as being relevant to heptane soot [47].

Using the *Lorentz-Mie* theory, the absorption efficiency (Q_{Abs}) may be expressed by:-

$$Q_{Abs} = \frac{48\pi nkr}{\lambda(4n^2k^2 + (n^2 - k^2 + 2)^2)} \tag{B.3}$$

In light of the aforesaid assumptions, equation B.2 can then be re-arranged:-

$$\kappa(l) = \frac{36\pi nk}{\lambda(4n^2k^2 + (n^2 - k^2 + 2)^2)} \int_0^\infty N\frac{4}{3}\pi r^3 dr,$$
$$= \frac{36\pi nk}{\lambda(4n^2k^2 + (n^2 - k^2 + 2)^2)} fv,$$
$$= \ln \frac{I_0}{I(l)} \quad \text{(B.4)}$$

Where fv is the soot volume fraction. By using equation B.4, light extinction measurements are able to discern soot volume fraction due to the relationship to the measurable light intensity ratio.

Appendix C

Governing Equations

The three basic conservation equations to be considered are:

- Conservation of momentum (Newton's second law)
- Conservation of mass (continuity)
- Conservation of energy (first law of thermodynamics)

Adding equations of state will allow solution of temperature, T, pressure, P, density, ρ, and the velocity vector $u\imath+v\jmath+wk$. For the reacting flows involved with fire, equations for the conservation of species are also necessary, as are relations for the transport properties such as viscosity, μ, for momentum diffusion, and thermal conductivity, κ, for energy diffusion.

In the Reynolds Averaged Navier Stokes (RANS) type field models, the basic Navier-Stokes equations are averaged in order to obtain values for time-mean flow. The governing equations were derived for isothermal incompressible flow, which is not applicable for flows with large variations in density, such as in the presence of combustion. Reynolds averaging therefore when applied to variable density flows introduces a number of further averaged correlations which includes the density fluctuation terms. These

additional correlations also require modelling leading to a far more complex solution procedure. A more convenient description which avoids this complexity is achieved via Favre (density weighted) averaging.

The problem of closure for the averaged equations implies that some model has to be introduced for the Reynolds stress tensor and the turbulent scalar fluxes. The most commonly-adopted and wide-spread models are based on the eddy viscosity hypothesis and the two equation $k - \varepsilon$ turbulence models which involves two additional partial differential equations for the turbulent kinetic energy, k, and the energy dissipation rate ε.

C.1 Conservation of Momentum

Newton's second law relates the acceleration, **a**, of a body to the Force, **F**, acting on it. Thus for a particle of mass, m,

$$\mathbf{F} = m\mathbf{a} \tag{C.1}$$

A restatement of the same principle, suitable to applications in fluid mechanics, is the momentum principle, which states that the force is equal as a vector to the time-rate of change of linear momentum, **mu**

$$\mathbf{F} = \frac{d}{dt} m\mathbf{u} \tag{C.2}$$

The above equation for a finite control volume (CV) fixed in space with surfaces (CS) can be written as [121]:

$$\frac{d}{dt}\int_{CV} \rho\mathbf{u}dv = \mathbf{F} - \int_{CS} \mathbf{u}\rho\mathbf{u}d\mathbf{A} \tag{C.3}$$

where dv is a volume element and $d\mathbf{A} = dA\mathbf{n}$ is the orientated surface with area dA and the unit normal vector $\mathbf{n}$ perpendicular to the surface and pointing outwards from the element. The quantity $\rho \mathbf{u} d\mathbf{A}$ is the mass flux through an element $d\mathbf{A}$. If $\mathbf{u}d\mathbf{A}$ is positive, one has an outflow, whereas, if $\mathbf{u}d\mathbf{A}$ is negative, one has an inflow.

In conservation form, the equation of motion can be described by the following equation:

$$\frac{\partial(\bar{\rho}\tilde{u}_i)}{\partial t} + \frac{\partial(\bar{\rho}\tilde{u}_i\tilde{u}_j)}{\partial x_j} = -\frac{\partial \bar{P}}{\partial x_i} - \frac{\partial}{\partial x_j}\left(\overline{\tau_{ij}} + \overline{\rho u_i'' u_j''}\right) + \bar{S}_i \tag{C.4}$$

The first term on the left hand side is the rate of change (increase) of momentum with time in the control volume and the second term represents the convective momentum loss per unit volume through the surface of the control volume. On the right hand side, the penultimate term accounts for the surface forces (normal and shear forces resulting from the flow field) on a per unit volume basis and includes the normal and shear stress tensor, τ. Momentum sources (sinks) conclude the equation which include the body forces which act through the entire control volume. For the purposes of this work, gravity is the only body force that is considered.

The components of the combined stress tensor, σ_{ij} are:

$$\sigma_{ij} = \begin{pmatrix} \tau_{ii} & \tau_{ij} & \tau_{ik} \\ \tau_{ji} & \tau_{jj} & \tau_{jk} \\ \tau_{ki} & \tau_{kj} & \tau_{kk} \end{pmatrix} \tag{C.5}$$

where each stress term is located in a plane perpendicular to the direction specified by the first subscript and acts in a direction indicated by the second subscript. The diagonal terms with the repeated indices are thus normal stresses, while the six remaining off-diagonal terms represent the shear stresses. Since the stress tensor is symmetric: $\tau_{ij} = \tau_{ji}$, $\tau_{jk} = \tau_{kj}$ and $\tau_{ik} = \tau_{ki}$, only six independent terms result.

Symmetry is required to prevent the angular acceleration for a fluid parcel from going

to infinity as the volume approaches zero.

Pressure and stresses act upon the surface of the control volume resulting in a microscopic momentum flux across the surface. Assuming that a linear dependence between stress and rate of strain provides a path for relating the stress terms in Equation C.5 to the flow field for the molecular rate of transport of momentum:

$$\sigma_{ij} = -\rho\delta_{ij} + \mu\left(\frac{\partial u_i}{\partial x_j} + \frac{\partial u_j}{\partial x_i}\right) + \delta_{ij}\mu\prime\frac{\partial uk}{\partial x_k} \tag{C.6}$$

where μ is the coefficient of viscosity, $\mu\prime$ is the second coefficient of viscosity and δ_{ij} takes a value of 1 along the diagonal(i=j) and a value of 0 for off diagonal terms (i≠j).

The advantage of using a momentum equation in conservation form is that global momentum conservation (no artificial sources or sinks created) can be satisfied.

It is an unnecessary duplication to provide a derivation of the Navier-Stokes equations here, which can be found in many text books (e.g Schlichting [122].

C.2 Conservation of Mass

The continuity equation in conservation form for an infinitesimally small fluid element fixed in space is:

$$\frac{\partial\rho}{\partial t} + \frac{\partial(\rho u)}{\partial x} + \frac{\partial(\rho v)}{\partial y} + \frac{\partial(\rho w)}{\partial z} = 0 \tag{C.7}$$

which describes the rate at which density in the element increases plus the mass flux through the surface of the element must equal zero (assuming no sources or sinks).

Using index notation, Equation C.7 for cartesian coordinates is:

$$\frac{\partial\rho}{\partial t} + \frac{\partial(\rho u_j)}{\partial x_j} = 0 \tag{C.8}$$

The Favre-averaged form of the governing equation is:

$$\frac{\partial(\overline{\rho})}{\partial t} + \frac{\partial(\overline{\rho}\widetilde{u}_j)}{\partial x_j} = 0 \tag{C.9}$$

The restriction introduced by Boussinesq assumes that density variations may be neglected, that is held constant, with the exception of buoyancy (gravity terms). This assumption requires that the density be much larger than the local differences. In addition, a linear relationship between temperature and density is assumed for the evaluation of the buoyancy term.

C.3 Conservation of Energy

Applying the first law of thermodynamics representing the change in internal energy, E, and work, W, done by the addition of heat, Q, to a control volume

$$\frac{dQ}{dt} = \frac{dE}{dt} + \frac{dW}{dt} \tag{C.10}$$

to an infinitesimal element provides the starting point for the energy equation based on enthalpy

$$\frac{\partial(\rho h)}{\partial t} + \frac{\partial(\rho u_j h)}{\partial x_j} = \frac{\partial p}{\partial t} - \frac{\partial q_j}{\partial x_j} + \rho u_j f_j + \frac{\partial(u_i \sigma_{ij})}{\partial x_j} + S_E \tag{C.11}$$

The two terms on the left hand side of equation C.11 represent the rate of increase in enthalpy per unit volume and the enthalpy per unit volume transferred by convection through the control surface. On the right hand side, this equals the sum of the rate of change of static pressure, heat transfer through the surface by temperature and concentration gradients, work done by body and surface forces and finally energy sources such as energy generation and radiation absorption-emission. Potential and kinetic energies for fires will be considered small (zero) when compared to the enthalpy of the fluid.

The $\frac{d(u_i\sigma_{ij})}{dx_j}$ term is a dissipation function which represents the conversion of mechanical energy into heat as a result of viscous surface losses due to fluid motion. Since fire velocities are generally low, viscous dissipation can be dismissed as very small. Simplifying equation C.11 yields:

$$\frac{\partial(\rho h)}{\partial t} + \frac{\partial(\rho u_j h)}{\partial x_j} = \frac{\partial p}{\partial t} - \frac{\partial q_j}{\partial x_j} + S_E \tag{C.12}$$

Turning to the gradient term, it represents the transfer of energy through the surface by conduction and molecular diffusion of species with different enthalpies:

$$\frac{\partial q_j}{\partial x_j} = \frac{\partial q_{cond,j}}{\partial x_j} + \frac{\partial q_{diff,j}}{\partial x_j} \tag{C.13}$$

Fourier's law is used for the heat conduction formulation:

$$q_{cond} = -k\frac{\partial T}{\partial x_j} \tag{C.14}$$

Energy exchange due to concentration gradients between n different species (Dufour effect), although small, is given for species α by:

$$q_{diff} = -\sum_{\alpha}^{n} \Gamma_\alpha h_\alpha \frac{\partial Y_\alpha}{\partial x_j} \tag{C.15}$$

Where Γ_α is the molecular diffusion coefficient. Y_α is the species mass fraction and h_α is the enthalpy of species. Substituting into equation C.12 yields:

$$\frac{\partial(\rho h)}{\partial t} + \frac{d(\rho u_j h)}{\partial x_j} = \frac{\partial p}{\partial t} - \frac{\partial}{\partial x_j}\left[-k\frac{\partial T}{\partial x_j} - \sum_{\alpha}^{n} \Gamma_\alpha h_\alpha \frac{\partial Y_\alpha}{\partial x_j}\right] + S_E \tag{C.16}$$

This version of the energy conservation relation is coupled to the conservation of species through both the conduction and concentration gradient terms. Radiation is included as a source.

The conservation equations outlined above are formulated for a continuous domain. The first step in solving the set of non-linear PDEs is to replace the continuous formulations with algebraic approximations (differences) to the derivatives which are evaluated at a discrete number of locations (grid nodes).